
**SYNTHESIS AND CHARACTERIZATION OF COPPER
CHALCOGENIDE NANOPARTICLES AND THEIR USE IN
SOLUTION PROCESSED PHOTOVOLTAICS**

Mubiayi Pierre Kalenga
(367937)

**A Thesis submitted to the Faculty of Science, School of Chemistry at
University of the Witwatersrand, in fulfilment of the requirements for the
degree of Doctor of Philosophy**

Supervisors: Dr. Nosipho Moloto (Wits, School of Chemistry)
Prof. Justice Moloto (VUT, Chemistry)
Dr. Lucky M. Sikhwivhilu (Mintek, AMD)

Johannesburg 2015

DECLARATION

I declare that this thesis is my own, unaided work. It is being submitted for the degree of Doctoral of Philosophy in Science at the University of the Witwatersrand, Johannesburg. It has not been submitted before for any degree or examination in any other University.

MUBIAYI PIERRE KALENGA



18th Day of May 2015

ABSTRACT

Photovoltaic cells offer a good alternative to the fossil fuels. Several approaches are being analysed in order to have solar cells that are capable to conquer the energy market all around the world. Quantum dots (QDs) have already proven features that can be taken into account to improve the properties of solar cells. Metal selenide nanoparticles (NPs) possess semiconducting behaviours that can vary with their structural and optical properties evolving from their synthesis. The reaction parameters such as the method, time, solvent and precursors can affect the growth and nucleation of particles and thus impose on the properties of the synthesized materials. The performance of solar cells made of the synthesized metal selenides will then be dependent upon the properties of the NPs used as active layer. Furthermore, the electrical current generation also depends on the structure of the deposited active layer and its interface with other films to be assembled for the device. The binary copper selenide, ternary copper indium selenide (CISe), quaternary copper indium gallium selenide (CIGSe) and quinary copper zinc tin sulphur selenide (CZTSSe) NPs were synthesized via conventional colloidal method (CCM) and microwave assisted method (MAM). The MAM has a particular interest as it is less time consuming and can easily be a large scale synthesis. Photovoltaic devices were fabricated from the synthesized materials as proof of concept for photovoltaic activities. The CCM was used to optimize various parameters for the synthesis of each type of the chalcogenide materials as this is easily controllable than the ones from the sealed vessel from MAM. The dependency of properties of all copper chalcogenide NPs on the time, precursor concentration, temperature and solvent of synthesis have been demonstrated via various characterization techniques including ultraviolet-visible-near infrared spectroscopy, photoluminescence spectroscopy, X-ray diffractometry and transmission electron microscopy.

The binary copper selenide was first synthesized and considered as a template for evaluation of the use of copper chalcogenide materials in solar cells. Relatively smaller copper selenide NPs with average sizes of 4.5 and 6.0 nm were obtained from conventional colloidal and microwave assisted methods respectively. The sample yielded from the microwave assisted method possessed less polydispersed NPs. The later had better crystallinity in which prevailed a single cubic Cu_2Se phase. To the best of our knowledge this is the first evidence of defined shapes and nearly single phase of small sized copper selenide NPs synthesized by mean of the MAM. The copper selenide particles synthesized via this method were used to fabricate a Schottky device. The conditions of copper selenide synthesis were optimized to 250 °C, 30

min of CCM synthesis using oleylamine (OLA) and a Cu/Se ratio of 1:1. Nearly hexagonal facets with blue-shifted absorption band edge of monodispersed NPs sizing 4-8 nm in diameter were obtained. The synthesized copper selenide showed better crystallinity with a single cubic Cu₂Se phase. A Schottky device using MAM synthesized copper selenide NPs as the semiconducting layer was fabricated at room temperature. The diode effect was demonstrated with the electrical parameters such as the ideality factor, barrier height and the series resistances extracted from the experimental current-voltage data using the thermionic theory and Cheung's modification. The thermionic theory resulted in the ideality factor of 4.35 and the barrier height of 0.895 eV whilst the Cheung's method resulted in the ideality factor, barrier height and series resistance of 1.04, 2.59×10^{-3} eV and 0.870Ω respectively.

The ternary copper indium selenide NPs showed that the MAM allowed the formation of copper rich NPs alongside secondary products. The synthesis of the ternary sample via CCM was optimized using uncapped precursors (no TOP was added) in OLA at 220 °C for 30 min. The synthesized CuInSe₂ NPs possessed a large blue-shift in their absorption band edges and emission peaks. The nearly stoichiometric CuInSe₂ particles with diameter sizes of 5-9 nm were found in tetragonal crystalline orientation. The cyclic voltametry (CV) and the absorption spectra showed a large blue-shifted energy gap, about 0.95 eV, an increase from the bulk, proving the quantum confinement effects of synthesized copper indium selenide quantum dots. The CuInSe₂ NPs were thus used as absorbing materials in the quantum dot sensitized solar cell devices (QDSSCs). The QDSSC devices were assembled via treatment of the titanium oxide, quantum dot layers and their interface. This was done by the treatment of copper indium selenide surface with mercapto-propionic acid (MPA) and ethanedithiol (EDT) during the deposition of the quantum dots onto TiO₂ films. The MPA treatment did not reveal positive effects on copper indium selenide thin film and the assembled device under our optimized working conditions. However the use of EDT allowed the improvement of electron transport. The short circuit current (J_{sc}), open circuit voltage (V_{oc}) and fill factor (FF) obtained from the current-voltage (J-V) curves reached the values of $324 \mu\text{A cm}^{-2}$, 487 mV and 43% respectively, indicating that the investigated quantum dots possess electrical properties.

For the quaternary copper indium gallium selenide, relatively small sized NPs were synthesized via CCM and MAM. The CCM synthesized CIGSe NPs were less agglomerated

with a shorter tailing in absorption than those from MAM. The stoichiometric $\text{CuIn}_{0.75}\text{Ga}_{0.25}\text{Se}_2$ showed less agglomerated and highly crystalline particles with a large blue-shifted absorption band edge and a smaller full width at half maximum (FWHM) of the emission peak compared to $\text{CuIn}_{0.5}\text{Ga}_{0.5}\text{Se}_2$ and $\text{CuIn}_{0.25}\text{Ga}_{0.75}\text{Se}_2$. The use of OLA as solvent of synthesis improved the growth and dispersivity of copper indium gallium selenide NPs. The particles with a large blue-shifted absorption band edge, a lattice of tetragonal phase, more monodispersed CIGSe and possessing an average size of 6.5 nm were obtained from CCM synthesis using OLA. The OLA as-synthesized CIGSe NPs were used in thin film for the assembly of QDSSC. The device exhibited electrical properties with the J_{sc} , V_{oc} and FF of $168 \mu\text{A cm}^{-2}$, 162 mV and 33% respectively. The overall device performance was poor but may further be improved for further photovoltaic application.

The quinary CZTSSe NPs possessed large blue-shifted absorption band edges of 450-460 nm than the bulk material (827 nm). The emission peak at 532 nm and similar FWHM of less than 50 nm were observed in samples from both CCM and MAM. More monodispersed crystals were obtained with both methods whilst the average particle sizes of 10 and 9 nm were yielded from MAM and CCM respectively. The nanoparticles crystallized in tetragonal lattices between copper zinc tin sulphide and copper zinc tin selenide crystals. However, the MAM gave more crystalline phases. The CV and the absorption spectra showed a blue shifted energy gap, about 0.21 eV increase from the bulk which is located at 1.51 eV. This is indicative of the quantum confinement effects of synthesized NPs. The evidence of electrical properties was also shown in the QDSSCs fabricated using the MAM synthesized quinary QDs. This was done following the same treatments as for copper indium selenide devices. The J_{sc} , V_{oc} and FF were found at the maxima of $258 \mu\text{A cm}^{-2}$, 395 mV and 38% respectively. The MPA and EDT treatments did not improve the device performance under our working conditions. Nevertheless, the electrical properties observed in the assembled device were indicative of promising efficient solar cells from synthesized CZTSSe NPs.

DEDICATION

For you my loving parents and my children

ACKNOWLEDGEMENTS

This thesis is the fruit of lots of effort and could not be achieved without encouragement and support from several people.

- Busisiwe Mathebula, you strengthen me everyday with your true love, you complete my thoughts.
- Dr. Nosipho Moloto. You really have a heart of gold. You always guide, even spend some of your sleeping time to assist in my project. I do not have perfect words to explain the amicable interaction I had with you as my supervisor. I thank you very much for the easier way of understanding and sharing your hints with me throughout the project.
- I also thank Dr. Lucky Sikhwivhilu and Prof. Justice Moloto for guidance and for accepting the coordination of this project regardless of their commitments.
- I am so considerate to Prof. Neil Coville for his advice, guidance and contribution to my scientific strength.
- DMI/CTI in Brazil for providing me with the perfect atmosphere during all my stay in Campinas and during my entire project. I particularly thank Thebano Emilio, for allowing me to be at CTI and facilitate all that could be needed. I am grateful to Dr. Jilian N. Freitas for using her valuable time to coordinate the project and to share ideas.
- CATOMMAT and Quantum Dot groups. You guys have no idea how you made me feel everyday I was in Humphrey Raikes building. The success in my work was definitely linked to the harmony among ourselves. I really thank everyone, in particular Mildred Airo, Dr. Isaac Beas, Stefan Govinradju, Siziwe Gqoba, Tumelo Phaahlamohlaka, David Ofori, Sifiso Mohotlhoane...
- I would like to thank all my family members including Joseph Kalombo and Dr Lucas Kazadi for your support. I am also grateful to the friendship and encouragement from Dr. Elysee Bakatula and Dr. Julien Lusilao.

PUBLICATIONS

Publications related to this PhD study

1. M.P. Kalenga, S. Govindraju, M. Airo, M.J. Moloto, L. Sikhwivhilu and N. Moloto. Fabrication of a Schottky Device using CuSe Nanoparticles: Colloidal versus Microwave Digestive Synthesis. (2015). *J. Nanosci. Nanotechnol.* 15(6), 4480–4486.
2. S. Govindraju, M.P. Kalenga, M. Airo, M.J. Moloto, L.M. Sikhwivhilu and N. Moloto. Size quantization in Cu₂Se nanocrystals. (2014). *Optical Materials* 38, 310–313.
3. N. Moloto, M.J. Moloto, M. Kalenga, S. Govindraju and M.Airo. Synthesis and characterization of MnS and MnSe nanoparticles: Morphology, optical and magnetic properties. (2014). *Optical Materials* 36, 31–35.
4. M. A. Airo, S. Gqoba, M. P. Kalenga, S. Govindraju, M. J. Moloto, N. Moloto. Synthesis and characterization of indium monoselenide nanosheets: A proposed pseudo top-down mechanism. (2014). *Journal of Crystal Growth* 406, 1–7.
5. N. Moloto, H. Puggens, S. Govindraju, B. Rakgalakane and M. Kalenga. Schottky solar cells: Anisotropic versus isotropic CuSe nanocrystals. (2013). *Thin Solid Films* 531, 446–450.
6. Paper proceeding: M.P. Kalenga, N. Moloto, M.J. Moloto and L. Sikhwivhilu. Time effects on the conventional colloidal synthesis of copper selenide nanocrystals. SAIP2012 proceedings, 57th annual conference of South African Institute of Physics. ISBN 987-1-86888-688-3.

Manuscripts (to be) submitted:

7. M.P. Kalenga, J.N. Freitas, N. Moloto, A. Flavia. A comparison of the effects of mercaptopropionic acid and ethanedithiol treatments in the CuInSe₂ and Cu₂ZnSn(SSe)₄ quantum dot-sensitized solar cells (submitted to *Thin Solid Films*, 2015).

8. M.P. Kalenga, J.N. Freitas, N. Moloto, M.J. Moloto, L.M. Sikhwivhilu. Quantum dot sensitized solar cells fabricated from colloidal copper indium selenide nanocrystals.
9. M.P. Kalenga, J.N. Freitas, N. Moloto, M.J. Moloto, L.M. Sikhwivhilu. Colloidal and microwave assisted syntheses of copper indium gallium selenide (CIGSe) nanoparticles.
10. M.P. Kalenga, J.N. Freitas, N. Moloto, M.J. Moloto, L.M. Sikhwivhilu. Copper zinc tin sulphur selenide quantum dots: from design to devices

Awards

- 3rd best oral presentation at NYRS symposium (November 2013): Synthesis and characterization of metal chalcogenide nanocrystals for photovoltaic applications.
- The Penny Huddle memorial award was received as best postgraduate teaching assistant in the School of Chemistry, University of the Witwatersrand (2012).

Research visit

Centro de Tecnologia da Informacao (CTI) Renato Archer in Brazil (Dec 2013 - Feb 2014): The application of quantum dots in devices as QDSSCs was performed in Division of Information Displays (DMI).

Conferences and Symposia

- **Effects of mercapto-propionic acid and ethanedithiol treatments in CuInSe₂ nanocrystals for quantum dot-sensitized solar cells.** Oral presentation at Macro- and Supramolecular Architectures and Materials (MAM), December 2014, Johannesburg, South Africa.
- **Metal selenide nanocrystals: from design to solar cells.** Oral presentation at Wits Science Slam, August 2014, at Science open day, Wits, Johannesburg, South Africa.
- **Synthesis and characterization of metal chalcogenide nanocrystals for photovoltaic applications.** Oral presentation at NanoAfrica, March 2014, Johannesburg, South Africa.

- **Synthesis and characterization of metal selenide nanocrystals for photovoltaic applications.** Oral presentation, Centra de Tecnologia da Informacao (CTI) Renato Archer, December 2013, Campinas, Brazil.
- **Designing metal selenide nanocrystals for photovoltaic applications.** Oral presentation, India-Brazil-South Africa (IBSA) solar cells, November 2013, Curitiba, Brazil.
- **Synthesis and characterization of metal chalcogenide nanocrystals for photovoltaic applications.** Oral presentation at Nanotechnology Young Researchers Symposium (NYRS), November 2013, CSIR, Pretoria, South Africa.
- **Colloidal and microwave digestive syntheses of Cu_xSe_y : fabrication of Schottky diode using Cu_xSe_y nanoparticles.** Oral presentation at Catalysis, Organo-Metallic and Materials (CATOMAT) group, September 2013, Wits, Johannesburg, South Africa.
- **Synthesis and characterization of Cu_ySe_x , CuInSe_2 and $\text{CuIn}_x\text{Ga}_{1-x}\text{Se}_2$ nanocrystals used as active layers in solar cells.** Poster presentation at Inorganic conference, July 2013, Durban, South Africa.
- **Synthesis and characterization of Cu_ySe_x , CuInSe_2 and $\text{CuIn}_x\text{Ga}_{1-x}\text{Se}_2$ nanocrystals used as active layers in solar cells.** Oral presentation at Brazil-Russia-India-China-South Africa (BRICS) energy, March 2013, Pretoria, South Africa.
- **Synthesis and characterization of Cu_ySe_x , CuInSe_2 and $\text{CuIn}_x\text{Ga}_{1-x}\text{Se}_2$ nanocrystals used as active layers in solar cells.** Oral presentation at CATOMAT, February 2013, Wits, Johannesburg, South Africa.
- **Fabrication of solar cells using Cu_ySe_x , CuInSe_2 and $\text{CuIn}_x\text{Ga}_{1-x}\text{Se}_2$ as active layers.** Oral presentation, India- Brazil-South Africa (IBSA) solar cells, October 2012, Johannesburg, South Africa.

-
-
- **Syntheses and characterization of copper selenide, copper indium selenide and copper indium gallium selenide nanoparticles for photovoltaic applications.** Poster presentation at Wits Postgraduate symposium, October 2012, Wits, Johannesburg, South Africa.
 - **Synthesis and characterization of copper selenide nanocrystals.** Oral presentation, South African Institute of Physics (SAIP) July 2012, Pretoria, South Africa.
 - **Synthesis and characterization of copper chalcogenide nanoparticles and their use in solution processed photovoltaics.** Oral presentation at CATOMAT, March 2012, Wits, Johannesburg, South Africa.

TABLE OF CONTENTS

DECLARATION	i
ABSTRACT	ii
DEDICATION	v
ACKNOWLEDGEMENTS	vi
PUBLICATIONS	vii
TABLE OF CONTENTS	xi
LIST OF FIGURES	xvi
LIST OF TABLES	xx
LIST OF ABBREVIATIONS	xxi
CHAPTER 1: SYNOPSIS	1
1.1 Brief description of the thesis.....	1
1.2 Problem statements	2
1.3 Project motivation	2
1.4 Project aims and objectives	2
1.5 Reference.....	3
CHAPTER 2: LITERATURE REVIEW	4
2.1 General introduction.....	4
2.2 Semiconducting nanocrystals	6
2.3 Synthesis of nanocrystals	8
2.3.1 Precipitative methods	8
2.3.2 Reactive methods in high boiling point solvents	9
2.3.3 Hydrothermal and solvothermal methods	9
2.4 Conditions affecting the synthesis and properties of metal chalcogenide nanocrystals ..	10
2.4.1 The time and temperature effects	10
2.4.2 The concentration effect	10
2.4.3 The solvent effect	11
2.5 Basics of solar cell devices and electrical parameters	12
2.5.1 Principles of photovoltaic devices.....	12
2.5.1.1 Absorption of photons and separation of charges	13
2.5.1.2 Transport and charge collection	13
2.5.2 Film deposition	16

2.5.3 Determination of device properties	17
2.6 References	19
CHAPTER 3: SYNTHESIS, CHARACTERIZATION OF COPPER SELENIDE NANOPARTICLES AND THEIR APPLICATION IN A SCHOTTKY DEVICE.....	38
3.1 Introduction	38
3.2 Experimental procedures.....	39
3.2.1 Chemicals and materials	39
3.2.2 Synthesis of copper selenide NPs	39
3.2.2.1 Conventional colloidal method	39
3.2.2.2 Microwave assisted method	40
3.2.3 Fabrication of copper selenide device.....	40
3.2.4 Characterization techniques	40
3.2.4.1 Optical and structural properties of synthesized Cu_xSe NPs.....	40
3.2.4.2 Thin film and device properties	41
3.3 Results and discussion.....	41
3.3.1 The effect of the conventional colloidal and microwave assisted methods on the synthesis of Cu_xSe NPs.....	41
3.3.1.1 Principles of the CCM and MAM methods	41
3.3.1.2 Optical properties of the CCM and MAM synthesized Cu_xSe NPs.....	43
3.3.1.3 Structural properties of the CCM and MAM synthesized Cu_xSe NPs.....	45
3.3.2 Time effect on the synthesis of Cu_xSe via CCM.....	48
3.3.2.1 Optical properties of the Cu_xSe NPs synthesized at different times	48
3.3.2.2 Structural properties of the Cu_xSe NPs synthesized at different times	50
3.3.3 Precursor concentration effect on the synthesis of Cu_xSe via CCM	51
3.3.3.1 Optical properties of Cu_xSe NPs synthesized from different precursor concentrations.....	51
3.3.3.2 Structural properties of Cu_xSe NPs synthesized from different precursor concentrations	53
3.3.4 Solvent effect on the synthesis of Cu_xSe NPs via CCM	55
3.3.4.1 Optical properties of Cu_xSe NPs synthesized in HDA and OLA.....	55
3.3.4.2 Structural properties of Cu_xSe NPs synthesized in HDA and OLA.....	57
3.3.5 Temperature effect on the synthesis of Cu_xSe via CCM	61

3.3.5.1 Optical properties of Cu _x Se NPs synthesized at different temperatures	61
3.3.5.2 Structural properties of Cu _x Se NPs synthesized at different temperatures	62
3.3.6 Fabrication of a Schottky device using MAM synthesized Cu _x Se NPs.....	64
3.4 Conclusions	70
3.5 References	70
CHAPTER 4: SYNTHESIS, CHARACTERIZATION OF COPPER INDIUM SELENIDE NANOPARTICLES AND THEIR APPLICATION IN QUANTUM DOT SENSITIZED SOLAR CELLS	77
4.1 Introduction	77
4.2 Experimental protocols	79
4.2.1 Chemicals and materials.....	79
4.2.2 Synthesis of copper indium selenide nanoparticles.....	79
4.2.2.1 Conventional colloidal method	79
4.2.2.2 Microwave assisted method.	80
4.2.3 Substrate cleaning	80
4.2.4 Chemical treatment of the TiO ₂ /QDs layers	80
4.2.5 Device assembly.....	80
4.2.6 Characterization techniques	81
4.3 Results and discussion.....	82
4.3.1 Method effect on the synthesis of copper indium selenide NPs	82
4.3.1.1 Optical properties of CISe NPs synthesized via MAM and CCM.....	82
4.3.1.2 Structural properties CISe NPs synthesized via MAM and CCM	83
4.3.2 Effect of precursors capped by TOP on the synthesis of CISe NPs.....	86
4.3.2.1 Optical properties of CISe NPs synthesized from uncapped and TOP-capped precursors.....	86
4.3.2.2 Morphology of CISe NPs synthesized from uncapped and TOP-capped precursors.....	89
4.3.3 Fabrication of CISe quantum dot sensitized solar cell devices	91
4.3.3.1 Cyclic voltametry of thin film of copper indium selenide NPs.....	91
4.3.3.2 The effects of mercapto-propionic acid and ethanedithiol treatments on copper indium selenide quantum dot sensitized solar cell properties	94
4.4 Conclusions	101
4.5 References	101

CHAPTER 5: SYNTHESIS, CHARACTERIZATION OF COPPER INDIUM GALLIUM SELENIDE NANOPARTICLES AND THEIR APPLICATION IN QUANTUM DOT SENSITIZED SOLAR CELLS. 108

5.1 Introduction	108
5.2 Experimental procedures	109
5.2.1 Conventional colloidal method	109
5.2.2 Microwave assisted method	110
5.2.3 Thin film treatment and device assembly	110
5.2.3 Characterization of materials	110
5.3 Results and discussion.....	111
5.3.1 Synthesis of copper indium gallium selenide nanoparticles via conventional colloidal and microwave assisted methods.....	111
5.3.1.1 Optical properties	111
5.3.1.2 Structural properties	113
5.3.2 Stoichiometric effect on the properties of copper indium gallium selenide synthesized via conventional colloidal method	114
5.3.2.1 Optical properties	115
5.3.2.2 Structural properties	117
5.3.3 Solvent effect on the properties of copper indium gallium selenide synthesized via conventional colloidal method.....	118
5.3.3.1 Optical properties	118
5.3.3.2 Structural properties	120
5.3.4 Copper indium gallium selenide device assembly	122
5.4 Conclusions	124
5.5 References	124

CHAPTER 6: SYNTHESIS, CHARACTERIZATION OF COPPER ZINC TIN SULPHUR SELENIDE NANOPARTICLES AND THEIR APPLICATIONS IN QUANTUM DOT SENSITIZED SOLAR CELLS

..... **128**

6.1 Introduction	128
6.2 Experimental procedures.....	129
6.2.1 Chemicals and materials.....	129
6.2.2 Synthesis of copper zinc tin sulphide selenide nanoparticles	129

6.2.2.1 Conventional colloidal method	129
6.2.2.2 Microwave assisted method	129
6.2.5 Thin film treatment and device assembly	130
6.2.6 Characterization of the materials.....	130
6.3 Results and discussion.....	130
6.3.1 Properties of CZTSSe synthesized via conventional colloidal and microwave assisted methods	130
6.3.1.1 Optical properties	130
6.3.1.2 Structural properties	132
6.3.2 Cyclic voltametry of copper zinc tin sulphur selenide thin film	134
6.3.3 The effects of mercapto-propionic acid and ethanedithiol treatments on the electrical properties of quantum dot sensitized solar cell devices.....	136
6.4 Conclusions	139
6.5 References	139
CHAPTER 7: GENERAL CONCLUSIONS AND RECOMMENDATIONS	142
7.1 Conclusions	142
7.1.1 Synthesis and characterization of Cu_xSe , CISE, CIGSe and CZTSSe NPs.....	142
7.1.2 Devices fabricated from Cu_xSe , CISE, CIGSe and CZTSSe NPs	143
7.2 Recommendations	144
Appendix	145
Band gap determination from the energy curves	145
Chapter 3	146
Chapter 4	147
Chapter 5	151
Chapter 6	154

LIST OF FIGURES

Fig. 2.1 Schematic diagram showing a direction of low to selective contacts in the charge transport.....	14
Fig. 2.2 Current- voltage (J-V) curve determined after measurement of a metal selenide solar device	18
Fig. 3.1 Heating path for synthesis of Cu_xSe nanoparticles via CCM and MAM	43
Fig. 3.2 Absorption spectra of Cu_xSe NPs synthesized via CCM and MAM.....	44
Fig. 3.3 Emission spectra of Cu_xSe NPs synthesized via CCM and MAM.....	44
Fig. 3.4 XRD patterns of CCM and MAM synthesized Cu_xSe NPs.....	46
Fig. 3.5 TEM images and size distribution of CCM and MAM synthesized Cu_xSe NPs.....	47
Fig. 3.6 Absorption spectra of Cu_xSe NPs synthesized at 220 °C in HDA for 1:1 mole ratio of Cu:Se at 10, 30 and 60 min	49
Fig. 3.7 Emission spectra of Cu_xSe NPs synthesized at 220 °C in HDA for 1:1 mole ratio of Cu:Se at 10, 30 and 60 min	49
Fig. 3.8 XRD patterns of Cu_xSe NPs synthesized at 220 °C for 30 min in a 1: 1 of Cu:Se ratio.....	50
Fig. 3.9 TEM images of Cu_xSe synthesized at 30 min and particle size distribution	51
Fig. 3.10 Absorption spectra of Cu_xSe synthesized from different precursor concentrations at 220 °C for 30 min	52
Fig. 3.11 Emission spectra of Cu_xSe NPs synthesized from different precursor concentrations at 220 °C for 30 min	53
Fig. 3.12 XRD patterns of Cu_xSe NPs synthesized at different precursor concentrations at 220 °C for 30 min	54
Fig. 3.13 TEM images of Cu_xSe NPs synthesized at different precursor concentrations and their particles size distribution	55
Fig. 3.14 Absorption spectra of Cu_xSe NPs synthesized at 220 °C in HDA and OLA.....	56
Fig. 3.15 Emission spectra of Cu_xSe NPs synthesized at 220 °C in HDA and OLA.....	57
Fig. 3.16 XRD patterns of Cu_xSe NPs synthesized in HDA and OLA.....	59
Fig. 3.17 TEM images of Cu_xSe synthesized in HDA and OLA with their corresponding particle size distribution and respectively	60
Fig. 3.18 UV-Vis absorption spectra of Cu_xSe NPs synthesized at different temperatures for 30 min at 1:1 of Cu: Se ratio	61

Fig. 3.19 Photoluminescence spectra of Cu_xSe NPs synthesised at different temperatures for 30 min at 1:1 of Cu: Se ratio	62
Fig. 3.20 XRD Patterns of Cu_xSe NPs synthesized at different temperatures	63
Fig. 3.21 TEM images Cu_xSe NPs synthesized at different temperatures and their corresponding size distributions	64
Fig. 3.22 Schottky device fabricated from MAM synthesized Cu_xSe NPs.....	65
Fig. 3.23 AFM image of film of MAM synthesized Cu_xSe NPs	65
Fig. 3.24 J-V characteristics of the Al/ Cu_xSe Schottky diode at 298 K in the dark	66
Fig. 3.25 LnI-V characteristics of the Al/ Cu_xSe Schottky diode at 298 K in the dark	68
Fig. 3.26 $dV/d\text{LnI}$ -I characteristics of the Al/ Cu_xSe Schottky diode at the temperature of 298 K in the dark.....	69
Fig. 3.27 H(I)-V characteristics of the Al/ Cu_xSe Schottky diode at the temperature of 298 K in the dark	69
Fig. 4.1 Absorption spectra of CCM and MAM synthesized CISE NPs.....	82
Fig. 4.2 Emission spectra of CCM and MAM synthesized CISE NPs.....	83
Fig. 4.3 XRD patterns of CISE powder obtained from CCM and MAM syntheses	84
Fig. 4.4 TEM images of CCM and MAM synthesized CISE NPs and their size distribution..	85
Fig. 4.5 Raman spectrum of CISE QDs.....	86
Fig. 4.6 Absorption spectra of CISE NPs synthesized at 220 °C with uncapped and TOP-capped precursors	88
Fig. 4.7 Emission spectra of CISE nanoparticles respectively synthesized at 220 °C with uncapped and TOP-capped precursors	88
Fig. 4.8 XRD pattern of CISE NPs synthesized at 220 °C with uncapped and TOP-capped precursors	90
Fig. 4.9 TEM images and particles size distribution of CISE synthesized from uncapped and TOP- capped precursors	91
Fig. 4.10 CV and energy levels of CISE QD solution deposited onto FTO substrate.....	93
Fig. 4.11 Optical microscopic images of untreated CISE film MPA treated film and EDT treated thin films and their corresponding absorption spectra energy curves	96
Fig. 4.12 J-V curves obtained from untreated, MPA and EDT treated CISE films	98
Fig. 4.13 J-V curves obtained from EDT treated devices using I^-/I_3^- and $\text{S}^{2-}/\text{S}_n^{2-}$ electrolytes	100
Fig. 5.1 Structure of CIGSe QDSSC device	111

Fig. 5.2 Absorption of CIGSe nanoparticles synthesized in HDA via MAM and CCM.....	112
Fig. 5.3 Emission spectra of CIGSe nanoparticles synthesized in HDA via MAM and CCM.....	112
Fig. 5.4 XRD patterns of CIGSe NPs synthesized in HDA via MAM and CCM	113
Fig. 5.5 TEM images of CIGSe NPs synthesized in HDA via MAM and CCM.....	114
Fig. 5.6 UV-vis absorption spectra of $\text{CuIn}_{0.5}\text{Ga}_{0.5}\text{Se}_2$, $\text{CuIn}_{0.25}\text{Ga}_{0.75}\text{Se}_2$ and $\text{CuIn}_{0.75}\text{Ga}_{0.25}\text{Se}_2$ NPs synthesized in HDA via CCM	116
Fig. 5.7 PL emission spectra of $\text{CuIn}_{0.5}\text{Ga}_{0.5}\text{Se}_2$, $\text{CuIn}_{0.25}\text{Ga}_{0.75}\text{Se}_2$ and $\text{CuIn}_{0.75}\text{Ga}_{0.25}\text{Se}_2$ NPs synthesized in HDA via CCM.....	116
Fig. 5.8 XRD patterns of $\text{CuIn}_{0.5}\text{Ga}_{0.5}\text{Se}_2$, $\text{Cu In}_{0.25}\text{Ga}_{0.75}\text{Se}_2$ and $\text{CuIn}_{0.75}\text{Ga}_{0.25}\text{Se}_2$ NPs synthesized in HDA via CCM	118
Fig. 5.9 TEM images of $\text{CuIn}_{0.5}\text{Ga}_{0.5}\text{Se}_2$, $\text{CuIn}_{0.75}\text{Ga}_{0.25}\text{Se}_2$ and $\text{CuIn}_{0.25}\text{Ga}_{0.75}\text{Se}_2$ NPs synthesized in HDA via CCM.....	118
Fig. 5.10 Absorption spectra $\text{CuIn}_{0.75}\text{Ga}_{0.25}\text{Se}_2$ NPs synthesized via CCM in HDA and OLA.....	119
Fig. 5.11 Emission spectra $\text{CuIn}_{0.75}\text{Ga}_{0.25}\text{Se}_2$ NPs synthesized via CCM in HDA and OLA	120
Fig. 5.12 XRD patterns of $\text{CuIn}_{0.75}\text{Ga}_{0.25}\text{Se}_2$ NPs synthesized in HDA and OLA via CCM.	121
Fig. 5.13 TEM images of $\text{CuIn}_{0.75}\text{Ga}_{0.25}\text{Se}_2$ NPs synthesized via CCM in HAD and OLA; size distribution and EDS spectrum of $\text{CuIn}_{0.75}\text{Ga}_{0.25}\text{Se}_2$ NPs synthesized via CCM in OLA	122
Fig. 5.14 Optical microscopic image and $(\alpha h\nu)^2/h\nu$ curve of CIGSe thin film.....	123
Fig. 5.15 J-V curve of CIGSe QDSSC device	124
Fig. 6.1 CZTSSe QDSSC device setup	130
Fig. 6.2 Absorption spectra of CZTSSe NPs synthesized via MAM and CCM	131
Fig. 6.3 Emission spectra of CZTSSe NPs synthesized via MAM and CCM	132
Fig. 6.4 XRD patterns CZTSSe powders prepared from MAM and CCM	133
Fig. 6.5 TEM images and size distribution of MAM and CCM synthesized CZTSSe NPs..	134
Fig. 6.6 CV and energy levels of CZTSSe QD solution deposited onto FTO substrate	135
Fig. 6.7 J-V curves of CZTSSe devices from untreated, MPA and EDT treated films	138
Fig. A3.1 Energy curves of Cu_xSe synthesized via CCM and MAM.....	146
Fig. A4.1 Energy curves of CIGSe synthesized via CCM and MAM	147
Fig. A4.2 Energy curves of CIGSe synthesized from TOP-capped and uncapped precursors	147
Fig. A4.3 The XRD of CIGSe synthesized at 180, 220, and 320 °C	148

Fig. A4.4 TEM images and size distribution of CIGSe NPs synthesized at 180, 220, and 320 °C	149
Fig. A5.1 Energy curves of MAM and CCM synthesized CIGSe NPs.	151
Fig. A5.2 Energy curves of CIGSe synthesized in HDA with In/Ga ratios of 1:1, 1:3 and 3:1	151
Fig. A5.3 Energy curves of CCM synthesized CIGSe using HDA and OLA	152
Fig. A5.4 FT-IR spectra of pure OLA and $\text{CuIn}_{0.75}\text{Ga}_{0.25}\text{Se}_2$ synthesized with OLA	152
Fig. A5.5 AFM images of CIGSe thin film spin-coated onto substrate.....	153
Fig. A6.1 Energy curves of MAM and CCM synthesized CZTSSe NPs	154
Fig. A6.2 XRD patterns of CZTS and CZTSe NPs synthesized via MAM.....	154
Fig. A.6.3 TEM images and size distribution of MAM synthesized CZTS and CZTSe NPs	156

LIST OF TABLES

Table 3.1 Optical parameters of CuxSe NPs synthesized via CCM and MAM.....	45
Table 3.2 Optical parameters of CuxSe NPs synthesized at 10, 30 and 60 min	50
Table 3.3 Optical parameters of CuxSe NPs synthesized at Cu/Se ratios of 1:1, 1:2 and 2:1 .	53
Table 3.4 Optical parameters of CuxSe NPs synthesized in HDA and OLA	57
Table 3.5 Optical parameters of the CuxSe NPs synthesized at 180, 220 and 320 °C.....	62
Table 3.6 Diode parameters obtained from the J-V data of CuxSe Schottky device.....	68
Table 4.1 Optical parameters of CCM and MAM synthesized CISE NPs	83
Table 4.2 Optical properties of CISE synthesized via CCM using uncapped and TOP-capped precursors	89
Table 4.4 Homo-Lumo and BG approximations of CISE dispersed in pyridine.....	93
Table 4.5 MPA and EDT effects on the electrical properties of CISE devices	99
Table 4.6 J-V Electrical parameters of EDT treated CISE devices using I/I_3^- and S^{2-}/S_n^{2-} electrolytes	101
Table 5.1 Optical parameters of MAM and CCM synthesized CIGSe nanoparticles.....	113
Table 5.2 Synthesis of stoichiometric CIGSe nanoparticles via CCM	115
Table 5.3 Optical parameters of CIGSe synthesized at different stoichiometries	117
Table 5.4 Optical parameters of CCM synthesized CIGSe using HDA and CCM	120
Table 6.1 Optical parameters of MAM and CCM synthesized CZTSSe	132
Table 6.2 Homo-Lumo and BG approximations of CZTSSe from CV	136
Table 6.3 Electrical properties of CZTSSe devices	139
Table A4.1 Temperature effect on the size of CCM synthesized CISE nanoparticles	150

LIST OF ABBREVIATIONS

BG: Band gap

CCM: conventional colloidal method

CIGSe: copper indium gallium selenide

CISE: copper indium selenide

Cu_xSe: copper selenide (general abbreviation)

Cu_{2-x}Se: stoichiometric or nearly stoichiometric Cu₂Se

CV: cyclic voltammetry

CZTS: copper zinc tin sulphide

CZTSe: copper zinc tin selenide

CZTSSe: copper zinc tin sulphide selenide

EDS: energy dispersive spectroscopy

EDT: ethane dithiol

FF: fill factor

FTO: fluoride doped tin oxide

FWHM: full width at half maximum

HDA: hexadecyl amine

ITO: indium tin oxide

J_{sc}: short circuit current density

MAM: microwave assisted method

MPA: mercaptopropionic acid

NCs: nanocrystals

NPs: nanoparticles

OLA: octadecyl amine

PCE: power conversion efficiency

PEDOT/PSS: poly(3,4-ethylenedioxythiophene) Polystyrene sulfonate

PL: photoluminescence

Pmx.cal: calculated maximum power

Pmx.th: theoretical maximum power

Pyr: pyridine

QD: quantum dot

QDSSC: quantum dot sensitized solar cell

SEM: scanning electron microscopy

TBABF₄: tetrabutyl ammonium tetrafluoroborate

TEM: transmission electron microscopy

TOP: tri-n-octylphosphine

Tol: toluene

Voc: open circuit voltage

XRD: X-ray diffractometry

CHAPTER 1: SYNOPSIS

1.1 Brief description of the thesis

This chapter outlines the main topics of the thesis. The problem statement, the motivation, the aims and objectives of the project are stated. The second chapter describes the preparation of semiconducting nanocrystals and the conditions affecting their properties. A background on solar cells including their main constituents, their evolution, the problems related to their performances is provided. The use of different materials such as metal selenide based-compounds in solar cells is also explained.

The third chapter describes the synthesis and characterization of copper selenide (Cu_xSe) nanoparticles in hexadecylamine and oleylamine and the application of Cu_xSe nanoparticles obtained from optimized synthesis in a Schottky device to explain their properties. The work shown in this chapter is mostly from a paper that has been published [1].

The fourth chapter describes the synthesis of ternary copper chalcogenide using the method similar to what described in Chapter 3. The properties of the resultant copper indium selenide (CISe) nanoparticles are discussed. Quantum dots sensitized solar cells based on copper indium selenide are further discussed. A manuscript is made from this chapter and it is being submitted for publication.

The fifth chapter describes the synthesis of copper indium gallium selenide nanoparticles using the method adapted on that in Chapter 3. The properties of the resultant copper indium gallium selenide (CIGSe) nanoparticles are discussed. The fabrication of copper indium gallium selenide quantum dot sensitized solar cell device is then made to give the evidence of the photovoltaic performance. A manuscript made from this chapter is being submitted for publication.

The sixth chapter involves the preparation of copper zinc tin sulphide selenide (CZTSSe) nanoparticles. The nanoparticles are characterized and employed as an active layer in quantum dot sensitized solar devices. This chapter will be submitted to a journal for publication. The seventh chapter covers the general conclusions on this project and the recommendations for future work are highlighted.

1.2 Problem statements

Second generation photovoltaics based on thin films of semiconducting materials have failed to surpass the efficiency of silicon solar cells. The lower efficiency has resulted in the overall cost of the second generation photovoltaics to be similar to silicon solar cells thus limiting their domestic and commercial use. Hence, efforts have been made through the third generation solar cells to improve efficiencies while lowering the production costs through simple processing technologies. The exploration of new materials with new properties may be an advantage in improving the performance of photovoltaic devices and expending the associated technology.

1.3 Project motivation

Three-dimensionally quantum confined semiconductor nanocrystals possess excellent optical, electronic and physical properties compared to their quantum wells counter parts. Their band gap can be engineered by the manipulation of their size and shape. Additionally, these materials are solution processable, small amount can easily be used along with other types of materials as polymers, and other inorganic materials to form hybrid structures and thus present the possibility to produce low cost nanocrystals solution based-thin film solar cell devices to harness the properties of 3D confined nanoparticles.

1.4 Project aims and objectives

The aim of the project was to synthesize and characterize Cu_xSe , CuInSe_2 , CuInGaSe_2 and $\text{Cu}_2\text{ZnSn}(\text{S},\text{Se})_4$ nanoparticles and to use them as active layer in solar cell devices. In order to fulfil the above mentioned aim, the following objectives were identified:

- Synthesis and characterization of Cu_xSe , CuInSe_2 and $\text{CuIn}_x\text{Ga}_{1-x}\text{Se}_2$, $\text{Cu}_2\text{ZnSn}(\text{S},\text{Se})_4$ nanoparticles using a conventional colloidal and microwave assisted colloidal methods.
- Fabrication and characterization of solar cell devices from synthesized nanocrytals to demonstrate their photovoltaic activities.

1.5 Reference

- [1] Kalenga, M.P., Govindraju, S., Airo, M., Moloto, M.J., Sikhwivhilu, L.M. and Moloto, N. (2015). *J. Nanosci. Nanotechnol.* 15, 4480-4486.

CHAPTER 2: LITERATURE REVIEW

2.1 General introduction

Around 80% of world energy is produced from fossil fuels such as coal, oil and natural gases [1-8]. Renewable energy provides better solution to various activities around the world by preserving a good environment for a better future. Photovoltaics and wind power are the main sources of renewable energy and can offer better economic advantages. Photovoltaic devices are superior in improving green energy consumption and overcoming the environmental concerns yielded from the current most dominant energy sources. Solar energy is being used because of its low environmental impact and as a perfect candidate for alternative energy resources due to its global availability. The photovoltaic cells are subdivided into three groups including first, second and third generations. Up to date, the conversion of sunlight into electricity using any photovoltaic device through its active layer remains a challenge although the third generation cells tend to overcome the issues encountered with the predecessors.

The first generation PVs are largely made up of pure single-crystalline silicon. Though relatively high in efficiency, the large amount of materials needed and the production steps to make to the first generation cells are relatively expensive. This prompted the development of the second generation of solar cells. The second generation solar cells have been under intense development from the 90s to the early 2000s. They are generally low-cost and low-efficiency cells. These are most frequently associated with thin film solar cell designs that use minimal materials and cheap manufacturing processes. The most popular materials used for second generation solar cells are copper indium gallium selenide (CIGSe), cadmium telluride (CdTe), amorphous silicon and micromorphous silicon. Because of the low efficiency, the overall cost of second generation cells are said to be similar to that of first generation solar cells [9-11]. Third generation solar cells are currently under research and the aim is to manufacture high efficient solar cells at low cost. Technologies associated with third generation solar cells include multi-junction photovoltaic cells, tandem cells, nanocrystals based cells and etc. [12-15].

The development of the solar cell industry is affected by the use of different materials in devices. The main component of a photovoltaic device is the active layer. The later should be

well built together with other components so as its intrinsic properties are fully utilised in the device. The architecture and the use of the solar cell face several problems including the cost of the process, the power conversion efficiency and long lasting activity of the product. Photovoltaic devices have been developed based on the active layers among which metal chalcogenide materials have gained particular attention. The optical and electrical properties of both bulk and nanosized metal chalcogenides have been studied and are intensively targeted for photovoltaic applications [16-22]. However, more studies are still needed to clearly explain the properties of these materials from their preparation to the devices. This is particularly the case for nanosized materials since they can possess new properties compared to their bulk counterparts. Studies have shown that nanomaterials can possess unique optical, structural and electrical properties due to the reduction of size [23-27].

The structure of layers to be assembled in the devices, modules, panels as well as the procedure for the device assembly dependently affect the cost and/or the overall efficiency. Silicon based solar cells are currently dominating the solar cell industry due to the earth abundance of silicon, the 4 electrons on outer shell are capable of forming bonds giving rise to a good crystalline structure needed for photovoltaics. When the sunlight strikes the crystal, some of the bonds break and electrons start moving freely within the crystal and thus creating electrical current. Several materials are used in silicon devices to adjust the electrical properties and increase the efficiency. However the efficiency and the cost of either amorphous (with atoms of Si randomly distributed within the lattice), single crystalline or polycrystalline silicon based solar cells are yet to satisfy the market and conquer the level occupied by non-environmentally friendly energy sources [28-32]. Several other semiconductor materials are used in photovoltaics. Namely, cadmium telluride (CdTe), gallium arsenide (GaAs) and copper indium gallium selenide (CIGSe). These bulk materials have given rise to thin films and multijunction cells. These films were extensively made via physical deposition techniques. While methods such as electrodeposition technique can be employed to deposit compounds for the layer as thin film, several layers can also be stacked together and heterojunction solar cells can be fabricated via linking other semiconductors such as CdS or Cu_xSe [33-36]. However, the cost of the cell is high because of the quantity of material needed while trying to overcome the efficiency of the assembled solar cells. Bhattacharya *et al.* [37] elaborated on the 3-stage electro-deposition processes where metal precursors were deposited through current-voltage mechanism of the solutions on Mo and

selenized substrates. Although the films were found with several voids, the device fill factor and PCE were 66% and 10.9% respectively. Gabor *et al.* [38] reported the preparation of copper indium selenide and copper indium gallium selenide films through thermal evaporation of metal precursors. The authors fabricated the devices that showed an efficiency of 15%.

Metal selenide based materials are generally known to be p-type semiconductors. Their band gap energies can be tuned as the materials are prepared into a nanosized level. Copper chalcogenide nanoparticles possess unique properties that can result in novel electrical behaviours [39-42]. Solar cells made from semiconductor nanocrystals are said to surpass the efficiency of single-crystalline silicon solar cells [43]. This is due to the intrinsic properties of semiconductor nanocrystals in which the surface area increases, the radius of the synthesized nanoparticles becomes less than the Bohr radius and the energy increases due to the quantum confinement effect [44, 45]. Because of tunable optical properties, semiconductor nanocrystals can absorb light from the ultra-violet to the near infra-red regions of the solar spectrum. Secondly, semiconductor nanocrystals have been shown to be capable of multiple exciton generation from one phonon compared to single-crystalline silicon where one exciton is generated for every one phonon. This means that nanocrystalline based solar cells have more charge carrier density resulting in potentially improved efficiency. Equally important, the synthetic methods of the proposed semiconductor nanocrystals are relatively easy, reproducible and cheap. And as a result of the processibility of these nanocrystals (can dissolve in most solvents and can be embedded in polymers), simple processing techniques such as spin coating, dip coating and drop casting can be utilized. This can therefore result in the realization of high efficiency, low cost solar cells.

2.2 Semiconducting nanocrystals

Semiconductor nanocrystals are typically characterized by particles with diameters less than 20 nm. The small dimensions result in material properties that are not similar to those of corresponding bulk materials due to quantum confinement effects [46]. The electrons and holes become squeezed in all three dimensions when the size of particle is significantly reduced until the energy between the hole and the electron orbitals become size dependent. Various sized nanoparticles with new properties have been synthesized using different methods and can be employed for many applications including biology, optics, sensors and

photovoltaics. The photoexcitation and shift of electron from the valence band to conduction band without transport of electric current generate a band gap. The latter is the main reason of using semiconductors in solar cells [47, 48]. Size-dependent properties are the reason for the significant impact of semiconductor nanocrystals in photovoltaic applications. Most of the materials used in nanocrystal based solar cells have already shown potential as quantum wells in second generation solar cells. Some of the examples are CdTe solar cells that have achieved an efficiency of 16.7% and CIGSe with an efficiency of 20%. These values are however much lower than the multijunction silicon solar cells that have achieved an efficiency of 41.6% [49]. Semiconductor nanocrystal solar cells therefore offer an opportunity to improve on the already existing materials. A number of researchers have theoretically shown that semiconductor nanocrystals are capable of generating multiple electron-hole pairs by a single photon of light [50-53]. This opens avenues for improving their applications in various devices. Furthermore, the tuning of size of the nanocrystals has been studied extensively and the consequence of size tunability is the ability of a single type of material absorbing in a wider range [52, 54].

Much of the work on semiconductor nanocrystal solar cells has focused on CdSe or PbS and PbSe as the active nanocrystal material. Robel *et al.* [55] reported on TiO₂/CdSe hybrid quantum dot solar cell that exhibited a photon-to-charge carrier efficiency of 12%. Whilst McDonald and co-workers [56] reported on a solution processed PbS infrared quantum dots photovoltaics. They employed a nanocomposite approach in which PbS nanocrystals tuned by quantum size effect sensitized the conjugated polymer poly [2-methoxy-5-(2'-ethylhexyloxy-p-phenylene)] (MEH-PPV). Zhou *et al.* [57] elaborated the importance of inorganic network on the increase of efficiency of hybrid solar cells. They added CdSe nanowires to quantum dots in the ration of 1/2 to obtain a PCE of 2.8% while the addition of low band gap polymer poly [2,1,3-benzothiadiazole - 4,7- diyl[4,4-bis(2-ethylhexyl)- 4H- cyclopenta(2,1-b:3,4b') dithiophene -2,6-diyl] (PCPDTBT) to QDs in hexanoic acid lead to more than 3% of PCE.

A few attempts at fabricating copper selenide nanocrystals based-solar cells have been reported. Guo *et al.* [58] used a solution synthesis based on a selenium powder, CuCl and InCl₃ precursors in oleylamine to prepare sphalerite (37 ± 11 nm in diameter) or chalcopyrite structure CuInSe₂. The fabricated solar cell had an efficiency of 3.2% under AM1.5 illumination. Riha *et al.* [59] studied the effects of air exposure on the surface composition,

crystal structure, and electronic properties of thin film devices of Cu₂Se nanoparticles synthesized by hot injection method. The conductivity of the photovoltaic devices could increase by tuning the electronic properties of each layer of Cu₂Se through controlled oxidation of Cu⁺ and Se²⁻. Tang *et al.* [60] reported the synthesis of 12 - 18 nm CIGS nanoparticles in oleylamine and their solution in toluene were drop-casted onto substrate to produce thick film onto interdigitated electrode (IDE) glass test chips. A promise of the device for PV application was shown by an increase of current through illumination. Wada *et al.* [61] reported on the soaking of CIGS film in an aqueous InCl₃ and thioacetamide solution, which was then used to fabricate the solar cell device with ITO/ZnO/CdS/CIGS/Mo/ glass structure. An efficiency of 17.6% was obtained after evaluation of the device performance under AM 1.5 illumination.

2.3 Synthesis of nanocrystals

Several methods of synthesis of copper selenide, copper indium selenide and copper indium gallium selenide semiconducting nanoparticles have been proposed by researchers and the well known methods are listed below. Researchers have recently engaged in the synthesis of ternary and quaternary nanocrystals with the aim of improving the properties of traditional ternary and quaternary compounds. Traditional ternary and quaternary materials are quantum wells (thin films) synthesized by physical methods [62-65].

2.3.1 Precipitative methods

The nanoparticles are produced in solution by precipitation of salts (based on relative solubility of inorganic salts) in these methods. The synthesis occurs through vigorous agitation or stirring of precursors at low temperatures. Pradhan and Peng [66] added Na₂SeSO₃ to a complex formed by mixture of triethanolamine and CuCl₂ to form a black precipitate which was then used for preparation of copper (I) selenide nanocrystalline films. Wu *et al.* [67] heated Indium (III) chloride, Copper (I) chloride and gallium (III) chloride in polyol solution where they were reduced to metal particles. Elemental Se was then added to the solution to form CISE and CIGSe which were dissolved in ethanol and precipitated by nucleation process to form the nanocrystals. The same authors reported the use of sodium borohydride, solution of elemental Se in anhydrous ethanol, InCl₃ and CuCl in diethylene glycol to prepare CISE nanocrystals at 240 °C after precipitation with ethanol whilst CIGSe was prepared at 280 °C by adding GaCl₃ and using tetraethylene glycol as solvent.

2.3.2 Reactive methods in high boiling point solvents

Trioctyl phosphine (TOP) and trioctyl phosphine oxide (TOPO) are mainly used to prepare the precursor. Mane *et al.* [68] dissolved copper and selenium precursors in TOP which were then added to a boiling TOPO to synthesize nearly 10 nm size of hexagonal Cu₂Se nanoparticles under inert conditions using standard Schlenk line and glovebox techniques. Koo *et al.* [69] used selenourea as a Se source, oleylamine as a coordinating solvent and carefully controlled the reaction temperature and the way that reactants combined to synthesize trigonal pyramidal CuInSe₂ nanocrystals. Cu, In, and Ga nitrates and SeCl₄ dissolved in 1-propanol were used as precursors by Lee *et al.* [70] to prepare CIGSe powder with various sizes (10 to few hundred nm) and shapes in xylene. The product was annealed at 450 °C and a paste coated by sulfurization at same temperature allowed the formation of CIGSe film on glass substrate for solar cell devices.

2.3.3 Hydrothermal and solvothermal methods

In these methods, which are considered as alternatives to the colloidal method, high boiling point solvents are heated in a sealed vessel (autoclave) in which the pressure and temperature exceed the ambient pressure and the boiling point of the solvents. Solvothermal method involves the heating of precursors at high temperature and pressure during which the equilibrium is varied with temperature. The particles are formed and dissolved before recrystallizing out at constant temperature. Relatively long reaction times are used to obtain good quality nanocrystals [71-73]. A variant to this method is the microwave assisted synthesis, consisting of relatively lower pressure usage under microwave irradiation for the applied power. Autoclave methods are generally time consuming as compared to microwave assisted method and colloidal methods [74, 75]. Gu *et al.* [74] employed solvothermal method in which Cu, In, GaCl₃, and Se were added to ethylenediamine into the autoclave at 230 °C for 24 h. Single phase CIGSe was obtained after washing the product with water followed by drying at 100 °C. The particle sizes were less than 100 nm and were agglomerated. Grisaru *et al.* [75] synthesized 85 nm sized tetragonal structures of CuInSe₂ using the microwave-assisted polyol method in which triethylene glycol acted as both the solvent and the reducing agent. Hosseinpour-Mashkani *et al.* [76] reported the effect of microwave irradiation power for the synthesis of copper indium sulphide particles from copper complex precursors. The particles sized between 10 to 90 nm were prepared but they were found to agglomerate.

2.4 Conditions affecting the synthesis and properties of metal chalcogenide nanocrystals

The quality of metal chalcogenide nanocrystals influences their properties. Attempts to control the synthesized nanocrystals are through many parameters which play critical roles in their properties. The major parameters affecting the synthesis of nanocrystals including the time, temperature, precursor concentration and solvent are described below. Defect-free, well dispersed and homogeneous nanocrystals are highly desired for different applications. However optimizing each of the parameters to obtain ideal crystals may be complex and practically difficult [77, 78].

2.4.1 The time and temperature effects

The synthesis of nanoparticles involves the growth and nucleation of particles from their precursors heated in a coordinating solvent [79-83]. This is carefully monitored by investigating the time and temperature for a given synthesis [84-87]. The Ostwald ripening effect is the main feature to overcome when optimizing the time and temperature for synthesis of nanoparticles. This ripening effect allows particles to group together with smaller ones tending to deposit onto big ones to form larger materials [88, 89]. Li *et al.* [90] reported the synthesis of microsphere units of covellite CuS at 90 and 120 °C for 24 h while increasing the temperature at same synthesis time reduced some of CuS into digenite phase as Cu₉S₅ nanorods. The same findings were shown when varying the time of synthesis at 150 °C. Higher synthesis times or temperatures caused the particles to aggregate and form chain-like materials. Tang *et al.* [91] reported the synthesis of copper indium gallium selenide nanoparticles using hot injection method. The formation of the nanoparticles is made by a rapid injection of precursors in oleylamine at elevated temperatures. However, higher injection temperatures such as 270 °C favoured the growth of larger particles. Govindraju *et al.* [92] reported the synthesis of copper selenide by varying the time from 2 min up to 60 min. The particles growth was observed as the time increased. Although the particles grew bigger, sizing 7 nm at 60 min, they became more monodispersed and crystallized in centered cubic phase of Cu₂Se.

2.4.2 The concentration effect

Metal selenide based-materials can be prepared from precursors in different concentrations whether the desired materials are prepared in bulk or at nanoscale. However the range of size,

shape and their applications are mostly related to the stoichiometry of the constituents. Controlling the concentration of precursors through optimization is considered as one of the critical challenges encountered in scaling up the material preparation, especially when synthesizing nanoparticles [93-98]. Kristl M. and Kristl J. [99] reported the synthesis copper selenide with less than 28 nm sizes by varying the concentration of precursors. Several stoichiometric copper selenide with different sizes and showing different properties were obtained. Moloto N. [100] described the use of different reactant ratios for synthesis of nickel selenide nanoparticles. Monodispersed and poly-dispersed nickel selenide nanocrystals exhibiting different optical, morphological and structural properties were obtained. Panthani *et al.* [101] employed various concentrations of Ga and In in the synthesis of copper indium gallium selenide nanoparticles. The shift of diffraction peaks to higher 2θ was observed when the indium content decreased in favour of gallium in the crystal composition. The band gap energy determined from UV-Vis absorption spectroscopy was higher as the Ga:In ratios increased. Kheraj *et al.* [94] reported the synthesis of copper zinc tin sulphide by varying the amount of metal precursors. The copper zinc tin sulphide material with good crystalline quality was obtained by decreasing the zinc content in favour of that of the tin while the amount of sulphur was exceeded by 40% than the required 2:1:1:4 ratio in the composition of $\text{Cu}_2\text{ZnSnSe}_4$. The band gap of 1.45 eV was estimated in the material that may be used as absorbing layer. However this band gap is similar to the bulk copper zinc tin sulphide compound suggesting that the optical and electronic properties were not tuned.

2.4.3 The solvent effect

The properties of target materials suggest that the affinity of precursors with the solvent could play an imminent role during the synthesis. Various solvents can be employed for synthesis of metal selenide nanoparticles. However different paths and additives can be adopted in order to optimise the synthesis and obtain nanoparticles with good properties [97, 98, 102]. While many solvents can be employed for synthesis of metal selenide nanoparticles, polyols, long chain phosphine and amine solvents are generally used for good growth control and stability of quantum dots [86, 103-105]. Murray *et al.* [106] employed degassed hot tri-n-octylphosphine oxide (TOPO) to synthesize CdS, CdSe and CdTe nanocrystallites from the metal precursors in tri-n-octyl phosphine (TOP), bis (trimethylsilyl) sulphur, bis (trimethylsilyl) selenium and bis (tert-butyl dimethylsilyl) tellurium. The authors suggested the generalisation of the method used for various new materials. Yordanov *et al.* [107]

prepared spheroid core-shell core/shell CdSe/CdS QDs in liquid paraffin. The dots were solubilised with the amphiphilic triblock copolymer pluronic F68 after which butyl-2-cyanoacrylate monomer in acetone was added to form the hybrid nanoparticles that were fluorescent for bio-imaging applications. Gacem N. and Diao P. [108] reported the control formation of nanoparticles aggregates by modulating the polarity of the solvent. The ratio of water to ethanol added on RhCl_3 - polyvinylpyrrolidone solution affected the PVP coated rhodium nanoparticles by reducing the interaction of long hydrophobic chains of hydrocarbons of PVP. Higher temperatures favoured more aggregates while high ethanol content solution allowed the formation of stable and monodispersed particles. Li *et al.* [109] reported the synthesis of copper selenide via microwave assisted method using a range of alcohols. The metal precursors were heated at the boiling point of the solvent used. The synthesis with absolute ethanol and isopropanol did not generate any product while cyclohexanol and benzanol gave cubic Cu_{2-x}Se and hexagonal CuSe crystals respectively. The authors have optimized the reaction time to 10 min although higher irradiation times were investigated without success for synthesis in ethanol and isopropanol. Lin *et al.* [110] reported the preparation of CuInSe_2 nanoalloys via solvothermal method using ethylenediamine/ethanol and ethylenediamine/deionized water as mixture of solvents. The 1:2.33 ratio of ethylenediamine/ethanol solvent system gave highly crystalline chalcopyrite in tetragonal phase with a band gap energy of 1.27 eV. Zhong *et al.* [111] prepared self stabilized aqueous copper zinc tin sulphide nanoink through water based solvents. Water soluble or pure metal sources were mixed with the thiourea water solution and stirred vigorously to form a transparent yellow brown ink of copper zinc tin sulphide. The ink was deposited onto a glass substrate via spin-coating then annealed at elevated temperature under S/Se atmosphere to form a copper zinc tin sulphur selenide film capable of good electrical performance.

2.5 Basics of solar cell devices and electrical parameters

2.5.1 Principles of photovoltaic devices

The general structure of solar cell devices consists of a glass substrate, front contact electrode, absorbing layer and back contact electrode. The active layer is generally thicker (up to few micrometers) than other deposited films on the substrate to increase the reception of photons. The negative contact (transparent electrode) is optimized to its thinnest shape to about 100 nm to allow the photons to penetrate through and reach the active layer while

keeping its role for collection of holes. The metal electrode or back contact thickness is made between 100 to about 500 nm and ideally deposited by sputter coating technique for compact adhesion to the photoelectric absorbing layer [112-116].

2.5.1.1 Absorption of photons and separation of charges

The sunlight strikes the device through the glass substrate; the photons are collected by the active layer where photoelectrons are generated. The excitation generates electron-hole pair when a semiconductor is the absorbing layer in the solar device. For a good charge separation and transfer, the quality of the film to be used as active layer need to be with good quality so as there is enough energy created through the charge generation [117]. A film of cadmium sulphide is mostly built on the chosen active layer to passivate the interface in order to avoid oxidation and thus improve the performance of the device. Thermodynamically, the separation of Fermi levels occurs when the active layer is at a lower ambient temperature T_0 than the radiation temperature, T_p , of the sun or any other source. A Carnot cycle argument gives the following upper limit for the open circuit voltage:

$$\Delta\mu = \left(1 - \frac{T_0}{T_p}\right) (E_H - E_L) \quad (2.1)$$

where $\Delta\mu$ is the change in mobility, E_H is the energy at the excited state and E_L is the energy at the ground state. The lifetime of an exciton directs the separation on electron-hole pair although this occurs in the order of picoseconds. In other respects, the energy of the separated charge should allow the transfer to other components and transport to collecting electrodes for the electrical output [118-122].

2.5.1.2 Transport and charge collection

Selective contacts are used in the charge-separation step. These contacts are transparent to one carrier type (e.g. electrons) and blocked completely to the other (e.g. holes), as illustrated in Fig. 2.1 below. A potential barrier can also be created at the interface of NCs thin film and metal contact allowing electrons to be pushed onto the metal and holes on TCO.

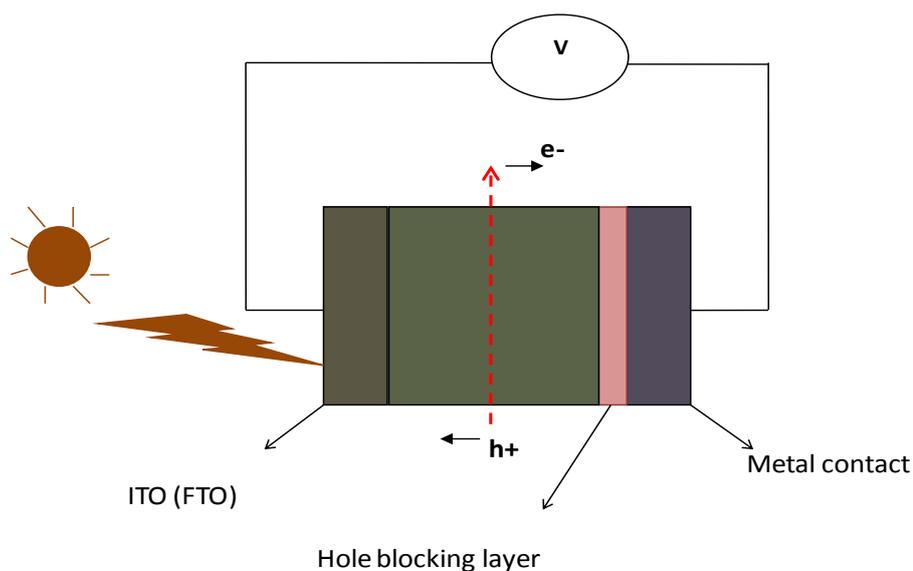


Fig. 2.1 Schematic diagram showing the charge transport to selective contacts

In the general structure of the devices, several films can be intercalated in the existing layers to improve the properties of the cell. The hole and electron transporting layers are added to facilitate the motion of charge from separation in the active layer to collection at the electrode. MoO_3 , V_2O_5 , PEDOT-PSS are mostly used as hole transporting layers while the transport of electrons is generally done with TiO_2 , ZnO , Cs_2CO_3 films deposited next to the cathode [123-128].

i) Transparent conducting electrodes

The transparent conducting electrode in devices is made up of a relatively thin layer of metal oxide which is permeable to photons needed to strike the active material. This electrode is mostly completing the circuit for electron transport as current. Indium tin oxide is currently the most used transparent conducting electrode because of high adhesion, high transmittance and low sheet resistance. This n-type semiconductor made of In_2O_3 and SnO_2 possesses a band gap energy of nearly 4 eV [123, 129-134]. Due to high cost and fragility, ITO is being replaced by graphene, aluminium, gallium, indium or tin doped-zinc oxide. However, apart from the cost, the properties of pure ITO, including resistance to moisture and as described above, are still preferred compared to other alternatives [135-141]. The doping of ITO with fluorine is thus important for further usage. Higher temperature treatments involve the use of fluorine doped tin oxide (FTO) as the most convenient conducting electrode [142-144].

ii) Metal contacts

A metal contact is generally used as electrode to collect electrons and transport to the external circuit. Several materials can be used as metal contacts including Pt, Al, Au, graphene, carbon nanotubes, CoS, MoS, polypyrrole, polyaniline. Several oxides such as ZnO can also be used as or doped with Al and Pt to decrease the amount of metal layer used as electrode although struggling to keep the resistivity and thus the performances of the device [145-151]. Platinum remains the most utilised metal contact for dye sensitized solar cells due to good stability, high conductivity and its excellent catalytic activity for the reduction of triiodide that is mostly used as part of electrolytes. Pt does not need special and expensive treatments to be employed for the counter electrode. ITO layer together with other materials such as graphene can be coupled with Pt to increase the performance of the device or to decrease the amount of Pt used. [152-159]. Guai *et al.* [156] prepared the counter electrodes from controlled composition made of Pt, ITO and graphene. They reduced the loading of Pt to 64 % from Pt-ITO layer and added graphene to obtain the electrode which allowed the assembly of dye sensitized solar cell with better performances and better PCE.

iii) Blocking layer-buffer layer

A blocking layer (generally in form of oxide), placed between the transparent electrode and the active layer prevents recombination due to short circuit and current loss [160]. An atomic layer (Ga_2O_3 , ZrO_2 , Nb_2O_5 ...) which is deposited-blocks electron recombination and leads to an increase of the open circuit potential and efficiency [161]. A buffer layer is added to the main films of the device in order to facilitate the cell performances through the enhancement of light absorption and the mediation for charge transport to the electrodes. The anode buffer layer such as CuO_x deposited onto ITO facilitates the extraction of holes at the anode, decreases the resistance, and improves V_{oc} , J_{sc} then the efficiency of the device [162, 163]. In order to improve the ohmic contact for the device assembly, an anode buffer layer made of transition metal oxides such as molybdenum oxide, nickel oxide, tungsten oxide or vanadium oxide can be placed as layer between indium-tin oxide (ITO) and the photon absorbing layers [164,165]. CdS is used as conventional buffer layer (used also as QDSSC, CdS/CdSe, where it sensitizes TiO_2). Tan *et al.* [166] reported the use of Rhenium oxide (ReO_x) as anode buffer layer to enhance absorption and electric properties in polymer solar cells.

iv) Electrolytes

The electrolytes are exclusively employed in dye sensitized solar cells (DSSCs) and related devices as special requirement for these device types. The oxidation-reduction couple used as electrolyte helps reconstituting the dye by providing the electron lost in the active layer. The commonly used electrolytes in dye sensitized solar cells include I_3/I^- , S^{2-}/S_n^- and Co^{2+}/Co^{3+} [167-170]. The electrolytes are liquid, bringing many issues in the device as they can easily get dry. A high volume of electrolyte would cause leakage and compromise the activity of the contacts. The solid state, quasi-solid state, polymer-based electrolytes [171-176] are being studied as alternatives to liquid oxidation-reduction couples in DSSCs.

2.5.2 Film deposition

Various techniques are employed to deposit a layer in the device assembly. Vacuum deposition methods include sputtering, evaporation and laser deposition. The non-vacuum techniques are used when there is no need of air or gas controlled conditions. Spray pyrolysis, doctor Blade, electrochemical process, colloidal methods such as drop casting and spin coating are considered as non- vacuum techniques [101,177-182]. Techniques such as doctor Blade, spin coating, drop casting are relatively cost effective and simple but the solution concentration and the properties of the materials often make the optimization of these techniques quite complex. The additional layers in the devices depend on the method used to assemble the devices and the conditions under which layers should be deposited. Molybdenum is the back contact of choice when the device is built under higher temperature conditions. This metal can display a very good stability when heated at higher temperatures and allows for good adhesion of the active layer [101,183-186]. However, several works have assessed other conditions including the materials and deposition techniques in the assembly of the device [101,187-189].

High temperature sintering was used by Guo *et al.* [185] to make $CuInSe_2$ film in the device structured as $Mo/CuInSe_2/CdS/ZnO/ITO$. The authors showed that the device had a fill factor of 39% and the power conversion efficiency of 2.8%. Akhavan *et al.* [190] reported similar work where gold was used instead of molybdenum in a device with same structure as that of Guo *et al.* but with different deposition techniques and conditions, higher values of fill factor and power conversion efficiency (46% and 3.1% respectively) were achieved. High temperature sintering conditions were employed by Liu *et al.* [191] for bulk copper indium

gallium selenide in Al:ZnO/ZnO/CdS/CIGS(bulk)/Mo/glass solar cell. They obtained the fill factor and efficiency of 27.6% and 2.4% respectively. Lee *et al.* [192] used the same device structure and same active layer with nanoparticles following other deposition techniques. The fill factor of 50% and the efficiency of 2.6% were obtained. Akhavan *et al.* [184] reported the preparation of the thin film of nanoparticles using various deposition techniques. The spray-coating of the nanocrystal inks could allow a formation of uniform crack and pin hole-free films. The authors made the devices with structures such as: glass/Au/CuInSe₂/CdS/ZnO/ITO in which the substrate, the back and front electrodes were varied. The fill factor and power conversion efficiency were in the range of 28-54% and 0.34-3.06% respectively.

2.5.3 Determination of device properties

The electrical properties are determined by measuring several parameters in the device by means of various techniques among which the current (I), voltage (V) and resistance (R) are commonly measured. The current can be calculated within the device area as current density (J) which is generated from the applied voltage in the device. The curve shown in Fig. 2.2, known as a J-V curve, is yielded from the generated current density by applying a specific voltage. The current density yielded from the device when there is no applied voltage is the short circuit current (J_{sc}) and the voltage at which there is no current within the device is known as open circuit voltage (V_{oc}). The product of short circuit current density and open circuit voltage gives the maximum power of the device in the ideal condition. This power means that the energy received by the device from the sunlight has been fully converted into electrical current. Practically this cannot yet be achievable and therefore this power is just theoretical (P_{max.th.}). From the data generated with the J-V curve, one can determine the experimental maximum power (P_{max}) to which the current density (J_{P_{max}}) and voltage (V_{P_{max}}) are attributed as depicted in Fig. 2.2. The fill factor (FF) is defined as a ratio of the experimental power to the theoretical power. This later is a measure of the junction quality and series resistance. The device has better performance when the fill factor tends to the unity. The efficiency or power conversion efficiency (PCE) is then determined by the ratio of the maximum power to the product of applied light power and the active area (equation 2.2) [193].

$$PCE = P_{\max} / (P_{\text{light}} \cdot \text{Active area}) \quad (2.2)$$

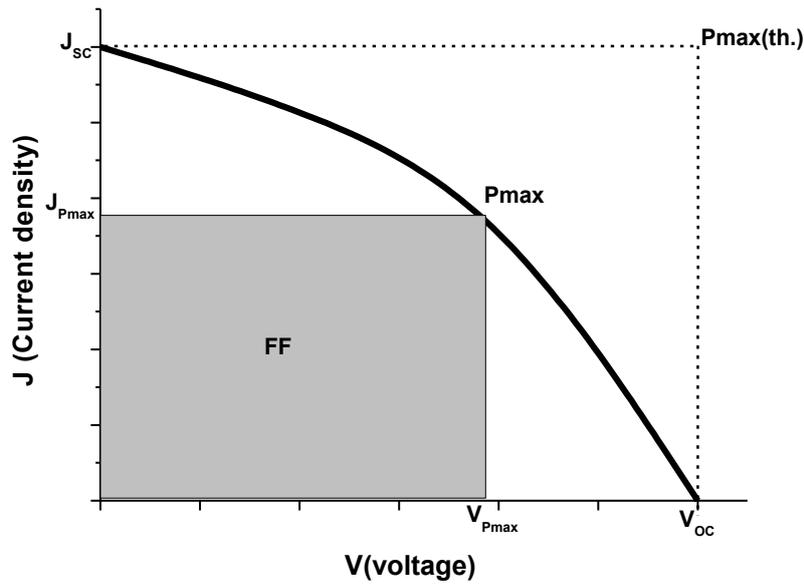


Fig. 2.2 Current- voltage (J-V) curve determined after measurement of a metal selenide solar device. The data generated from the curve allow the extraction and calculation of the electrical parameters (J_{sc} , V_{oc} , $J_{P_{max}}$, $V_{P_{max}}$, P_{max} , $P_{max} (th.)$, FF and PCE).

The Schottky devices involve a potential energy barrier formed at metal- semiconductor junction, resulting in rectifying characteristics such as Schottky barrier height which depends on the combination of metal-semiconductor [194]. The Schottky diode is characterised by the current-voltage curve where the forward bias has high current than the reversed bias for the same applied voltage. Schottky and Cheung methods are used to extract the properties which are exhibited by the device. The main properties include the series resistance, ideality factor and barrier height. The series resistance (R_s) involves the movement of current, resistance between top and back contacts, metal contact and the active layer. This resistance reduces the fill factor while maintaining high J_{sc} . The ideality factor or the deviation factor (n) is the conformity of the diode to pure thermionic emission and arises from image force and surface effects such as surface charges and an interfacial dielectric layer between the metal and the semiconductor [194,195]. The barrier height (ϕ_B) is the difference between the potential at the surface and in the bulk of semiconductor, it shows the flow of the current and is affected by the type of material with which semiconductor is in contact or the potential difference between the Fermi energy of the metal and the band edge where the majority carriers reside. The barrier properties allow the understanding of the effect of the junction and to properly build devices involving cell junction and this is the case of hetero-junction or multi-junction

solar cells [196]. The closer the barrier height is to 0, the more ohmic the contact and thus no good performances of the device can be yielded. The Schottky method is just a generalised method that does not consider other parameter that might affect the properties of the device such as thermionic emission. Several authors have considered all other parameters to modify the schottky method [197-199].

Quantum dot sensitized solar cells (QDSSCs) are made of quantum dots as absorbing layer and follow the same principles as the dye sensitized solar cells. After absorption of photon, the exciton is formed; the electron in conduction band is injected in the conduction band of the wide energy gap semiconductor (such as ITO or TiO₂) and transported to the contact through percolation. That electron goes on the outside load and then completes the circuit by returning to the counter electrode. The oxidation of the electrolyte refills the hole left beyond in the quantum dots to allow further photon absorption while reduction of electrolyte at the contact with counter electrode regenerates the electron [200, 201]. QDs are mainly used in QDSSCs is due to the unique and tuneable properties including the band gap tunability, rapid charge separation, hot electron injection and multiple exciton generation. Several parameters including the size of the QDs, the injection of electrons in wide band gap metal oxide and often the pH of the dot solution have to be considered in order to obtain good QDSSCs [202, 203].

Im *et al.* [204] reported the fabrication of 6.54% efficient QD-sensitized solar cell based on perovskite (CH₃NH₃) PbI₃ sensitizer. The fabricated solar cell was among the best efficient inorganic cells made of QDs and the electrical properties were much more improved than the conventional standard N719 dye sensitized solar cell fabricated under the same conditions. Ip *et al.* [205] reported the passivation of the colloidal quantum dots with halide anions mixed to the ligands to fabricate PbS QDSSC with record efficiency of 7%. Several other authors have studied the deposition of the quantum dots onto the TiO₂, the film deposition for device assembly, the coverage and attachment of dot to the wide band gap particles and possible recombination within the device [200, 206-209].

2.6 References

- [1] Kalenga, M.P., Govindraj, S., Airo, M., Moloto, M.J., Sikhwivhilu, L.M. and Moloto, N. (2015). *J. Nanosci. Nanotechnol.* 15, 4480-4486.

- [2] Moloto, N., Puggens, H., Govindraj, S., Rakgalakane, B. and Kalenga, M. (2013). *Thin Solid Films* 531, 446-450.
- [3] Payne, J.E. (2010). A survey of the electricity consumption-growth literature. *Applied Energy* 87, 723-731.
- [4] Omri, A. (2013). *Energy Economics* 40, 657-664.
- [5] Wang, W., Zhang, M. and Li, P. (2014). *Renewable and Sustainable Energy Reviews* 30, 943-949.
- [6] Kabashi, S., Bektashi, S., Ahmetaj, S., Kabashi, G., Najdovski, D., Zidansek, A. and Slaus, I. (2011). *Applied Energy* 88, 473-478.
- [7] Knapp, V., Pevec, D. and Matijevic, M. (2010). *Energy Policy* 38, 6793-6803.
- [8] Ewing, R.C., Runde, W. and Albrecht-Schmitt, T.E. (2010). Environmental impact of the nuclear fuel cycle: fate of actinides, *MRS Bulletin* 35. 859-866.
- [9] Hegedus, S. (2006). *Progr. Photovolt.: Res. Appl.* 14, 393.
- [10] Slaoui, A. and Collins, R.T. (2007). *MRS Bull.* 32, 211.
- [11] Reddy, R.G., Deepak, T.G., Anjusree, G.S., Thomas, S. Vadukumpully, S., Subramanian, K.R., Nair S.V. and Nair, A.S. (2014). *Phys. Chem. Chem. Phys.* 16, 6838-6858.
- [12] Yoon, H., Granat, J., Hebert, P., King, R.R., Fetzer, C.M., Colter, P., Edmondson, K.M., Law, D., Kinsey, G.S., Krut, D.D., Ermer, J.H., Gillanders, M.S. and Karam N.H. (2005). *Prog. Photovolt: Res. Appl.* 13, 133-139.
- [13] Green, M. (2003). *Advanced Solar Energy Conversion*. Springer, New-York, 1-63.

- [14] Chacara, L.E., Iamonta, L.A. and Zeinb, N.E. (2011). Review of photovoltaic technologies 15, 2165-2175.
- [15] Choubey, P.C., Oudhia, A. and Dewangan, R. (2012). Recent Research in Science and Technology 4, 99-101.
- [16] Wang, X., Koleilat, G.I., Tang, J., Liu, H., Kramer, I.J., Debnath, R., Brzozowski, L., Barkhouse, D., Levina, L., Hoogland, S. and Sargent, E.H. (2011). Nature Photonics 5, 480-484.
- [17] Yu, S., Yang, J., Qian, Y. Yoshimura, M. (2002). Chem. Phys. Lett. 361,362.
- [18] Yang, J., Zeng, J., Yu,S., Yang, L., Zhou, G. and Qian,Y. (2009). Chem. Mater. 12, 3259.
- [19] Zhan, J., Yang, X. and Wang, D. (2000). Adv. Mater. 12, 1348.
- [20] Chen, Y. Ding, J. Guo, Y. Kong, L. and Li, H. (2002). Mater. Chem. Phys. 77,734.
- [21] Jun, Y.W., Choi, J.S. and Cheon, J. (2006). Angew Chem. Int. Ed. 45, 3414.
- [22] Auffan, M., Rose, J., Bottero, J.Y., Lowry, G.V., Jolivet, J.P. and Wiesner, M.R. (2009). Nature Nanotechnology 4, 634 - 641.
- [23] Alivisatos, A.P. (1996). Science 721, 933.
- [24] Tan, T.T., Selvan, S.T., Zhao, L., Gao, S., Ying, J.Y. (2007). Chem. Mater. 19, 3112.
- [25] Norris, D.J., Sacra, A., Murray, C.B., Bawendi, M.G. (1994). Phys. Rev. Lett. 72, 2612.
- [26] Robel, S., Kuno, M., Kamat, P.V. (2007). J. Am. Chem. Soc. 129, 4136.

- [27] Moloto, N., Revaprasadu N., Moloto M.J., O'Brien, P. and Helliwell, M. (2007).
Polyhedron 26, 3947.
- [28] Green, M.A., Basore, P.A. , Chang, N., Clugston, D., Egan, R., Evans, R., Hogg, D.,
Jarnason, M., Keevers, M., Lasswell, P., Sullivan, J.O., Schubert, U., Turner, A.,
Wenham, S.R. and Young, T.(2004). Solar Energy 77, 857-863.
- [29] Flores, R.M., coal and coal bed gas, fuelling the future, 2014, 41-96, DOI:10.1016/B978
- 0-12-396972-9.00002-1.
- [30] Al-Tayyar, T.Z. and Salman, N.A. (2014). Energy Procedia 50, 488-493.
- [31] Yu, S., Wei, Y., Guo, H. and Ding, L. (2014). Applied Energy 114, 290-300.
- [32] Yu, S. and Wei Y. (2012). Energy Policy 42, 521-529.
- [33] Lincot, D., Guillemoles, J.F., Taunier, S., Guimard, D., Sicx-Kurdi, J., Chaumont, A.,
Roussel, O., Ramdani, O., Hubert, C., Fauvarque, J.P., Bodereau, N., Parissi, L.,
Panheleux, P., Fanouillere, P., Naghavi, N., Grand, P.P, Benfarah, M., Mogensen, P.,
Kerrec, O. (2004) Solar Energy 77, 725-737.
- [34] Bhattacharya, R.N., Fernandez, A.M. (2003). Solar Energy Materials & Solar Cells 76,
331-337.
- [35] Bhandari, K.P., Roland, P.J., Mahabaduge, H., Haugen, N.O, Grice, C.R., Jeong, S.,
Dykstra, T., Gao, J., Randy, J. Ellingson, R.J.(2013). Solar Energy Materials & Solar
Cells 117, 476-482.
- [36] Seo Y., Lee B., Jo, Y., Kim H., Choi, Y., Ahn, S., Yoon, K.H., Woo K., Moon J., Ryu B.
and Jeong S. (2013). J. Phys. Chem. C. 117, 9529-9536.
- [37] Bhattacharya, R.N., Oh, M.K. and Kim, Y. (2012). Solar Energy Materials & Solar Cells
98, 198-202.

- [38] Gabor, A.M., Tuttle, J.R., Albin, D.S., Contreras, M.A., Noufi, R. And Hermann, A.M. (1994). *Appl. Phys. Lett.* 65, 198-200.
- [39] Yin, Y., Alivisatos. A. P. (2005). *Nature* 437, 664–670.
- [40] Peng, Z.A. and Peng, X. (2001) *J. Am. Chem. Soc.* 2001, 123, 183–184.
- [41] O’Brien, P. and Pickett, N. L. (2003). *Comp. Coord. Chem. II* (9), 1005-1063.
- [42] McCleverty, J. A. and Meyer, T. J., Eds.(2004). Elsevier Ltd. Oxford, U.K.,vol. 9, 1005-1063.
- [43] Brown G.F and Wu J. (2009). *Laser and photon* 3(4), 394-405.
- [44] Buhro W.E. and Colvin V.L.(2003). *Nature Materials* 2, 138 – 139.
- [45] Zhong, X., Feng, Y. Knoll, W. and Han, M. (2003). *J. Am. Chem. Soc.* 125, 13559-13563.
- [46] Trindade, T., O’Brien, P. and Pickett, N.L. (2001). *Chem. Mater.*13, 3843-3858.
- [47] Haug, H. and Koch. S.W.(1994). *Quantum theory of the optical and electronic properties of semiconductors*, 3rd ed, world scientific publishing co Pte, Ltd, London. 169-180, 381-392.
- [48] Schmidt, T., Lischka, K., and W. Zulehner. (1992). *Phys.rev.B* 45, 8989.
- [49] National renewable energy laboratory (NREL), United States at <http://www.nrel.gov/pv/>
Downloaded on 13 November 2013.
- [50] Schaller, R. D. and Klimov, V. I. (2004). *Phys. Rev. Lett.* 92, 186601.

- [51] Ellingson, R. J., Beard, M. C., Johnson, J. C., Yu, P.; Micic, O. I., Nozik, A. J., Shabaev, A. and Efros, Al. L. (2005). *Nano Lett.* 5, 865.
- [52] Schaller, R. D., Sykora, M., Pietryga, J. M. and Klimov, V. I. (2006). *Nano Lett.* 6, 424.
- [53] Murphy, J. E., Beard, M. C., Norman, A. G., Ahrenkief, S. P., Johnson, J. C., Yu, P., Micic, O. I., Ellingson, R. J. and Nozik, A. J. (2006). *J. Am. Chem. Soc.*, 128, 3241.
- [54] Auffan, M., Rose J., Bottero, J.Y., Lowry, G.V., Jolivet, J.P. and Wiesner, M.R. (2009). *Nature Nanotechnology* 4, 634 - 641.
- [55] Robel, I. Subramanian, V., Kuno, M. and Kamat, P.V. (2006). *J. Am. Chem. Soc.* 128, 2385-2393.
- [56] McDonald, S. A., Konstantatos, G., Zhang, S., Cyr, P.W., Klem, E.J, Levina, L. and Sargent, E.H. (2005). *Nature Materials* 4, 138-142.
- [57] Zhou, Y., Eck, M., Men C., Rauscher F., Niyamakom, P., Yilmaz, S., Dumsch, I., Allard, S., Scherf U. and Kruger, M. (2011). *Solar Energy Materials & Solar Cells* 95, 3227-3232.
- [58] Guo, Q., Kim, S.J. Kar, M. Shafarman, W.N. Birkmire, R.W. Stach, E.A., Agrawal, R. and Hillhouse, H.W. (2008). *Nano Lett.* 8, 2982-2987.
- [59] Riha, S.C., Johnson, D.C. and Prieto, A.L. (2011). *J. Am. Chem. Soc.* 133, 1383-1390.
- [60] Tang, J., Hinds S., Kelley, S. O. and Sargent, E.H.(2008).*Chem. Mater.* 6906-6910.
- [61] Wada, T., Hashimoto Y., Nishiwaki S., Satoh T., Hayashi S., Negami T. and Miyake H. (2001). *Solar Energy Materials & Solar Cells* 67, 305-310.
- [62] Thouin, L. and Vedel, J. (1995). *J. Electrochem. Soc.* 142, 2996-3001.

- [63] Souilah, M., Lafondn, A., Guillot-Deudon, C., Harel, S., Evain, M. (2010). *Journal of Solid State Chemistry*. 183, 2274-2280.
- [64] Panicker, M.P.R., Knaster, M., Kroger, F.A. (1978). *J. Electrochem. Soc.* 125, 566-572.
- [65] Chassaing, E., Ramdani, O., Grand, P.P., Guillemoles, J.F. and Lincot, D. (2008). *Phys. Status. Solidi C* 5, 3445-3448.
- [66] Pradhan, N., Peng, X.G. (2007). *J. Am. Chem. Soc.* 3339-3347.
- [67] Wu, J. D., Wang, L.T. and Gau, C. (2012). *Solar Energy Materials & Solar Cells* 98, 404-408.
- [68] Mane, R.S., Kajve, S.P., Lokhande, C.D. and Han, S.H. (2006). *Vacuum* 80, 631-635.
- [69] Koo, B., Patel, R.N. and Korgel, B.A. (2009) *J. Am. Chem. Soc.* 131, 3134-3135.
- [70] Lee E., Cho J.W., Kim J., Yun J., Kim J.H. and Min B.K.(2010). *Journal of Alloys and Compounds* 506, 969-972.
- [71] Laudise, R.A. (1986). *Chem. Eng. News* 28, 30.
- [72] Byrappa, K. and Yoshimura, M. (2001). *Handbook of Hydrothermal Technology*.
- [73] Roy, R. (1994). *Journal of Solid State Chemistry* 111, 11.
- [74] Gu, S.I., Shin, H.S., Yeo, D.H., Hong, Y.W., Nahm, S. (2011). *Current Applied Physics* 11, S99-S102.
- [75] Grisar, H., Palchik, O., Gedanken, A., Palchik V., Slifkin, M.A., and Weiss, A.M. (2003). *Inorg. Chem.* 42, 7148-7155.
- [76] Hosseinpour-Mashkani, S.M., Salavati-Niasari, M., Mohandes, F. and Venkateswara-

- Rao, K. (2013). *Mat.Sc. in Semic. Proc.* 16, 390-402.
- [77] Gacem, N. and Diao, P. (2013). *Colloids and Surfaces A: Physicochem. Eng. Aspects* 417, 32-38.
- [78] Zhong, X., Han, M., Dong, Z., White, T.J. and Knoll, W. (2003). *J. Am. Chem. Soc.* 125, 8589-8594.
- [79] Gebauer, D., Volkel, A. and Colfen, H. (2008). *Science* 322, 1819.
- [80] Koziej, D., Rossel, M.D., Ludi, B., Hintennach, A., Novak P., Grunwaldt, J-D. and Niederberger, M. (2011). *Small* 7, 377-387.
- [81] Olliges-Stadler, I., Jan Stötzel, Koziej, D., Rossell, M.D., Grunwaldt, J-D., Nachtegaal, M., Frahm, R. and Niederberge, M. (2012). *Chem. Eur. J.* 18, 2305-2312.
- [82] Ludi, B., Süess, M.J., Werner, I.A. and Niederberger, M. (2012). *Nanoscale* 4, 1982-1995.
- [83] Carriazo, D., Rossell, M.D., Zeng, G. Bilecka, I., Erni, R. and Niederberger, M. (2012). *Small* 8, 2231-2238.
- [84] Cho, A., Ahn, S., Yun, J.H., Gwak, J., Ahn, S.K., Shin, K., Yoo, J., Song, H. and Yoon, K. (2013). *Thin Solid Films* 546, 299-307.
- [85] Gou, L. F. and Murphy, C. J. (2004). *Journal of Materials Chemistry* 14, 735-738.
- [86] Li, M., Zhou, W., Guo, J., Zhou, Y., Hou, Z., Jiao, J., Zhou, Z., Du, Z., and Chua, S.W. (2012). *J. Phys. Chem. C* 116, 26507-26516.
- [87] Sun, Y. G., Mayers, B. and Xia, Y. N. (2003). *Nano Lett.* 3, 675-679.

- [88] Ostwald, W. (1901). *Z. Phys. Chem.* 37, 385.
- [89] Voorhees, P.W. (1985). *Journal of Statistical Physics* 38, 231-252.
- [90] Li, F., Wu, J., Qin, Q, Li, Z., Huang, X. (2010). *Powder Technogy* 198, 267-274.
- [91] Jiang Tang, J., Sean Hinds, S., Kelley, S.O. and Sargent, E.H. (2008). *Chem. Mater.* 20, 6906-6910.
- [92] Govindraju, S., Kalenga, M.P., Airo M., Moloto M.J., Sikhwivhilu, L.M. and Moloto, N. (2014). *Optical Materials* 38, 310-313.
- [93] Haas, W., Rath, T. Pein, A., Rattenberger, J. Trimmel, G. and Hofer, F. (2011). *Chemical Communications* 47, 2050-2052.
- [94] Kheraj, K. Patel, K.K. Patel, S.J. and Shah, D.V. (2013). *Journal of Crystal Growth* 362, 174-177.
- [95] Liu, C.P. and Chuang, C.L. (2012). *Solar Energy* 86, 2795-2801.
- [96] Rath, T. Haas, W., Peina, A. Saf, R. , Maier, E. , Kunert, B. , Hofer, F. , Resel,R. and Trimmel, G. (2012). *Solar Energy Materials & Solar Cells* 101, 87-94.
- [97] Hosseini, M.S. and Jahanbani, H. (2013). *J. Lumin.* 140, 65-70.
- [98] Talapin, D.V., et al. (2003). *Nano Letters* 3, 1677-1681.
- [99] Kristl, M. and Kristl J.(2014). *Chalcogenide letters* 11, 59-66.
- [100] Moloto, N. (2010). *Syntheses, properties and applications of Mn, Co, Ni and Cu chalcogenide nanoparticles*, Doctor of Philosophy thesis, University of the Witwatersrand, Johannesburg, 156-178.

- [101] Panthani, M.G., Akhavan, V., Goodfellow, B., Schmidtke, J.P., Dunn, L., Dodabalapur, A., Barbara P.F. and Korgel, B.A. (2008). *J. Am. Chem. Soc.* 130, 16770-16777.
- [102] Fiore, A., Mastria, R., Lupo, M.G., Lanzani, G., Gianni, C., Carlino, E., Morello, G., Giorgi, M., Li, Y., Cingolani, R. and Manna, L. (2009). *J. Am. Chem. Soc.* 131, 2274-2282.
- [103] Kwon, S.G. and Hyeon, T. (2011). *Small* 7, 2685.
- [104] Tang, J., Hinds, S., Kelley, S.O. and Sargent, E.H. (2008). *Chem. Mater.* 20, 6906-6910.
- [105] Zhoua, Y., Ecka, M., Men, C., Rauscher, F., Niyamakom, P., Yilmaz, S., Dumsch, I., Allard, S., Scherf, U. and Kruger, M. (2011). *Solar Energy Materials & Solar Cells* 95, 3227-3232.
- [106] Murray, C.B., Norris, D.J. and Bawendi, M.G. (1993). *J. Am. Chem. Soc.* 115, 8706-8715.
- [107] Yordanov, G., Simeonova, M., Alexandrova, R., Yoshimura, H. and Dushkin, C. (2009). *Colloids and Surfaces A: Physicochem. Eng. Aspects* 339, 199-205.
- [108] Gacem, N. and Diao, P. (2013). *Colloids and Surfaces A: Physicochem. Eng. Aspects* 417, 32-38.
- [109] Li, J., Fa, W., Li, Y., Zhao, H., Gao, Y. and Zheng, Z. (2013). *Solid State Sciences* 16, 125-129.
- [110] Lin, Y., Liu, W., Chu, H., Chen, T., Hsu, S. and Chen, C. (2014). *J. Chin. Chem. Soc.* 61, 274-278.
- [111] Zhong, J., Xia, Z., Zhang, C., Li, B., Liu, X., Cheng, Y. and Tang, J. (2014). *Chem. Mater.* 26, 3573-3578.

- [112] Seyrling, S., Calnan, S., Bücheler, S. Hüpkes, J. Wenger, S. Brémaud, D. Zogg, H. and Tiwari, A.N. (2009). *Thin Solid Films* 517, 2411-2414.
- [113] Petermann, J.H., Zielke, D., Schmidt, J., Haase, F., Rojas, E.G., and Brendel, R. (2012). *Prog. Photovolt: Res. Appl.* 20, 1-5.
- [114] Hegedus, S.S. and Shafarman, W.N. (2004). *Prog. Photovolt: Res. Appl.* 12, 155-176.
- [115] Law, M., Greene, L.E., Justin, C., Johnson, J.C., Saykally, R. and Yang, P. (2005). *Nature Materials* 4, 455-459.
- [116] Katagiri, H., Saitoh, K., Washio, T., Shinohara, H., Kurumadani, T., Miyajima, S. (2001). *Sol. Energy Mater. Sol. Cells* 65, 141-148.
- [117] Pawlawski, M., Zabierowski, P., Bacewicz, R. and Barreau, N. (2013). *Thin Solid Films* 535, 336-339.
- [118] Kagan, C.R., Murray, C.B., Nirmal, M. and Bawendi, M.G. (1996). *Physical Review Letters* 76, 1517-1520.
- [119] Kagan, C.R., Murray, C.B. and Bawendi, M.G. (1996). *Physical Review B: Condensed Matter* 54, 8633-8643.
- [120] Franzl, T., Koktysh, D.S., Klar, T.A., Rogach, A.L., Feldmann, J. and Gaponik, N. (2004). *Applied Physics Letters* 84, 2904-2906.
- [121] Larson, D.R., Zipfel, W.R., Williams, R.M., Clarck, S.W., Bruchez, M.P., Wise, F.W., Webb, W.W. (2003). *Science* 300, 1434-1436.
- [122] Miller, D.A., Chemla, D.S., Damen, T.C., Gossard, A.C., Wiegmann, W., Wood, T.H., Burrus, C.A. (1984). *Phys. Rev. Lett.* 53, 2173-2176.

- [123] Kim, J.Y., Lee, K., Coates, N.E, Moses, D., Nguyen, T., Dante, M. and Heeger, A.J. (2007). *Science* 317, 222-225.
- [124] Sun, Y., Se, J.H., Takacs, C.J., Seifert, J. and Heeger, A.J. (2011). *Adv. Mater.* 23, 1679-1683.
- [125] Li, G., Chu, C-W., Shrotriya, V., Huang, J. and Yang, Y. (2006). *Appl. Phys. Lett.* 88, 253503.
- [126] Waldauf, C., Morana, M., Denk, P., Schilinsky, P. Coakley, K., Choulis, S.A. and Brabec, C.J. (2006). *Appl. Phys. Lett.* 89, 233517.
- [127] Irwin, M.D., Buchholz, D.B., Hains, A.W., Robert, P. H., Chang, P.H. and Marks, T.J. (2008). *PNAS* 105, 2783-2787.
- [128] Kim, Y., Lee, S., Noh, J. and Han, S. (2006). *Thin Solid Films* 510, 305-310.
- [129] Becerril, H.A., Mao, J., Liu, Z.F., Stoltenberg, R.M., Bao, Z. and Chen, Y.S. (2008). *ACS Nano* 2, 463-470.
- [130] Wu, J., Becerril, H.A., Bao, Z., Liu, Z.F., Chen, Y.S. and Peumans, P. (2008). *Appl. Phys. Lett.* 92, 263302.
- [131] Eda, G., Fanchini, G. and Chhowalla, M. (2008). *Nature Nan.* 3, 270 - 274.
- [132] Wu, H., Hu, L.B., Rowell, M.W., Kong, D., Cha, J.J., and McDonough, J.R. (2010) *Nano Lett.* 10, 4242-4248.
- [133] Slassi, A., Naji, S., Benyoussef, A., Hamedoun, M. and El Kenz, A. (2014). *Journal of Alloys and Compounds* 605, 118-123.
- [134] Eda, G., Fanchini, G. and Chhowalla, M. (2008). *Nature Nanotechnology.* 3, 270-274.

- [135] Shinde, S.S., Korade, A.P., Bhosale, C.H. and Rajpure, K.Y. (2013). *J. Alloys. Comp.* 551, 688-693.
- [136] Meenakshi, P., Karthick, R., Selvaraj, M. and Ramu, S. (2014). *Solar Energy Materials & Solar Cells* 128, 264-269.
- [137] Shelke, V., Bhole, M.P. and Ptil, D.S. (2013). *J. Alloys. Comp.* 560, 147-150.
- [138] Crossay, A., Buecheler, S., Kranz, L., Kranz, L., Perrenoud, J., Fella, C.M., Romanyuk, Y.E. and Tiwari, A.N. (2012). *Solar Energy Materials & Solar Cells* 101, 283-288.
- [139] Estrich, N.A., Hook, D.H., Smith, A.N., Leonard, J.T., Laughlin, B., Maria, J.P. (2013). *Appl. Phys.* 113, 233703, 1-5.
- [140] Li, J., Xu, J., Xu, Q. and Fang, G. (2012). *J. Alloys Comp.* 542, 151-156.
- [141] Clatot, J., Campet, G., Zeinert, A., Labrugère, C., Nistor, M. and Rougier, A. (2011). *Solar Energy Materials & Solar Cells* 95, 2357-2362.
- [142] Mende, L. S., Fechtenkötter, A., Mullen, K., Moons, E., Friend, R.H. and MacKenzie, J. D. (2001). *Science* 293, 1119.
- [143] Ito, S., Murakami, T.N., Comte, P., Liska, P., Grätzel, C., Nazeeruddin, M.K. and Grätzel, M. (2008). *Thin Solid Films* 516, 4613-4619.
- [144] Bach, U., Lupo, D., Comte, P., Moser, J. E., Weissortel, F., Salbeck, J., Spreitzer, H. and Grätzel, M. (1998). *Nature* 395, 583.
- [145] Oh, B., Jeong, M., Moon, T. Lee, W., Myoung, J., Hwang, J. and Seo, D. (2006). *J. Appl. Phys.* 99, 124505, 1-4.
- [146] Park, S., Tark, S. J., Lee, J. S., Lim, H., Kim, D. (2009). *Solar Energy Materials &*

Solar Cells 93, 1020-1023.

- [147] Huang, Z., Liu, X., Li, K., Li, D., Luo, Y., Li, H., Song, W., Chen, L. and Meng, Q. (2007). *Electrochemistry Communications* 9, 596.
- [148] Hong, W., Xu, Y., Lu, G., Li, C. and Shi, G. (2008). *Electrochemistry Communication* 10, 1555-1558.
- [149] Wada, T., Kohara, N., Negami, T. and Nishitani, M. (1996). *Jpn. J. Appl. Phys.* 35, L1253.
- [150] Orgassa, K., Schock, H.W. and Werner, J.H. (2003). *Thin Solid Films* 431, 387-391.
- [151] Grätzel, M. (2001). *Nature* 414, 338-344.
- [152] Lin, C-Y., Lin, J.-Y., Wan, C-C. and Wei, T-C. (2011). *Electrochimica Acta* 56, 1941-1946.
- [153] Lan, Z., Wu, J., Lin, J., Huang, M. and Wang, X. (2012). *Thin Solid Films* 522, 425-429.
- [154] Syrokostas, G., Siokou, A., Leftheriotis, G., Yianoulis, P. (2012). *Solar Energy Materials & Solar Cells* 98, 404-408.
- [155] Xiao, Y., Wu, J., Yue, G., Lin, J., Huang, M., and Lan, Z. (2011). *Electrochimica Acta*, 56, 8545-8550.
- [156] Guai, G.H., Song, Q.L., Guo, C.X., Lu, Z.S., Chen, T. N., C.M. and Li, C.M. (2012). *Solar Energy*, 86, 2041-2048.
- [157] Tachan, Z., Shalom, M., Hod, I., Ruhle, S., Tirosh, S. and Zaban, (2011). *J. Phys. Chem. C.* 115, 6162-6166.

- [158] Shengyuan, Y., Nair, A. S., Peining, Z. and Ramakrishna, S. (2012). *Mater. Lett.* 76, 43-46.
- [159] Balis, N., Dracopoulos, V., Bourikas, K. and Lianos, P. (2013). *Electrochimica Acta* 91, 246-252.
- [160] Memesa, M., Weber, S., Lenz, S., Perlich, J., Berger, R., Buschbaum, P.M. and Gutmann, J.S. (2009). *Energy Environ.Sci.* 2, 783-790.
- [161] Chandiran, A.K., Nazeeruddin, M.K. and Gratzel, M. (2014). *Advanced functional materials* 24, 1615-1623.
- [162] Szaniawski, P., Lindahl, J., Törndahl, T., Zimmermann, U. and Edoff, M. (2013). *Thin Solid Films* 535, 326-330.
- [163] Xu, Q., Wang, F., Tan, T., Li, L., Li, S., Hou, X., Sun, G., Tu, X., Hou, J. and Li, Y. (2013). *ACS Appl. Mater. Interfaces* 5, 10658-10664.
- [164] Zhang, M.L., Irfan, Ding, H.J., Gao, Y.L., Tang, C.W. (2010). *Appl.Phys. Lett.* 96, 183301/1-183301/3.
- [165] Lin, H., Xia, W., Wu, H.N. and Tang, C.W. (2010). *Appl. Phys. Lett.* 97, 123504/1-123504/3.
- [166] Tan, Z., Li, L., Wang, F., Xu, Q., Li, S., Sun, G., Tu, X., Hou, X., Hou, J. and Li, Y. (2014). *Advanced Energy Materials* 4, 1300884.
- [167] Chakrapani, V., Baker, D. and Kamat, P. V. (2011). *J. Am. Chem. Soc.* 133, 9607-9615.
- [168] Boix, P. P., Larramona, G., Jacob, A, Delatouche, B., Mora- Sero, I. and Bisquert, J. (2012). *J. Phys. Chem. C* 116, 1579-1587.

- [169] Jovanovski, V., Gonzalez-Pedro, V., Gimenez, S., Azaceta, E., Cabanero, G., Grande, H., Tena-Zaera, R., Mora-Sero, I., Bisquert, J. A (2011). *J. Am. Chem. Soc.* 133, 20156-20159.
- [170] Ning, Z. J., Yuan, C. Z., Tian, H. N., Fu, Y., Li, L., Sun, L. C. and Agren, H.(2012). *J. Mater. Chem.* 22, 6032-6037.
- [171] Wang, P., Zakeeruddin, S.M., Comte, P., Exnar, I. and Gratzel, M. (2003). *J. Am. Chem. Soc.* 125, 1166-1167.
- [172] Kumara, G. R. A., Konno, A., Shiratsuchi, K., Tsukaraha, J. and Tennakone, K. (2002). *Chem. Mater.* 14, 954.
- [173] Senadeera, G. K. R., Jayaweera, P. V. V., Perera, V. P. S., Tennakone, K. (2002). *Solar Energy Materials & Solar Cells* 73, 103.
- [174] Li, B., Wang, L., Kang, B., Wang, P. and Qiu, Y. (2006). *Solar Energy Materials & Solar Cells* 90, 549-573.
- [175] Perera, V.P.S. and Tennakone, K. (2003). *Solar Energy Materials & Solar Cells* 79, 249.
- [176] Kubo, W., Murakoshi, K., Kitamura, T., Yoshida, S., Haruki, M., Hanabusa, K, Shirai, H., Wada, Y. and Yanagida, S. (2001). *J. Phys. Chem. B* 105, 12809.
- [177] Katagiri, H., Ishigaki, N., Ishida, T. and Saito, K. (2001). *Jpn. J. Appl. Phys.* 40, 500.
- [178] Kamoun, N., Bouzouita, H. and Rezig, B. (2007). *Thin Solid Films* 515, 5949-5952.
- [179] Ding, I., Melas-Kyriazi, J., Cevey-Ha, N., Chittibabu, K.G., Zakeeruddin, S.M., Grätzel, M. and McGehee, M.D. (2010). *Organic Electronics* 11, 1217-1222.

- [180] Lincot, D., Guillemoles, J.F., Taunier, S., Guimard, D., Sicx-Kurdi, J., Chaumont, A., Roussel, O., Ramdani, O., Hubert, C., Fauvarque, J.P., Bodereau, N., Parissi, L. Panheleux, P., Fanouillere, P., Naghavi, N., Grand, P.P., Benfarah M., Mogensen P. and Kerrec, O. (2004). *Solar Energy* 77, 725-737.
- [181] Zhang, L., Jiang, F.D. and Feng, J.Y. (2003). *Solar Energy Mater. Solar Cells* 80, 483-490.
- [182] Jerankoa, T., Tributscha, H., Sariciftib, N.S. and Hummelen, J.C. (2004). *Solar Energy Materials & Solar Cells* 83, 247-262.
- [183] Dhere, N.G. (2011). *Solar Energy Materials & Solar Cells* 95, 277-280.
- [184] Akhavan, V.A., Goodfellow, B.W., Panthani, M.G. Steinhagen, C., Harvey, T.B., Stolle, J.C. and Korgel, B.A. (2012). *Journal of Solid State Chemistry* 189, 2-12.
- [185] Guo, Q., Kim, S.J. Kar, M. Shafarman, W.N. Birkmire, R.W. Stach, E.A., Agrawal, R. and Hillhouse, H.W. (2008). *Nano Lett.* 8, 2982-2987.
- [186] Liu, C.P. and Chuang, C.L. (2001). *Solar Energy Solar Energy Materials and Solar Cells* 65, 141-148.
- [187] Li, L., Coates, N. and Moses, D. (2010). *J. Am. Chem. Soc.* 132, 22-23.
- [188] Steinhagen, C., Panthani, M.G., Akhavan, V., Goodfellow, B., Koo, B. and Korge, B.A. (2009). *J. Am. Chem. Soc.* 131, 12554-12555.
- [189] Coscia, U., Ambrosone, G., Basa, d.K, Rogato, V., Ferrero, S. and Virga, A. (2013). *Thin Solid Films* 543, 27-31.
- [190] Akhavan, V.A., Panthani, M.G., Goodfellow, B.W., Reid, D.K. and Korgel, B.A. (2010), *Energy Express* 18, A411-A420.

- [191] Liu, C.P. and Chuang, C.L. (2012). *Solar Energy* 86, 1605-1610.
- [192] Lee, J.H., Chang, J. Cha, J-H., Lee, Y., Han, J.E., Jung, D-Y., Choi, E.C. and Hong, B. (2011). *Eur. J. Inorg. Chem.* 2011, 647-651.
- [193] Gratzel, M. (2000). *Prog. Photovol. Res. Appl.* 8, 171.
- [194] Rhoderick, E.H. (1988). *Metal–Semiconductor Contacts*, Clarendon, Oxford.
- [195] Hackam, R. and Harrop, P. (1972). *Solid-state electronics* 15, 1031-1032.
- [196] Beyer, B., Griese, D., Schirrmann, C., Pfeiter, R., Kahmann, S., Hild, O. and Leo, K. (2013). *Thin Solid Films* 536, 206-210.
- [197] Cheung, S.K. and Cheung, N.W. (1986). *Appl. Phys. Lett.* 49, 85-87.
- [198] Idrichan, G. P., Sorokina, G.Z. and Kaptar L. P. (1974). *Inorg. Mater.* 10, 1537.
- [199] Tang, J., Hinds, S., Kelley, S. O. and Sargent, E.H. (2008). *Chem. Mater.* 20, 6906-6910.
- [200] Jun, H.K., Careem, M.A. and Arof, A.K. (2013). *Renewable and Sustainable Energy Reviews* 22, 148-167.
- [201] O'Regan, B., Gratzel, M. (1991). *Nature* 353, 737-740.
- [202] Kongkanand, A., Tvrđy, K., Takechi, K., Kuno, M. and Kamat, P.V. (2008). *J. Am. Chem. Soc.* 130, 4007-4015.
- [203] Chakrapani, V., Tvrđy, K. and Kamat, P.V. (2010). *Journal of the American Chemical Society* 132, 1228-1229.

-
- [204] Im, J-H., Lee, C-R., Lee, J-W., Park, S-W. and Park, N-G. (2011). *Nanoscale* 3, 4088-4093.
- [205] Ip, A.H., Thon, S.M., Hoogland, S., Voznyy, O., Zhitomirsky, D., Debnath, R., Levina, L., Rollny, L.R., Carey, G.H., Fischer, A., Kemp, K.W., Kramer, I.J., Ning, Z., Labelle, A.J., Chou, K.W., Amassian, A. and Sargent, E.H. (2012). *Nature Nanotechnology* 7, 577-582.
- [206] Chang, C. H. and Lee, Y. L. (2007). *Appl. Phys. Lett.* 91, 1-3.
- [207] Sarkar, O. S., Pejoux, S. K., Rühle, C. S., Cahen, S. and Hodes, D. (2006). *J. Photochemistry and Photobiology A*, 181, 306-313.
- [208] Guijarro, N., Lana-Villarreal, T., Mora-Seró, I., Bisquert, J., Gómez, R. (2009). *J. Phys. Chem. C*, 113, 4208-4214.
- [209] Tvrdy, K. and Kamat, P. V. (2009). *J. Phys. Chem. A*, 113, 3765-3772.

CHAPTER 3:

SYNTHESIS, CHARACTERIZATION OF COPPER SELENIDE NANOPARTICLES AND THEIR APPLICATION IN A SCHOTTKY DEVICE

3.1 Introduction

Copper selenide is a p-type I–VI semiconductor that has gained particular interest due to the excellent optical, electronic and electrical properties [1-3]. Copper selenide nanoparticles are mostly found as CuSe, Cu₂Se and Cu₃Se₂ with their bulk materials possessing band gap energies between 1 and 2.3 eV [4-13]. Copper selenide nanoparticles are considered as the basic material from which many derived compounds can be prepared for photovoltaic applications. Copper selenide is a good precursor for fabrication of chalcopyrite copper indium selenide based nanostructures on a large scale [14]. Copper selenide materials are used in Schottky cells, heterojunction solar cells, as one of the components of the active layer and as counter electrode enforcement [15-19]. The tunable properties of copper selenide nanoparticles have much contributed to the building of other materials and their photovoltaic devices [20-25]. Various methods have been elaborated for the synthesis of copper selenide nanoparticles but colloidal and solvothermal syntheses have been the most employed. These methods resulted in various shaped and sized particles [3, 14, 37-41]. Fewer studies have been reported on the synthesis of copper selenide using a microwave assisted synthesis route [2, 19, 56-59]. Nevertheless the few reports on this method have yielded poor quality nanoparticles with no defined shapes or sizes.

The process and the yield of copper selenide suggest that more is still needed for further knowledge and usage of copper selenide nanoparticles. The crystalline phase and size of copper selenide nanoparticles and thus their properties are determined by the stoichiometry and synthetic method [13, 26-30]. Although copper selenide can be synthesized in various stoichiometries including CuSe, Cu_{2-x}Se and Cu₃Se₂ [9-13], tremendous efforts have been invested in synthesizing copper selenide nanocrystals with various shapes and sizes. Regular shaped and sized particles decrease the trapping of electrons in the absorbing materials and thus lead to a more efficient device [31]. Several parameters are controlled to synthesize copper selenide nanoparticles with specific shapes and size [29, 32-36]. The effects of

synthesis time on particle growth and size distribution in conventional colloidal method are important in order to obtain nanocrystals with desired properties. However, the major challenge of synthesizing copper selenide nanocrystals is to control in a reproducible manner the stoichiometry. Various compositions of copper selenide have been reported and synthesized using various methods. CuSe nanospheres, Cu₃Se₂ nanoplates, CuSe nanotubes and Cu_{2-x}Se nanocubes and their corresponding hierarchical nanodendrites have been produced by thermolysis of single-source precursor, ultrasonochemical techniques, template-directed reaction, by an electrochemical crystallization process, and a hydrothermal method, respectively [37-46]. In this chapter we investigated the synthesis of copper selenide nanoparticles via conventional colloidal and microwave assisted methods [60]. Several parameters were studied during the synthesis including the method, time, temperature, precursor concentration and solvent. The properties of the synthesized copper selenide nanoparticles were determined and a Schottky device was fabricated then characterized.

3.2 Experimental procedures

3.2.1 Chemicals and materials

Copper (II) chloride, copper (I) chloride, selenium powder, hexadecylamine (HDA), triethanolamine (TEA), tri-n-octylphosphine (TOP), deionized water, methanol, ethanol, acetone, chloroform, toluene, hexane, tin doped-indium oxide (ITO), hexadecylamine (HDA), octadecylamine (OLA), trioctylphosphine (TOP) were purchased from Sigma Aldrich.

3.2.2 Synthesis of copper selenide nanoparticles

3.2.2.1 Conventional colloidal method

About 6.0 g of hexadecylamine (HDA) was placed in a clean three-neck round bottom volumetric flask and mounted on Schlenk line then heated to 100 °C on a heating mantle. The content of the flask was subsequently placed under vacuum until the bubbles disappeared from the surface of HDA. The content was then purged with argon several times and a 1 ml of 1M solution of CuCl in tri-n-octylphosphine (TOP) was added to the flask. The mixture was heated to around 220 °C where 1ml of 1M solution of Se in TOP was then be added. The content was heated for 30 min after which the temperature was decreased to 60 °C (Equation 3.1). Methanol was then added to the mixture to flocculate the nanoparticles. The

centrifugation (at 3000 rpm for 20 min) was used to separate copper selenide nanoparticles. The precursor concentrations, synthesis time and temperature were investigated.

3.2.2.2 Microwave assisted method

A range of solvents were investigated during this synthesis. This included HDA, ethylene diamine (EDA), triethylene glycol (TEG) and triethanol amine (TEA). 2 ml of TOPCuCl was placed in a teflon vessel liner containing 5 ml of solvent. The vessel liner was mounted on the rotor then purged with argon for 2 min before being placed in the Microwave. The system was heated for 10 min at a power 500 W and then cooled to 70 °C where 2 ml of TOPSe 1M was then quickly added and the system was purged for 5 min with argon before continuing heating the mixture for another 10 min at 600W. After cooling down to about 50 °C, methanol was added and the product was centrifuged at 3000 rpm for 20 min then washed with methanol at 3000 rpm for 10 min. This method was adapted from the reaction (3.1) below.



3.2.3 Fabrication of copper selenide device

The device assembly was made by spin coating 50 µl of a toluene solution containing copper selenide nanoparticles on the substrate. The later was spun at 3000 rpm and allowed to dry, forming a thin film coating. The aluminium top contact was sputtered through a shadow mask to generate an array of patterned electrodes. The Al was deposited by thermal evaporation in high vacuum of better than 5×10^{-5} Pa at a rate of 0.2 nm s^{-1} . The final device area of 0.08 cm^2 was defined by overlap between the top ITO and the bottom Al electrodes. The assembled device was structured as ITO/Cu_xSe/Al.

3.2.4 Characterization techniques

3.2.4.1 Optical and structural properties

The optical properties of the materials were determined by placing the toluene dispersion of the nanoparticles into quartz cuvettes (1 cm path length). A Perkin Elmer Lambda 75S UV–Vis–NIR Spectrophotometer and an Analytica Jena Specord 5D UV-Vis Spectrophotometer were used to carry out the optical measurements. A Perkin Elmer LS55 with a xenon lamp (150 W) and a 152 P photo multiplier tube as a detector were used to measure the photoluminescence of the particles.

The morphology of the NPs was determined on Technai G² TEM Spirit operated at 200 kV. Transmission electron microscopy (TEM) samples were prepared by drop-casting the nanocrystal dispersion in toluene onto the carbon-coated copper grids and allowed to dry at room temperature. The diffraction patterns were determined using Bruker D2 Phaser Powder X-ray diffractometer using a Co (1.78898 nm) radiation source.

3.2.4.2 Thin film and device properties

i) Atomic force microscopy of copper selenide thin film

The atomic force microscopy (AFM), Veeco 3100 SPM was used to determine the surface morphology of the deposited layer of the synthesized copper selenide nanoparticles. The substrate was loaded on the stage under vacuum where the laser alignment was processed. The tapping mode was employed to obtain the AFM images.

ii) Electrical measurements

The photovoltaic properties such as current (I) and voltage (V) were determined using a digital source meter (Keithley Instruments Inc., Model 2400) in the dark and under an illumination of a solar simulator at AM 1.5, 1000 W m⁻².

3.3 Results and discussion

3.3.1 The effect of the conventional colloidal and microwave assisted methods on the synthesis of copper selenide nanoparticles

3.3.1.1 Principles of the CCM and MAM methods

The conventional colloidal method was first introduced by Murray *et al.* [61]. The method involved the injection of cold TOP solution of precursors into a hot TOPO coordinating solvent. The mechanism for this type of reaction has been shown to follow the La Mer and Dinegar's nucleation and growth through Ostwald's ripening mechanism [62]. The injection leads to the instantaneous formation of nuclei. Due to a drop in temperature after the addition of the cold TOP solutions, the formation of new nuclei is prevented. This result in a suspension of reasonably mono-disperse nuclei together with considerable amounts of free precursors. Increasing the temperature, but below 300 °C, leads to slow growth of the existing nuclei but with no formation of new nucleation. The TOPO molecules slow down the growth considerably by coordinating to the surface of the nanocrystal thus forming a steric barrier for reactants. The slow growth at relatively high temperatures allows the

nanocrystals to anneal and to form nearly defect-free crystal lattices, which are identical to the bulk lattice. In this current study, the TOPO molecules are replaced with HDA molecules. The conventional colloidal method in this case offers more versatility compared to the hydrothermal method. The method eliminates the use of an autoclave by employing the standard three-neck glass vessel. The reaction is carried under atmospheric pressure conditions as well as at low temperatures. Ordinarily the selenium powder is non-reactive and will not interact with the metal salt to form the metal selenide, but by first reducing the selenium into a more reactive selenium species, the reaction proceeds with minimum energy requirements. This also allows the reaction to be carried out in shorter time of synthesis which results in controlled nucleation and growth. In addition instantaneous monitoring of the reaction can occur because of the accessible reaction vessel. The reaction path is shown in Fig. 3.1. The colloidal method has been known to result in very small and monodispersed nanocrystals [63]. Since then, various adaptations to this method have been undertaken.

The energy of a microwave photon with a frequency of 2.45 GHz corresponds to 1.01×10^{-5} eV which is about 3 orders of magnitude lower than the bond energy of a covalent bond in a molecule. This suggests that direct excitation of the electron from a chemical bond cannot be caused by the absorption of microwave photons and therefore no reaction will take place. However, it has been shown that microwave irradiance does result in an occurrence of a reaction. This has led to two main postulated mechanisms for microwave heating. The two main heating mechanisms in microwave chemistry are dipolar polarization and ionic conduction. Heating by dipolar polarization stems from the orientation of dipoles in the electromagnetic field. Dipoles tend to align in the direction of an external electric field. The degree of orientation is governed by the field strength and the static dielectric constant. When an oscillating electric field is applied to a material, for instance microwave radiation, the dipoles are constantly trying to align with the changing electric field. The frequency of the field determines how the orientation of dipoles will affect the material. With a very high frequency the dipoles cannot adapt to the electric field and orientation does not occur. With a low frequency the dipoles are in a constant equilibrium state with field, acting as dipoles in a static electric field. In between these frequencies the alignment of the dipoles, lagging behind the changing electric fields, causes molecular friction, which in turn is converted into heat. The mechanism of ionic conduction is similar to that of dipolar polarization. When charge carriers in a material are subjected to an electric field, they are subjected to a force. The

alternation of the electric field causes the direction of the force to alternate equally. This alternation leads to molecular motion, and collision, and thus heat [24, 64-65]. As a result of the heating method, microwave result in homogeneous and rapid heating. The methods are illustrated in Scheme Fig.3.1.

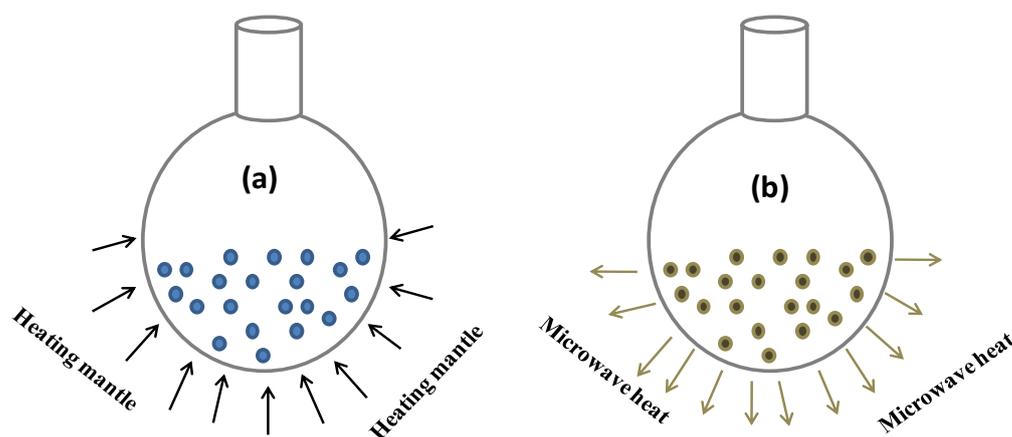


Fig. 3.1 Heating path for synthesis of Cu_xSe NPs via (a) CCM and (b) MAM

3.3.1.2 Optical properties of the CCM and MAM synthesized Cu_xSe nanoparticles

The optical properties of copper selenide NPs synthesized via the CCM and MAM were investigated using UV-Vis absorption and photoluminescence spectroscopy. The absorption spectra of CCM and MAM synthesized nanoparticles are shown in Fig. 3.2. A large blue-shift absorption from their bulk material was observed for both the CCM and MAM synthesized copper selenide nanoparticles. This was also confirmed by the band gap estimation from the energy curves shown in Fig. A3.1 of the appendix (the method for determination of the band gap using the energy curve is also provided in appendix). This is indicative of decrease in particle size resulting in quantum confinement effect. Table 3.1 shows the values related to the optical characterization. The absorption spectra revealed the band edge for the CCM synthesized NPs to be at 420 nm while the band edge from MAM was located at 445 nm. The band-edges suggest that the particles obtained from the MAM are slightly larger than those obtained from the CCM. The emission spectra of CCM and MAM synthesized nanoparticles are shown in Fig. 3.3. The emission maxima were found to be at 450 nm and 580 nm for NPs synthesized using the CCM and MAM respectively. The MAM full width at the half maximum (FWHM) of the emission peak was 67 nm, slightly smaller than that of CCM

sample being 71 nm. This indicates a narrower size distribution in MAM than CCM samples. A large Stokes shift was observed for the NPs synthesized using MAM (135 nm) compared to 30 nm from the CCM. The shortest gap observed between the band-edge and the emission peak from NPs synthesized using the CCM may be attributed to the differences in stoichiometry of the NPs compared to the MAM synthesized NPs. This would result in different electronic structures of the materials.

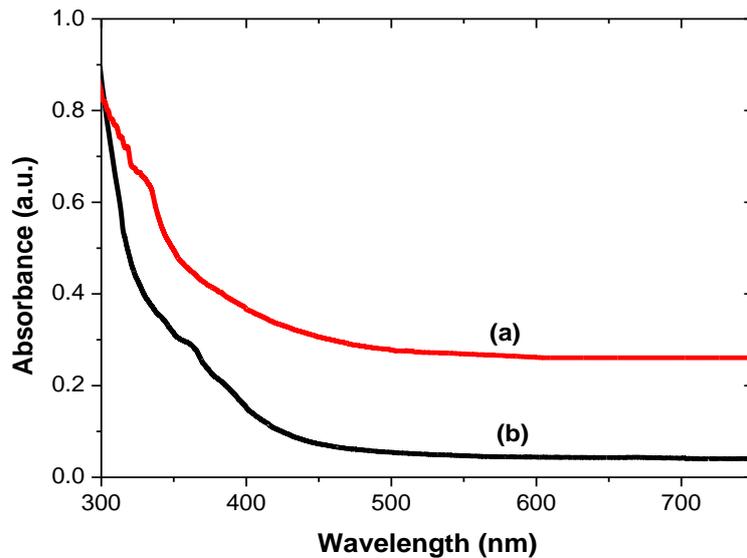


Fig. 3.2 Absorption spectra of Cu_xSe NPs synthesized via (a) CCM and (b) MAM

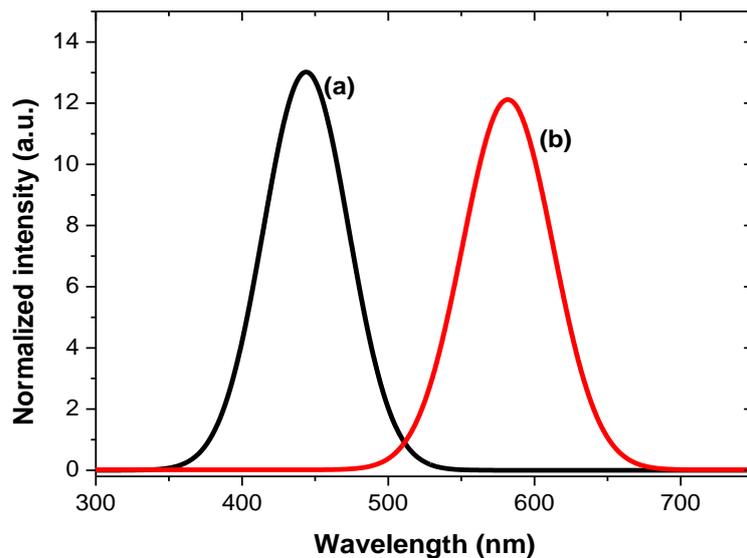


Fig. 3.3 Emission spectra of Cu_xSe NPs synthesized via (a) CCM and (b) MAM

Table 3.1 Optical parameters of Cu_xSe NPs synthesized via CCM and MAM

Method	Band Edge Abs (nm)	Emission peak (nm)	Stokes Shift (nm)	FWHM (nm)
CCM	420	450	30	71
MAM	445	580	135	67

3.3.1.3 Structural properties of the CCM and MAM synthesized Cu_xSe nanoparticles

XRD patterns and TEM images were undertaken to determine the structural properties of copper selenide nanoparticles synthesized by both CCM and MAM. The XRD patterns from CCM and MAM synthesized NPs are shown in Fig. 3.4. The copper selenide nanoparticles were obtained in both methods and showed a mixture of phases namely, a dominant cubic phase Cu_{2-x}Se corresponding to (111), (200), (220), (311), (400) and (422) crystal planes for the 2θ values 31°, 36°, 52°, 62°, 72° and 85° respectively (JCPDF file no 010710044) and a less dominant CuSe hexagonal phase with the diffraction planes located at 2θ values 29°, 46° and 59° (JCPDF file no 000491457). The peak ratio of Cu_{2-x}Se and CuSe phase suggests that the NPs synthesized from the MAM are purer than the particle synthesized from the CCM. Furthermore the sharpness of the peaks in MAM synthesized NPs are indicative of larger sizes and a good crystallinity of copper selenide nanoparticles than those from CCM. This might be due to the fact that the mixture in CCM is not evenly heated whilst MAM employs a more evenly distributed heat on the reactant mixture.

The TEM images of copper selenide NPs (Fig. 3.5) generally revealed that the particles were hexagonal in shape. The average particle diameter was 4.22 ± 0.157 nm for the CCM synthesized NPs and 5.95 ± 0.233 nm for the MAM synthesized NPs confirming the optical properties yielded from UV absorption and PL emission spectra as well the XRD data. However the size distribution was not homogeneous for both CCM and MAM as proven by the emission spectra. The MAM gave smaller population but with bigger sizes than CCM. The size distribution from MAM samples gave a better Gaussian fit ($R^2=0.904$) compared to that from CCM (0.720). This may indicate good determination of polydispersivity in MAM synthesized nanoparticles. Larger particles from MAM may be attributed to a long microwave heating exposure of all precursors and solvent mixed in the vessel liner before synthesis, which then favoured the Ostwald ripening effect. Due to the size distribution and

the purity of these nanoparticles and possibility of up-scaling the synthesis, a Schottky device based on the MAM copper selenide was thus fabricated. In addition several reaction parameters were varied on the CCM method in order to improve the size distribution and investigate their overall effect on the properties of the resultant particles.

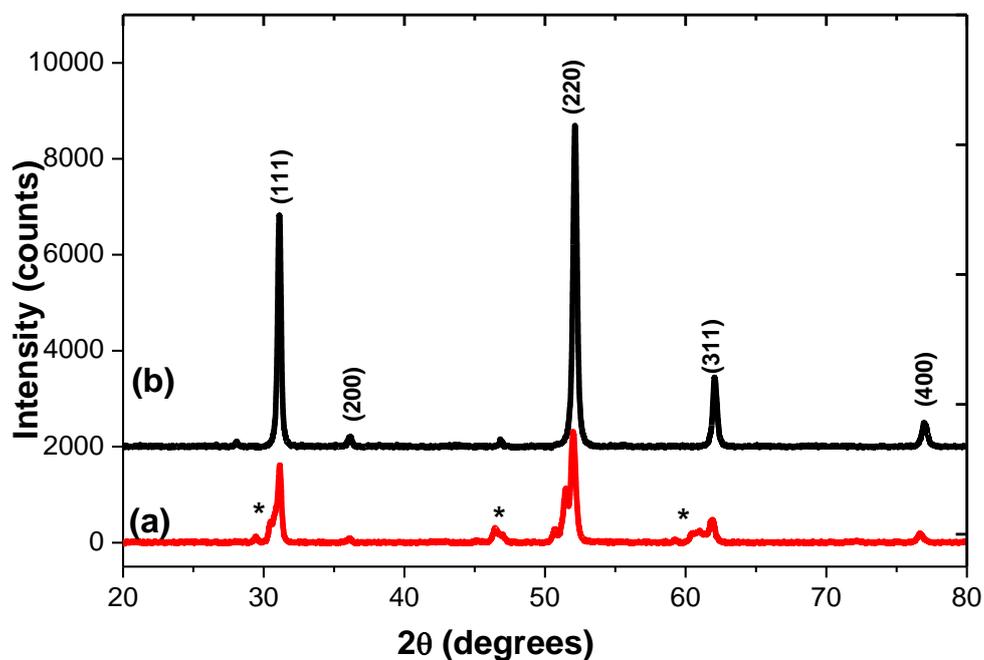


Fig. 3.4 XRD patterns of (a) CCM and (b) MAM synthesized Cu_xSe nanoparticles; with (*) the less dominant hexagonal phase

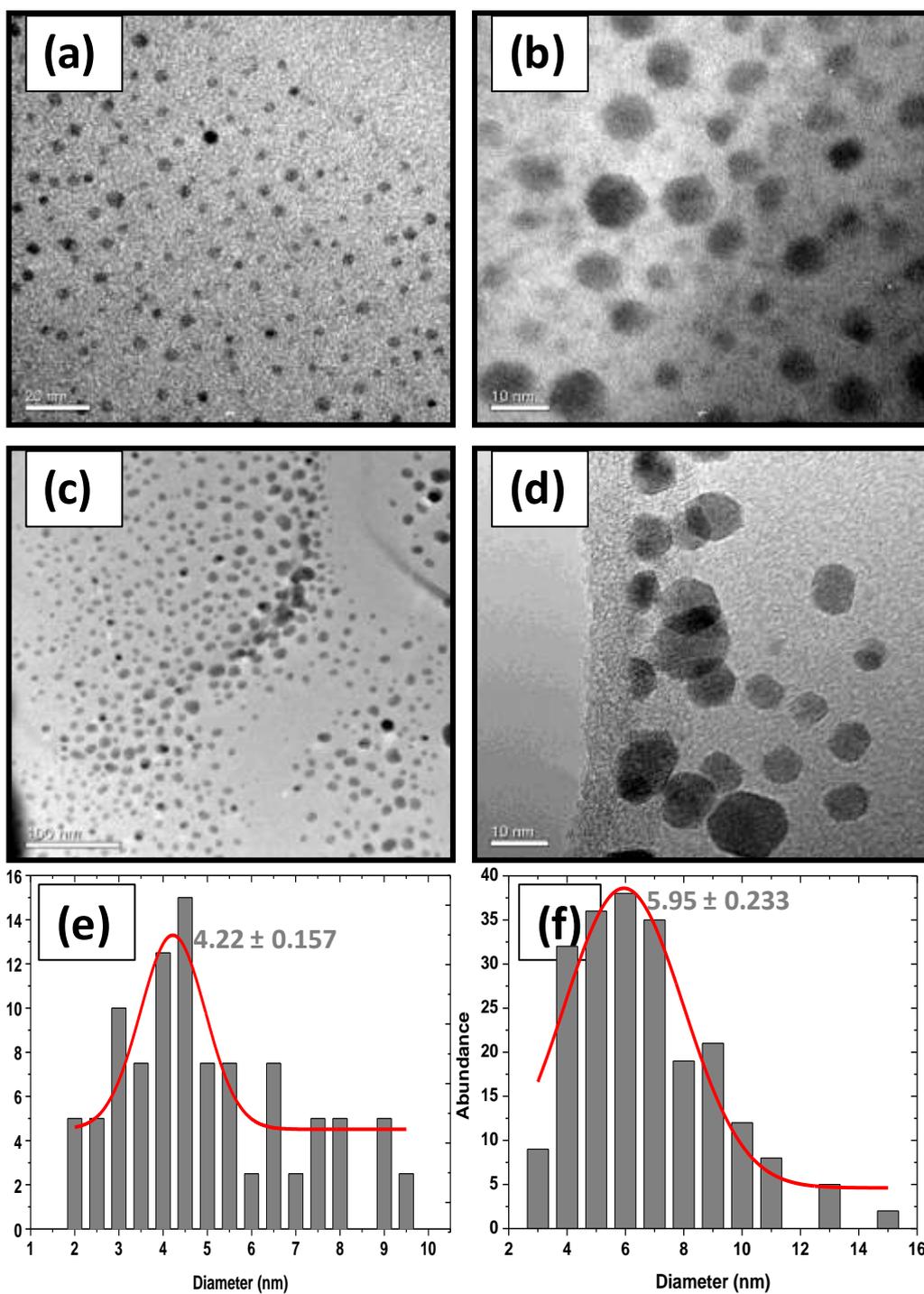


Fig. 3.5 TEM images and size distribution curve of (a), (b), (e) CCM and (c), (d), (f) MAM synthesized Cu_xSe NPs

3.3.2 Time effects on conventional colloidal method

3.3.2.1 Optical properties of the CCM synthesized copper selenide nanoparticles at different times

In this section, copper selenide quantum dots synthesized via conventional colloidal method in which 1 mole copper chloride and 1 mole of Se solutions were injected into hot HDA according to the method mentioned in section 3.2.2.1. The time was programmed to 10, 30 and 60 min and the temperature of synthesis was just set at 220 °C. The effect of time on the copper selenide QDs was investigated via various techniques including UV, PL and TEM. The UV- Vis absorption spectra of copper selenide nanoparticles synthesized at 10, 30 and 60 min are shown in Fig. 3.6. The absorption band edges were blue-shifted from the bulk absorption band edge of 1180 nm. However the band edge seemed to be less dependent upon the time of synthesis. The extracted optical parameters of copper selenide synthesized at different times are assembled in Table 3.2. The spectra, especially those obtained from synthesis at 10 min and 60 min had a higher degree of tailing and thus made it impossible to accurately locate the band edges. However, the nanoparticles synthesized for 30 min gave a band edge around 352 nm. The large blue shift may be indicative of very small sizes or different stoichiometry as the quoted bulk band edge is for copper monoselenide.

The PL spectra are shown in Fig. 3.7. The broad peaks observed on PL spectra suggest the samples are polydispersed; however the 30 min sample shows a lesser degree of polydispersity. This is in agreement of the UV-Vis absorption spectra as the 30 min showed less tailing in comparison to the two other intervals. The Stokes Shift was found in the range of 86-98 nm, suggesting that the particles had similar defects in all synthesized copper selenide samples. The emission maximum for all samples was located at about 450 nm. The maximum is the same for all samples suggesting similarities of the properties. The full width at half maximum (FWHM) of the 30 min sample was 69 nm. It is however smaller than the others located at 106 and 132 nm for 10 min and 60 min respectively. This suggests that 30 min is a more monodispersed sample, hence this was characterized further.

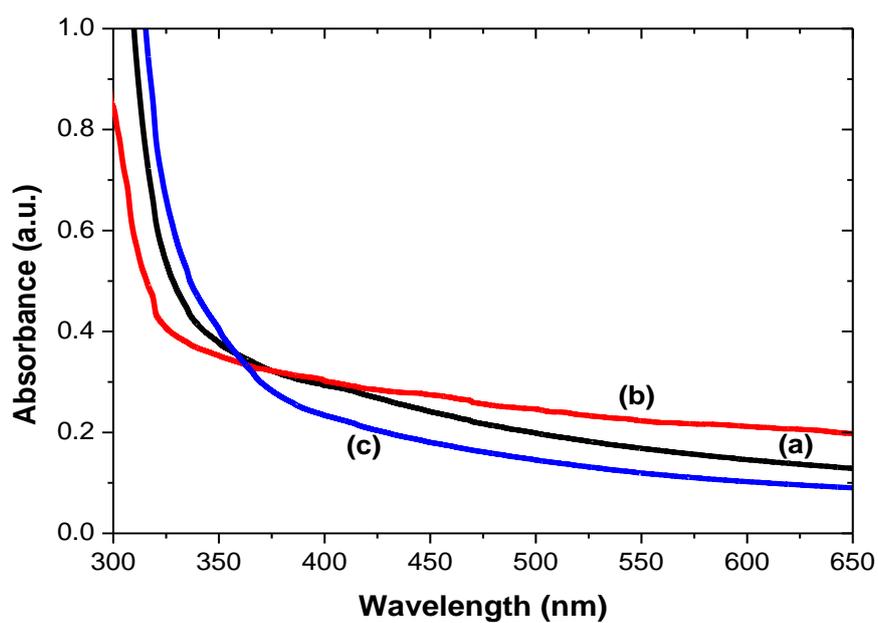


Fig. 3.6 Absorption spectra of Cu_xSe NPs synthesized for (a) 10 min, (b) 30 min and (c) 60 min at 220 °C in HDA for 1:1 mole ratio of Cu:Se

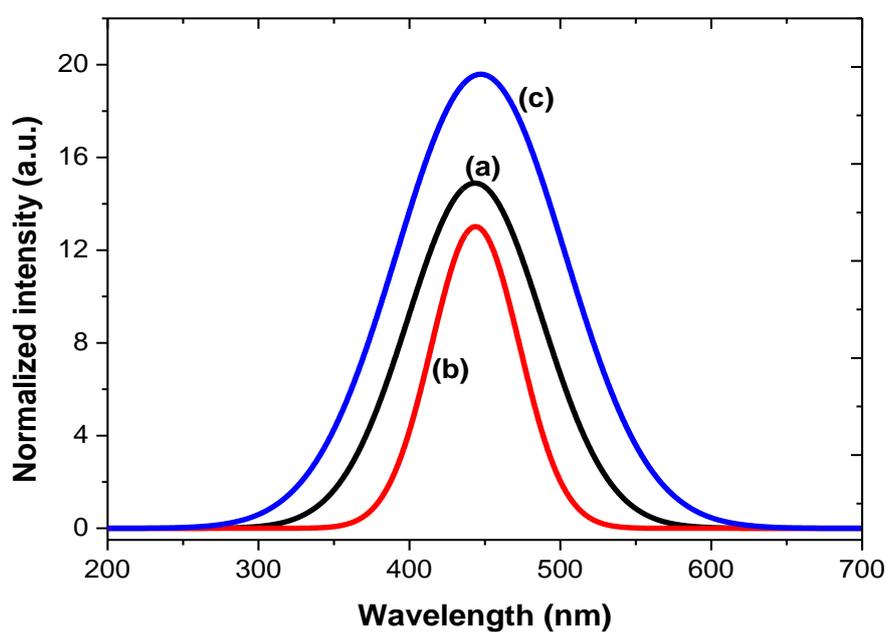


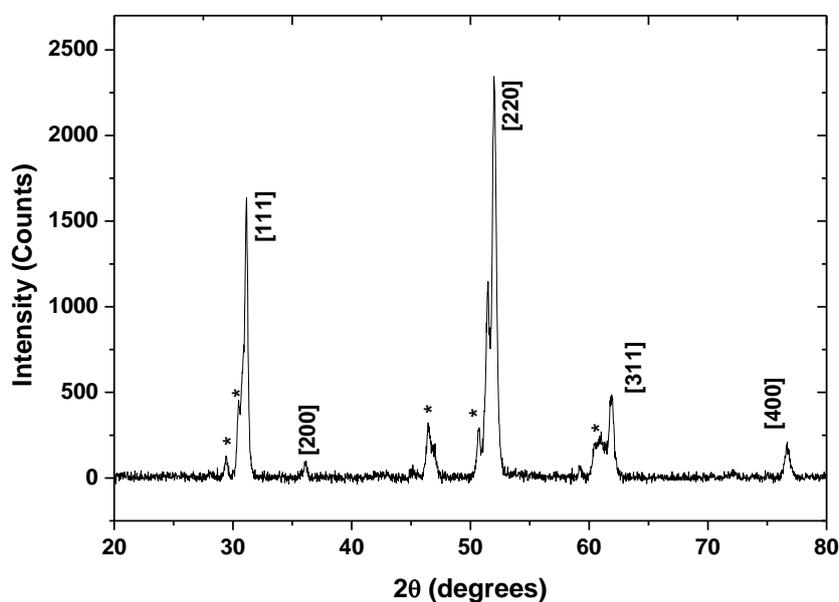
Fig. 3.7 Emission spectra of Cu_xSe NPs synthesized for (a) 10 min, (b) 30 min and (c) 60 min at 220 °C in HDA for 1:1 mole ratio of Cu:Se

Table 3.2 Optical parameters of Cu_xSe NPs synthesized at different times

Time (min)	Band edge (nm)	Band gap (eV)	Emission (nm)	Stokes shift (nm)	FWHM (nm)
10	360	2.01	450	90	106
30	352	2.15	450	98	69
60	364	1.89	450	86	132
Bulk	1180	1.45	-	-	-

3.3.2.2 Structural properties of Cu_xSe NPs synthesized for 30 min via CCM

The structural property analysis was only carried out on a 30 min precessed sample as it gave best quality particles in term of size and size distribution (suggested from UV-Vis absorption and emission spectra in section 5.2.1). The crystallinity of the nanoparticles was confirmed using XRD as shown in Fig. 3.8. They were found to crystallize in a predominant cubic Cu₂Se phase (PDF no 010710044) and encountered minor impurity phase of hexagonal CuSe (PDF no 000491457).

**Fig. 3.8** XRD patterns of [cubic] and (* hexagonal) phases of copper selenide nanoparticles synthesized at 220 °C for 30 min in Cu:Se mole ratio of 1:1

The TEM image of copper selenide nanoparticles (Fig. 3.9) revealed that the particles were hexagonal in shape and were polydispersed with no evidence of agglomeration. The average particle diameter was 4.22 ± 0.157 nm, far smaller than the Bohr radius of copper selenide and hence this is in corroboration with the large blue shift of the band edge observed in the absorption spectrum. The nanoparticles synthesized at 30 min gave the narrower size distribution, the smaller sized and monodispersed nanoparticles (standard deviation of 0.157 nm) with a more blue-shifted absorption band edge. The synthesis time of 30 min was then used to determine the effect of precursor concentration on the properties of copper selenide nanoparticles.

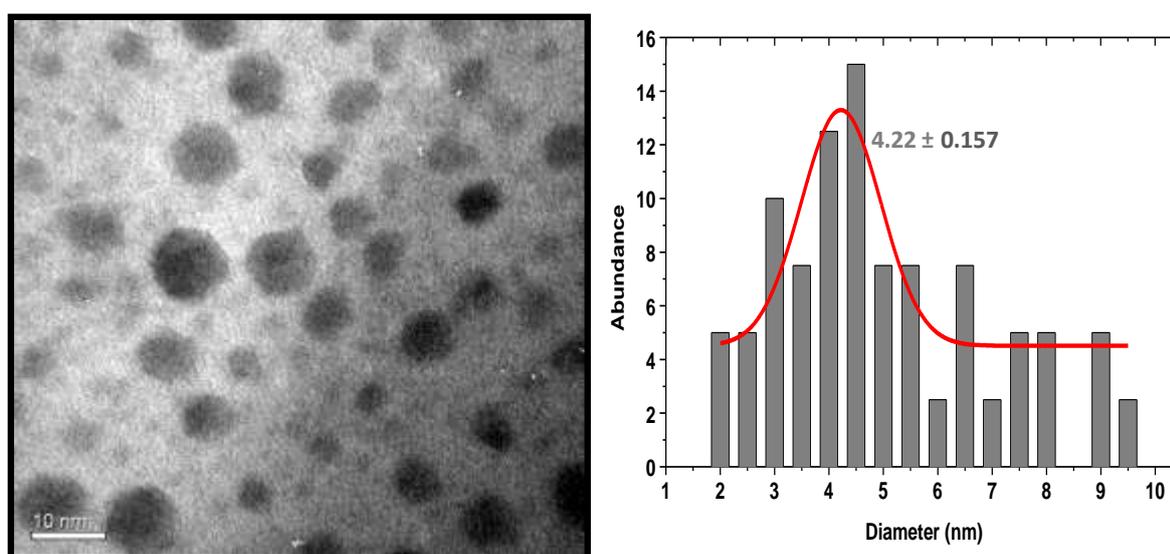


Fig. 3.9 TEM image of Cu_xSe synthesized at 30 min and particle size distribution

3.3.3 Precursor concentration effects on the synthesis of copper selenide nanoparticles

3.3.3.1 Optical properties

Copper selenide nanoparticles were synthesized via conventional colloidal method at $220\text{ }^\circ\text{C}$ for 30 min through varied concentrations of precursors in TOP. Copper and selenium precursors were investigated in concentration ratios of 1:1, 1:2 and 2:1. The optical parameters obtained from the absorption and emission spectra are shown in Table 3.3. The UV-Vis spectra obtained from all three concentrations are assembled in Fig. 3.10. The particles synthesized with the considered ratios gave blue shifted absorption band edges. The concentration ratio of 1:1 gave an absorption band edge at 525 nm which is more blue-shifted than those of 2:1 or 1:2 under our working conditions. This suggests a presence of smaller sizes in 1:1 sample. The absorption spectra also showed some degree of tailing signifying

polydispersed samples. This is also observed with the emission spectra shown in Fig. 3.11. The emission peaks were at maxima of nearly 600 nm for all three ratios. The Stokes-shift of 75, 40 and 10 nm were observed for 1:1, 2:1 and 1:2 ratios respectively. These values are however not very accurate due to the degree of tailing of the absorption spectra as a result of polydispersity of the samples making it difficult to accurately calculate the Stokes-shift. However, a small FWHM of 33 nm for the emission peak of 1:1 ratio was obtained, less than half of those of 1:2 and 2:1 which were 73 and 67 nm respectively suggesting that higher monodispersity was achieved with the 1:1 sample.

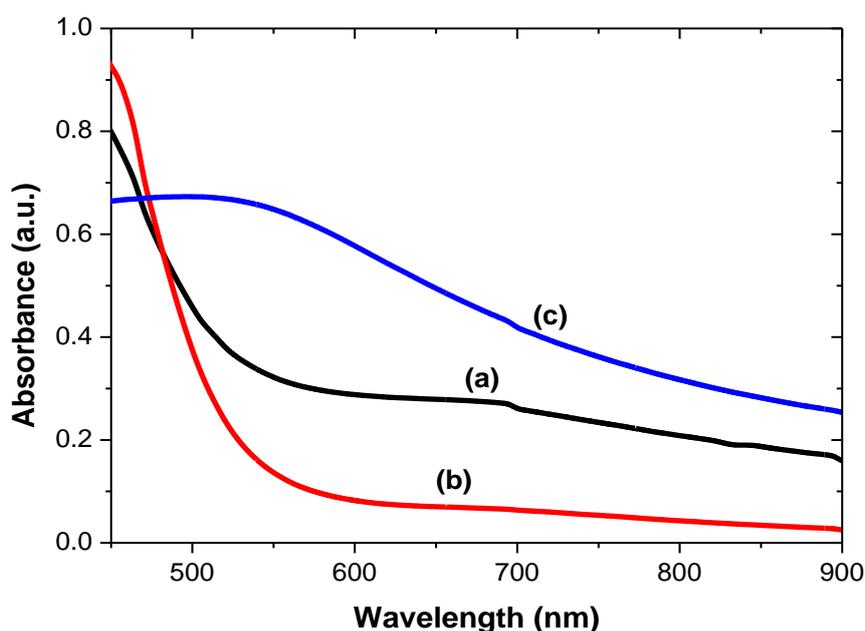


Fig. 3.10 Absorption spectra of Cu_xSe NPs synthesized from precursor concentrations of Cu: Se ratio of (a) 1:1, (b) 1:2 and (c) 2:1

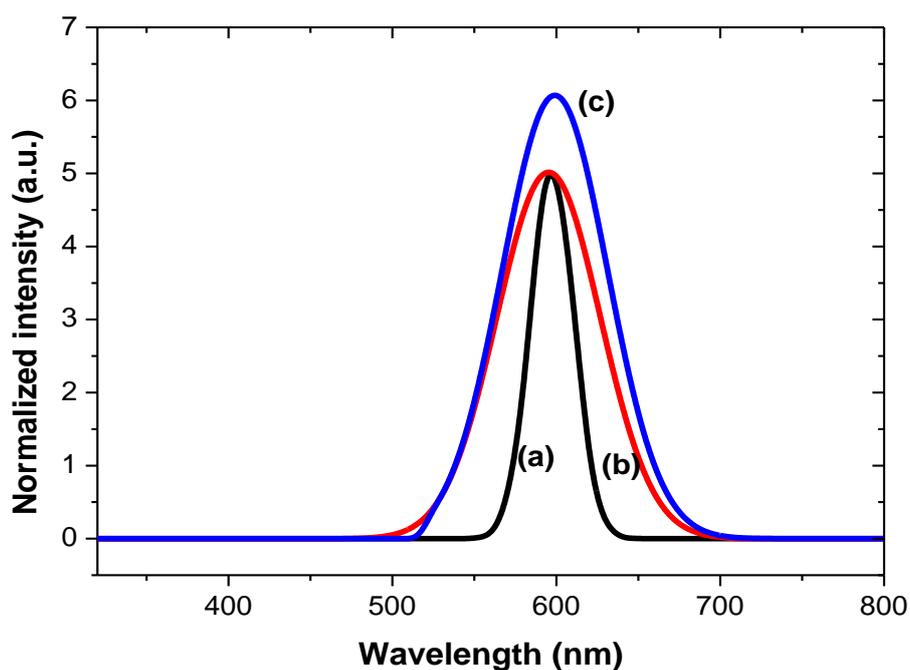


Fig. 3.11 Emission spectra of Cu_xSe NPs synthesized from precursor concentrations of Cu: Se ratio of (a) 1:1, (b) 1:2 and (c) 2:1

Table 3.3 Optical parameters of Cu_xSe NPs synthesized from different precursor concentrations

Cu/Se ratio	Band edge (nm)	Emission (nm)	Stokes shift (nm)	FWHM (nm)
1:1	525	600	75	33
1:2	560	600	40	73
2:1	590	600	10	67
Bulk	1180	-	-	

3.3.3.2 Structural properties

The XRD patterns of synthesized materials from the different precursor ratios are shown in Fig. 3.12. The XRD patterns showed that the particles yielded were indeed copper selenide with mainly a cubic Cu_2Se phase. The sharpness of the peaks observed in Fig. 3.12(a)

suggests that the particles synthesized from 1:1 ratio gave more crystalline nanoparticles and the position of the peaks matched perfectly with the Cu_2Se with no detection of impurities. However the peaks of the nanoparticles from the Cu:Se ratios of 1:2 and 2:1 tended to shift from the standard position. This could be as result of more strain and defects in the nanoparticles. One could also deduce that more impurities could be present due to the unreacted materials or secondary products such as additional phases of copper selenide, elemental copper or selenium. The TEM images of all synthesized copper selenide nanoparticles and the corresponding size distributions are shown in Fig. 3.13. The nanoparticles were in various shapes dominated by hexagonal facets. The diameters of 8.51 ± 0.415 nm, 8.75 ± 0.531 nm and 9.18 ± 0.857 nm were determined for Cu:Se ratios of 1:1, 1:2 and 2:1 respectively. The particles from 1:1 Cu:Se ratio were smaller with a better Gaussian fit ($R^2=0.8797$) and narrower size distribution (standard deviation of 0.415 nm) than other stoichiometries, confirming the findings from the optical properties. Hence the 1:1 ratio was used to determine the effect of solvent on the CCM synthesis of copper selenide nanoparticles.

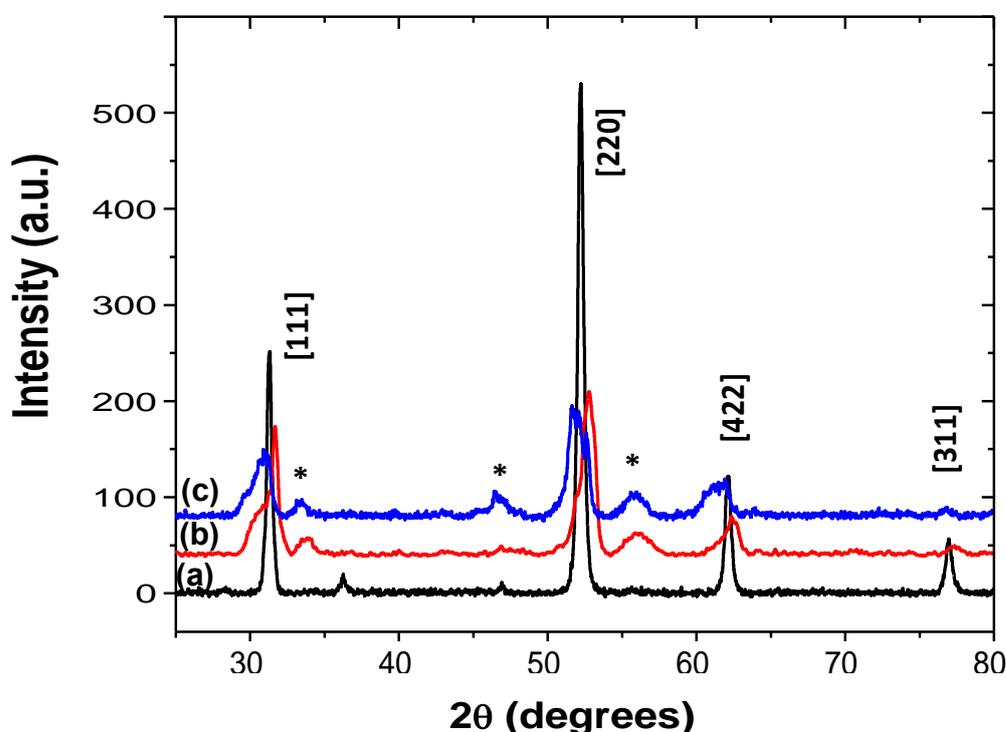


Fig. 3.12 XRD patterns of Cu_xSe NPs synthesized from precursor concentrations of Cu: Se ratio of (a) 1:1, (b) 1:2 and (c) 2:1

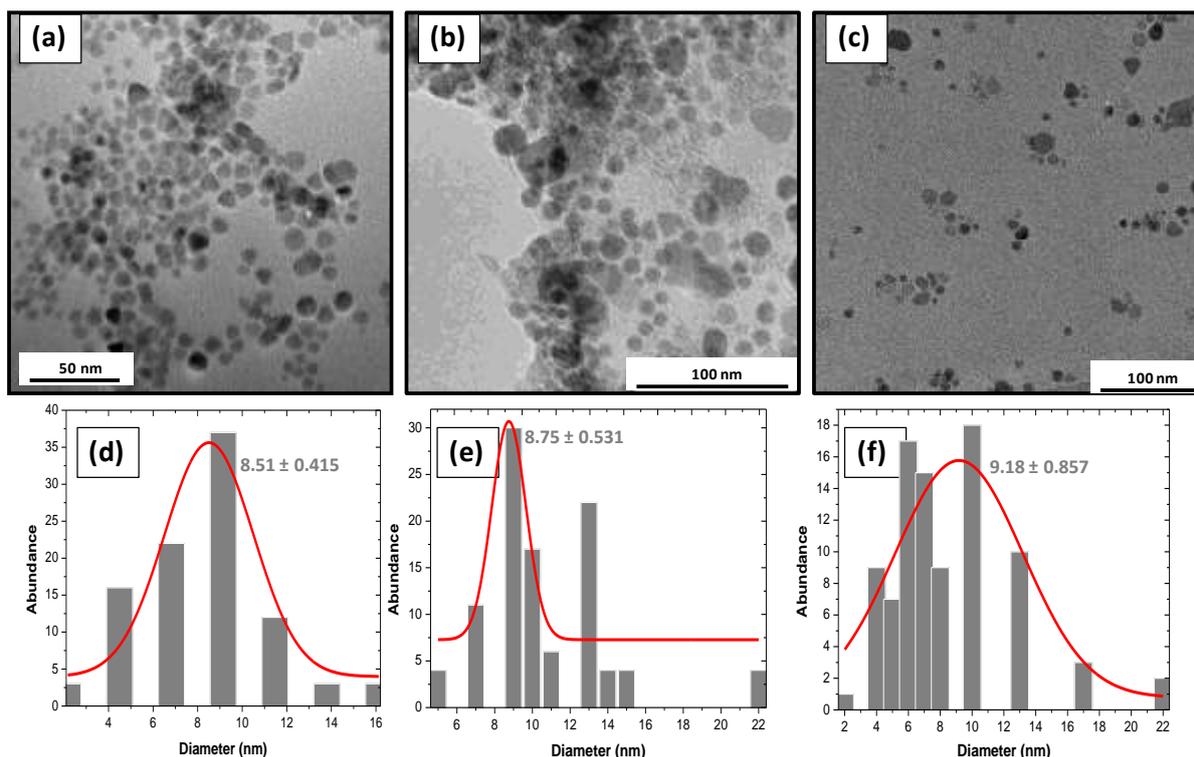


Fig. 3.13 TEM images of Cu_xSe synthesized from precursor concentrations of Cu: Se ratios of (a) 1:1, (b) 1:2 and (c) 2:1 with their particles size distribution (d), (e) and (f) respectively

3.3.4 Solvent effects on the synthesis of copper selenide nanoparticles

3.3.4.1 Optical properties

As a result of the reduced FWHM, the more blue-shifted absorption band edge, the less polydispersity and crystallinity of nanoparticles from the 1:1 ratio, the ratio was maintain when further investigation of the effects of the solvent was performed. The role of the solvent on the colloidal synthesis of the nanoparticles was investigated. Hexadecylamine and oleylamine were the two solvents investigated. They were used as surfactants and stabilisers in the synthesis of nanoparticles. While both have a terminal amine functional group, their aliphatic chains differ as well as their physical properties. Hexadecylamine has a 16 carbons chain of alkyl, with a boiling point of $330\text{ }^\circ\text{C}$ and the density of 0.78 g cm^{-3} . This solvent is solid at room temperature. Oleylamine has a boiling point of $350\text{ }^\circ\text{C}$, a density of 0.813 g cm^{-3} and it is liquid at room temperature. Oleylamine has a longer chain than hexadecylamine and it is formed of 18 carbons chain of alkylene [66, 67].

The absorption spectra are shown in Fig. 3.14 and the extracted optical parameters are shown in Table 3.4. Large blue-shifted band edges are observed. This is indicative of the tuning of energy due to the nanoscale sized particles. The band edges were found at 430 nm and 515 nm for nanoparticles synthesized using HDA and OLA respectively. This may be indicative of difference in crystalline structures and defects in both samples. The emission spectra are shown in Fig. 3.15. The maxima of emission peaks were found at 597 nm and 609 nm for HDA and OLA respectively. They were red-shifted from their corresponding absorption band edges. The FWHM of OLA synthesized copper selenide nanoparticles was 82 nm, broader than that of HDA which was at 33 nm. This suggests that the OLA nanoparticles were more polydispersed and in broader size distribution compared to HDA. However a Stokes shift of 167 nm was determined with nanoparticles synthesized using HDA, indicating more loss of energy due to the structure of synthesized copper selenide while the contrary can be observed with the OLA synthesis that gave a lower Stoke-shift of nearly 96 nm. It was therefore crucial to investigate the structure of both OLA and HDA synthesized copper selenide in order to complement these optical properties.

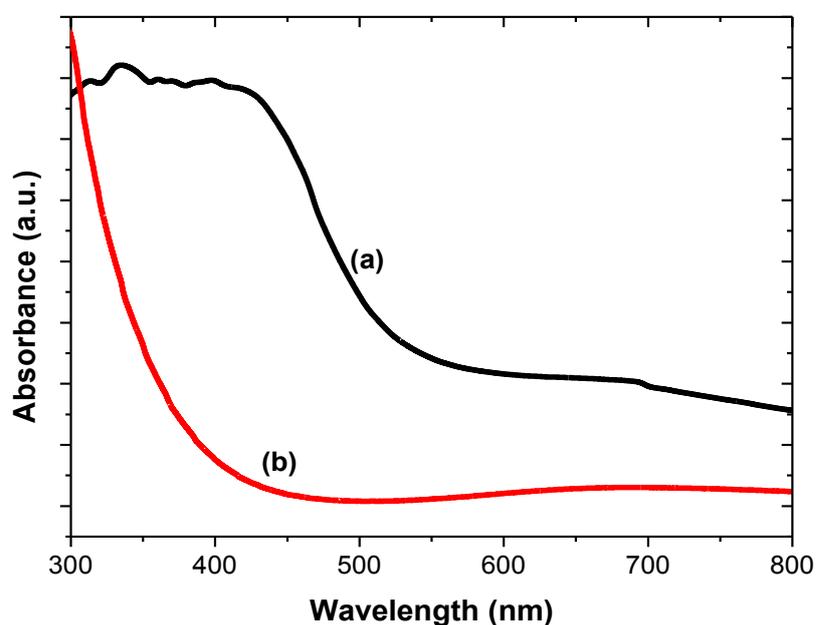


Fig. 3.14 Absorption spectra of Cu_xSe NPs synthesized from Cu:Se ratio of 1:1 in (a) HDA and (b) OLA

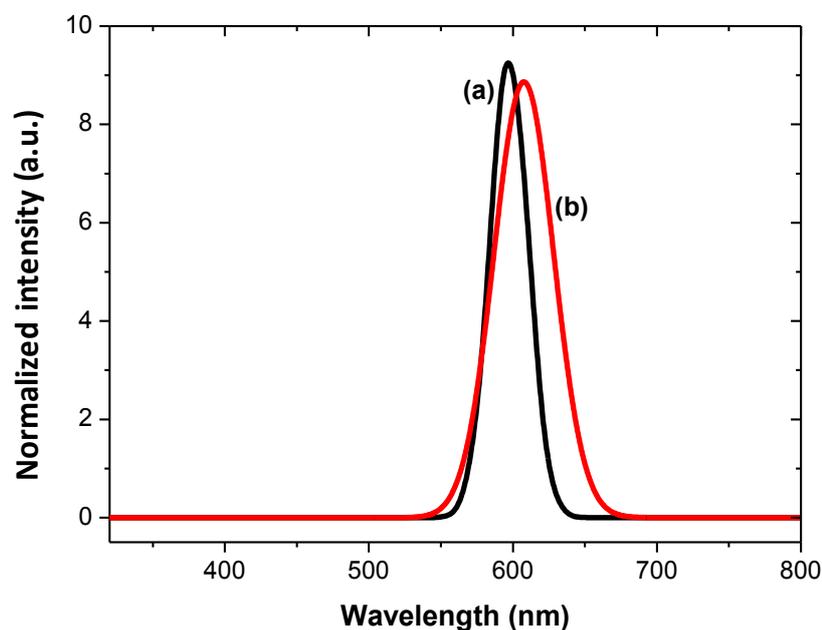


Fig. 3.15 Emission spectra of Cu_xSe NPs synthesized from Cu:Se ratio of 1:1 in (a) HDA and (b) OLA

Table 3.4 Optical parameters of Cu_xSe NPs synthesized via CCM using HDA and OLA

Solvent	Band edge (nm)	Emission (nm)	Stokes shift (nm)	FWHM
HDA	430	597	167	33
OLA	515	609	94	82
Bulk	1180	-	-	

3.3.4.2 Structural properties of Cu_xSe NPs synthesized in HDA and OLA

Fig. 3.16 shows the XRD patterns of the copper selenide nanoparticles synthesized with both HDA and OLA solvents. A single cubic Cu_2Se phase was observed from material synthesized using oleylamine whilst hexagonal CuSe phase mixed with a cubic Cu_2Se phase were found for particles synthesized using HDA. This can be confirmed from the peaks where OLA gave single, well defined peaks than HDA and can further explain the differences in optical

properties of the two samples as detailed in section 3.3.4.1. The peak broadness observed in Fig. 3.16 (b) suggests that smaller particles were obtained from synthesis using OLA than the HDA as solvent. However these findings do not align with optical properties where HDA gave a blue shift absorption band edge and a smaller FWHM than OLA. This can be due to the solvent adsorbed as ligands onto the surface of nanoparticles. Since HDA and OLA differ in their properties as shown earlier in this section, so would their capped nanoparticles. Therefore the choice of solvent may contribute to the properties of the yielded copper selenide nanoparticles under set synthesis conditions. This is demonstrated by the mixed phase of Cu₂Se and CuSe crystals determined in HDA than the pure single Cu₂Se crystal obtained using OLA. The TEM images, the size distributions and the EDS spectrum of copper selenide nanoparticles synthesized using HDA and OLA are shown in Fig. 3.17. The EDS analysis confirmed the presence of copper and selenium as the only constituents of the nanoparticles. The excess of copper is due to the contribution from the copper grid. The TEM images gave nearly spherical particles with average sizes of 7.89 ± 0.560 nm and 4.00 ± 0.336 nm for HDA and OLA synthesized copper selenide particles respectively. The OLA synthesized particles were far smaller and more monodispersed with a narrower size distribution (standard deviation of 0.336 nm) than those from HDA. This corroborated with the findings from XRD detailed above and may add more light to the optical properties shown earlier. Furthermore, the variation of the temperature for the synthesis of copper selenide nanoparticles was investigated.

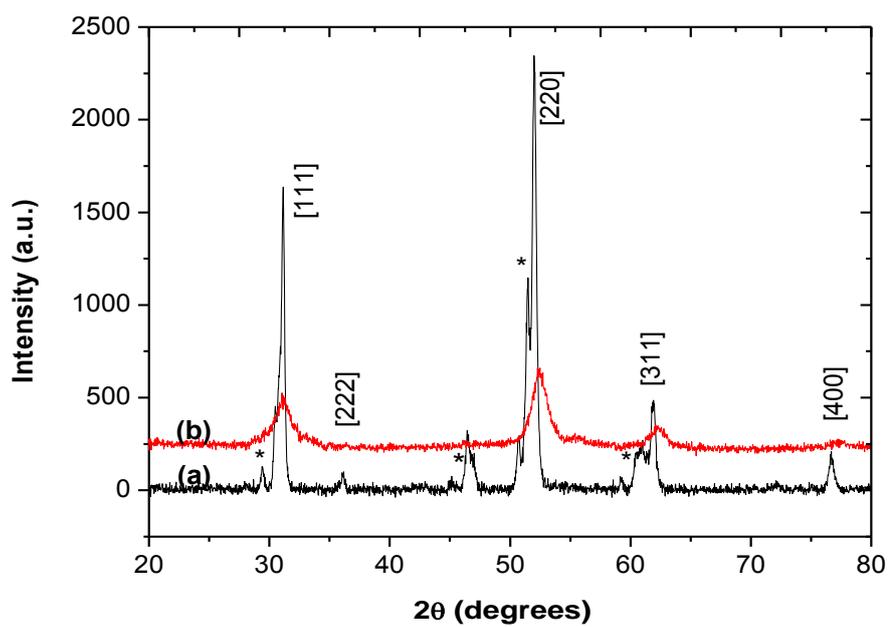


Fig. 3.16 XRD patterns of Cu_xSe NPs synthesized from Cu:Se ratio of 1:1 in (a) HDA (*less dominant cubic phase) and (b) OLA

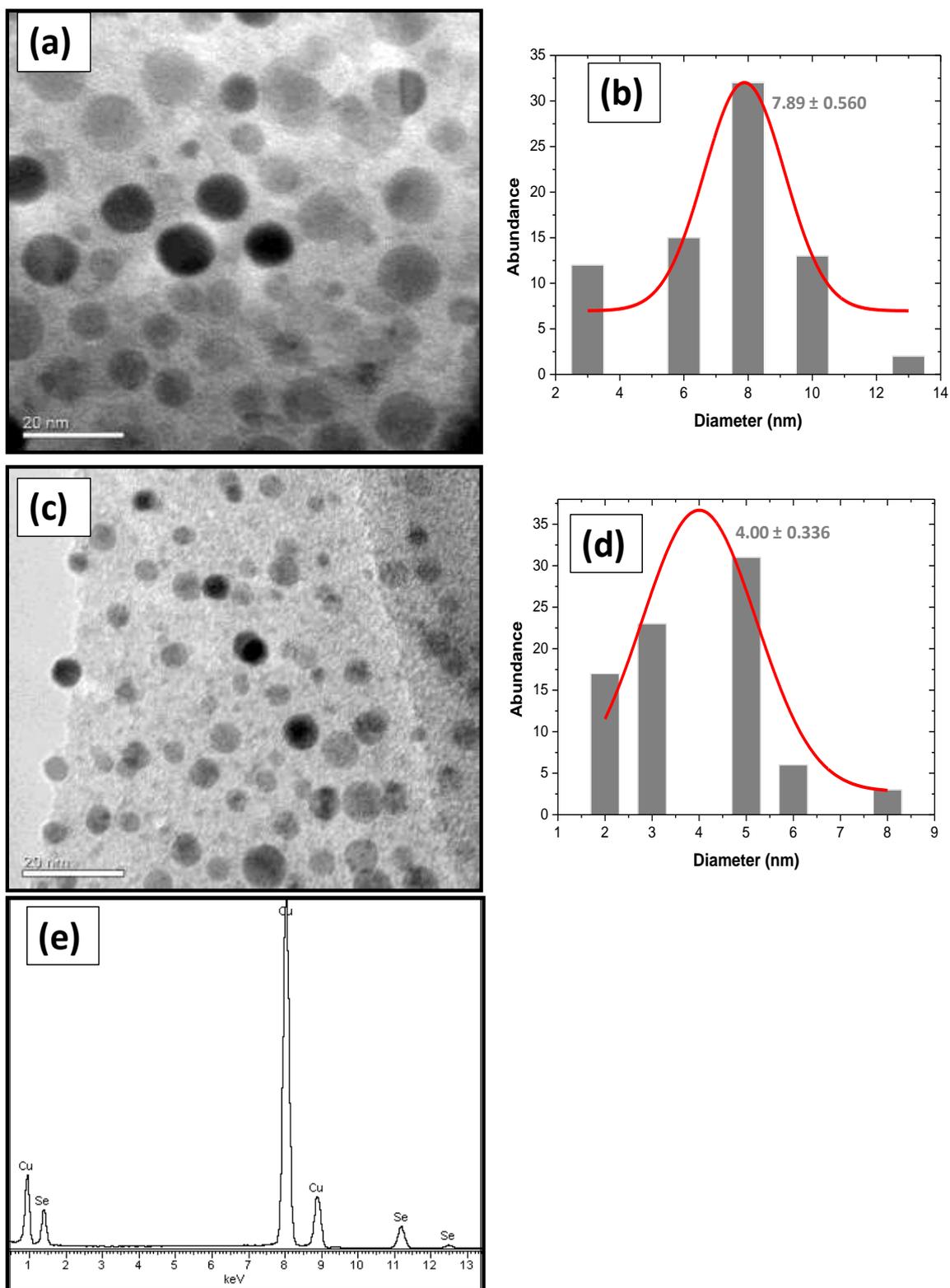


Fig. 3.17 TEM images of Cu_xSe NPs synthesized from Cu:Se ratio of 1:1 in (a) HDA and (c) OLA with their corresponding particle size distribution (b) and (d) respectively; with (e) the EDS spectrum showing the elemental composition of the NPs.

3.3.5 Temperature effects on the synthesis of Cu_xSe nanoparticles

3.3.5.1 Optical properties of the CCM synthesized Cu_xSe nanoparticles

The UV-Vis absorption and the emission spectra of copper selenide solutions are shown in Fig. 3.18. The absorption band edges were found to be 465, 520 and 500 nm for nanoparticles synthesized at 180, 220 and 320 °C respectively. They were all blue-shifted from the bulk copper selenide. As the temperature is increased, there is a slight red-shift of the band edge suggesting an increase in particle size as shown in Table 3.5. This is a readily observed phenomenon in nanoparticles and it is suggested that this occurs through the Ostwald ripening process [47-48]. However, there is a decrease in wavelength to 500 nm for particles synthesized at 320 °C. This suggests a slight decrease in size or possibility of more monodispersed sample. Nevertheless the blue-shift of all the band edges results from quantum confinement effects [49]. Fig. 3.19 shows the emission spectra of copper selenide nanoparticles synthesized at 180, 220 and 320 °C. The photoluminescence spectra are red-shifted from their corresponding absorption band edges. The emission maxima as a function of temperature are shown in Table 3.5. More important to note is the broadness of the peaks. The FWHM decreases as the temperature increases. This suggests that the particle size distribution is become more mono-dispersed as the temperature is increasing.

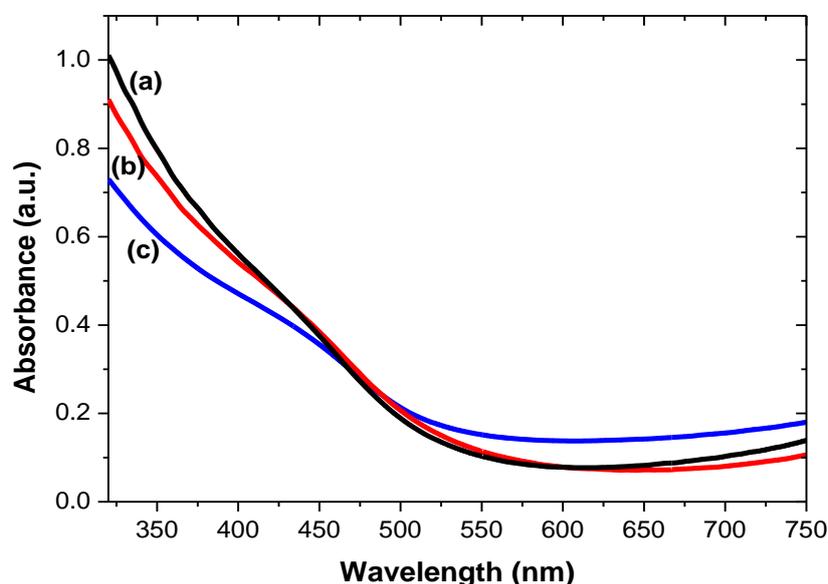


Fig. 3.18 UV-Vis absorption spectra of Cu_xSe NPs synthesized at (a) 180 °C, (b) 220 °C and (c) 320 °C for 30 min at Cu: Se ratio of 1:1

Table 3.5 Optical parameters of the Cu_xSe NPs synthesized at 180, 220 and 320 °C

Temperature (°C)	Band edge (nm)	Band gap (eV)	Emission (nm)	Stokes shift (nm)	FWHM (nm)
180	465	2.67	590	125	52
220	520	2.38	596	76	32
320	500	2.04	573	73	27
Bulk	1180	1.45	-	-	

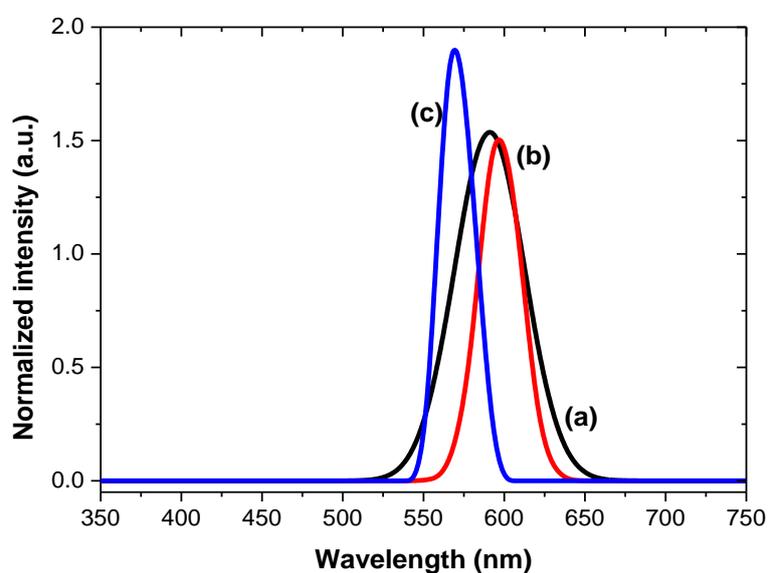


Fig. 3.19 Emission spectra of Cu_xSe NPs synthesized at (a) 180 °C, (b) 220 °C and (c) 320 °C for 30 min at Cu: Se ratio of 1:1

3.3.5.2 Structural properties of copper selenide nanoparticles synthesized at different temperatures

Fig. 3.20 shows the PXRD patterns of copper selenide particles synthesized at 180, 220 and 320 °C. The materials synthesized at all three temperatures had a unit cell of the crystals appearing in cubic face centered attributed to Cu₂Se (PDF number 03-065-2982) since the Miller indices of the main peaks appeared at the same 2θ values. The additional peak found at 2θ=58° on the patterns of the nanoparticles synthesized at 320 °C is due to unreacted

selenium. The diffraction peaks are relatively broad signifying nanosized samples. The shape and size distribution of the nanoparticles obtained from TEM are shown in Fig. 3.21. The TEM image of the particles synthesized at 180 °C shows hexagonal shapes. A small degree of agglomeration was observed. The particles synthesized at 220 °C and 320 °C had well defined shapes. The triangular and diamond-like shapes were the most dominant at 220 °C while increasing the temperature to 320 °C allowed the formation of pyramidal and hexagonal morphologies. Fig. 3.13 (d), (e) and (f) show the size distributions, Gaussian size distributions for particles synthesized at 180, 220 and 320 °C respectively. The average sizes of the three samples and their standard deviations are also shown inset. The mean diameter for nanoparticles synthesized at 180 °C is larger than that of particles at 220 °C, which is not in agreement with the results from UV-Vis absorption spectra (band edge of 465 nm at 180 °C compared to 520 nm at 220 °C). This discrepancy may be due to the degree of agglomeration in sample from 180 °C synthesis as observed from the corresponding TEM image. Furthermore, the 180 °C sample is more polydispersed (standard deviation of 1.31 nm), which is in agreement with the observed broad PL emission peak.

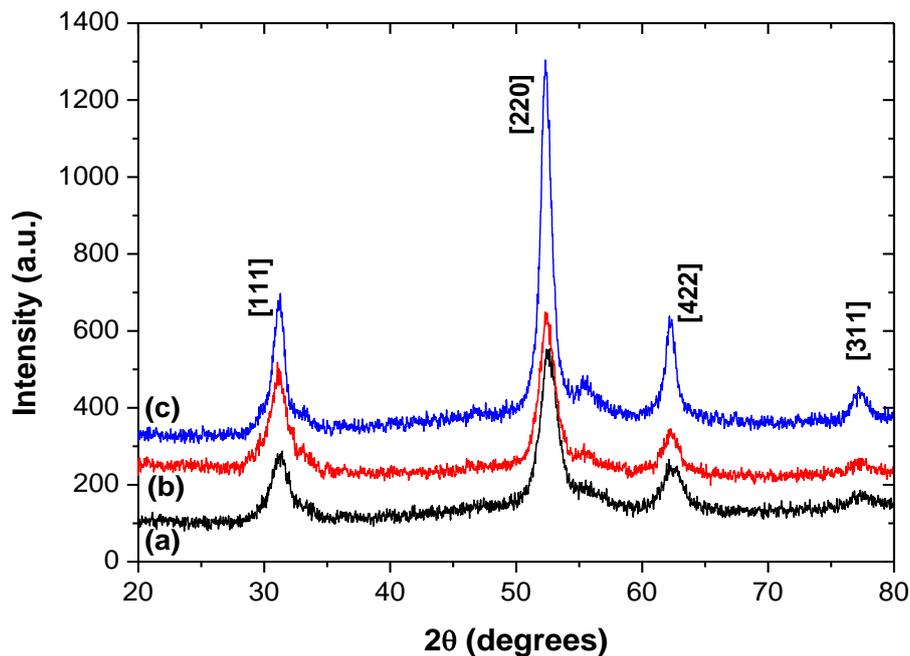


Fig. 3.20 XRD Patterns of Cu_xSe nanoparticles synthesized at temperatures of (a) 180, (b) 220 and (c) 320 °C using OLA.

The mean diameter of the nanoparticle synthesized at 320 °C is larger compared to that of nanoparticles synthesized at 220 °C and the sample has a wider size distribution (standard deviation of 1.11 nm). This is contrary to the results from UV-Vis absorption and photoluminescence spectra. The TEM analysis while powerful in nanotechnology can sometimes be susceptible to biasness as the entire sample is not imaged but only selected areas, hence the image might not be a true representation of the entire sample. Although the FWHM of the 220 °C emission peak was slightly higher than that of 320 °C, smaller size nanoparticles with defined shape in a narrower distribution (standard deviation of 0.415 nm) were obtained with 220 °C synthesis.

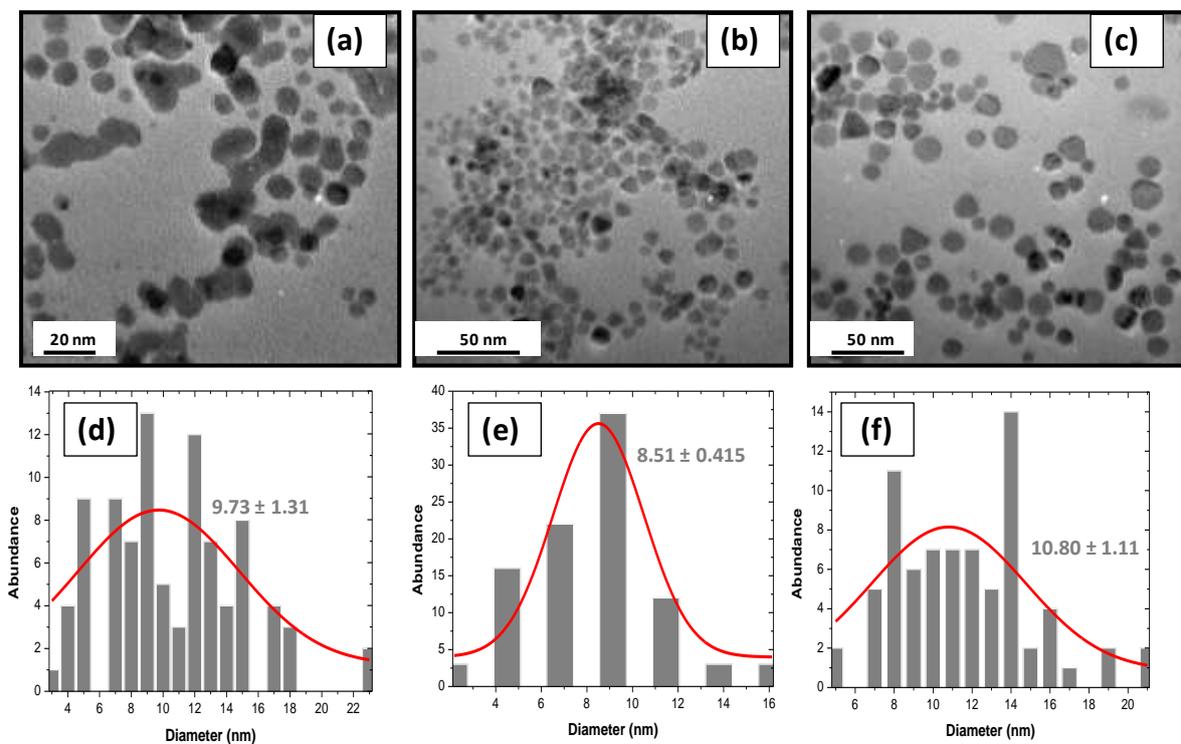


Fig. 3.21 TEM images of Cu_xSe NPs synthesized at (a) 180 °C, (b) 220 °C and (c) 320 °C with their corresponding size distributions (d), (e) and (f) respectively

3.3.6 Fabrication of Schottky devices using MAM synthesized copper selenide

The schottky devices are of particular importance in photovoltaics. The determination of barrier height and the characteristics of the forward bias current allow accessing the potential of the Schottky diodes. This can thereafter be considered in rectifying the performance of heterojunction cells. The principles of a Schottky device are shown in Chapter 2. The nanoparticles obtained from the MAM were solution processed into a Schottky device [60].

The microwave assisted synthesis is of particular interest as it easily allows for large scale synthesis. The assembly of the Schottky diode using MAM synthesized Cu_{2-x}Se nanoparticles as the semiconducting layer with aluminium as the metal contact was made at 298 K. The diode parameters such as the ideality factor, barrier height and the series resistances were extracted from the experimental I - V data using the thermionic theory and Cheung's modification which confirmed the electrical properties of the fabricated device.

The device architecture is shown in Fig. 3.22 with an active device area of 0.08 cm^2 . The thickness layer of the nanoparticles was approximately 200 nm, this was determined from the AFM (Fig. 3.23). Schottky barrier heights were measured from the I - V characteristics. Fig. 3.24 shows an experimental I - V curve of MAM synthesized Cu_{2-x}Se NPs device at 298 K.

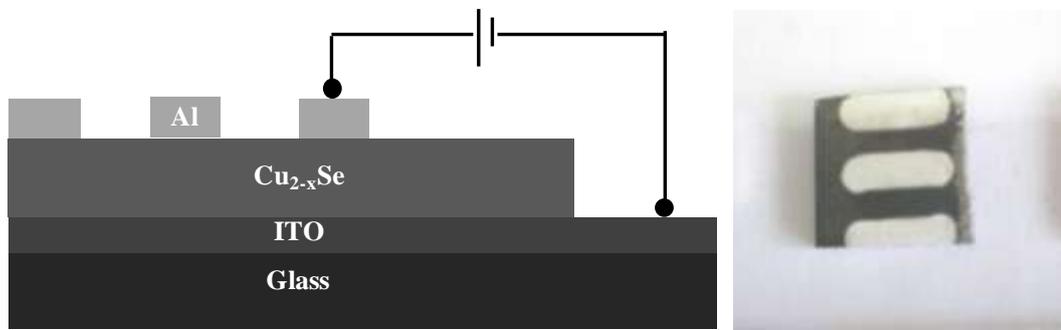


Fig. 3.22 Schottky device fabricated from MAM synthesized Cu_{2-x}Se

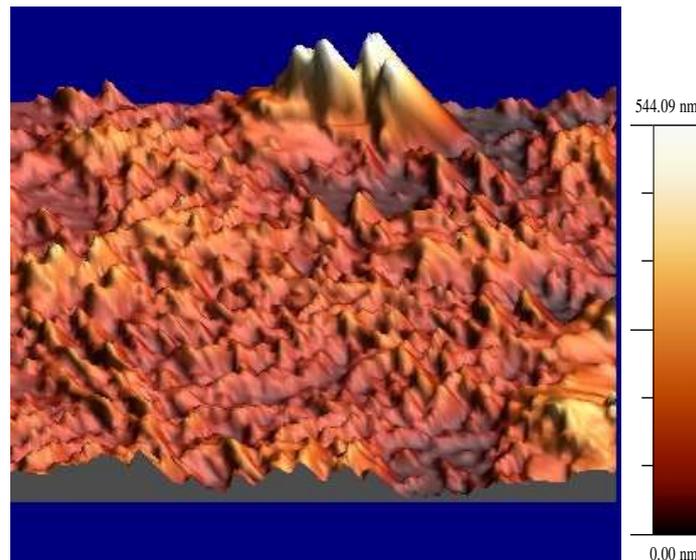


Fig. 3.23 AFM image of film of MAM synthesized Cu_{2-x}Se NPs

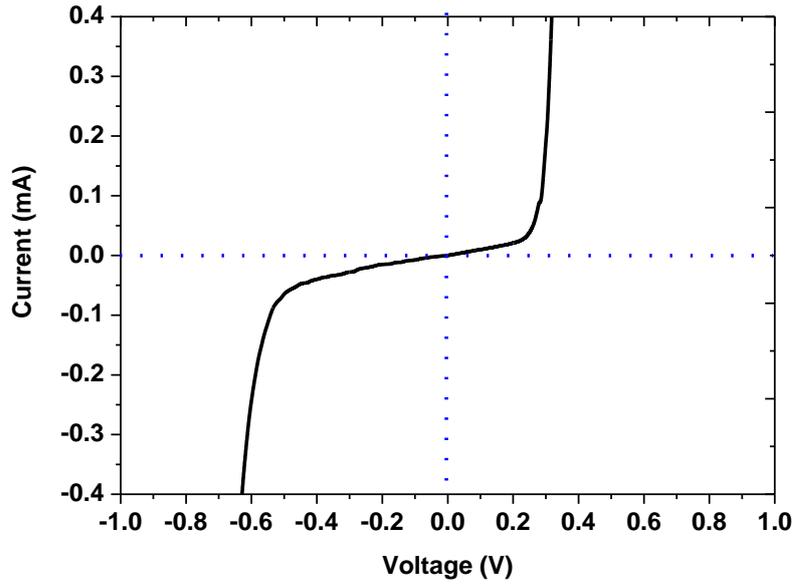


Fig. 3.24 J-V characteristics of the Al/ Cu_{2-x}Se Schottky diode at 298 K in the dark

According to the Schottky theory [64] the dependence of the forward current I on the applied voltage V is given by the relation:

$$I = I_0 \left[\exp\left(\frac{qV}{nkT}\right) - 1 \right] \quad (3.2)$$

where q is the electronic charge, k the Boltzmann constant, T the ambient temperature, and n is a dimensionless factor indicating the deviation from the ideal Schottky cell characteristics. This deviation arises from image force and surface effects such as surface charges and an interfacial dielectric layer between the metal and the semiconductor. I_0 is the saturation current represented by Eq. (3.3).

$$I_0 = SA^* T^2 \exp\left(-\frac{q\phi_B}{kT}\right) \quad (3.3)$$

$$\ln I = \ln I_0 + \frac{q}{nkT} V \quad (3.4)$$

with $A^* = A (m^*/m_0)$, where A is the Richardson constant ($A = 120 \text{ cm}^{-2} \text{ K}^{-2}$), m^* the effective electron mass equal to $0.6 m_0$ for Cu_{2-x}Se [68], ϕ_B is the barrier height, and S the area of the cell. The coefficient n evaluated from the slope of $\ln I$ vs. V (Eq. (3.4)), and the

value ϕ_B calculated from Eq. (3.3). The n value calculated from the slope of Fig. 3.25 is 4.35. The high value of n is due in part to defects induced by cleaving of the semiconductor in the junction region. The barrier height ϕ_B was found to be 0.895 eV. However, this method only works for diodes with low series resistance which can be neglected in the low forward region of I - V curve which in the case of our diode it seems as if it did not. Series resistance R_s is an important parameter that influences the electrical characteristics of Schottky diodes so we used Cheung method as an efficient method to evaluate n , ϕ_B and R_s . The forward bias current-voltage characteristics due to thermionic emission of a Schottky barrier diode with series resistance can be expressed as Cheung's functions [69]:

$$\frac{dV}{d\ln I} = n \frac{kT}{q} + IR_s \quad (3.5)$$

$$H(I) = V + n \frac{kT}{q} \ln\left(\frac{1}{SA^{*2}}\right) \quad (3.6)$$

$$H(I) = n\phi_B + IR_s \quad (3.7)$$

Experimental $dV/d\ln I$ - I plot of our Cu_{2-x}Se Schottky diode at the temperature of 298 K is presented in Fig. 3.26. After fitting the curve to a straight line and using (3.5), $n = 1.04$ and $R_s = 0.533 \Omega$ can be determined from the intercept and the slope of the line. The value of n and the data of I - V characteristics are used to define $H(I)$ from (3.6). Plotting $H(I)$ - V should give a straight line as shown in Fig. 3.27 which according to (3.7) its slope and y-axis intercept will give a second determination of R_s and $n\phi_B$. The value of R_s obtained from $H(I)$ - I plots is 1.206Ω and the average R_s is 0.870Ω . The data for the three methods is summarized in Table 3.7 below.

Table 3.7 Diode parameters obtained from the J-V data

No.	Method	Ideality factor n	Barrier height ϕ_B (eV)	Series resistance R_s (Ω)
1	LnI-V	4.35	0.895 eV	-
2	dV/dLnI-I	1.04	-	0.533 Ω
3	H(I)-I	-	-	1.206 Ω
4	Combined (2) and (3)	1.04	259 10^{-5} eV	0.870 Ω

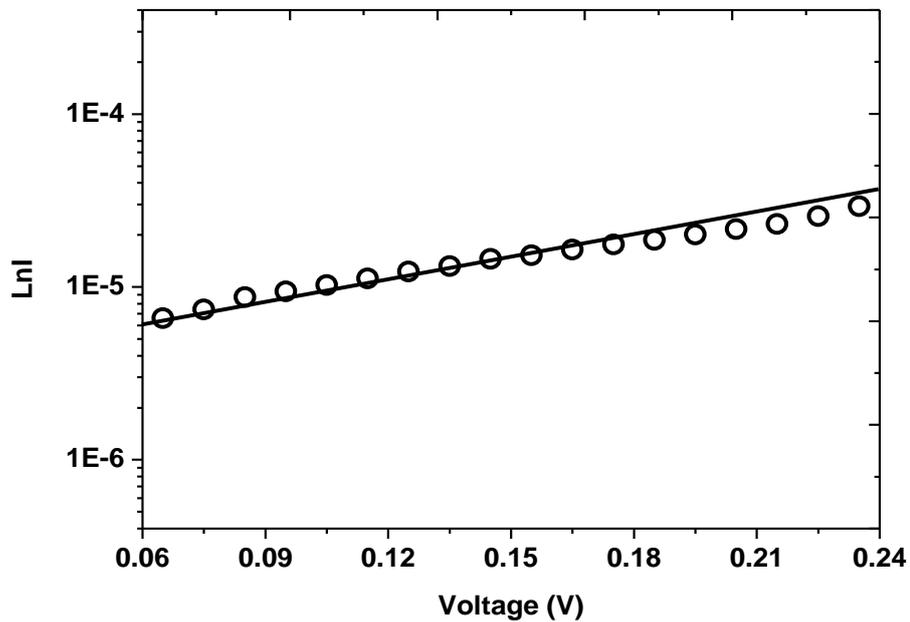


Fig. 3.25 LnI-V characteristics of the Al/ Cu_{2-x}Se Schottky diode at 298 K in the dark

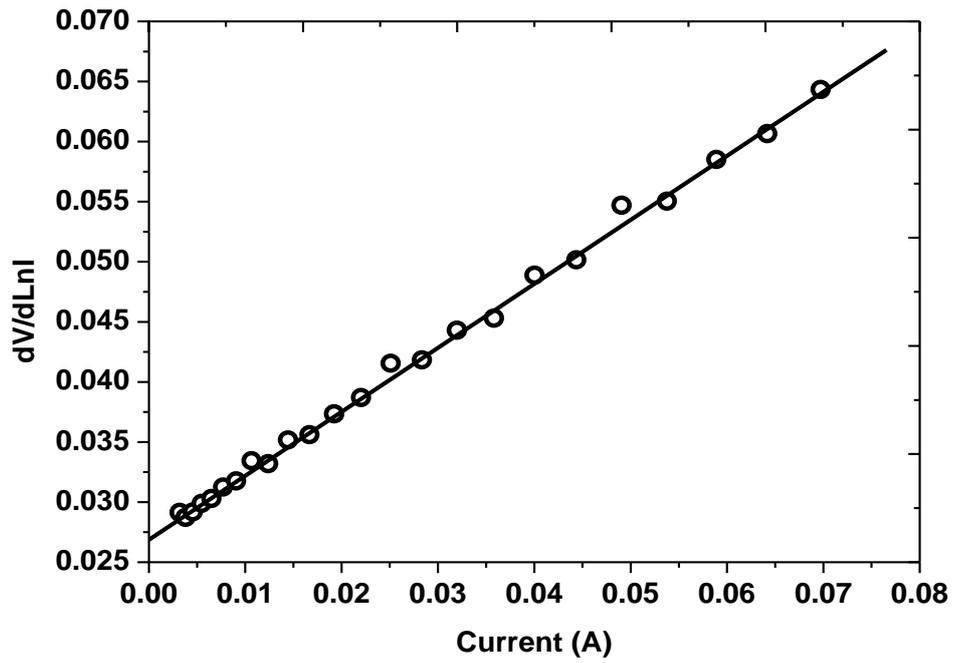


Fig. 3.26 $dV/d\ln I$ -I characteristics of the Al/ Cu_{2-x}Se Schottky diode at the temperature of 298 K in the dark

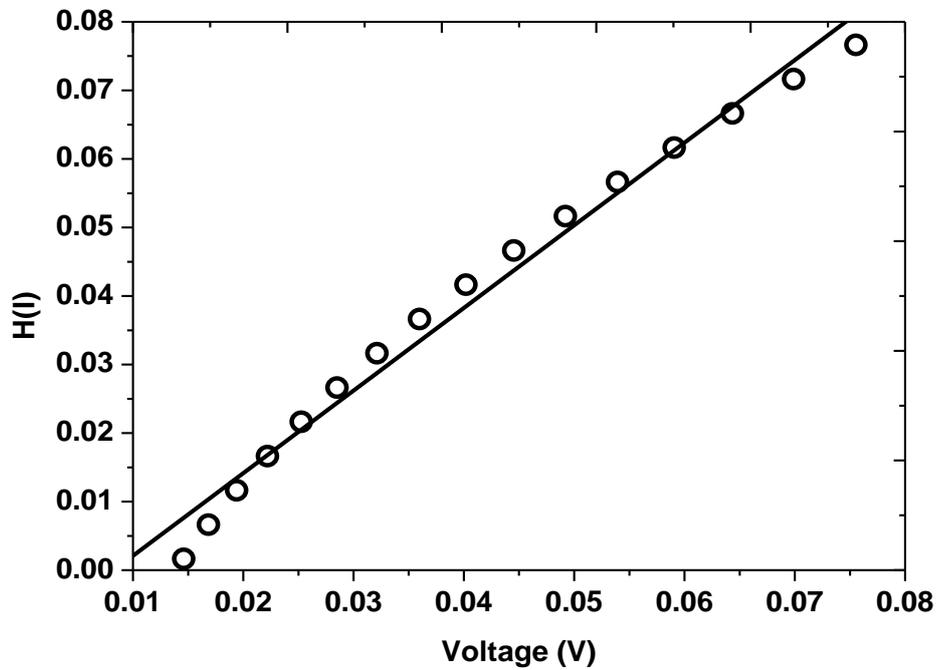


Fig. 3.27 $H(I)$ -V characteristics of the Al/ Cu_{2-x}Se Schottky diode at the temperature of 298 K in the dark

3.4 Conclusions

Relatively small sized copper selenide nanoparticles were successfully synthesized by mean of conventional colloidal method and microwave assisted digestion. The method, time, temperature, precursor concentration and solvent effects on the synthesis of copper selenide nanoparticles were studied. Large blue-shifted nanoparticles with average diameters in the range of 4.5 to 9 nm were found with cubic (Cu_{2-x}Se) and hexagonal (CuSe) crystalline phases proving that copper selenide nanoparticles with well defined crystallinity could therefore be prepared. However the investigated parameters showed that optimised conditions could be determined. Typically, using copper and selenium precursors in the molar ratio of 1 to 1 for 30 min of CCM synthesis at 220 °C in OLA gave the best properties as compared to the MAM and other reaction conditions. Similar properties were found in MAM synthesized nanoparticles at 600 W for 10 min. However a cubic crystalline phase was found mixed with the hexagonal phase. The synthesized nanoparticles possessed properties that could be used for photovoltaic applications. The MAM synthesized copper selenide nanocrystals were deposited onto ITO substrate to prepare the device. The I-V characteristics of the Al/ Cu_xSe Schottky barrier diode was measured at room temperature. The parameters obtained from the characteristic I-V of the diode were compared with those obtained from the Cheung's method. The ideality factor obtained from the characteristic I-V was large indicating a deviation from an ideal diode. However the value did not take into account the series resistance which is one of the reasons for deviation from ideality. Cheung's method resulted in a decrease in the ideality factor to 1.04 with small series resistance being observed. The observed Schottky diode behaviour of the MAM synthesized Cu_{2-x}Se nanoparticles is indicative of its potential as an active layer in solar cells. The copper selenide syntheses as simple binary compound were used as templates to prepare the multinary chalcogenide materials.

3.5 References

- [1] Yoon, H., Granata, J., Hebert, P., King, R.R., Fetzer, C.M., Colter, P., Edmondson, K.M., Law, D., Kinsey, G.S., Krut, D.D., Ermer, J.H., Gillanders, M.S. and Karam, N.H. (2005). Prog. Photovolt: Res. Appl.13, 133-139.
- [2] Green M. (2003). Advanced Solar Energy Conversion. Springer, New York.12, 1-93.

- [3] Auffan, M., Rose, J., Bottero, J.Y., Lowry, G.V., Jolivet, J.P. and Wiesner, M.R. (2009). Nature Nanotechnology 4, 634-641.
- [4] Chaara, L.E., Iamonta, L.A. and Zeinb, N.E. (2011). Review of photovoltaic technologies 15, 2165-2175.
- [5] Brown, G.F and Wu, J. (2009). Laser and photon 3, 394-405.
- [6] Trindade, T., O'Brien, P. and Pickett, N.L. (2001). Chem. Mater.13, 3843-3858.
- [7] National renewable energy laboratory (NREL), United States at <http://www.nrel.gov/pv/> . Downloaded on 13 November 2013.
- [8] Schaller, R. D. and Klimov, V. I. (2004). Phys. Rev. Lett. 92, 186601.
- [9] Gracia, V.M., Nair, P.K. and Nair, M.T.S. (1999). Journal of Crystal Growth 203, 113-124.
- [10] Riha, S.C., Johnson, D.C and Prieto, A.L.(2010). J. Am. Chem. Soc. 133, 1383-1390.
- [11] Estrada, C.A., Nair, P.K., Nair, M.T.S., Zingaro, R.A. and Meyers, E.A. (1994). J. Electrochem. Soc. 141, 802.
- [12] Schafer, A., Kouwitz, M. and Ahlrichs, R.(1996). J. Chem. Phys. 104, 7113.
- [13] Hermann, A.M. and Fabick, L. (1983). Journal of Crystal Growth 61, 658.
- [14] Robel, I., Subramanian, V., Kuno, M. and Kamat, P.V. (2006). J. Am. Chem. Soc. 128, 2385-2393.
- [15] Bi, H., Zhao, W., Sun, S., Cui, H., Lin, T., Huang, F., Xie, X. and Jiang, M. (2013). Carbon 61, 116-123.

- [16] Balis, N., Dracopoulos, V., Bourikas, K. and Lianos, P. (2013). *Electr. Acta* 9, 246-252.
- [17] Swapnil, B., Ambade, R.S., Mane, S.S., Kale, S.H., Sonawane, Arif V., Shaikh and Han, S.H. (2006). *Applied Surface Science* 253, 2123-2126.
- [18] Mane, R.S., Kajve, S.P., Lokhande, C.D. and Han, S.H. (2006). *Vacuum* 80, 631–635.
- [19] Zhu, J.J. Palchik, O., Chen, S.G and Gedanken, A. J. (2000). *Phys. Chem. B* 104, 7344.
- [20] Yu, S., Yang, J., Qian Y. and Yoshimura, M. (2002). *Chem. Phys. Lett.* 361, 362.
- [21] Yang, J., Zeng, J., Yu, S., Yang, L., Zhou, G. and Qian, Y. (2009). *Chem. Mater.* 12, 3259.
- [22] Zhan, J., Yang, X. and Wang, D. (2000). *Adv. Mater.* 12, 1348.
- [23] Chen, Y., Ding, J., Guo, Y., Kong, L. and Li, H. (2002). *Mater. Chem. Phys.* 77,734.
- [24] Jun, Y., Choi, J. and Cheon, J. (2006). *Angew. Chem. Int. Ed.* 45, 3414.
- [25] Yu, R., Ren, T., Sun, K., Feng, Z., Li, G. and Li, C. (2009). *J. Phys. Chem. C* 113, 10833-1037.
- [26] Ellingson, R. J., Beard, M. C., Johnson, J. C., Yu, P., Micic, O. I., Nozik, A. J., Shabaev, A. and Efros, Al. L. (2005). *Nano Lett.* 5, 865.
- [27] Schaller, R. D., Sykora, M., Pietryga, J. M., Klimov, V. I. (2006). *Nano Lett.* 6, 424.
- [28] Murphy, J. E., Beard, M. C., Norman, A. G., Ahrenkief, S. P., Johnson, J. C., Yu, P., Micic, O. I., Ellingson, R. J. and Nozik, A. J. (2006) *J. Am. Chem. Soc.* 128, 3241.
- [29] Pickett, N.L., Forster, D.F. and Cole, D.L. (1996). *J. Mater. Chem.* 6, 507.

- [30] Han, Z.H., Li, Y.P., Zhao, H.Q., Yu, S.H., Yin, X.L. and Qian, Y.T. (2000). *Materials Letters* 44, 366.
- [31] Lakshmikumar, S. T., Rastogi, A. C. (1994). *Sol. Energy Mater. Sol. Cells* 32, 7.
- [32] Dhanam, M., Manoj, P.K. and Prabhu-Rajeev, R. (2005). *Journal of Crystal Growth* 280, 425-435.
- [33] Kemmler, M., Lazell, M., O'Brien, P., Otway, D.J., Park, J.H. and Walsh, J.R.(2002). *J. Mater. Sci. Mater. Electron* 13, 531-535.
- [34] Heyding, R. D. and Murray, R.M.(1976). *Can J. Chem.* 54, 841-848.
- [35] Kumar, P. and Singh, K.(2011). *Struct. Chem.* 22, 103-110.
- [36] Zhang, W.X, Zhang, X.M, Zhang, L., Wu, J.X., Hui, Z.H., Cheng, Y.W, Liu, J.W., Xie Y. and Qian Y.T.(2000). *Inorg. Chem.* 39, 1838.
- [37] McDonald, S. A., Konstantatos, G., Zhang, S., Cyr, P.W., Klem, E.J, Levina, L. and Sargent, E.H. (2005). *Nature Materials* 4, 138-142.
- [38] Zhou, Y., Eck, M., Men, C., Rauscher, F., Niyamakom, P., Yilmaz, S., Dumsch, I., Allard, S., Scherf, U. and Kruger, M. (2011). *Solar Energy Materials & Solar Cells* 95, 3227-3232.
- [39] Thouin, L. and Vedel, J. (1995). *J. Electrochem. Soc.* 142, 2996-3001.
- [40] Souilah, M., Lafondn, A., Guillot-Deudon, C., Harel, S., Evain, M. (2010). *Journal of Solid State Chemistry* 183, 2274-2280.
- [41] Panicker, M.P.R., Knaster, M., Kroger, F.A. (1978). *J. Electrochem. Soc.* 125, 566-572.

- [42] Yoon, S., Yoon, T., Lee, K.S., Yoon, S., Ha, J.M., Choe, S.(2009). Solar Energy Materials & Solar Cells 93, 783.
- [43] Xie, Y., Zheng, X., Jiang, X., Lu, J., Zhu, L.(2002). Inorg. Chem. 41, 387.
- [44] Zhang, S.Y., Fang, C. X., Tian, Y.P., Zhu, K.R., Jin, B.K., Shen, Y.H and Yang, J.X.(2006). Cryst. Growth Des. 6, 2809.
- [45] Zhang, Y., Qiao, Z.P. and Chen, X.M.(2002). J. Mater. Chem.12, 2747-2748.
- [46] Bakshi, M.S, Thakur, P., Khullar, P., Kaur, G. and Banipal, T.S. (2010). Cryst. Growth Des. 10, 1813.
- [47] www.eng.utah.edu/~Izang/images/lecture-of-ostwald-ripening-particle-coarsening.
Downloaded on 2013-05-17.
- [48] Ostwald, W.Z. (1901). Phys. Chem. 1901, 37, 385.
- [49] Smith, A. M and Shuming, N. (2010). Accounts of chemical Research, 43, 190-200.
- [50] Pickett, N.L., Forster, D.F. and Cole, D.L.(1996). J. Mater. Chem. 6, 507.
- [51] Dhanam, M., Manoj P.K. and Prabhu-Rajeev, R. (2005). Journal of Crystal Growth 280, 425-435.
- [52] Kemmler, M. Lazell, M., O'Brien, P., Otway, D.J., Park, J.H. and Walsh, J.R.(2002). J. Mater. Sci. Mater. Electron 13, 531-535.
- [53] Heyding, R.D. and Murray, R.M.(1976). Can. J. Chem. 54, 841-848.
- [54] Kumar, P. and Singh, K. (2011). Struct Chem 22, 103-110.

- [55] Zhang, W.X., Zhang, X.M., Zhang, L., Wu, J.X., Hui, Z.H. Cheng, Y.W., Liu, J.W, Xie, Y. and Qian, Y.T.(2000). *Inorg. Chem.* 39, 1838.
- [56] Chassaing, E., Ramdani, O., Grand, P.P., Guillemoles, J.F. and Lincot, D. (2008). *Phys.Stat. Sol. C* 5, 3445–3448.
- [57] Pradhan, N., Peng, X.G. (2007). *J. Am. Chem. Soc.* 129, 3339-3347.
- [58] Zhang, Y., Qiao, Z.P., and Chen, X.M. (2002). *J. Mater. Chem.* 12, 2747-2748.
- [59] Cao, X., Zhao, C., Lan, X., Gao, G., Qian, W. and Guo, Y. (2007). *J. Phys. Chem. C* 111, 6658-6662.
- [60] Kalenga, M. P., Govindraju, S., Airo, M., Moloto, M. J., Sikhwivhilu, L. M., and Moloto, N. J. (2015). *Nanosci. Nanotechnol.* 15, 4480-4486.
- [61] La Mer, V. K. and Dinegar, R. H. (1950). *J. Am.Chem. Soc.* 72, 4847.
- [62] Smith, M. B. J., March, March's Advanced Organic Chemistry 5th ed., John Wiley & Sons, Inc., 2001.
- [63] Murray, C.B., Norris, D.J., Bawendi, M.G. (1993). *J. Am. Chem. Soc.* 115, 8706.
- [64] Tang, J., Hinds, S., Kelley, S. O. and Sargent, E.H. (2008).*Chem. Mater.* 20, 6906-6910.
- [65] Wada, T., Hashimoto, Y., Nishiwaki, S., Satoh, T., Hayashi, S., Negami, T. and Miyake, H. (2001). *Solar Energy Materials & Solar Cells* 67, 305-310.
- [66] www.sigmaaldrich.com/catalog/product/aldrich/o7805. Downloaded on 2014-12-02.
- [67] www.sigmaaldrich.com/catalog/product/aldrich/445312. Downloaded on 2014-12-02.

[68] Rhoderick, E. H. and William, R.H. (1988). Metal-Semiconductor Contacts. Clarendon, Oxford, 2nd ed.133.

[69] Sorokin, G. P., Idrichan, G. Z., Sorokina, Z. M and Kaptar, L. P. (1974). Inorg. Mater. 10, 1537.

CHAPTER 4:

SYNTHESIS, CHARACTERIZATION OF COPPER INDIUM SELENIDE NANOCRYSTALS AND THEIR APPLICATION IN QUANTUM DOT SENSITIZED SOLAR CELLS

4.1 Introduction

Copper indium selenide (CuInSe_2 shortened as CISE) is a p-type I–III–VI semiconductor chalcopyrite that has recently been studied due to high optical absorption coefficient. This ternary material can be prepared in different ways to tune its band gap energy. These properties have widely been exploited in the preparation of photovoltaic devices. Several solar cells made of CISE have been fabricated leading to the power conversion efficiencies exceeding 14% [1-6]. Copper indium selenide materials are mostly found as stoichiometric CuInSe_2 with the bulk material possessing band gap energy of 1.04 eV [2, 5]. Several reports have shown that though both Cu and In are bound to Se in CISE structure, the bonds (length) are not equal and depend on the structure of the synthesized CISE. The concentrations of precursors together with the temperature of synthesis are the main features in controlling the structure of CISE and thus the orientation of the bonds [7-12]. Many shapes of CISE have been reported, including o-ring, pyramidal, hexagonal and spherical nanoparticles [7, 13]. While the nearly stoichiometric CuInSe_2 ideally closes the gap between copper poor and copper rich material, the concentration of copper in the CISE material has a certain limit behind which the device performances are compromised due to the resultant poor electrical properties. Copper deficiency leads to reverse electronic barrier that decrease the FF and the overall performance of the device while copper rich favours the interface recombination which decreases the V_{oc} and thus affects the electrical performance of the solar cell [14-15]. Several methods have been reported for synthesis of copper indium selenide nanoparticles. Wu *et al.* [16] reported the synthesis of copper indium selenide and copper indium gallium selenide nanoparticles by adding elemental selenium to a hot solution of metal particles induced from heated mixture of indium (III) chloride, copper (I) chloride and gallium (III) chloride in polyol solution. The resultant particles were dissolved in ethanol, cleaned and precipitated by nucleation process to form the nanocrystals. The same authors reported the use of sodium borohydride solution of elemental Se in anhydrous ethanol, InCl_3 and CuCl in diethylene glycol to prepare CISE nanocrystals at 240 °C after precipitation with ethanol

whilst CIGSe was prepared at 280 °C by adding GaCl₃ and using tetraethylene glycol as solvent [16]. Other authors have reported the control of particle growth through the use of capping agents and/or the coordinating solvent. Reifsnyder *et al.* [7] prepared the tetragonal bipyramidal CIGSe nanoparticles from metal precursors capped with hexadecyl amine and n-octadecylphosphonic acid. The synthesis occurred in 1-octyldecene as solvent at 290 °C under inert conditions using a Schlenk line and glovebox techniques. Koo *et al.* [17] used selenourea as a Se source, oleylamine as a coordinating solvent and carefully controlled the reaction temperature and the combination of reactants to synthesize trigonal pyramidal CIGSe nanocrystals which were candidates for photovoltaic devices. The autoclave method is one of the common procedures often used to prepare copper indium selenide. This method requires high pressure and temperature exceeding the ambient pressure and boiling point of the solvents. The methods using autoclave setup are generally much time consuming as compared to other conventional methods mentioned here above [18-19]. A few studies have shown the use of microwave assisted method in the synthesis of CIGSe but could hardly confirm the formation of small size and regular shape CIGSe nanocrystals. Grisaru *et al.* [20] synthesized 85 nm sized tetragonal structures of CIGSe using the microwave-assisted polyol method in which triethylene glycol acted as both the solvent and the reducing agent. Sabet *et al.* [21] reported on the usage of microwave assisted digestion at 750 W for 10 min to synthesize cubic and tetragonal phases of CIGSe which had a band gap energy of 1.90 eV. However, the synthesized materials were relatively big without well defined shape.

The fabrication of various solar devices is done to improve the photovoltaic industry. The deposition of metals through heating evaporation process is one of the main techniques used to prepare the active layer in the device. Dye sensitized solar cell has recently been a focused point in making devices. The electrons generated from dyes (as sensitizers) in the device upon absorption of photon are quickly injected into semiconductor oxide then transported to the electrode while the electrolyte containing a redox couple regenerates the dye electronic structure and thus the cycle is continuous [22-34]. Several authors have shown that many benefits can be acquired when replacing the dye with quantum dots (QDs) to get quantum dot sensitized solar cell (QDSSC) [25,34-40]. In this chapter we report on the synthesis of copper indium selenide nanoparticles via conventional colloidal and microwave assisted methods. The influence of the method, capping agent and solvent on the synthesis of copper indium selenide nanoparticles were investigated. The properties of the synthesized copper indium

selenide nanoparticles were determined and the application of CISE QDs in solar devices such as QDSSC and the determination the electrical properties were done. The energy levels of the CISE QDs were also determined to understand the electronic and electrical properties of QDs. The preparation of thin films of CISE QDs was performed with or without mercaptopropionic acid and ethane dithiol treatments. The devices made of those films were assembled and characterized.

4.2 Experimental protocols

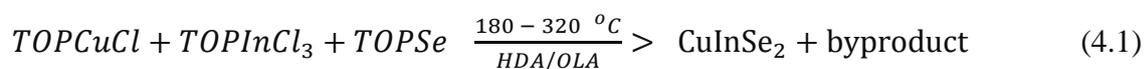
4.2.1 Chemicals and materials

Copper (I) chloride, Indium chloride, selenium powder, tri-n-octylphosphine (TOP), deionized water, methanol, ethanol, acetone, acetonitrile, chloroform, toluene, hexane, tin doped-indium oxide (ITO), and doped-fluorine oxide (FTO) substrates, tetrabutyl ammonium tetrafluoroborate (TBABF₄), mercaptopropionic acid (MPA), ethane dithiol (EDT), acetonitrile, standard Titanium oxide (TiO₂), hexadecylamine (HDA), octadecylamine (OLA), trioctylphosphine (TOP) were purchased from Sigma Aldrich and titanium oxide (TiO₂) from dyesol.

4.2.2 Synthesis of copper indium selenide nanoparticles

4.2.2.1 Conventional colloidal method

The conventional colloidal method (CCM) was used to prepare copper indium selenide QDs via a three-neck flask connected to a Shlenck line under an argon atmosphere. This method was adapted from copper selenide synthesis shown in the previous chapter. Typically, in a CCM, reaction (4.1) below was followed. About 6 ml of oleylamine (OLA) was heated to 100 °C. The mixture of 1 ml of 1 M of CuCl in TOP (TOPCuCl) and InCl₃ in TOP (TOPInCl₃) was added to the OLA solution. The resultant solution was then heated to 220 °C where 1 ml of 1 M solution of Se in TOP (TOPSe) was added. The content was heated for a further 30 min. The temperature was then decreased to 60 °C. Ethanol was added to the solution to flocculate the copper indium selenide (CISE) nanoparticles which were collected after centrifugation. The same method was also used but without dissolving the precursors in TOP.



4.2.2.2 Microwave assisted method

The synthesis of CISE using the MAM was adapted from the equation (4.1) above following the optimized method used to prepare copper selenide. 1 ml of TOPCuCl 1M and 1 ml of TOPInCl₃ 1M were placed in 5 ml of solvent in a vessel liner and mounted on the rotor then purged with argon for 2 min before being placed in the Microwave. The system was heated for 10 min at a power 500 W. After cooling to 70 °C, 2 ml of TOPSe 1M was quickly added. The system was purged for 5 min with argon before continuing heating the mixture for another 10 min at 600W. After cooling down to about 50 °C, methanol was added. The product was centrifuged at 3000 rpm for 20 min and washed with methanol at 3000 rpm for 10 min.

4.2.3 Substrate cleaning

The substrates were mechanically cut to small sizes using a diamond cutter then cleaned successively with extrane, acetone, iso-propanol and water for 10 min each under ultrasonic radiation. The substrates were then dried into a nitrogen stream.

4.2.4 Chemical treatment of the TiO₂/QDs layer

The photoelectrode consisted of titanium oxide (TiO₂) spread onto fluorine doped tin oxide (FTO) substrate using doctor Blade technique and sintered at 450 °C for 30 min. A film of about 10 μm thickness was obtained. The TiO₂ substrate without further treatment was placed in the CISE QD solution for 24 hours after which the excess material was washed out with the solvent used to prepare QD solution. Therefore the untreated device was made. Concurrently, another TiO₂ substrate was pre-treated by dipping in 1M MPA in acetonitrile for 8 hours, rinsed with acetonitrile then dried in ambient conditions. The prepared film was dipped into CISE QD solution for 24 hours, followed by washing with acetonitrile solution and drying in ambient conditions. For EDT treatment, 0.1 M EDT acetonitrile solution and a layer-by-layer assembly via dip coating were done. The TiO₂ film was dipped in EDT solution for 30 min, rinsed with acetonitrile and dipped in CISE QD solution for 15 min. This procedure was repeated prior to the last dip- casting in the quantum dot solution for 60 min.

4.2.5 Device assembly

After determination of optical properties of the film prepared above the device area was prepared by keeping all deposited materials on a 0.25 cm² area and by scratching out all

material from all other parts of FTO substrate. A thin polyvinyl chloride (~60 μm) was placed on the FTO to act as a spacer after which the electrolyte was then dropped onto the device area and quickly sandwiched by deposition of platinum foil. The CISE quantum dot sensitized solar cell (QDSSC) device was then clipped together and quickly followed by the current-voltage (J-V) determination.

4.2.6 Characterization techniques

The optical properties of the synthesized CISE were determined by placing the toluene dispersion of the nanoparticles into quartz cuvettes. UV-Visible spectroscopy (Analytik-Jena SPECORD 50) was used to determine the absorption properties of the NPs and the StellarNet miniature spectrofluorometer, equipped with 395 nm LED as an excitation source, was used to determine the emission properties of the NPs. The morphology of the NPs was determined on Technai G2 TEM Spirit operated at 200 kV. TEM samples were prepared by drop-casting the nanocrystal dispersion in toluene onto the carbon-coated copper grids and allowed to dry at room temperature. The diffraction patterns were collected using Bruker D2 Phaser Powder X-ray diffractometer using a Co (1.789 nm) radiation source. The Raman spectrum of CISE powder flattened on a clean glass substrate was determined from Raman spectroscopy Bruker Senterra with the laser power, objective magnification and integration time set at 2 mW, 50x and 10 sec respectively. The film absorbance was determined on Perkin Elemer Lambda 900 UV/VIS/NIR spectrometer while the surface images were determined using the optical microscope BX51-P Polarizing Microscope, Olympus America Inc. The J-V curves were, on one hand, obtained by connecting FTO and Pt electrodes of the assembled device to SS-0.5K Solar simulator Sciencetech Inc., with Polychromatic light intensity of 100 mW cm^{-2} under standard AM 1.5 conditions and attached to a Keithley 2410-C 1100V Sourcemeter. On the other hand, the same measurements were recorded with an Eco Chemie Autolab PGSTAT 10 potentiostat under standard AM 1.5 conditions using a 150W Xe lamp as light source and appropriate filters. The polychromatic light intensity at the electrode position was calibrated to 100 mW cm^{-2} with a silicon photodiode from Newport Optical Power Meter, model 1830-C. The cyclic voltametric graphs were obtained from an Eco Chemie Autolab PGSTAT 10 potentiostat at 50 mV s^{-1} using a three-electrode cell. The QD solution was drop-cast onto FTO substrate and creating 1 cm^2 device area. The substrate was clamped in 0.1M TBABF₄ in acetonitrile so as the all device area is completely immersed in the electrolyte. Pt and

Ag/AgCl electrodes connected to the electrolytic cell were used respectively as counter and reference electrodes.

4.3. Results and discussion

4.3.1 Method effect on the synthesis of CISE nanoparticles

4.3.1.1 Optical properties of CISE synthesized using CCM and MAM

The absorption and emission spectra are displayed in Fig. 4.1 and Fig. 4.2 respectively. The extracted optical parameters are assembled in Table 4.1. The as-synthesized QDs showed the blue-shift in absorption band edges at about 525 nm and 535 nm for CCM and MAM respectively. Both samples showed a similar tailing of absorption spectra, indicating similar dispersivity of the particles. The emission peaks at 635 and 632 nm were observed in CCM and MAM synthesized particles respectively. The red-shift in emission spectra may be attributed to trap states by lattice defects of the particles. Furthermore the particles were less polydispersed in CCM with a FWHM of 51 nm in comparison with the MAM sample which possessed a FWHM of 76 nm. The energy curves of the CCM and MAM are shown in Fig. A4.1 in the appendix. The optical band gap estimated from the threshold value of the absorption band is ~ 1.9 eV for both samples. This value is much larger than the band gap of 1.16 eV reported for conventional colloidal method synthesized CISE₂ QDs with tetragonal structure and 7.0 nm size by other authors [21].

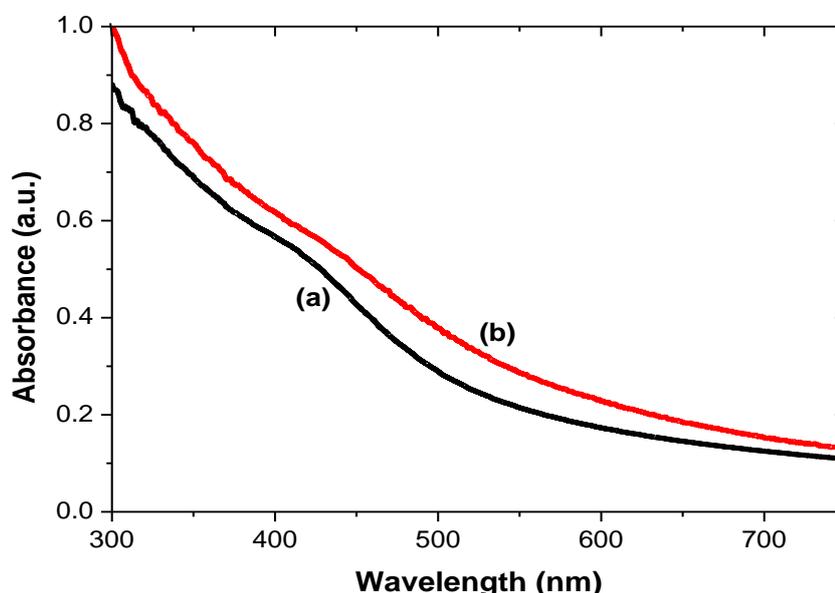


Fig. 4.1 Absorption spectra of (a) CCM and (b) MAM synthesized CISE NPs

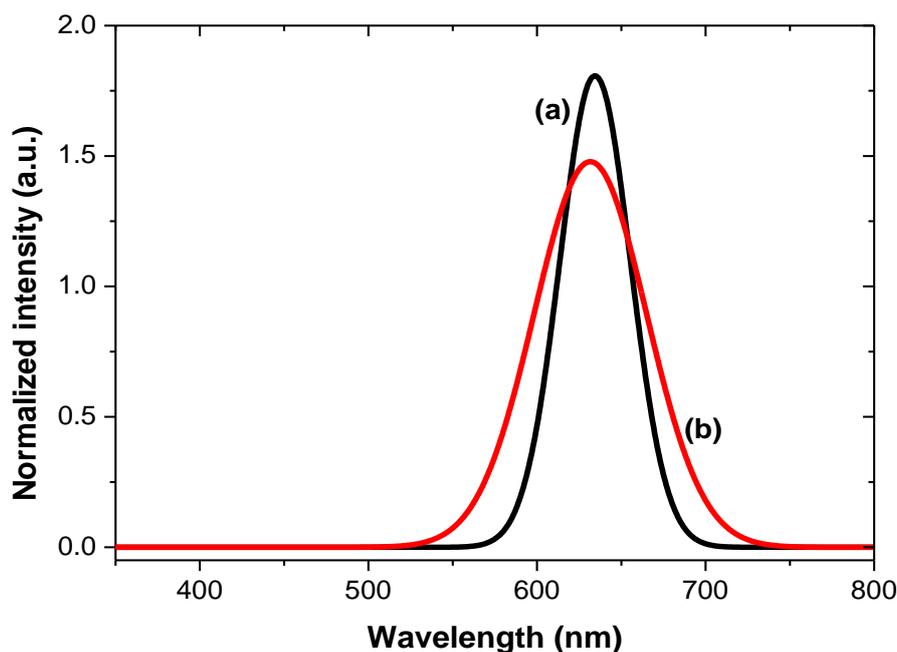


Fig. 4.2 Emission spectra of (a) CCM and (b) MAM synthesized CISE NPs

Table 4.1 Optical parameters of CCM and MAM synthesized CISE NPs

Method	Band edge (nm)	Emission (nm)	Stokes shift (nm)	FWHM (nm)
CCM	525	635	110	51
MAM	535	632	103	76
Bulk	1192	-	-	-

4.3.1.2 Structural properties of CISE NPs synthesized using CCM and MAM

Fig. 4.3 shows the X-ray diffraction patterns obtained from CCM and MAM synthesized CISE. The CCM synthesized CISE had a single phase of CuInSe_2 and crystallized in tetragonal orientation (PDF number 01-07-2208) and no peaks from impurities were found. The slight deviation of peak positions was provided by the amount of copper which was not exactly 1 as per lattice of CuInSe_2 . This brought change of crystalline composition to $\text{Cu}_{1-x}\text{In}_{1+x}\text{Se}_2$ where the slight deviation x was way less than 0.1[41]. That was confirmed by 220 and 122 peak orientations. The stoichiometries other than CuInSe_2 have been studied by several authors who reported poor properties as compared to those found with CuInSe_2 .

Relevant among those properties were the electric properties where the Voc and FF differed from values that are ideally needed [7, 12].

The TEM images of the CCM and MAM samples together with their corresponding size distributions and the EDS spectrum are shown in Fig. 4.4. The EDS analysis confirmed the presence of copper, indium and selenium in the synthesized nanoparticles. The excess of copper is due to the contribution from the grid. The particles were nearly spherical and nearly monodispersed (standard deviations of 0.129 and 0.291 nm for CCM and MAM respectively) with a smaller degree of agglomeration. The average sizes of CCM and MAM synthesized CISE particles were 5.02 ± 0.129 nm and 3.85 ± 0.291 nm respectively. This is also in agreement with the findings related to the optical properties. Fig. A.3 and Fig. A.4 of the appendix also show the structural properties of CCM CISE nanoparticles synthesized at 220 °C in comparison of those prepared at 180 °C and 320 °C.

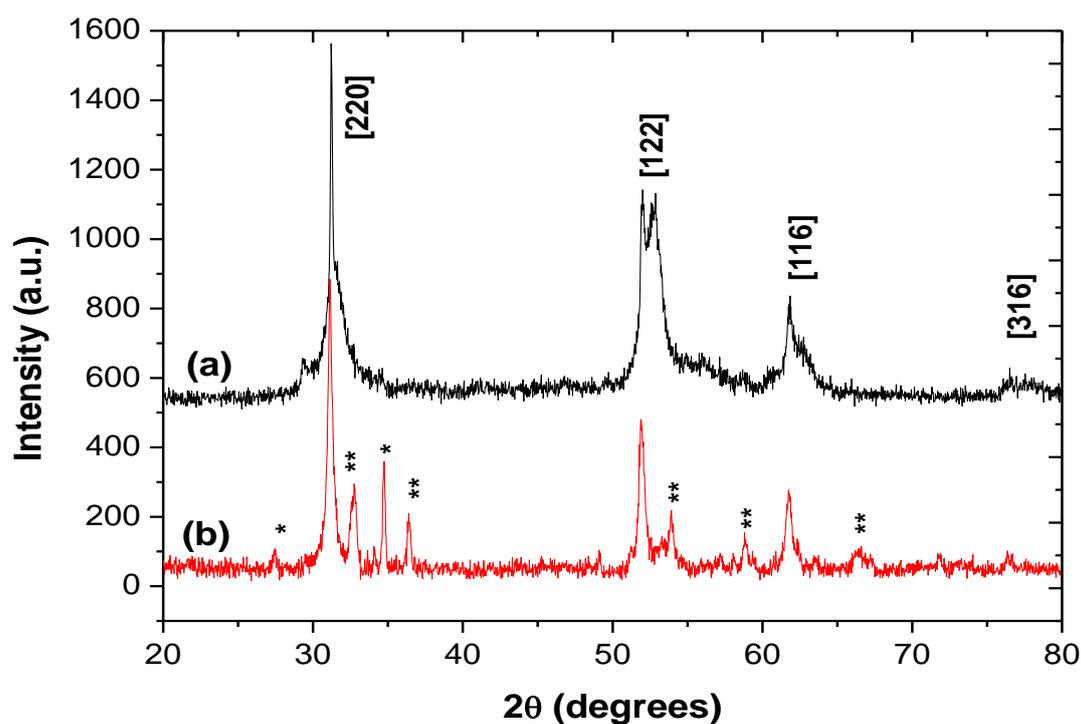


Fig. 4.3 XRD patterns of (a) CCM and (b) MAM synthesized CISE NPs

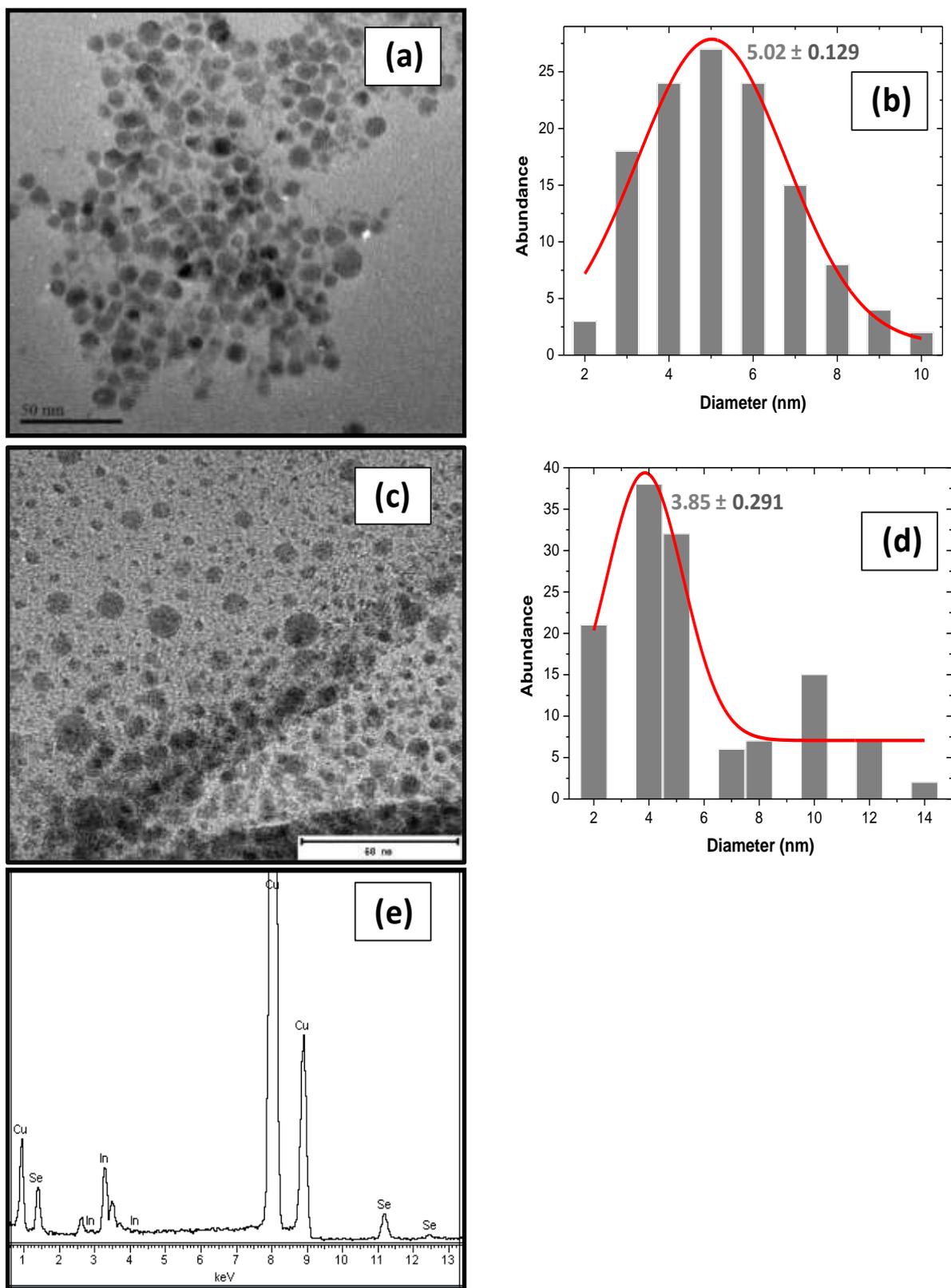


Fig. 4.4 TEM images of (a) CCM and (c) MAM synthesized CISE NPs with their size distributions, (b) and (d) respectively; with (e) the EDS spectrum showing the elemental composition of the NPs.

The structure was also confirmed by Raman spectroscopy as shown in Fig. 4.5. CuInSe_2 usually crystallizes in two structural forms, the chalcopyrite phase (CH) or the CuAu-like $P4m2$ primitive unit cell (CA) [42]. The 21 zone-center optical modes of the chalcopyrite structure (I42d space group) decompose according to the representation

$\Gamma_{opt} = 1A_1 + 2A_2 + 3B_1 + 3B_2 + 6E$. All these modes are Raman active except for the A_2 mode and their frequency assignment are reported by Rincon C. and Ramirez F.J. in an extensive study of CuInSe_2 single crystals [43]. Accordingly, the peak at 174 cm^{-1} is due to the A_1 mode. There are suggestions that the sharp peak at 124 cm^{-1} and the shoulder peak at 145 cm^{-1} may be due to the CA ordering of the atoms. However no evidence of CA ordering was detected from the XRD data. Ren et al. [42] suggested that these features may have also been caused by phonon recombination modes and it appears to be the case in this study as the nanocrystals only crystallized in the chalcopyrite phase.

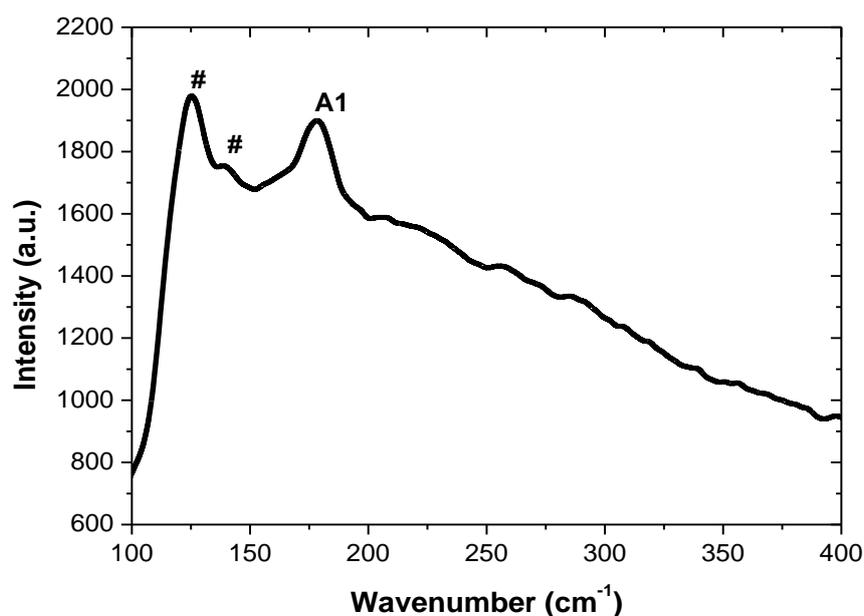


Fig. 4.5 Raman spectrum of CuInSe_2 NPs depicting the A_1 vibration mode and # depicting the recombination phonons or comparison of a chalcopyrite and a CuAu-like $P4m2$ primitive unit cells

4.3.2 Effect of precursors capped by TOP on the synthesis of CuInSe_2

4.3.2.1 Optical properties

The absorption and emission spectra of the synthesized CuInSe_2 NPs are shown in Fig. 4.6 and Fig. 4.7 respectively using capped and uncapped metal precursors and the optical values

determined from these graphs are shown in Table 4.2. The band edge of CISE nanoparticles synthesized using uncapped precursors was 497 nm while that of TOP-capped precursors was 513 nm and their respective emission peaks were 540 nm and 630 nm. The absorption band edges of both capped and uncapped precursors were blue shifted from the bulk CISE. Their corresponding band gaps were estimated from the $(\alpha h\nu)^2 / h\nu$ curves as shown in Fig. A4.2 in the appendix. The energy gaps were relatively higher than that of the bulk CISE material indicating the quantum confinement effect. However, the absorption wavelenths suggest that the CISE particles synthesized from uncapped precursors are relatively small than those from capped precursors. It was expected that the capped precursors would yield uniform and probably defined shape depending on the matrix formed by TOP as capping agent around metals and this was attested by the values obtained from emission wavelengths of the two types of synthesized CISE nanoparticles. The higher absorption wavelength in CISE synthesized from the TOP-capped precursors brought a higher Stokes shift of about 117 nm suggesting more trapping of electrons with the red-shifted emission peak than the CISE from uncapped precursors. The FWHM of the emission peaks was 23 nm for both samples suggesting the same size distribution. However, the size distribution suggested by the PL did not correspond to that from TEM, making it difficult to comprehend. The TOP-free precursors under our working conditions favoured the yield of small sized CISE nanoparticles. This is indicative of increase in energy gap due to quantum confinement effects [44].

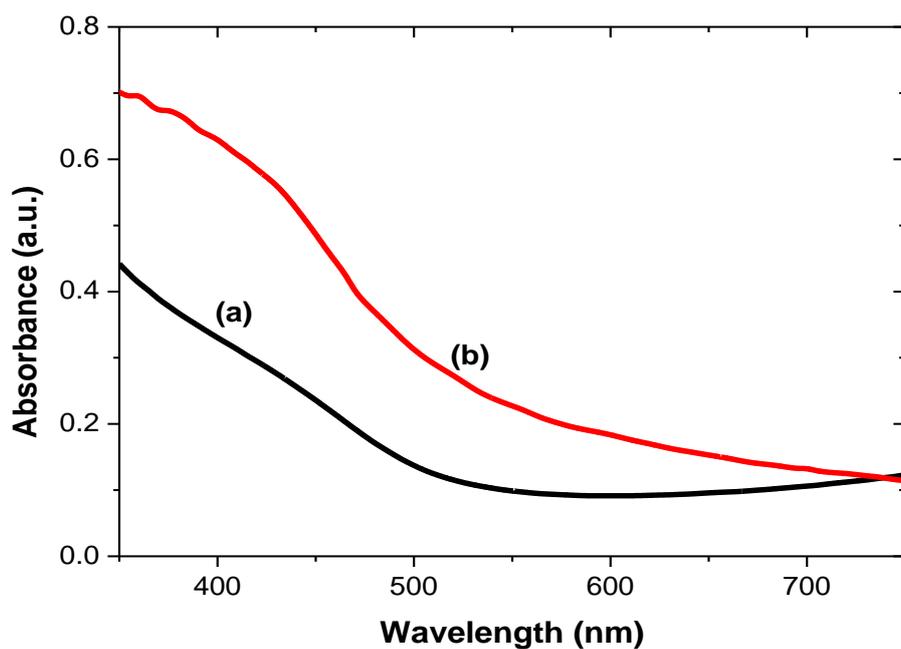


Fig. 4.6 Absorption spectra of copper selenide nanoparticles respectively synthesized at 220 °C with (a) uncapped and (b) TOP-capped precursors

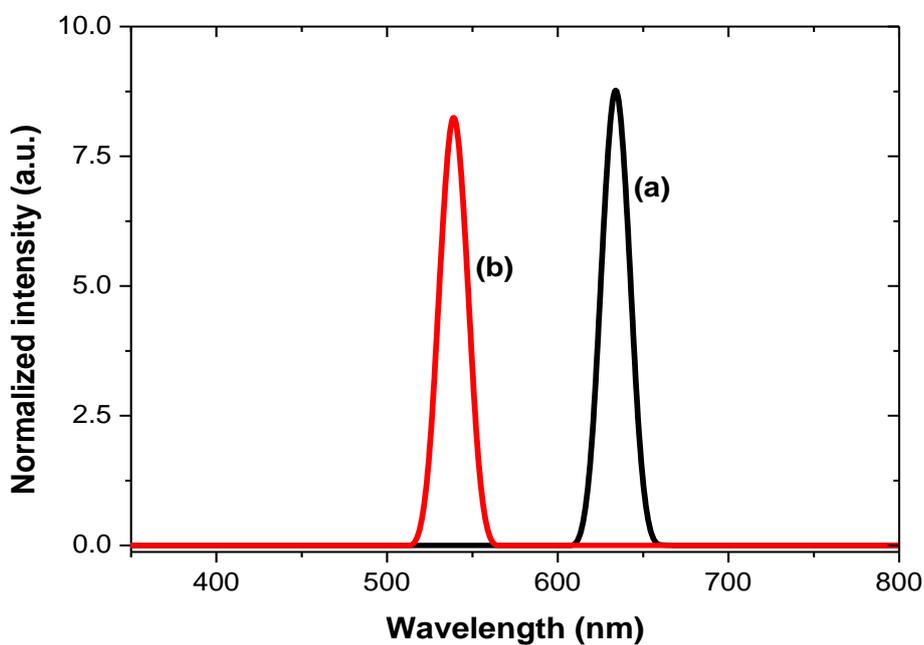


Fig. 4.7 Emission spectra of CISE NPs synthesized at 220 °C with (a) uncapped and (b) TOP-capped precursors

Table 4.2 Optical properties of CISE NPs synthesized from uncapped and TOP-capped precursors at 220 °C

Method	Band edge (nm)	Emission (nm)	Stokes shift (nm)	FWHM (nm)
Uncapped	497	540	43	23
TOP-capped	513	630	117	23
Bulk	1192	-	-	-

4.3.2.2 Morphology of CISE NPs synthesized from uncapped and TOP-capped precursors

The x-ray diffractions patterns of synthesized CISE from capped and uncapped precursors were shown in Fig. 4.8. The patterns confirmed that both the nanoparticles synthesized from the capped and uncapped metal precursors were made of nearly stoichiometric CuInSe₂ (PDF number 01-07-2208) with the unit cells corresponding to tetragonal crystals. The nanoparticles synthesized with uncapped precursors gave broader peaks compared to that of nanoparticles synthesised using TOP capped precursors. This confirmed that uncapped precursors gave smaller CISE nanoparticles. The shoulder peaks in CISE crystals prepared from uncapped precursors may be indicative of the lattice imperfection and this may justify the optical properties determined earlier. The TEM images and the particle size distributions of both samples are shown in Fig. 4.9. The average size values and the standard deviations obtained from the gaussian curves are shown inset. The particles were monodispersed (standard deviation of 0.008 nm) in hexagonal-liked shapes. The CISE nanoparticles from capped and uncapped metal precursors had the diameters of were 5.24 nm (undefined standard deviation) and 7.73 ± 0.008 nm respectively. This shows smaller particle size CISE synthesized from uncapped precursors in comparison with the CISE synthesized from TOP capped precursors, which is in agreement with the results from UV-Vis absorption spectrum.

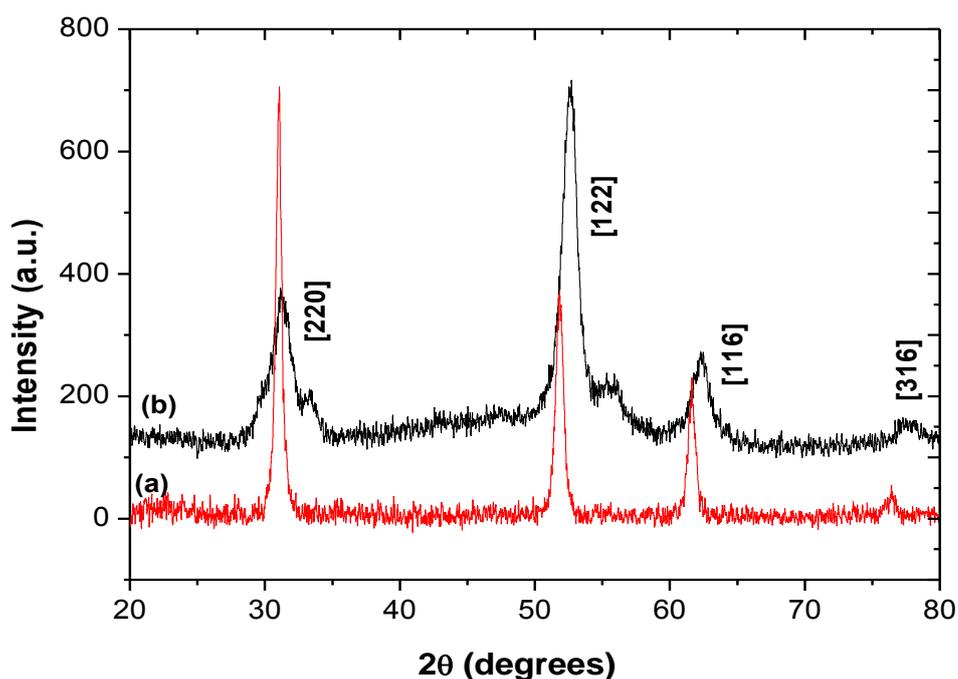


Fig. 4.8 XRD pattern of CISe NPs synthesized at 220 °C with (a) TOP-capped precursors and (b) uncapped precursors

The intense peaks in CISe powders obtained from both capped and uncapped metal precursors had different orientations. CISe synthesized from TOP capped precursors gave intense peak aligned to the 220 plane while the uncapped precursors gave the CISe powder with strong peak oriented along the 122 plane. TOP capped precursors gave similar CISe NPs as what was obtained using MAM although this more impurities were observed in the MAM sample. This suggested that the final stoichiometry may not be exactly the same in both capped and uncapped or in MAM synthesized materials. Ruffenach *et al.* [45] reported the structures of $\text{Cu}_{1.5}\text{In}_{0.5}\text{Se}_2$ and $\text{Cu}_{0.5}\text{In}_{1.5}\text{Se}_2$ absorbing layers after thermal annealing, the 112 orientation was more favoured by copper-rich layers while 204/220 orientation was favoured by Indium-rich layers. Similar findings using Raman spectroscopy were also discussed by several authors [40, 42].

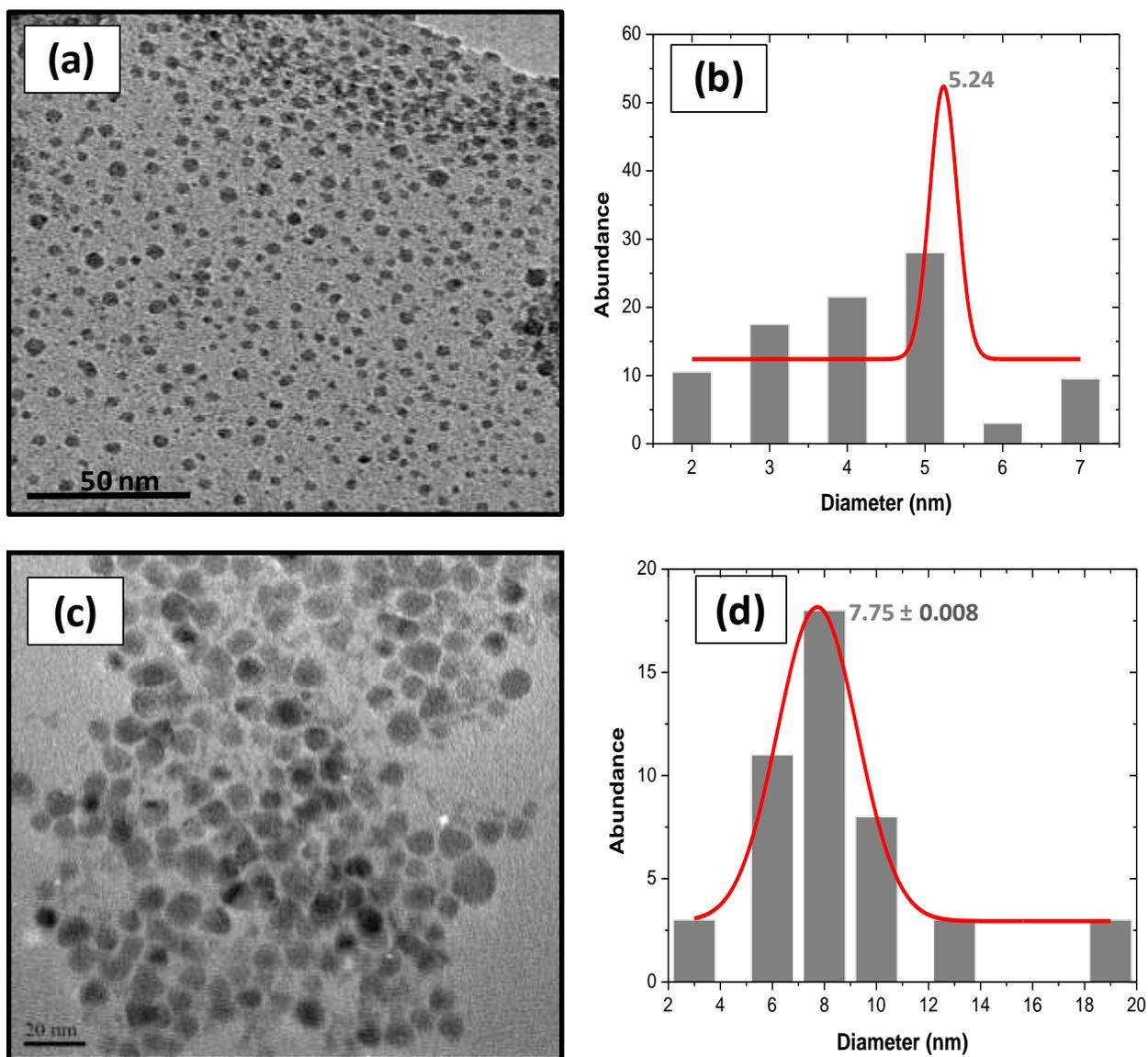


Fig. 4.9 TEM images and particles size distribution of CISE NPs synthesized from (a, b) uncapped and (c, d) TOP- capped precursors

4.3.3 Fabrication of CISE quantum dots sensitized solar cell devices

4.3.3.1 Cyclic voltammetry of the CISE thin film

The QDs solution was prepared by dispersing 5 mg of CISE nanoparticles in 1 ml of pyridine. The details of the procedure for cyclic voltammetry are shown in the experimental section. Fig. 4.10 shows the cyclic voltammogram of CISE where the conduction and valence band energy levels can be determined from the the oxidation and reduction onsets. The energy levels were calculated using equations (4.2) and (4.3). The corresponding values for the HOMO and LUMO as well as the band gap energies are shown in Table 4.4. The resultant HOMO and

LUMO of the sample were -5.8 eV and -3.8 eV respectively. The estimated LUMO value is close to the values estimated for CISE [46] and CuInS₂ [47] QDs synthesized via colloidal method by other groups. An electrochemical band gap of 2.0 eV was estimated with CV measurements. This energy is about 0.97 eV higher than that of the bulk material and clearly indicating a very large blue shift consistent with the absorption band edge found from UV-Vis-NIR spectrum of the solution and thin film of CISE QDs. However the electrochemical band gap is slightly different from the optical band gap estimated at 1.9 eV from the absorption spectrum. This could be related to the different binding energies of excitons created in the optical and electrochemical environments or caused by an influence of the stabilizing ligands on the charge injection process between the nanocrystals and the working electrode in CV measurements. Although the quality of the film of deposited QDs can also have an impact on device performance, the amount energy in the device setup may also be the source of trapping of electrons in the absorbing layer. This may compromise the electron transfer transfer into the wide band gap material TiO₂ (about 3.0 eV) of the QDSSC. These findings were similarly discussed by Ulbricht *et al.* [48] using 6 to 16 nm diameter sized cadmium telluride particles and by Pernik *et al.* [25] using CdSe QDs. Further and thorough investigations on these findings would get ways to control the high energy in the CISE layer and set all mechanisms such as a multiple exciton generation while easing the electron transport to the electrode. Another option would be to change the wide band gap electron accepting layer and/or to try the device with quantum dots synthesized to a size of more than 5 nm but less than 10 nm.

The band gaps and energy levels are vital parameters for the device design and material selection. Despite the limited accuracy, CV measurements are regarded as a useful and relatively easy tool to measure the absolute position of energy levels [49, 50]. From ternary QDs there is discrepancy in the absolute position of the energy levels measured by different groups. Generally, the problem is the low current intensity of the nanocrystals systems, which is comparable to the noise originating from the electrolyte [2]. This might also be caused by an influence of the stabilizing ligands on the charge injection process between the nanocrystals and the working electrode. According to some authors, the deviation from the values for CuInS₂ might also be related to the crystallographic structure of the synthesized nanocrystals (wurtzite, chalcopyrite and zinc-blend-structures) [49]. Yue *et al.* [51] reported the cyclic voltammogram of as-synthesized CuInS₂ QDs exhibiting an oxidation onset at

about 1.08 V and a reduction onset at about -0.72 V versus Ag/AgCl reference electrode (band gap ~1.8 eV). Yang *et al.* [50] reported the energy levels of -3.63 and -5.34 eV attributed to the conduction and valence band-edge energies of ~3.4 nm CuInSe₂ nanocrystals, with an electrochemical band gap of 1.71 eV. Zhong *et al.* [52] reported the energy gap of 1.88 eV for 5.2 nm sized CuInS₂ nanoparticles using CV. A binding energy of about 43 meV was found by these authors.

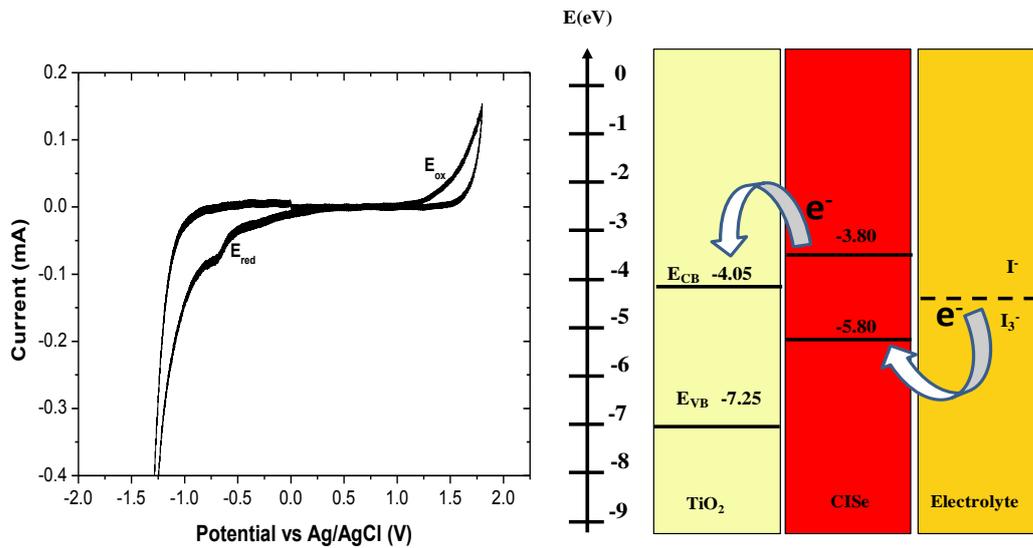


Fig. 4.10 CV and energy levels of CISe QD solution deposited onto FTO substrate

$$E(HOMO) = -E_{ox}^{onset} - 4.4 (eV) \quad (4.2)$$

$$E(LUMO) = -E_{red}^{onset} - 4.4 (eV) \quad (4.3)$$

Table 4.4 Homo-Lumo and BG approximations of CISe dispersed in pyridine

E_{ox} (V)	E_{red} (V)	E_{Homo} (eV)	E_{Lumo} (eV)	Approx. BG (eV)
1.40	-0.60	5.80	3.80	2.0

4.3.3.2 The effects of MPA and EDT treatments on CISE QDSSC properties

The MPA treatment was performed onto TiO₂ surface in order to increase the adhesion of CCM synthesized CISE QDs. MPA is expected to act as a linker molecule, connecting to the TiO₂ surface via the carboxylic groups to the CISE QDs surface by coordination of the thiol groups. The MPA treatment was done following the method shown in the experimental section. It was adapted from the procedure described by Kogkanand *et al.* [53]. The MPA is used as a linker molecule, through the formation of chemical bonds between the TiO₂ and the QDs. This molecule has thiol group that has affinity for metal atoms at the QD surface and carboxylate group that links to the TiO₂ surface. Thus, MPA treatment is expected to assist the attachment of CISE QDs to the nanostructured oxide film. This method has been used for sensitizing metal oxide films with chalcogenide based QDs (especially CdSe) for QDSSCs by several authors [25, 54-57]. While some comparisons between MPA and similar molecules suggested that this is a good choice for linker [54], others found that cysteine, for example, could be a more suitable choice [55, 57]. The procedure for EDT treatment is shown in the experimental protocols and was adapted from the method reported by Klem *et al.* [58]. EDT was used as a linker and a surface modifier due to the shorter chain and the terminal thiol groups which may result in a tightly packed QD layer [59, 60]. This approach has been successfully used for the formation of compact dense films for application in other types of solar cells containing PbS [58, 59, 61, 62].

The optical properties of the MPA and EDT treated films in comparison with the untreated CISE film are shown in Fig. 4.11. The absorption spectra showed the absorption at wavelengths of nearly 340 nm for both untreated and MPA treated films while EDT treatment showed a red-shift from the untreated film. A strong absorption in the range of 300-350 nm is expected to originate from contribution of both CISE nanoparticles and TiO₂ to light-harvesting. Importantly, only a discrete difference was observed in the absorption profile of the untreated and MPA treated films, suggesting that the MPA treatment may not have been effective for incorporation of a larger amount of QDs into the film in this particular case. It has been reported that MPA treated TiO₂ films sensitized with trioctylphosphine/trioctylphosphine oxide-capped CdSe QDs, resulted in very irreproducible and low sensitized photocurrents [63]. The sensitization by QDs on MPA-TiO₂ surfaces was not favored due to a high concentration of bulky organic surfactants in the sensitization solution, preventing the *in situ* ligand exchange. Thus, it was suggested that this process does not lead to covalently

bound QDs but to physisorption of CdSe QDs to MPA-TiO₂ (or unmodified TiO₂) surfaces in an uncontrolled fashion [63]. The absorption of EDT treated CISE film at wavelengths longer than 350 nm may be attributed solely to the contribution from CISE nanoparticles. However the characteristic of the lowest energy excitonic transition of CISE QDs is not clearly seen, as it is the case for the particles in solution (Fig. 4.1). Instead, what is seen is a tail in the visible spectral region. This is indicative of a strong agglomeration, resulting in optical characteristics that resemble the bulk solid rather than isolated QDs. Previously, it has been proposed that EDT treatment has the ability to remove the bulky oleate ligands from the surface of PbSe QDs [64].

The optical images were taken to probe the effect of the CISE thin film morphology on electrical properties (Fig. 4.11 i-ii). The untreated thin film showed poorer surface coverage as more voids were seen in comparison with the MPA treated sample. In addition, bigger crystal domains were observed suggesting a rough surface. The MPA showed better compaction and smaller crystal domains. Guijarro *et al.* [65] observed less agglomeration of CdSe QDs using MPA-treated TiO₂ films in comparison with direct adsorption to untreated films. The authors propose that, in the case of direct adsorption, the affinity of the dispersed QDs for already adsorbed ones may be similar to their affinity for the bare oxide surface, which could favor aggregation. In the case of MPA treated film, MPA molecules would render the interaction of QDs with the modified oxide surface more favorable than that with previously adsorbed QDs, reducing the tendency to aggregation. Nevertheless, other authors found no differences in surface coverages for CdSe deposition via direct adsorption or to MPA-modified surfaces [63] and agglomeration in both cases [25].

The treatment of sensitizer surface may be related to the deposition of CISE QDs in thin film, the film morphology, the size distribution and the structure orientation of the CISE QDs and TiO₂. The size of TiO₂ particles was investigated by Shalom *et al.* [66] who showed that large porous TiO₂ can be used in QDSSC to allow a good performance of the cell. The authors used mesoporous TiO₂ with about 100 nm pore size and allowed the QD multilayers of 100 nm thickness to be deposited in the pores. This created a good contact which gave an impressive efficiency beyond 3.86%.

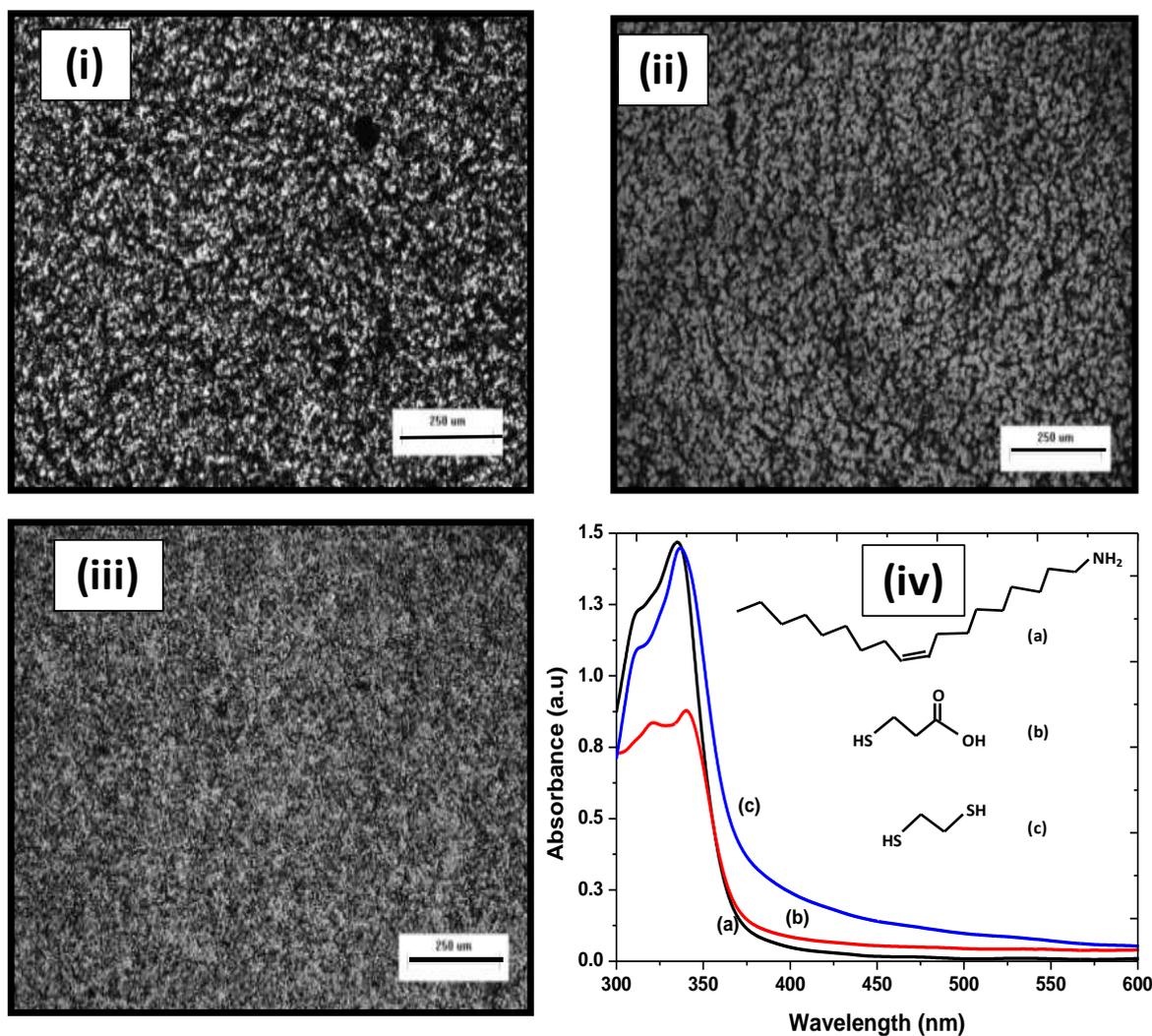


Fig. 4.11 Optical microscopic images of (i) untreated CISE film and (ii) MPA treated film; (iii) EDT treated thin films and (iv) their corresponding absorption spectra with the chemical structures (inset) for (a) OLA, (b) MPA and (c) EDT

The J-V curves obtained from untreated, MPA treated and EDT treated CISE film devices are shown in Fig. 4.12. The extracted short-circuit current density (J_{sc}), open circuit voltage (V_{oc}), fill factor (FF) and power conversion efficiency (PCE) for untreated and MPA treated CISE film device are assembled in Table 4.5. The J_{sc} of untreated, MPA treated and EDT devices were 54, 37 and 324 $\mu\text{A cm}^{-2}$ respectively while their corresponding V_{oc} were 220, 251 and 438 mV. The J_{sc} and V_{oc} from EDT treated device were significantly higher and the PCE was increased by 1 order magnitude compared to the untreated and MPA treated devices. Despite a considerable FF of 30-32%, the PCE in the untreated and MPA treated devices were very low, valued at 0.004 and 0.003% for the untreated and MPA treated CISE

film devices respectively. This is also justified by the optical characteristics of the CISE thin film and indicates that the MPA molecules used as modifiers on the TiO₂ surface could not easily replace the long chained oleylamine molecules on the surface of the QDs, to attach a higher amount of these molecules to the TiO₂ nanostructured CISE film. This resulted in the performance of the MPA treated device being similar to that of the untreated device. Several authors have already commented on the poor reproducibility and results obtained using MPA treatment in QDSSCs [63]. However, it is interesting to note that there is some discrepancy, and positive reports on the use of MPA are also found. For CdSe QDSSCs it has been demonstrated that the use of MPA improved the adsorption of toluene-suspended QDs onto TiO₂ films. On the one hand, the use of linker molecules might assist QDs adsorption onto the oxide films; alternatively the presence of these molecules may hinder charge transfer [25]. In another report, CuInS₂ QDs with sizes in the range of 2-8 nm were used to sensitize TiO₂ electrodes with MPA as a linker molecule. The electrodes were coated with ZnS, deposited by SILAR method. The best performance was achieved using the 3.5 nm CuInS₂ QDSSC, with J_{sc} of 2.02 mA cm⁻², V_{oc} of 0.515 V, FF of 0.69% and overall efficiency of 0.72%. According to the authors, an increase in the size of QD may lead to a decreased surface coverage of the TiO₂ films, thus affecting the light-harvesting and device performance [39].

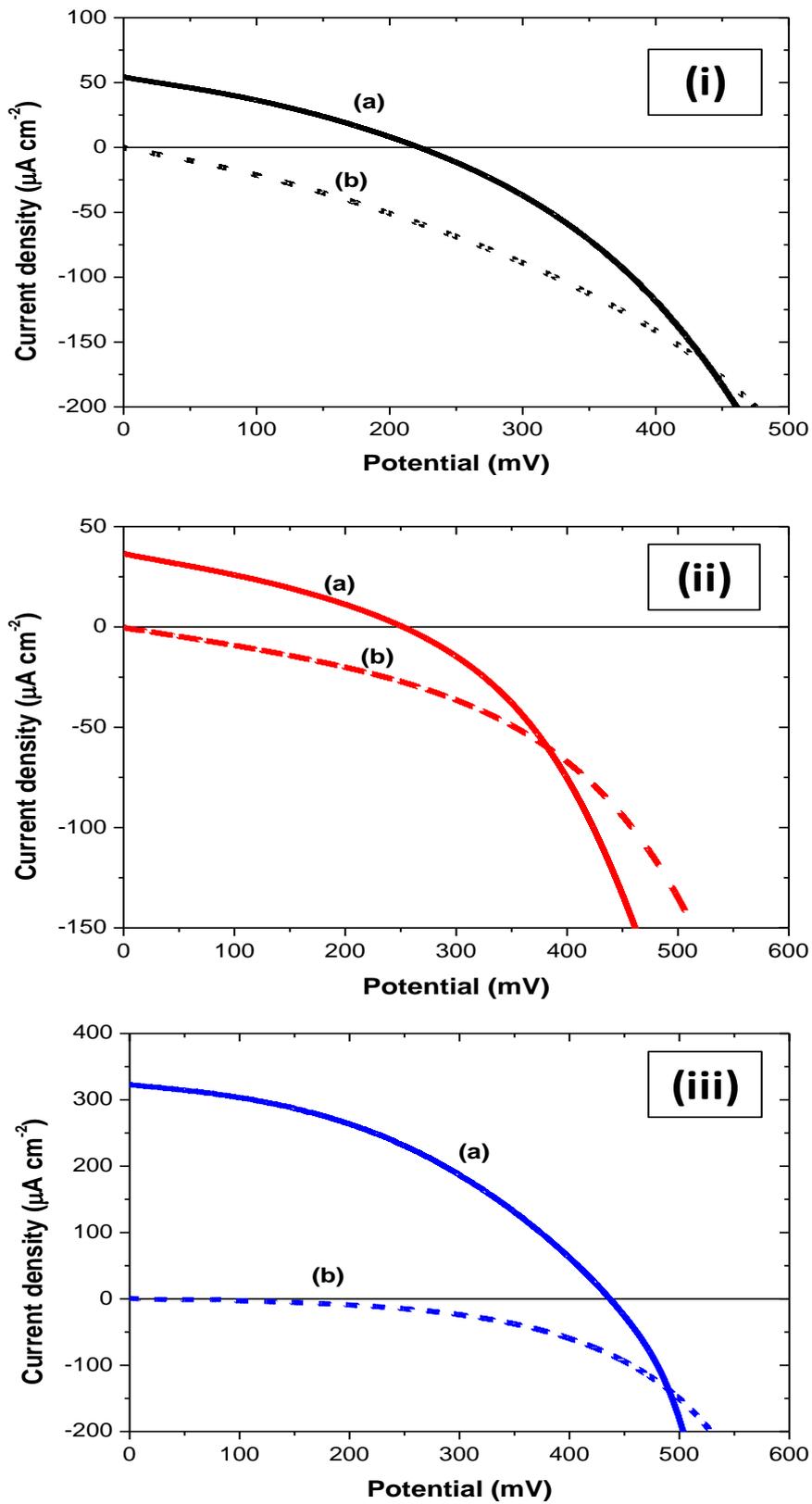


Fig. 4.12 J-V curves obtained from (i) untreated, (ii) MPA treated and (iii) EDT treated CISe films under (a) illumination with white light and (b) dark current

Table 4.5 MPA and EDT effects on the electrical properties of CISE QDSSC devices

Sample	Jsc ($\mu\text{A}\cdot\text{cm}^{-2}$)	Voc (mV)	FF (%)	PCE (%)
Untreated	54	220	30	0.004
MPA-treated	37	251	32	0.003
EDT-treated	324	438	41	0.058

A further study was therefore conducted on the electrolyte effect on the electrical properties of the EDT treated CISE film. The I^-/I_3^- and $\text{S}^{2-}/\text{S}_n^{2-}$ electrolyte couples were considered for the investigations. The J-V curves obtained from EDT treated film devices with I^-/I_3^- and $\text{S}^{2-}/\text{S}_n^{2-}$ electrolyte couples are shown in Fig. 4.13. The extracted electrical parameters are shown in Table 4.6. The Jsc, Voc, FF and PCE were $274 \mu\text{A cm}^{-2}$, 487 mV, 32.4% and 0.043% respectively for EDT treated device using the iodide electrolyte. The usage of sulfide electrolyte only gave a Jsc of $68 \mu\text{A cm}^{-2}$ and a Voc of 209 mV and no FF or PCE was quantified due to the poor shape of the J-V curve. The current was photogenerated in both cases of electrolyte usage by comparison with the dark current. The EDT treatment improved the device performance compared to untreated or MPA treated devices. The double thiol functional groups in EDT structure could effectively allow the attachment of EDT from TiO_2 surface to the QD. However, the I^-/I_3^- electrolytic couple gave better electrical parameters than $\text{S}^{2-}/\text{S}_n^{2-}$. The iodide electrolyte stability may be better for the device assembly than $\text{S}^{2-}/\text{S}_n^{2-}$ under our working conditions. This indicates that improved device performance may be related to the choice of electrolyte. Several authors have reported the use of $\text{S}^{2-}/\text{S}_n^{2-}$ as an electrolyte in devices and better performances were observed [49, 50, 66]. The $\text{S}^{2-}/\text{S}_n^{2-}$ electrolyte used in our project was prepared according to the recipe developed for CdSe QDSSCs [39].

Overall, the efficiencies reported here are low in comparison to the standard ruthenium-based devices or state-of-the-art QDSSCs. This may be a result of the presence of defects and surface traps in the synthesized QDs, as suggested by the low luminescence intensity during the optical characterization or due to thin film quality. Improvement in the CISE QDs properties should be readily achieved upon application of a selenization treatment after the synthesis or by the incorporation of a thin shell layer based on ZnS [67] and by optimizing the thin film fabrication process. Nevertheless, this contribution demonstrates that the use of EDT-based routes to produce thin films of QDs may also be applicable to QDSSCs.

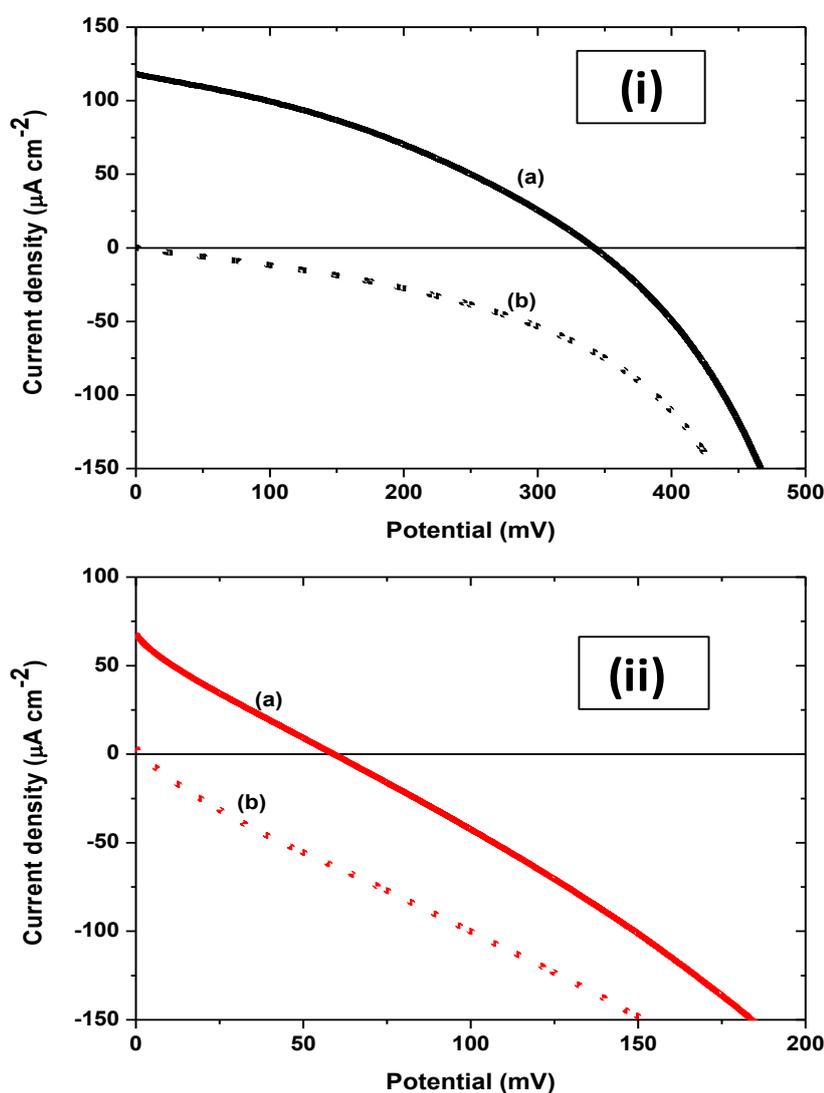


Fig. 4.13 J-V curves obtained from EDT treated devices using (i) I^-/I_3^- and (ii) S^{2-}/S_n^{2-} electrolytes under (a) illumination with white light and (b) dark current

Table 4.6 J-V Electrical parameters of EDT treated CISE devices using Γ/I_3^- and $\text{S}^{2-}/\text{S}_n^{2-}$ electrolytes

Electrolyte	Jsc ($\mu\text{A cm}^{-2}$)	Voc (mV)	FF (%)	PCE (%)
Γ/I_3^-	274	487	32.4	0.043
$\text{S}^{2-}/\text{S}_n^{2-}$	68	209	--	--

4.4 Conclusions

The CISE nanoparticles synthesized in OLA at 220 °C using uncapped precursors possessed better optical and structural properties as confirmed by the blue-shifted absorption and emission wavelengths, the well shaped, sized and dispersed nanoparticles. The tetragonal crystalline units with efficient composition of stoichiometric CuInSe_2 were defined. Thus photovoltaic activities can be predicted from these materials. However their homologue CISE synthesized using TOP-capped precursors were more polydispersed, with secondary phases of coexisting materials. The measurements of the energy levels done in on the CISE samples revealed a large blue-shifted energy gap of about 0.92 eV from their bulk materials. This indicates that the QDs had a quantum confinement effect. The application of CISE QDs in the devices as QDSSCs successfully confirmed that these QDs can absorb photons and the assembled device had photovoltaic performances although relatively low current densities (up to $324 \mu\text{A cm}^{-2}$) and open circuit voltage (209-484 mV) were obtained in this work. While the type of QDs affected the device setup, the CISE QD samples dispersed in pyridine and the treatment of TiO_2 and QD layers with EDT improved the device performance.

4.5 References

- [1] Zimmer, J.P., Kim, S.W., Ohnishi, S., Tanaka, E., Frangioni, J.V. and Bawendi, M.G. (2006). *J. Am. Chem. Soc.* 128, 2526-2527.
- [2] Aldakov, D., Lefrancois, A. Reiss, P. (2013). *J. Mater. Chem. C* 1, 3756.

- [3] Jackson, P., Hariskos, D., Lotter, E., Paetel, S., Wuerz, R., Menner, R., Wischmann, W. and Powalla, M. (2011). *Prog. Photovolt.: Res. Appl.*19, 894.
- [4] Beach, J.D. and McCandless, B.E. (2007). *MRS Bull.*32, 225-229.
- [5] Zhong, H. Wang, Z., Bovero, E., Lu, Z., van Veggel, F.C. and Scholes, G.D. (2011). *J. Phys. Chem. C*, 115, 12396.
- [6] AbuShama, J.A., Johnston, S., Moriarty, T., Teeter, G., Ramanathan, K. and Noufi, R. (2004). *Prog. Photovoltaics Res. Appl.*12, 39.
- [7] Reifsnyder, D.C., Xingchen, Y., Thomas, R.G., Chengyu S. and Murray C.B. (2013). *ACS Nano*. 7, 4307-4315.
- [8] Park, J., Dvoracek, C., Lee, K.H., Galloway, J.F., Bhang, H.C., Pomper, M.G. and Searson, P.C. (2011). *Small* 7, 3148-3152.
- [9] Zhong, H., Bai, Z. and Zou.B. (2012). *J. Phys. Chem. Lett.* 3, 3167.
- [10] Allen, P. M. and Bawendi, M.G. (2008). *J. Am. Chem. Soc.* 130, 9240.
- [11] Omata, T., Nose, K. and Otsuka.Y.M. (2011). *J. Nanosci. Nanotechnol.* 11, 4815.
- [12] Fischer, J., Larsen, J.K., Guillot, J., Aida, Y. Eisenbarth, T., Regesch, D., Depredurand, V., Fevre, N., Siebentritt, S. and Dale, P.J. (2014). *Solar Energy Materials & Solar Cells*126, 88-95.
- [13] Wasim, S.M., Rincon, C., Marin, G. and Delgado, J.M. (2000). *Appl. Phys. Lett.* 77, 94-96.
- [14] Turcu, M., Pakma,O. and Rau.U. (2009). *Appl. Phys. Lett.* 80, 2598-2600.
- [15] Turcu, M. and Rau, U. (2003). *Thin Solid Films* 431, 158-162.

- [16] Wu, J. D., Wang, L.T. and Gau, C. (2012). *Solar Energy Materials & Solar Cells* 98, 404-408.
- [17] Koo, B., Patel, R.N. and Korgel, B.A. (2009). *J. Am. Chem. Soc.* 131, 3134-3135.
- [18] Li, B., Xie, Y., Huang, J.X. and Qian, Y.T. (1999). *Adv. Mater.* 11, 1456-1459.
- [19] Jiang, Y., Wu, Y., Mo, X., Yu, W.C., Xie, Y. and Qian, Y.T. (2000). *Inorg. Chem.* 39, 2964-2965.
- [20] Grisar, H., Palchik, O., Gedanken, A., Palchik, V., Slifkin, M.A., and Weiss, A.M. (2003). *Inorg. Chem.* 42, 7148-7155.
- [21] Sabet, M., Niasari, M.S., Ghanbari, D., Amiri, O., Mir, N. and Dadkhah, M. (2014). *Materials Science in Semiconductor Processing* 25, 98-105.
- [22] Blackburn, J.L., Selmarten, D.C. and Nozik, A.J. (2003). *J. Phys. Chem. B* 107, 14154.
- [23] Boix, P.P., Larramona, G., Jacob, A., Delatouche, B., Mora-Seró, I. and Bisquert, J. (2012). *J. Phys. Chem. C* 116, 1579.
- [24] Shen, Q., Kobayashi, J., Diguna, L.J. and Toyoda, T. (2008). *J. Appl. Phys.* 103, 084304.
- [25] Pernik, D.R., Tvrđy, K., Radich, J.G. and Kamat, P.V. (2011). *J. Phys. Chem. C* 115, 13511.
- [26] Gorer, S. and Hodes, G. (1994). *J. Phys. Chem.* 98, 5338.
- [27] Santra, P.K. and Kamat, P.V. (2012). *J. Am. Chem. Soc.* 134, 2508.

- [28] Gratzel, M. (2003). *Journal of Photochemistry and Photobiology C: Photochemistry Reviews* 4, 145-153.
- [29] Hagfeldt, A., Boschloo, G., Sun, L.C., Kloo, L., Pettersson, H. (2010). *Chem. Rev.* 110, 6595-6663.
- [30] Lee, Y.L. and Lo, Y.S. (2009). *Advanced Functional Materials* 19, 604.
- [31] Rühle, S., Shalom M. and Zaban, A. (2010). *Chem. Phys.Chem.* 11, 2290.
- [32] Mora-Seró, I. and Bisquert, J. (2010). *J. Phys. Chem. Lett.* 1, 3046.
- [33] Genovese, M.P., Lightcap, I.V. and Kamat, P.V.(2012). *ACS Nano* 6, 865.
- [34] Sfaelou, S., Kontos, A.G. Givalou, L. Falaras, P. and Lianos, P. (2014). *Catalysis today* 230, 221-226.
- [35] Kamat, P.V. (2012). *Acc. Chem. Res.* 45, 1906.
- [36] Kuno, R. M. and Kamat, P.V. (2007). *J. Am. Chem. Soc.* 129, 4136.
- [37] Lekha, P., Balakrishnan, A., Subramanian, K.R.V. and Nair, S.V. (2013). *Mater. Chem. Phys.* 141, 216.
- [38] Peng, Z., Liu, Y., Shu, W. Chen, K. and Chen, W. (2012). *Eur. J. Inorg. Chem.* 5239.
- [39] Jun, H.K., Careem, M.A. and Arof, A.K. (2013). *Int. J. Photoenergy*, 942139.
- [40] Yamanaka, S., Konagai, M. and Takahashi, K. (1989). *Jpn. J. Appl. Phys.* 28, L1337.
- [41] Chen, B., Zhong, H., Zhang, W., Tan, Z., Li, Y., Yu, C., Zhai, T., Bando, Y., Yang, S., Zou, B. (2012). *Adv. Funct. Mater.* 22, 2081.

- [42] Ren, T., Yu, R., Zhong, M., Shi, J. and Li, C. (2011). *Solar Energy Materials & Solar Cells* 95, 510-520.
- [43] Rincon, C. and Ramirez, F.J. (1992). *J. Appl. Phys.* 72, 4321-4324.
- [44] Smith A.M. and Shuming, N. (2010). *Accounts of chemical Research*, 43, 190-200.
- [45] Ruffenach, S.Y., Robin, Y., Moret, M., Aulombard, R.L. and Briot, O. (2013). *Thin Solid Films* 535, 143-147.
- [46] Kergommeaux, A., Fiore, A., Bruyant, N., Chandezon, F., Reiss, P., Pron, A., de Bettignies, R. and Faure-Vincent, J. (2011). *Solar Energy Materials & Solar Cells* 95, S39-S43.
- [47] Zhong, H., Lo, S.S., Mirkovic, T., Li, Y., Ding, Y., Li, Y. and Scholes, G.D. (2010). *ACS Nano*, 4, 5253-5262.
- [48] Ulbricht, R., Pijpers, J.H., Groeneveld, E., Koole, R., Donega, C.M., Vanmaekelbergh, D., Delerue, C., Allan, G. and Bonn, M. (2012). *Nano Letters* 12, 4937-4942.
- [49] Radychev, N., Scheunemann, D., Kruszynska, M., Frevert, K., Miranti, R., Kolny-Olesiak, J., Borchert, H. and Paris, J. (2012). *Organic Electronics* 13, 3154-3164.
- [50] Yang, Y., Zhong, H., Bai, Z., Zou, B., Li, Y., and Scholes, G.D. (2012). *J. Phys. Chem. C* 116, 7280-7286.
- [51] Yue, W., Han, S., Peng, R., Shen, W., Geng, H., Wu, F., Tao, S. and Wang, M. (2010). *J. Mater. Chem.* 20, 7570.
- [52] Zhong, H., Lo, S.S., Mirkovic, T., Li, Y., Ding, Y., Li, Y. and Scholes, G.D. (2010). *ACS Nano* 4, 5253.

- [53] Kongkanand, A., Tvrdy, K., Takechi, K., Kuno, M., and Kamat, P.V. (2008). *J. Am. Chem. Soc.* 130, 4007-4015.
- [54] Robel, I., Subramanian, V., Kuno, M. and Kamat, P.V. (2006). *J. Am. Chem. Soc.* 128, 2385.
- [55] Mora-Sero, I., Gimenez, S., Moehl, T., Fabregat-Santiago, F., Lana-Villareal, T., Gomez, R. and Bisquert, J. (2008). *Nanotechnology* 19, 424007, 1-7.
- [56] Guijarro, N., Lana-Villarreal, T., Mora-Sero, I., Bisquert, J. and Gomez, R. (2009). *J. Phys. Chem. C* 113, 4208-4214.
- [57] Margraf, J.T., Ruland, A. Sgobba, V., Guldi, D.M. and Clark, T. (2013). *Langmuir* 29, 2434-2438.
- [58] Klem, E.D., MacNeil, D.D., Cyr, P.W., Levina, L. and Sargent, E.H. (2007). *Appl. Phys. Lett.* 90, 183113.
- [59] Seo, J., Cho, M.J., Lee, D. Cartwright, A.N. and Prasad, P.N. (2011). *Adv. Mater.* 23, 3984-3988.
- [60] Klem, E.D., Shukla, H., Hinds, S., MacNeil, D.D., L. Levina, L. and Sargent. E. H. (2008). *Appl. Phys. Lett.* 92, 212105.
- [61] Lawless, D., Kapoor, S. and Meisel, D. (1995). *J. Phys. Chem.* 99, 10329.
- [62] Rhodes, R., O'Brien, P. and Saunders, B.R. (2011). *Journal of Colloid and Interface Science* 358, 151-159.
- [63] Sambur, J.B., Riha, S.C., Choi, D. and Parkinson, B.A. (2010). *Langmuir* 26, 4839-4847.

-
- [64] Luther, J.M., Law, M., Song, Q., Perkins, C.L., Beard, M.C., Nozik.A.J.(2008). ACS Nano 2, 271-280.
- [65] Guijarro, N., Lana-Villarreal, T., Mora-Sero, I., Bisquert, J. and Gomez, R. (2009). J. Phys. Chem. C 113, 4208-4214.
- [66] Shalom, M., Buhbut, S., Tirosh, S. and Zaban, A. (2012). J. Phys. Chem. Lett. 3, 2436-2441.
- [67] Xu, G.P., Ji, S.L., Miao, C.H., Liu, G.D. Ye, C.H. (2012). J. Mater. Chem. 22, 4890-4896.

CHAPTER 5:

COPPER INDIUM GALLIUM SELENIDE NANOCRYSTALS: SYNTHESIS, CHARACTERIZATION AND QDSSCS

5.1 Introduction

Copper based chalcogenides are one of the most prominent materials used for photovoltaic applications. The optical, structural and electrical properties of those materials can be tuned to suit several applications needed to palliate to what is currently stopping the improvement of solar cells technology [1-6]. Copper indium gallium selenide (shortened as CIGSe) materials are I-III-VI p-type semiconductors with high optical absorption coefficient making them perfect candidates for solar applications [7, 8-9]. Polycrystalline CIGSe films are mostly prepared by simultaneous or sequential evaporation of the four constituent elements onto the substrate where the film is formed in single or multiple steps. This method is more successful and promising when performed under vacuum [10-12]. Another main technique for film preparation is electrodeposition where metals are prepared electrolytically from salt-containing electrolyte solutions and deposited on the cathode surface when the applied potential exceeds the standard reduction potential of the ions. However CIGSe film preparation via this method is limited by solubility of different salts in a common solvent, thereby making it difficult to control the stoichiometry [13-17].

Much work has been done to assemble performant devices based on bulk CIGSe films. The films with the band gap energy varying from 1.04 to 1.70 eV were made and the efficiency of 20% was achieved in the state of the art fabricated solar cell [18-21]. Recently much of the focus has been to synthesize nanosized CIGSe quantum dots with the aim to improve the efficiency of the solar cells beyond 20% at a reduced cost by using smaller material and solution processing methods. A number of endeavours have been done to synthesize nanosized CIGSe. Wu *et al.* [22] synthesized CIGSe and CIGSe via a precipitation method. Indium (III) chloride, Copper (I) chloride and gallium (III) chloride were heated in polyol solution where they were reduced to metal particles. Elemental Se was then added to the solution to form CIGSe and CIGSe which were dissolved in ethanol and precipitated by nucleation process to form the nanocrystals. Gu *et al.* [23] employed solvothermal method in which Cu, In, GaCl₃, and Se were added to ethylenediamine into the autoclave at 230 °C for

24h. A single phase CIGSe was obtained after washing the product with water and drying at 100 °C. The particles had a size of less than 100 nm and were strongly agglomerated. Although a rigorous control is now needed, the introduction of defined concentration of indium and/or gallium in copper selenide may render the semiconducting materials more susceptible to increase their properties [5, 24-26].

CIGSe can possess a defined stoichiometry but with several crystalline structures where the distribution of copper and indium have different possible orderings [27]. The order of addition of Se precursor to OLA (capping agent) affect the crystal structure of CIGSe. Sphalerite and chalcopyrite phases were obtained with injection of Se to and along the mixture of other precursors in OLA respectively [4]. The addition of one more element, gallium for instance, to CIGSe may be followed with similar or more approaches in order to obtain the quaternary chalcopyrite material with enhanced properties.

In this Chapter, the synthesis of CIGSe nanoparticles was done via conventional colloidal and microwave assisted methods where the dispersivity and reduction of nanoparticle size were studied. Furthermore, the effect of the reactant stoichiometry through addition of Ga to CIGSe synthesis was investigated. The influence of the coordinating solvent on the conventional colloidal method was also studied in order to improve the properties of the synthesized CIGSe nanoparticles and their photovoltaic capabilities.

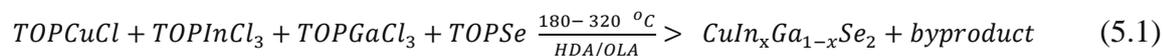
5.2 Experimental procedures

Copper (I) chloride (CuCl), indium chloride (InCl₃), gallium chloride (GaCl₃), selenium powder, TiO₂ (Dyesol), tri-n-octylphosphine (TOP), hexadecylamine (HDA), oleylamine (OLA), acetonitrile, hexane, methanol, ethanol, acetone tin doped-indium oxide (ITO), and doped-fluorine tin oxide (FTO) substrates were used as purchased.

5.2.1 Conventional colloidal method

The method was adapted from the reaction (5.1) below. An amount of about 6.0 g of HDA was heated to 100 °C. Then 1.0 ml of 1.0 M solution of CuCl in TOP (TOPCuCl), 0.5 ml (0.75 or 0.25 ml) of 1.0 M InCl₃ in TOP (TOPInCl₃) and 0.5 ml (0.25 or 0.75 ml) of 1M GaCl₃ in TOP (TOPGaCl₃) were added to the solution. The resultant solution was then heated to 180 °C where 1ml of 2.0 M solution of Se in TOP (TOPSe) was then added. The content

was heated to 220 °C for a further 30 min. The temperature was then decreased to 60 °C. Methanol was then added to the solution to flocculate the nanoparticles and CIGS nanoparticles were collected after centrifugation. The concentrations were varied in order to obtain the different stoichiometric CIGSe. The effect of the solvent was also studied.



5.2.2 Microwave assisted method

About 2 ml of 1.0 M TOPCuCl, 0.5ml of 1.0 M TOPInCl₃ and 0.5ml of 1.0 M TOPGaCl₃ were added to 5 ml of HDA in a Teflon vessel liner and mounted on the rotor and then purged with argon for 2 min before being placed in the microwave. The microwave was then heated for 10 min at a power of 500 W. The reaction occurred similarly as the reaction (5.1) above. The system was then cooled to 70 °C where 1 ml of 2 M TOPSe was quickly added. The vessel was then purged for 5 min with argon before continuing heating the mixture for another 10 min at 600 W. The heating was stopped and the microwave was allowed to cool to 50 °C. Methanol was then added to the solution to flocculate the nanoparticles and CIGSe nanoparticles were collected after centrifugation.

5.2.3 Thin film treatment and device assembly

The procedures for preparation of substrates and QDSSC device assembly using the untreated CIGSe thin film are as described in sections 4.2.3 to 4.2.5 of Chapter 4. Here, CIGSe materials are replaced by CIGSe. A schematic of the QDSSC device is shown in Fig. 5.1 below.

5.2.4 Characterization of the materials

The optical, structural and electrical properties of CIGSe NPs were determined using the same characterization techniques described in section 4.2.6 of Chapter 4. Furthermore, atomic force microscopy (AFM) Veeco 3100 SPM was used to determine the surface morphology of the CIGSe thin film.

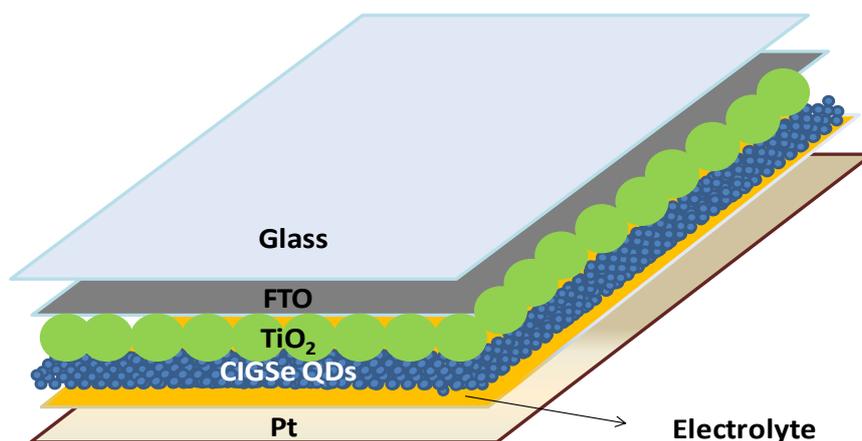


Fig. 5.1 Architecture of the CIGSe QDSSC device

5.3 Results and discussion

5.3.1 Synthesis of copper indium gallium selenide nanoparticles via conventional colloidal and microwave assisted methods

The details about the MAM and CCM have been discussed in our earlier report [28] and in Chapter 3. The current chapter only discusses the CIGSe properties related to these two methods.

5.3.1.1 Optical properties

The absorption and emission spectra of the MAM and CCM synthesized CIGSe nanoparticles are shown in Fig. 5.2 and Fig. 5.3 respectively. A large blue shift was observed in the materials synthesized via both MAM and CCM, confirming that the synthesized materials were relatively small, in sub-micron level at some extent. The optical parameters are assembled in Table 5.1. The MAM synthesized CIGSe nanoparticles showed the absorption band edge and emission peak at 680 nm and 720 nm respectively while CCM gave those optical parameters at 695 nm and 740 nm. The blue-shift is slightly pronounced in MAM than in CCM and may indicate a synergic effect from agglomeration due to excess of ligands adsorbed on the surface of the synthesized CIGSe nanoparticles. In addition, the MAM synthesized CIGSe gave longer tailing absorption spectrum showing more polydispersivity than the CCM. However a FWHM of 40 nm was determined in MAM sample. This was lower and indicates a higher degree of monodispersivity than the FWHM of CCM sample which was located at 88 nm. Higher band gap energies were estimated in both samples via their energy curves as shown in Fig. A5.1 of the appendix. A further characterization was then made for structural properties of MAM and CCM samples.

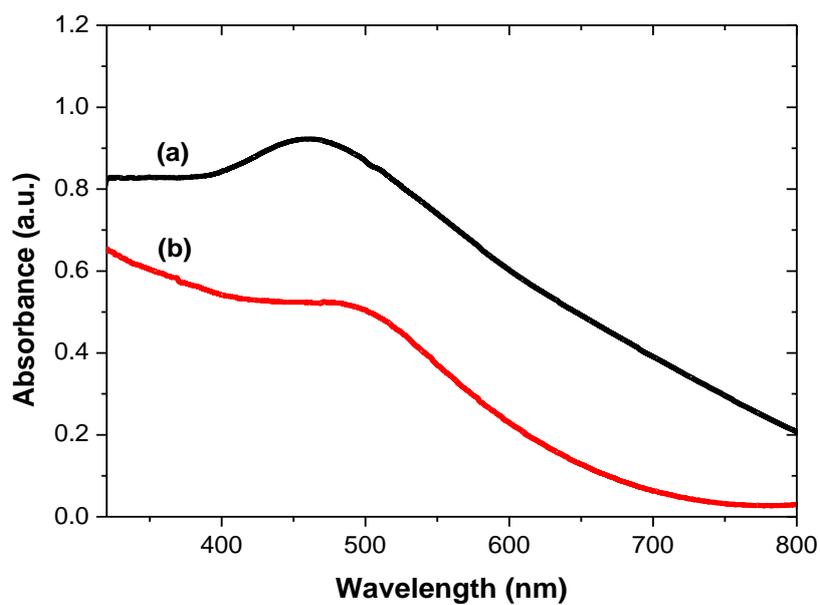


Fig. 5.2 Absorption spectra of CIGSe NPs synthesized in HDA via (a) MAM and (b) CCM

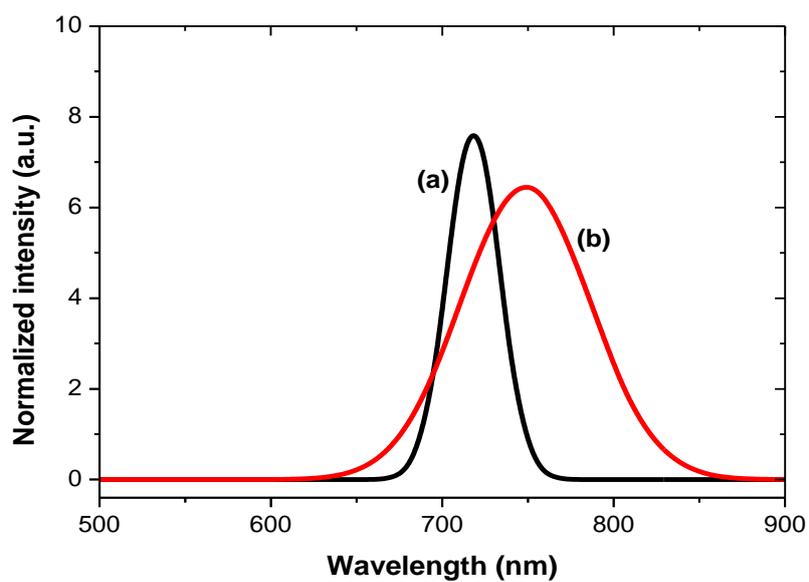


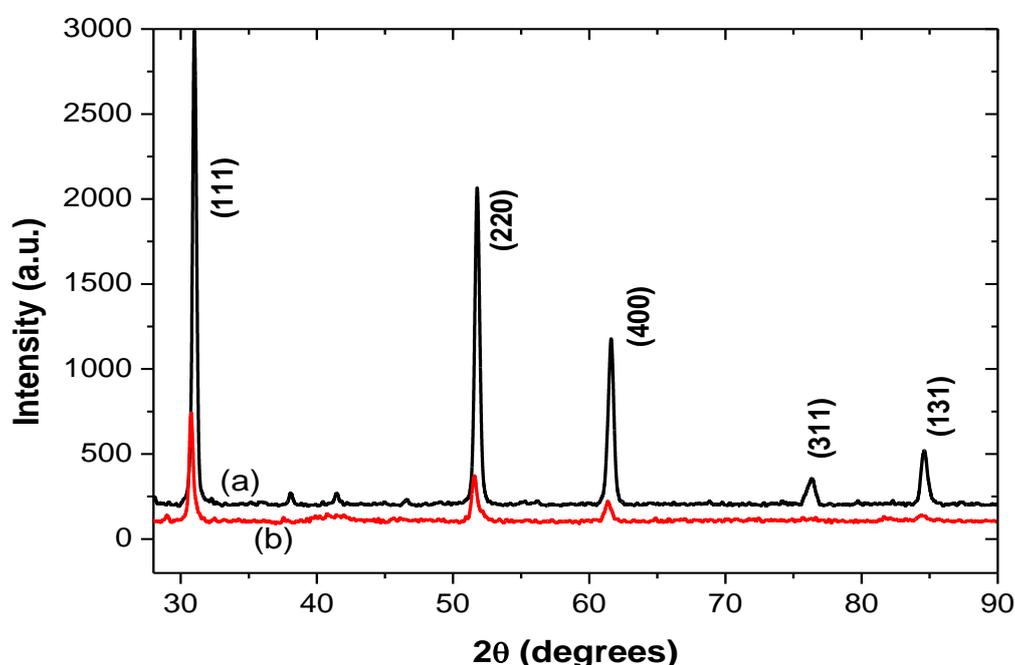
Fig. 5.3 Emission spectra of CIGSe NPs synthesized in HDA via (a) MAM and (b) CCM

Table 5.1 Optical parameters of MAM and CCM synthesized CIGSe NPs

Method	Band edge (nm)	Emission (nm)	Stokes shift (nm)	FWHM (nm)
MAM	680	720	40	40
CCM	695	740	45	88
Bulk	710-1192	-	-	-

5.3.1.2 Structural properties

The XRD patterns of CIGSe nanoparticles prepared via CCM and MAM are shown in Fig.5.4. All the peaks confirmed the crystalline nature of the synthesized material which is made with nanosize level particles. The peaks were indexed similarly as tetragonal crystal of $\text{CuIn}_{0.5}\text{Ga}_{0.5}\text{Se}_2$ (JCPDS 40-1487). The MAM sample showed all peaks with better crystallinity in defined lattice compared to CCM where the peak intensities such as those indexed in (311) and (131) showed a slight decrease due to the lattice imperfection. This phenomenon has been studied by several authors using other compounds [29-31].

**Fig. 5.4** XRD patterns of CIGSe NPs synthesized in HDA via (a) MAM and (b) CCM

The CIGSe nanoparticles shapes were determined by TEM as shown in Fig. 5.5. The images revealed mixed shapes that tended to form agglomerates thereby giving an overall irregular morphology. The MAM sample shows more agglomeration than conventional colloidal method under similar conditions. This may be due to the growth of particles as well as the heat provided by both methods. The sequential addition of precursors in CCM showed a better control of particle growth and dispersion than the addition of all precursors at once before MAM synthesis which promotes agglomeration of particles. The investigation of concentration of indium and gallium precursors was therefore done in order to identify the best stoichiometry for the synthesis of CIGSe NPs via CCM.

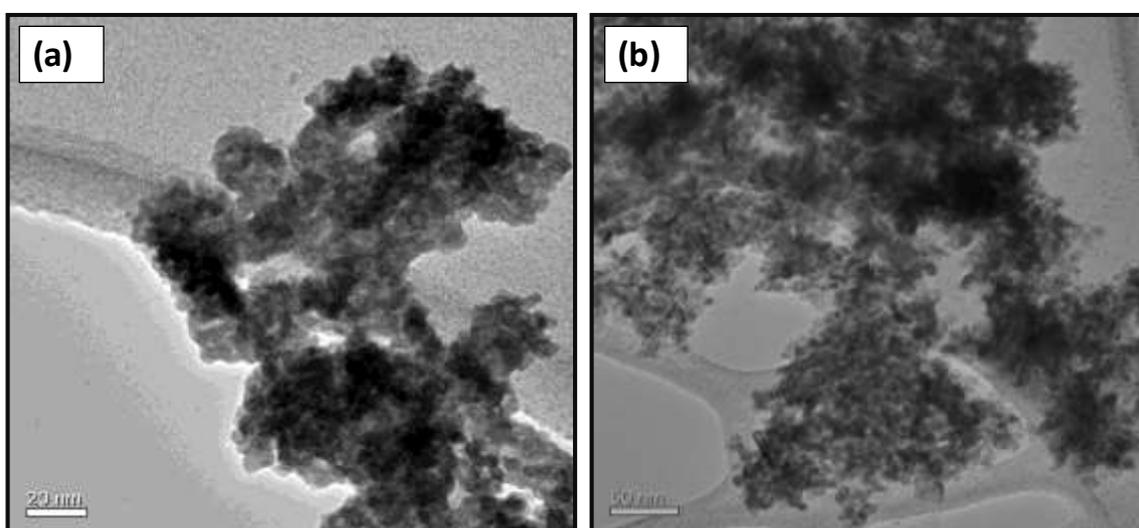


Fig. 5.5 TEM images of CIGSe NPs synthesized in HDA via (a) MAM and (b) CCM

5.3.2 Stoichiometric effects on the properties of CIGSe NPs synthesized via CCM

The concentrations of the precursors were varied with the aim to investigate the effect of stoichiometry on the properties of CIGSe synthesized in HDA via CCM. Table 5.2 shows various CIGSe samples prepared via CCM in HDA by varying the concentration of indium and gallium so as the number of moles of In+Ga is equal to that of copper. Thus, replacing half of copper in copper selenide by In+Ga atoms was investigated focusing on the amount of indium and gallium during the CCM synthesis. Indium and gallium concentrations were made at 1:1, 1:3 and 3:1 ratios of In/Ga.

Table 5.2 Synthesis of stoichiometric CIGSe NPs via CCM using HDA

CIGSe Sample	Stoichiometry			solvent
	Cu/(In+Ga)	In/(In+Ga)	In:Ga	
$\text{CuIn}_{0.25}\text{Ga}_{0.75}\text{Se}_2$	1	0.25	1:3	HDA
$\text{CuIn}_{0.50}\text{Ga}_{0.50}\text{Se}_2$	1	0.50	1:1	HDA
$\text{CuIn}_{0.75}\text{Ga}_{0.25}\text{Se}_2$	1	0.75	3:1	HDA

5.3.2.1 Optical properties of CCM synthesized stoichiometric CIGSe

The UV-Visible absorption and emission measurements were performed in order to investigate the optical properties of synthesized CIGSe nanoparticles as shown in Fig. 5.6 and Fig. 5.7. The values extracted from the spectra are shown in Table 5.3. The band edges from absorption spectra were observed at 695, 592 and 550 nm for $\text{CuIn}_{0.5}\text{Ga}_{0.5}\text{Se}_2$, $\text{CuIn}_{0.25}\text{Ga}_{0.75}\text{Se}_2$ and $\text{CuIn}_{0.75}\text{Ga}_{0.25}\text{Se}_2$ respectively. The emission peaks were found at 740, 697 and 635 nm, confirming that the synthesized nanoparticles were relatively small on nanoscale level. The stoichiometric $\text{CuIn}_{0.75}\text{Ga}_{0.25}\text{Se}_2$ prepared in HDA showed large blue-shifted UV-Vis absorption band edge and PL emission peak. In addition, the $\text{CuIn}_{0.75}\text{Ga}_{0.25}\text{Se}_2$ particles show a narrower size distribution as suggested by the FWHM of emission peak for $\text{CuIn}_{0.75}\text{Ga}_{0.25}\text{Se}_2$ which was 47 nm. This value is less than those from $\text{CuIn}_{0.5}\text{Ga}_{0.5}\text{Se}_2$ and $\text{CuIn}_{0.25}\text{Ga}_{0.75}\text{Se}_2$ particles located at 88 and 57 nm. The $\alpha h\nu/h\nu$ curves for band gap approximation are shown in Fig. A5.2 of the appendix. The energy gaps of $\text{CuIn}_{0.5}\text{Ga}_{0.5}\text{Se}_2$, $\text{CuIn}_{0.25}\text{Ga}_{0.75}\text{Se}_2$ and $\text{CuIn}_{0.75}\text{Ga}_{0.25}\text{Se}_2$ were respectively higher than the bulk CIGSe. This indicates that the synthesized materials may be used as absorbing layer. Saji *et al.* [16] reported similar findings where the concentration of metal precursors may lead to CIGSe with energy gap tuned from 1.04 to 2.4 eV.

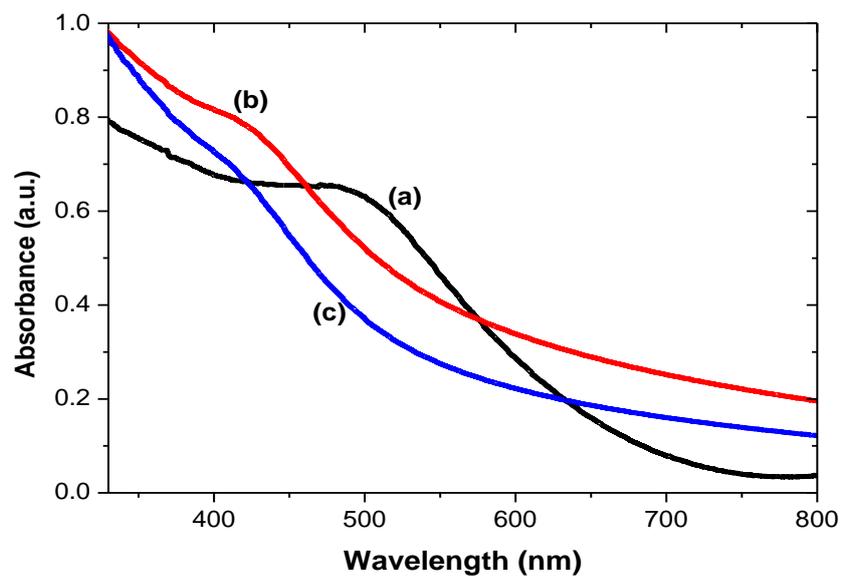


Fig. 5.6 UV-vis absorption spectra of (a) $\text{CuIn}_{0.5}\text{Ga}_{0.5}\text{Se}_2$, (b) $\text{CuIn}_{0.25}\text{Ga}_{0.75}\text{Se}_2$ and (c) $\text{CuIn}_{0.75}\text{Ga}_{0.25}\text{Se}_2$ NPs synthesized in HDA via CCM

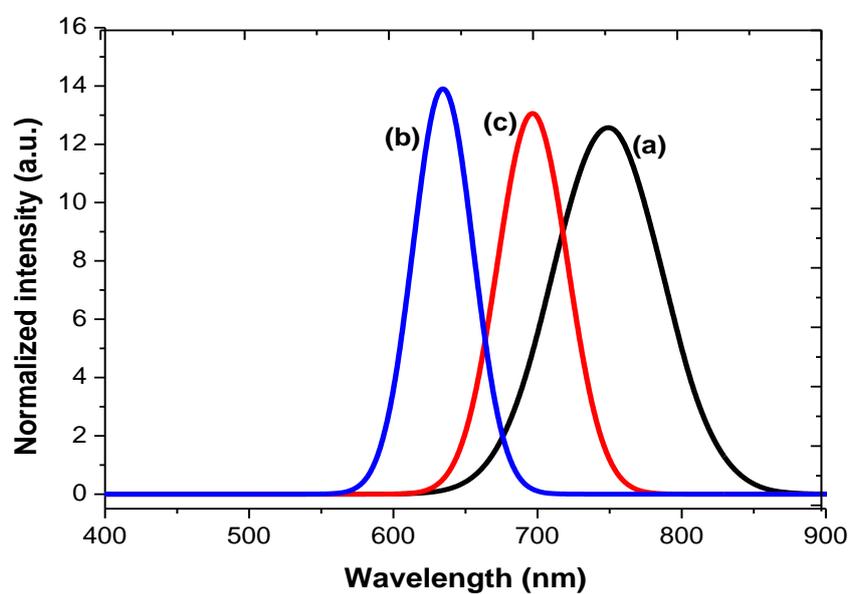


Fig. 5.7 PL emission spectra of (a) $\text{CuIn}_{0.5}\text{Ga}_{0.5}\text{Se}_2$, (b) $\text{CuIn}_{0.25}\text{Ga}_{0.75}\text{Se}_2$ and (c) $\text{CuIn}_{0.75}\text{Ga}_{0.25}\text{Se}_2$ NPs synthesized in HDA via CCM

Table 5.3 Optical parameters of CIGSe NPs synthesized at different stoichiometries

In/Ga ratio	Band edge (nm)	Emission (nm)	Stokes shift (nm)	FWHM (nm)
1:1	695	740	45	88
1:3	592	697	105	57
3:1	550	635	85	47
Bulk	710-1192	-	-	-

5.3.2.2 Structural properties of CCM synthesized stoichiometric CIGSe NPs

The XRD patterns are shown in Fig. 5.8. The $\text{CuIn}_{0.5}\text{Ga}_{0.5}\text{Se}_2$, $\text{CuIn}_{0.25}\text{Ga}_{0.75}\text{Se}_2$ and $\text{CuIn}_{0.75}\text{Ga}_{0.25}\text{Se}_2$ nanoparticles showed similar main peaks with indices (111; 220; 400; 311 and 131 from JCPDS 40-1487) corresponding to tetragonal lattice of copper indium gallium selenide. Small peaks encountered next to the identified patterns might be due to impurities from unreacted or partially formed compounds such as Cu_xSe . However more pure crystalline phase was identified in $\text{CuIn}_{0.75}\text{Ga}_{0.25}\text{Se}_2$ samples. The TEM images of stoichiometric CIGSe particles are shown in Fig.5.9. The images show nanosized particles dominated by pyramidal shapes in all synthesized materials. However less agglomerated nanosized particles were observed in $\text{CuIn}_{0.75}\text{Ga}_{0.25}\text{Se}_2$ than other prepared stoichiometric CIGSe, showing that increasing gallium content compromises the particle growth and dispersion. The aggregation may be due to many factors such as temperature or time of particle growth along with the concentration of precursors. The later can prove that the number of precursors added for a given synthesis may be a particular case to consider if a unique size and/or morphology are expected. While further cleaning of particles by much stronger solvents and long time of sonication may also be suggested to improve the particle dispersion, many other factors should be considered including the interaction between the solvent and capping agent used in the synthesis. Whether dispersed or aggregated in solution, the nanoparticles were crystalline and indeed with less than 50 nm size as suggested by the TEM images. The stoichiometric $\text{CuIn}_{0.75}\text{Ga}_{0.25}\text{Se}_2$ was therefore considered in the study of solvent for synthesis of CIGSe nanoparticles.

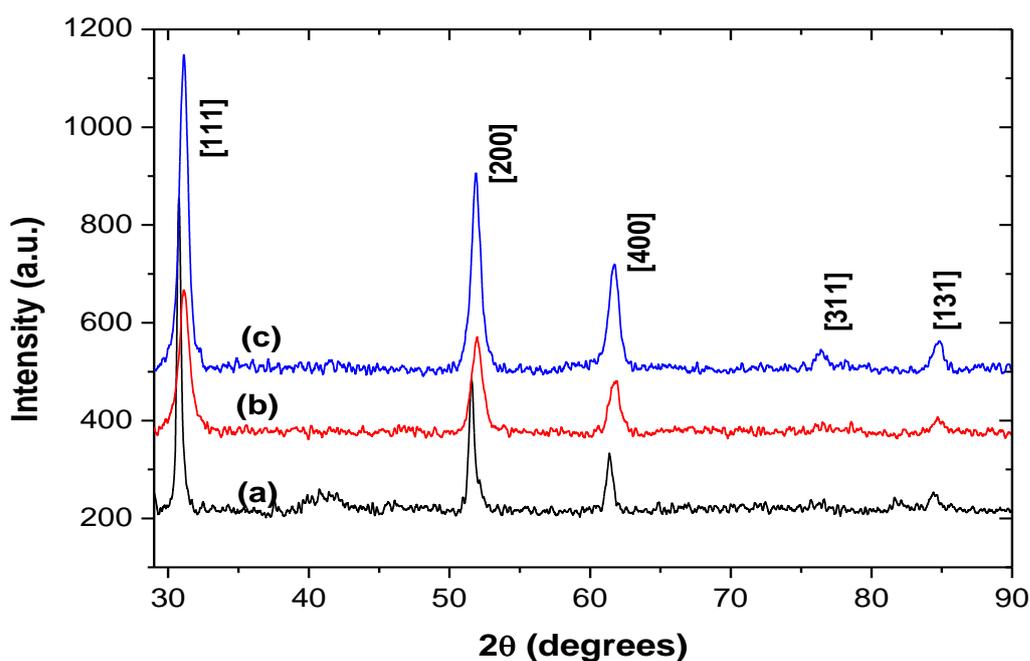


Fig. 5.8 XRD patterns of (a) $\text{CuIn}_{0.5}\text{Ga}_{0.5}\text{Se}_2$, (b) $\text{Cu In}_{0.25}\text{Ga}_{0.75}\text{Se}_2$ and (c) $\text{CuIn}_{0.75}\text{Ga}_{0.25}\text{Se}_2$ NPs synthesized in HDA via CCM

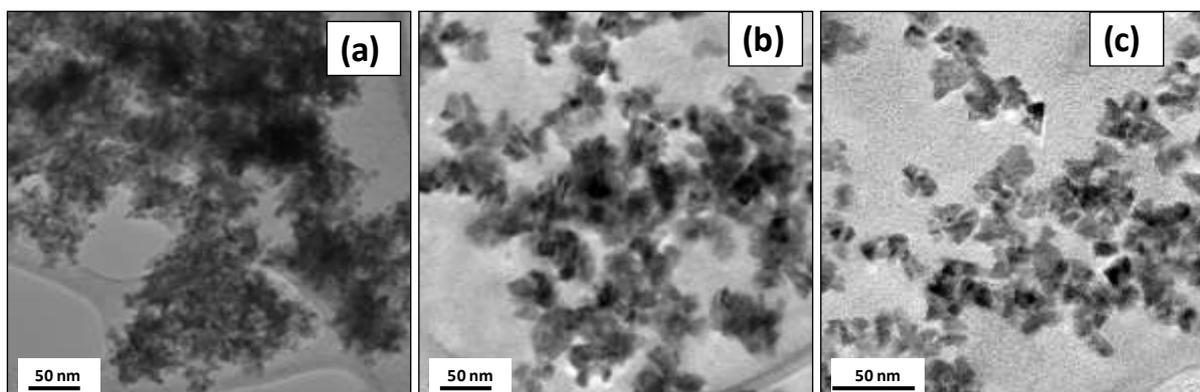


Fig. 5.9 TEM images of (a) $\text{CuIn}_{0.5}\text{Ga}_{0.5}\text{Se}_2$, (b) $\text{CuIn}_{0.25}\text{Ga}_{0.75}\text{Se}_2$ and (c) $\text{Cu In}_{0.75}\text{Ga}_{0.25}\text{Se}_2$ NPs synthesized in HDA via CCM. The size distribution was not determined due to agglomeration.

5.3.3 Solvent effects on the properties of CIGSe nanoparticles synthesized by CCM

5.3.3.1 Optical properties of CCM synthesized CIGSe using HDA and OLA

The solvent was varied from HDA to OLA while other parameters were kept constant for synthesis of $\text{CuIn}_{0.75}\text{Ga}_{0.25}\text{Se}_2$ in order to further optimise the properties. The optical absorption and emission spectra of $\text{CuIn}_{0.75}\text{Ga}_{0.25}\text{Se}_2$ nanoparticles are shown in Fig. 5.10 and

Fig. 5.11 respectively. The extracted optical parameters are shown in Table 5.4. The same FWHM of 50 nm and the same Stokes-shift of 95 nm were determined in both OLA and HDA samples suggesting similarities in $\text{CuIn}_{0.75}\text{Ga}_{0.25}\text{Se}_2$ particle dispersion. $\text{CuIn}_{0.75}\text{Ga}_{0.25}\text{Se}_2$ NPs synthesized in OLA showed a more blue-shift in optical behaviour with a band edge and a maximum emission peaks at 525 and 620 nm respectively as compared to the HDA counterparts which have the values red shifted to of 550 and 640 nm. This is due to the high dispersion and relatively smaller particle size encountered in the material synthesized in OLA than the HDA counterparts. The energy curves are shown in Fig. A5.3 in the appendix. The OLA synthesized CIGSe particles had a higher energy gap than those from HDA synthesis, confirming the good absorption at lower wavelengths.

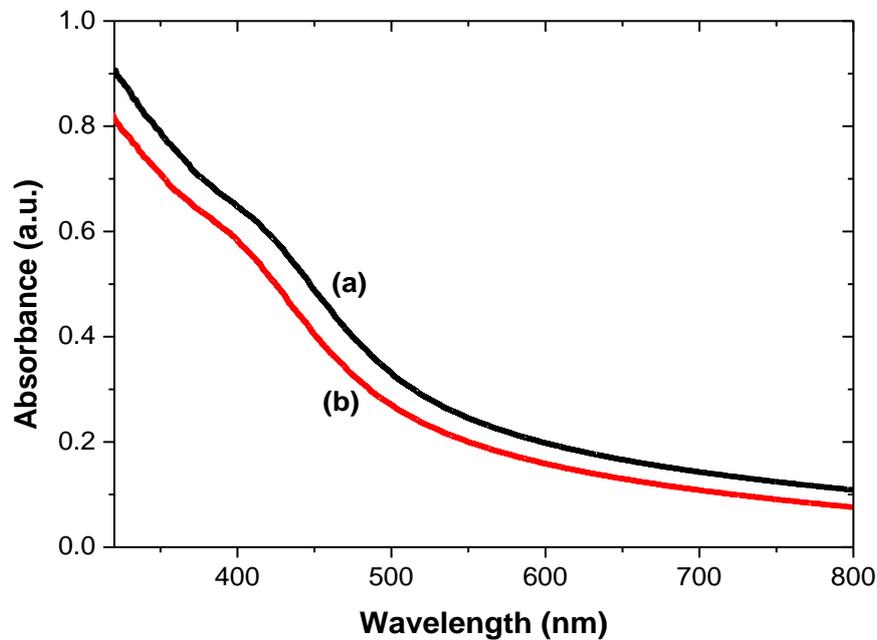


Fig. 5.10 Absorption spectra of $\text{CuIn}_{0.75}\text{Ga}_{0.25}\text{Se}_2$ nanoparticles synthesized via CCM in (a) HDA and (b) OLA

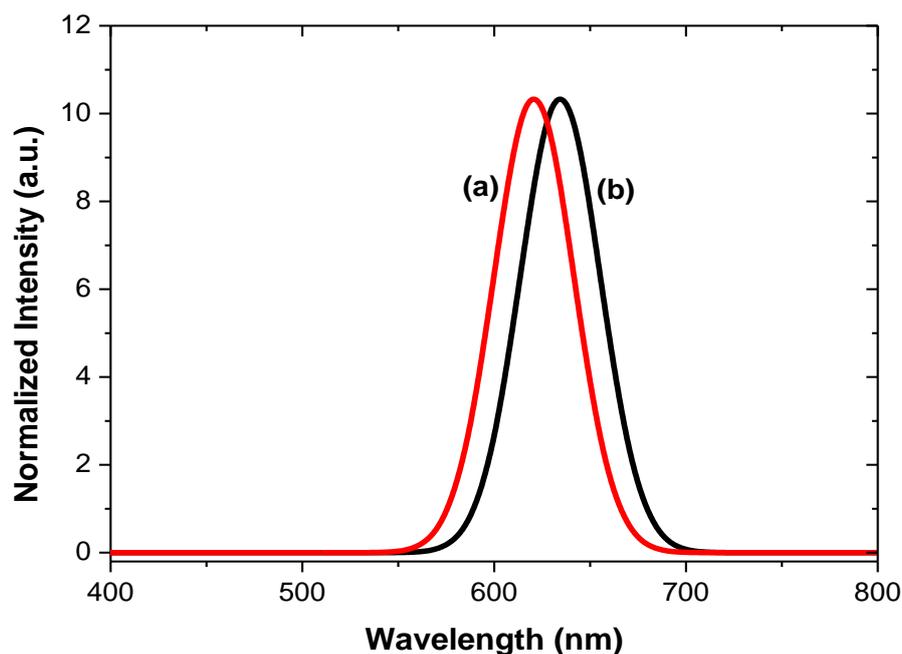


Fig. 5.11 Emission spectra of $\text{CuIn}_{0.75}\text{Ga}_{0.25}\text{Se}_2$ NPs synthesized via CCM in (a) HDA and (b) OLA

Table 5.4 Optical parameters of CCM synthesized CIGSe NPs using HDA and CCM

Solvent	Band edge (nm)	Emission (nm)	Stokes shift (nm)	FWHM (nm)
HDA	550	640	90	50
OLA	525	620	95	50
Bulk	710-1192	-	-	-

5.3.3.2 Structural properties of CCM synthesized CIGSe NPs using HDA and OLA

The XRD spectra of $\text{CuIn}_{0.75}\text{Ga}_{0.25}\text{Se}_2$ NPs synthesized in HDA and OLA via CCM are shown in Fig.5.12. The nanoparticles synthesized in both solvents were highly crystalline with sharp and well defined peaks. The diffraction peaks were indexed into tetragonal CIGSe crystalline orientations confirming that the particles were crystalline and at nano-level. The TEM images of HDA and OLA samples with size distribution and the energy dispersive spectrum (EDS) of CIGSe nanoparticles are shown in Fig.5.13. The particles were found in

pyramidal-like and nearly spherical shapes for HDA and OLA synthesized nanoparticles respectively. The TEM images of the two samples clearly show that the nanoparticles synthesized with OLA had a better dispersivity than when the solvent was replaced by HDA following the very same CCM route. The particle size distribution can therefore be determined from the OLA sample where the EDS spectrum was also collected. The particle sizes of $\text{CuIn}_{0.75}\text{Ga}_{0.25}\text{Se}_2$ synthesized in OLA were with a certain degree of polydispersion and the average diameter was 6.61 ± 0.60 nm. This indicates that Ostwald ripening effect may have occurred as the nanoparticles matured from nucleation during the synthesis. The EDS analysis proved that copper indium gallium selenide nanoparticles were synthesized. The carbon (not shown on the graph) chlorine and the excess of copper detected here originated from the copper grid, its lacy carbon, the solvent used to disperse the particles and the ligands adsorbed onto the surface of CIGSe particles. The size and functional groups in the two solvents can also be the cause of difference in properties of the synthesized particles. Since the molecular weight of OLA is greater than HDA the vibration and swelling properties of OLA would be less than those from HDA. While the amine group is expected to play a similar role in both HDA and OLA, the particular effect of OLA may be attributed to the double bond giving each OLA the possibility to bend the molecular chain creating much attraction toward growing particle during synthesis and therefore decreasing the space in which that particle should grow. Other details in comparing the two solvents are shown in Chapter 3. The $\text{CuIn}_{0.75}\text{Ga}_{0.25}\text{Se}_2$ nanoparticles synthesized in OLA were therefore used to fabricate a CIGSe QDSSC device.

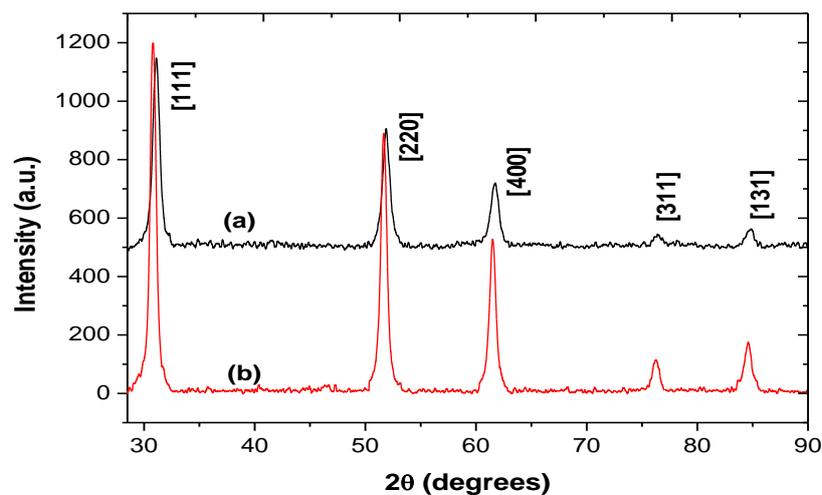


Fig. 5.12 XRD patterns of $\text{CuIn}_{0.75}\text{Ga}_{0.25}\text{Se}_2$ NPs synthesized via CCM in (a) HDA and (b) OLA

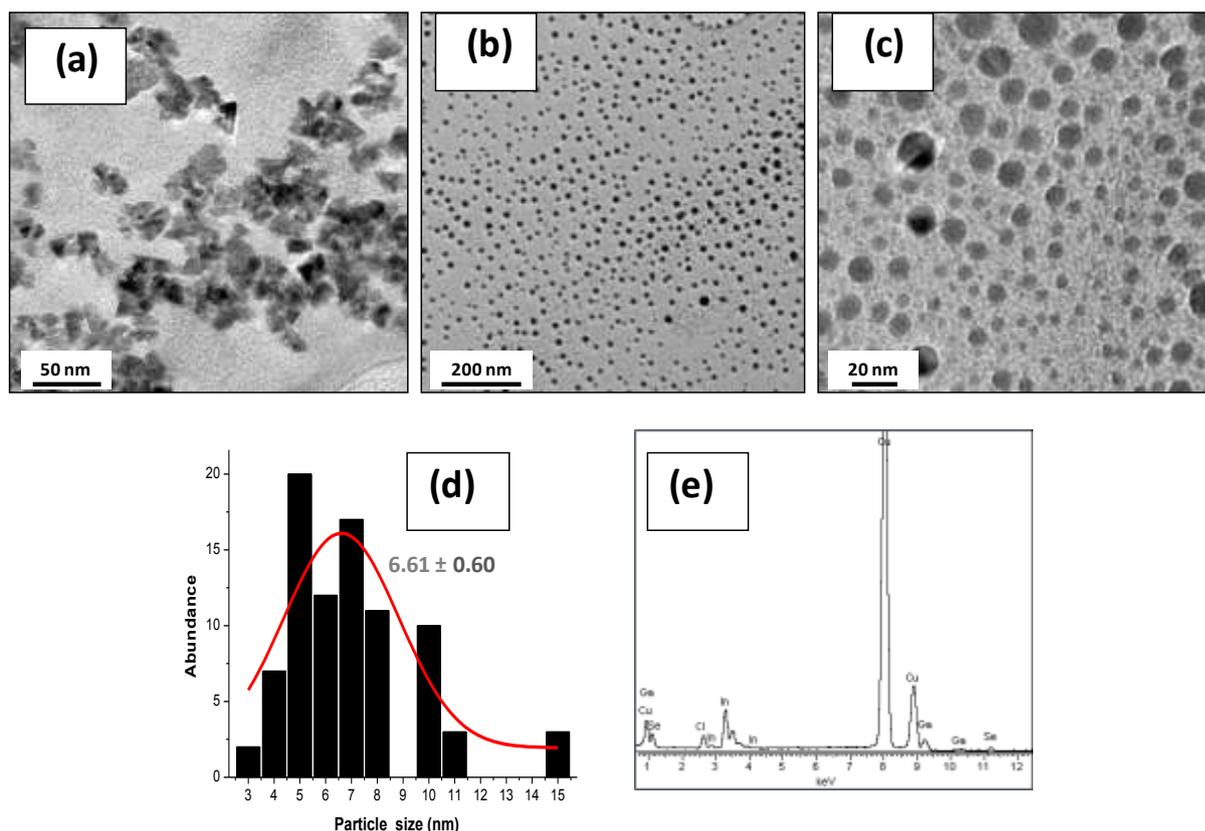


Fig. 5.13 TEM images of CuIn_{0.75}Ga_{0.25}Se₂ NPs synthesized via CCM in (a) HDA, (b) OLA, (c) OLA at higher magnification; with (d) size distribution and (e) EDS spectrum of CuIn_{0.75}Ga_{0.25}Se₂ NPs synthesized via CCM in OLA.

5.3.4 CIGSe device assembly

The QDSSC device was assembled from CIGSe film without further treatment. The optical microscopic image and the energy curve of CIGSe thin film are shown in Fig. 5.14. The optical band gap energy of the film was 1.93 eV, indicating that the film may be used as an absorbing layer in QDSSC. However, the film had many pin holes that can hinder the electric performance of the device. This was also confirmed by the AFM images as shown in Fig. A5.5 in the appendix. The electrical properties of the assembled QDSSC are shown in Fig. 5.15 with parameters values inset. The J_{sc} of 168 $\mu\text{A cm}^{-2}$ and V_{oc} of 162 mV were found in the device. Although a relatively better FF of 33% was yielded in the assembled device from CIGSe film, poor electric properties were observed, leading to a very small PCE. Several factors may be the cause of the poor performance of the device. The quality of the CIGSe film could not favour a good transfer of electrons from the absorber to the wide band gap layer of TiO₂. Monig *et al.* [28] reported the difference of J-V curves from grain to grain bringing a high density of defect states at the CIGSe surface. The authors suggested a

preferential oxidation of particular grains, which passivates the defect levels at the surface of the film. While this phenomenon may contribute to multiple exciton generation to a certain extent, the charge recombination processes may forbid electron to move from the active layer to the electrodes and therefore compromise the role of the assembled device as QDSSC. Although EDT was used as ligand exchange molecules, the attachments of CIGSe particles on the TiO_2 surface was not optimized. The role of the electrolyte can be another attempt to consider as this regenerates the charge in the absorbing layer. The Γ/I_3^- couple should be permanently stable in the device in order for the latter to perform better. However the electrolyte can leak anytime of the working conditions.

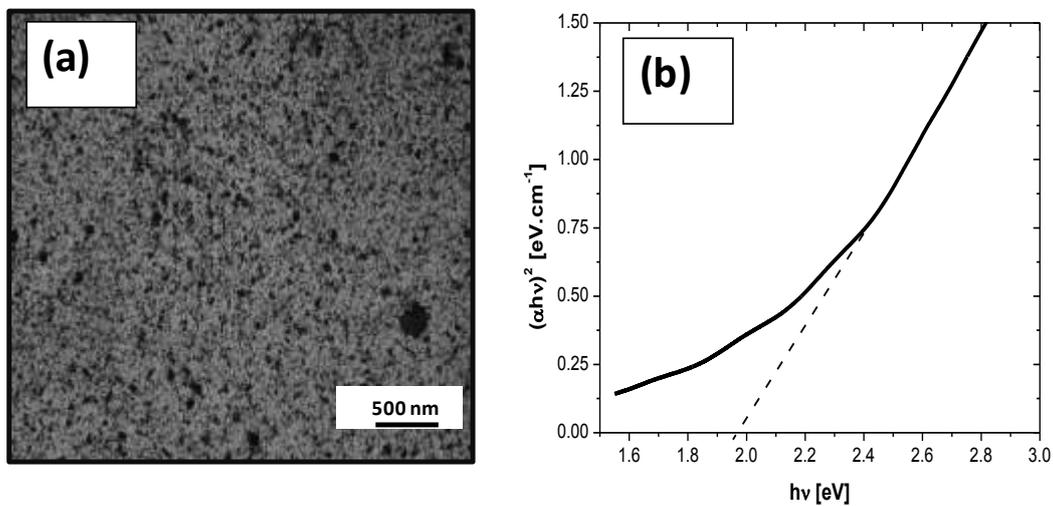


Fig. 5.14 Properties of CIGSe thin film: (a) optical microscopic image showing some openings within the film and (b) $(\alpha h\nu)^2/h\nu$ curve of CIGSe thin film

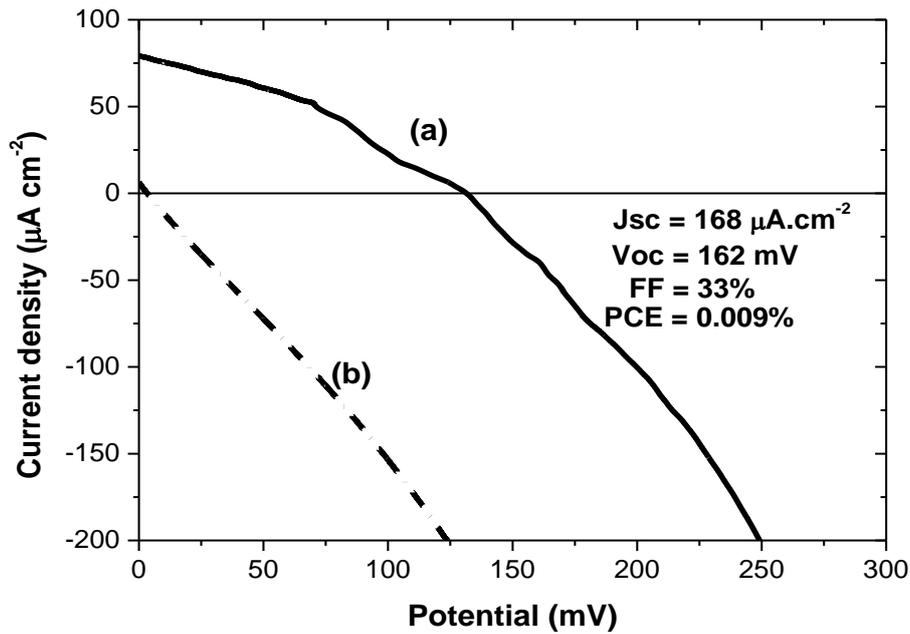


Fig. 5.15 J-V curve of CIGSe QDSSC device under (a) illumination with white light and (b) dark current

5.4 Conclusions

Relatively small sized copper indium gallium selenide nanoparticles were prepared through CCM and MAM. The optimization of the parameters of synthesis including the method, concentration ratio of indium and gallium precursors and solvent resulted in well dispersed and relatively small size copper indium gallium selenide nanoparticles with improved optical and structural properties. $\text{CuIn}_{0.75}\text{Ga}_{0.25}\text{Se}$ was the best stoichiometric CIGSe synthesized via CCM using oleylamine at 220 °C for 30 min. The nearly hexagonal nanoparticles sizing 6.5 nm in diameter were obtained under these conditions. The synthesized particles were used as thin film in QDSSC device. The evidence of concept of photovoltaic activities was demonstrated in the assembled device although poor performances were obtained. This may therefore be a keystone in developing any photovoltaic device based on copper indium gallium selenide nanoparticles.

5.5 References

- [1] Scheer, R., Walter, T., Schock, H.W., Fearheiley, M.L. and Lewerenz, H.J. (1993). Appl. Phys. Lett. 63, 3294-3296.

- [2] Green, M.A., Emery, K., King, D.L., Hishikawa, Y. and Warta, W. (2007). Prog. Photovolt.: Res. Appl. 15, 35-40.
- [3] Green, M.A., Emery, K., Hishikawa, Y. and Warta, W. (2010). Prog. Photovolt.: Res. Appl. 18, 346-352.
- [4] Guo, Q., Kim, S.J., Kar, M., Shafarmans, W., Birkmire, R., Stach, E.A., Agrawal, R. and Hillhouse, H.W. (2008). Nano Letters 8, 2982-2987.
- [5] Panthani, M.G., Akhavan, V., Goodfellow, B., Schmidtke, J.P., Dunn, L., Dodabalapur, A., Barbara, P.F. and Korgel, B.A. (2008). J. Am. Chem. Soc. 130, 16770-16777.
- [6] Contreras, M.A., Egaas, B., Ramanathan, K., Hiltner, J., Swartzlander, A., Hasoon, F., Noufi, R. (1999). Prog. Photovolt.: Res. Appl.7, 311-316.
- [7] Miller, A. Mackinnon, A. and Weaire, D. (1981). Solid State Physics 36, 119-175.
- [8] Kodigala, S.R. (2010). Thin Films and Nanostructures – Cu (In_{1-x} Ga_x)Se₂ based Thin Film Solar Cells, vol. 35. Academic Press, Elsevier, San Diego.
- [9] Wallin, E., Malm, U., Jarmar, T. Edoff, M., Lundberg, O. and Stolt, L. (2012). Prog. Photovolt. Res. Appl. 20, 851-854.
- [10] Schleussner, S., Zimmermann, U., Watjen, T., Leifer, K. and Edoff, M. (2011). Solar Energy Materials & Solar Cells 95, 721-726.
- [11] Venkatachalam, M., Kannan, M.D., Muthukumarasamy, N., Prasanna, S, Jayakumar, S., Balasundaraprabhu , R. and Saroja, M. (2009). Solar Energy 83, 1652-1655.
- [12] Kaelin, M., Rudmann, D. and Tiwari, A.N. (2004). Solar Energy 77, 749-756.
- [13] Dini, J.W. (1992). Electrodeposition, the Materials Science of Coatings and Substrates. Noyes Publications, New York, 141.

- [14] Li, J., Liu, F., Lai, Y., Zhang, Z. and Liu, Y. (2010). Indium and gallium incorporation mechanism during electrodeposition of Cu(In,Ga)Se thin film. In: 217th ECS Meeting, Abstract-1176, Vancouver.
- [15] Bhattacharya, R.N. (2010). *J. Electrochem. Soc.* 157, D406-D410.
- [16] Saji, V.S. Lee, S.M., Lee, C.W. (2011). *J. Korean Electrochem. Soc.* 14, 61-70.
- [17] Saji, V.S., Choi, I. and Lee, C. (2011). *Solar Energy* 85, 2666-2678.
- [18] Contreras, M.A. AbuShama, K.R., Hasoon, F., Young, D.L., Egaas, B. and Noufi, R. (2005). *Prog. Photovolt. Res. Appl.* 13, 209-216.
- [19] Jager-Waldau, A. (2011). *Solar Energy Materials & Solar Cells* 95, 1509-1517.
- [20] Repins, I., Contreras, M.A., Egaas, B., DeHart, C., Scharf, J., Perkins, C.L., To, B. and Noufi, R. (2008). *Prog. Photovolt. Res. Appl.* 16, 235-239.
- [21] Jackson, P., Hariskos, D., Lotter, E., Paetel, S., Wuerz, R., Menner, R., Wischmann, W. and Powalla, M. (2011). *Progress in Photovoltaics* 19, 894.
- [22] Wu, J.D. Wang, L.T. and Gau, C. (2012). *Solar Energy Materials & Solar Cells* 98 404-408.
- [23] Gu, S.I., Shin, H.S., Yeo, D.H., Hong, Y.W., Nahm, S. (2011). *Current Applied Physics* 11, S99-S102.
- [24] Delahoy, A.E., Chen, L.M. Akhtar, M., Sang, B. and S. Guo, S.(2004). *Solar Energy*, 77, 785-793.
- [25] Klimov, V.L., Mikhailowsky, A.A., Xu, S., Malko, A., Hallingsworth, J.A. and Leatherdole, C.A. (2000). *Science* 290, 340.

-
- [26] Battaglia, D. and Peng, X. (2002). *Nano Lett.* 2, 1027.
- [27] Stanley, B.J. (2002). *Critical Rev. Solid State Mater. Sci.* 27, 73-117.
- [28] Kalenga, M.P., Govindraju, S., Airo, M., Moloto, M.J., Sikhwivhilu, L.M. and Moloto, N. (2015). *J. Nanosci. Nanotechnol.* 15, 4480-4486.
- [29] Cullity, B.D. (1978). *Elements of X-Ray Diffraction*, M. Cohen (Ed.), 2nd ed., Addison-Wesley, 32-58.
- [30] Yeh, J.W., Chen, S.K., Lin, S.J., Gan, J.Y., Chin, T.S., Shun, T.T., Tsau, C.H. and Chang, S.Y. (2004). *Adv. Eng. Mater.* 6, 299-303.
- [31] Dederichs, P.H. (1971). *Phys. Rev. B* 4, 1041.
- [32] Monig, H. Caballero, R., Kaufmann, C.A., Schmidt, T.L., Lux-Steiner M.C. and Sadewasser, S. (2011). *Solar Energy Materials & Solar Cells* 95, 1537-1543.

CHAPTER 6:

SYNTHESIS, CHARACTERIZATION OF COPPER ZINC TIN SULPHUR SELENIDE NANOCRYSTALS AND THEIR APPLICATION IN QDSSCS

6.1 Introduction

Copper zinc tin sulphur selenide material (CZTSSe) is one of the most promising semiconductor chalcogenides needed in developing the trend in photovoltaics [1-5]. CZTSSe has a particular focus since the starting metals are relatively cheaper, earth abundant than indium and gallium of the leading CIGSe material. There is an increased possibility, as quinary material at nanoscale level, to further tune the energy gap and therefore improve the efficiency. There are various vacuum and non-vacuum based techniques that have been reported for thin film deposition of CZTSSe. Lechner *et al.* [6] reported the development of sputter deposition of Cu, Zn and Sn metals followed by the thermal evaporation of the chalcogen in chalcogen containing ambient for the formation of $\text{Cu}_2\text{ZnSn}(\text{S},\text{Se})_4$ thin films for solar cells. The assembled device gave the electrical properties with PCE above 6%. However of interest are the solution based techniques as they more cost effective and can yield high throughput. Recently, Todorov *et al.* reported the use of hydrazine-based solution for the fabrication of CZTSSe via spin coating to yield solar cells with PCE of 9.6% [7].

Several device configurations can be used to fabricate CZTSSe solar cell devices among which is that of dye sensitized solar cells (DSSCs). The details on the mechanisms for charge generation, transport and regeneration in a DSSC are shown in Chapter 2 and have also been shown in several reports [8-19]. Zhua *et al.* [20] reported on a modified standard dye sensitized solar cell (DSSC) with 2 layers of CZTS and CZTSe annealed at 500 °C and used as photocathodes on TiO_2 sensitized with N719. The assembled device gave good electrical properties with an overall PCE of 8.8%. In this chapter, the synthesized CZTSSe quantum dots (QDs) was used to fabricate solar cells similar to the DSSC. The dye was replaced by CZTSSe QDs to give quantum dot sensitized solar cells (QDSSCs). The preparation of the thin films of QDs was performed with or without mercapto-propionic acid (MPA) and ethanedithiol (EDT) treatments. The energy levels were also determined to understand the

electronic and electrical properties of CZTSSe QDs after which the devices made of the CZTSSe films were assembled and characterized.

6.2 Experimental procedures

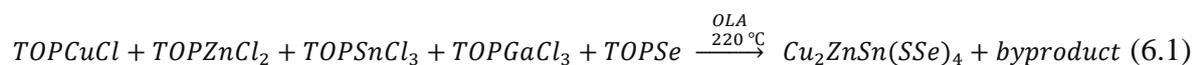
6.2.1 Chemicals and materials

Fluorine doped tin oxide (FTO) substrates, titanium oxide (TiO₂) from dyesol, oleylamine, liquid N₂, Ar, CuCl, ZnCl₂, SnCl₃, sulphur and selenium powders, mercapto-propionic acid (MPA), ethane dithiol (EDT), acetonitrile, toluene, pyridine, acetone, ethanol, tetrabutyl ammonium tetrafluoroborate (TBABF₄).

6.2.2 Synthesis of copper zinc tin sulphur selenide nanoparticles

6.2.2.1 Conventional colloidal method

The conventional colloidal method (CCM) consisted of preparing the metal selenide QDs using a three-neck flask connected to a Shlenck line under argon flowing gas. This was done following the reaction (6.1). Typically, in conventional colloidal method (CCM), 6 ml of oleylamine (OLA) was heated to 100 °C. Then 1 ml of 1.0 M solution of CuCl in OLA, 1.0 M of ZnCl₂ in OLA and 1.0 M of SnCl₃ in OLA were added to the solution. The resultant solution was then heated to 220 °C where 1 ml of 1.0 M solution of Se in OLA and 1 ml of 1M solution of sulphur were then added. The content was heated for a further 30 min. The temperature was then decreased to 60 °C. Ethanol was added to the solution to flocculate the copper zinc tin sulphur selenide (CZTSSe) nanoparticles which were collected after centrifugation.



6.2.2.2 Microwave assisted method

The microwave assisted method for CZTSSe was followed similarly to the reaction (6.1). This was done by adding 2 ml OLA solution of each 1.0 M CuCl, 1.0 M ZnCl₂, 1.0 M SnCl₃ to 5 ml of OLA in a Teflon vessel liner and mounted on the rotor. The content was purged with argon for 2 min prior to the microwave heating. The microwave was then heated for 10 min at a power of 500 W. The system was then cooled to 70 °C where 2 ml of each 1M of S and 1 M of Se in OLA were quickly added. The vessel was then purged for 5 min with argon before continuing heating the mixture for another 10 min at 600 W. The heating was stopped

and the microwave was allowed to cool to 50 °C. Methanol was added to the solution to flocculate the CZTSSe nanoparticles which were collected after centrifugation.

6.2.3 Thin film treatment and device assembly

The procedures for preparation of substrates and QDSSC device assembly using the untreated, MPA treated and EDT treated CZTSSe thin film are as described in sections 4.2.3 to 4.2.5 of Chapter 4. Here, CISe materials were replaced by CZTSSe. The Fig. 6.1 below shows the structure of the CZTSSe assembled device.

6.2.4 Characterization of the materials

The optical, structural and electrical properties of CZTSSe NPs were determined using the same characterization techniques described in section 4.2.6 of Chapter 4. However, CISe NPs were replaced by CZTSSe materials.

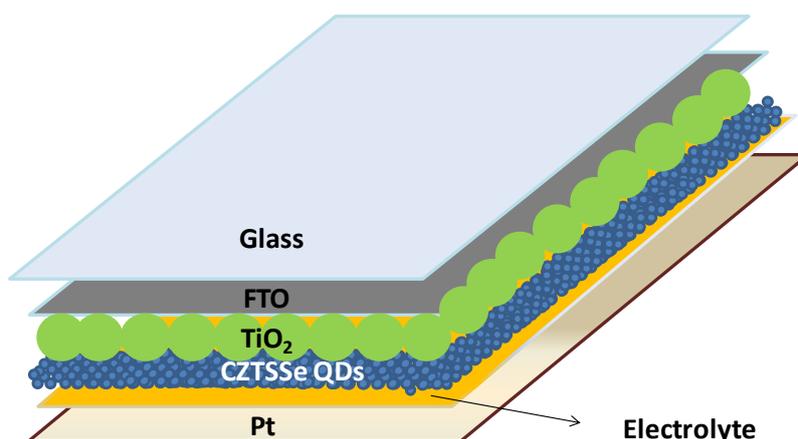


Fig. 6.1 CZTSSe QDSSC device setup

6.3 Results and discussion

6.3.1 Properties of MAM and CCM synthesized CZTSSe QDs

6.3.1.1 Optical properties of MAM and CCM synthesized CZTSSe QDs

The absorption and emission spectra of MAM and CCM synthesized CZTSSe nanoparticles are shown in Fig. 6.2 and Fig. 6.3 respectively. The optical parameters are shown in Table 6.1. The absorption band edges for MAM and CCM samples were at 460 and 450 nm respectively. Both MAM and CCM gave blue-shifted absorption band edges than the bulk CZTSSe located at 827 nm. This is indicative of the quantum confinement effect in both samples. The slight blue-shift of CCM than MAM is indicative of smaller sized particles

yielded from MAM. The MAM and CCM emission spectra had the same maximum peak at 532 nm but their FWHMs were 44 and 47 nm respectively. This is indicative of a narrow size distribution in both samples. The $(\alpha h\nu)^2/h\nu$ curves for the band gap energies of MAM and CCM CZTSSe nanoparticles are shown in Fig. A6.1 in appendix. The MAM and CCM synthesized nanoparticles possess higher energies than that of the bulk CZTSSe amounting to 1.51 eV. This is indicative of the confinement effect as equally proven by the absorption of both sample. The slight difference in optical properties of the two samples indicates that the same kind of materials was prepared by either MAM or CCM. A further characterization was done on the samples to determine their structures and to show whether this may help emphasizing on the optical properties.

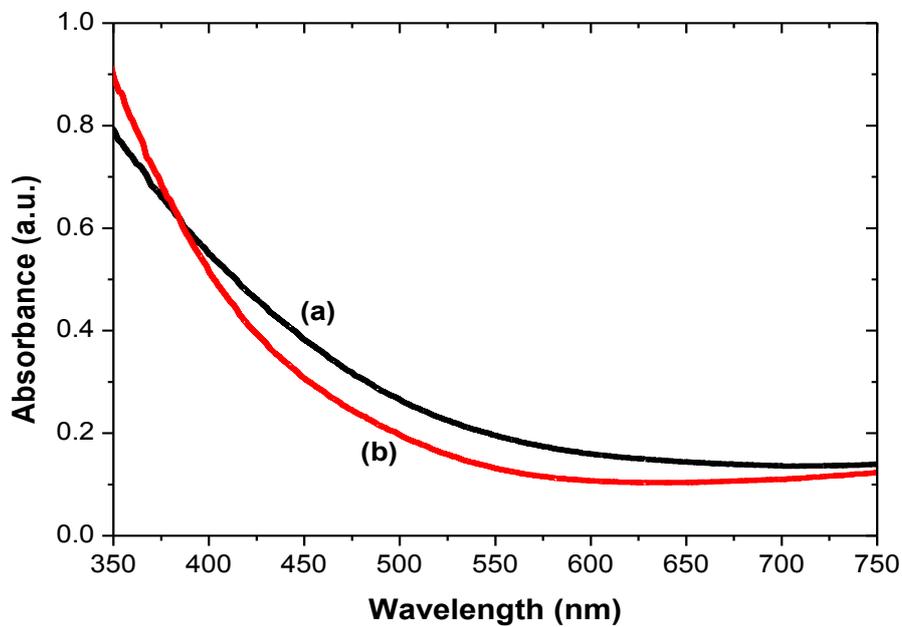


Fig. 6.2 Absorption spectra of CZTSSe NPs synthesized via (a) MAM and (b) CCM

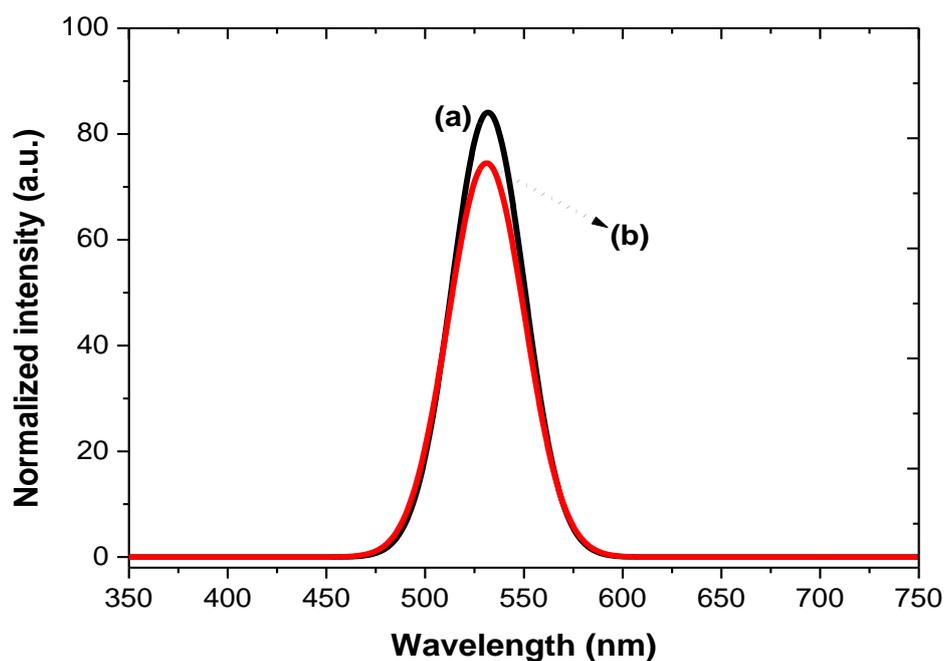


Fig. 6.3 Emission spectra of CZTSSe NPs synthesized via (a) MAM and (b) CCM

Table 6.1 Optical parameters of MAM and CCM synthesized CZTSSe

Method	Band edge (nm)	Emission (nm)	Stokes shift (nm)	FWHM (nm)
MAM	460	532	72	44
CCM	450	532	82	47
Bulk	827	-	-	-

6.3.1.2 Structural properties of MAM and CCM synthesized CZTSSe NPs

The XRD patterns of CZTSSe NPs synthesized via MAM and CCM are shown in Fig. 6.4. The diffraction peaks of both samples show indices corresponding to $\text{Cu}_2\text{ZnSn}(\text{SSe})_4$ of a hybrid tetragonal crystalline structure between CZTS (PDF 00260575) and CZTSe (PDF 000520868). The structural properties of synthesized CZTS and CZTSe nanoparticles including the diffraction patterns and TEM images are shown in Fig. A6.2 and Fig. A6.3 in the appendix. The CZTSSe synthesized via MAM gave more intense and defined diffraction peaks than the CCM. Thus the MAM synthesized CZTSSe nanoparticles were more crystalline.

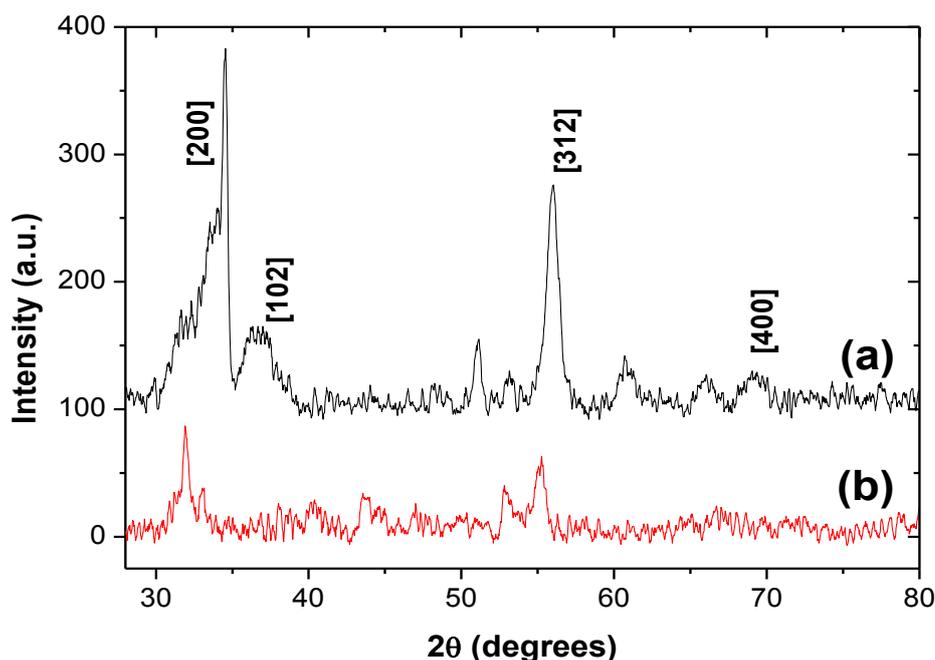


Fig. 6.4 XRD patterns CZTSSe powders prepared from (a) MAM and (b) CCM

The TEM images of MAM and CCM synthesized CZTSSe nanoparticles with their corresponding size distributions and the EDS spectrum are shown in Fig. 6.5. The EDS analysis proved that the synthesized nanoparticles are made of copper, zinc, tin, sulphur and selenium. The excess of copper detected here originated from the copper grid. The nanoparticles with hexagonal-like facets were identified in both samples but the particles from CCM were slightly more monodispersed with a standard deviation of 0.216 nm compared to those from MAM which possessed a standard deviation of 0.259 nm. The synthesized chalcogenides had the average sizes of 10.09 nm and 8.86 nm for MAM and CCM respectively. This is in agreement with the optical properties observed earlier. Generally the properties of CZTSSe nanoparticles were similar in both MAM and CCM. However XRD findings result in the usage of the MAM synthesized CZTSSe nanoparticles for fabrication of the QDSSC devices.

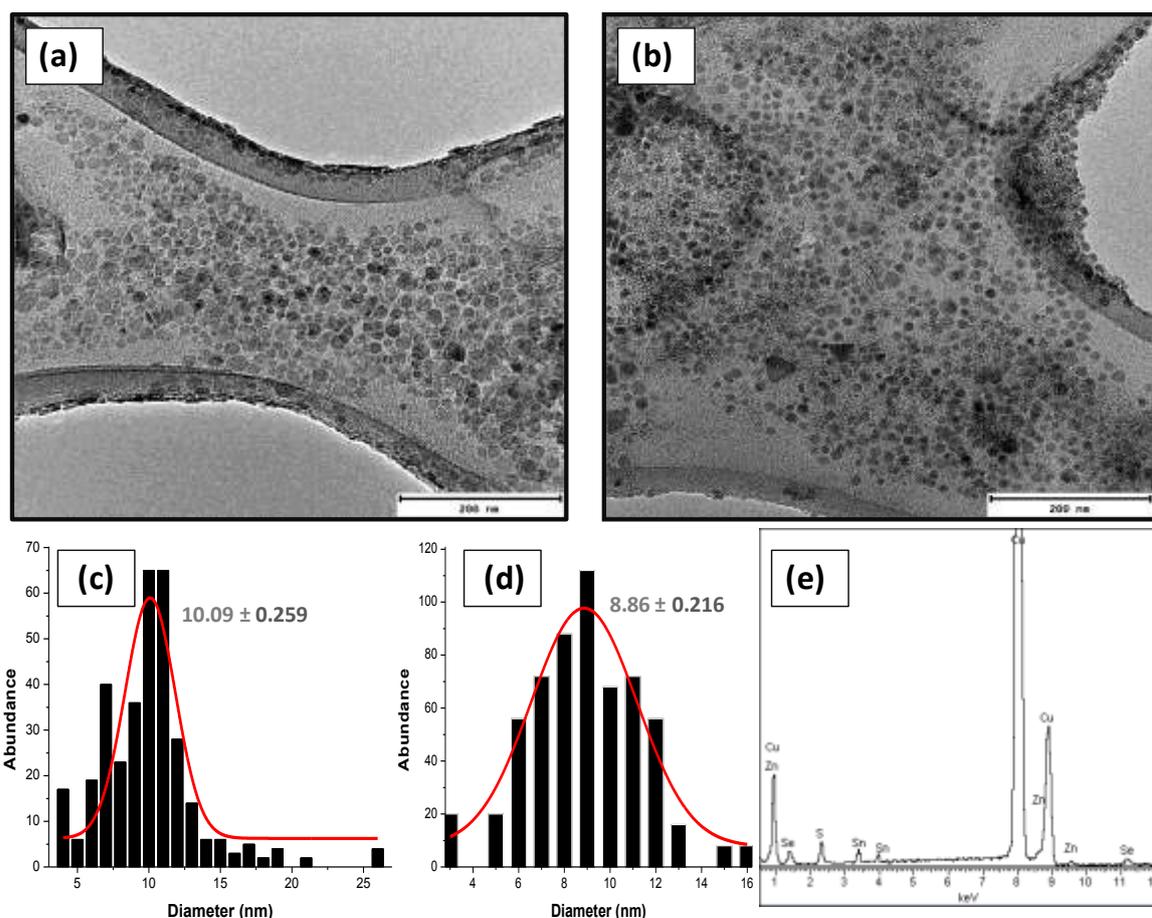


Fig. 6.5 TEM images of (a) MAM and (b) CCM synthesized CZTSSe NPs and their corresponding size distributions (c) and (d) respectively; with (e) the EDS spectrum confirming the elements of CZTSSe NPs.

6.3.2 Cyclic voltammetry of CZTSSe thin film

The CZTSSe QD solutions were prepared by dispersing 5 mg of CZTSSe NPs in 1 ml of toluene. The details of the CV procedure are shown in the experimental section. Fig. 6.6 shows the voltammogram obtained (with depicted oxidation and reduction energies) and the energy levels related to the assembled QDSSC. Table 6.2 shows the values of energy levels and band gap energies of synthesized CZTSSe QDs. The CV gave a the conduction band level at 3.61 eV which is higher than that of TiO₂ confirming that the active layer made of CZTSSe could transfer electron to the electrode. The band gap energy of CZTSSe film was 1.72 eV, which is about 0.21 eV higher than that of the bulk material. This clearly indicates a very large blue shift as confirmed by the absorption band edge found from UV-Vis-NIR

spectrum of the solution and thin film of CZTSSe QDs. This energy is also indicative of a quantum confinement effect that was also attributed to the small size, way less than that of the Bohr radius (10 nm or the diameter of 20 nm). Cao *et al.* [21] employed chemical bath deposition CBD and sulfurization treatment to prepare CZTS thin films that exhibited a band gap of 1.48 eV. The ZnO:Al CdS/CZTS/Mo/glass layered device gave a PCE of 0.30%. Although the homogeneity of the film of deposited QDs can also have an impact on the device performance, the energy in the device setup may signify that upon absorption of photon, electrons could be excited but their transfer into a wide band gap material TiO₂ (about 3.0 eV), was being slowed because the electrons may have been trapped in high energy CZTSSe layer instead of moving into TiO₂. Other authors also reported similar findings [1, 22-23]. The band gaps and energy levels are vital parameters for the device design and material selection. Despite the limited accuracy, CV measurements are regarded as a useful and relatively easy tool to measure the absolute position of energy levels. For ternary and quaternary QDs there is discrepancy in the absolute position of the energy levels measured by different groups. Generally, the problem is the low current intensity of the nanocrystal systems, which is comparable to the noise originating from the electrolyte. This may also be attributed to an influence of the stabilizing ligands on the charge injection process between the nanocrystals and the working electrode [24, 25]. Some authors have reported the deviation of energy levels as function of the composition and crystallographic structure of synthesized particles [1, 4, 26].

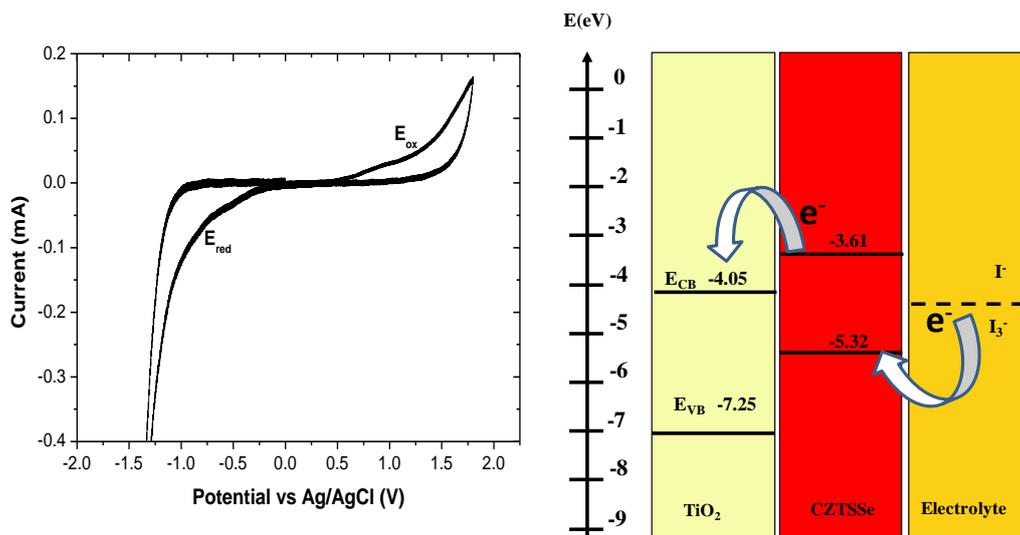


Fig. 6.6 CV and energy levels of CZTSSe QD solution deposited onto FTO substrate

Table 6.2 Homo-Lumo and BG approximations of CZTSSe from CV

QDs	E_{ox} (V)	E_{red} (V)	E_{Homo} (eV)	E_{Lumo} (eV)	Approx. BG (eV)	QD size (nm)
CZTSSe	0.92	-0.79	5.32	3.61	1.71	8

6.3.3 The effects of EDT and MPA treatments on the electrical properties of CZTSSe QDSSC devices.

The MPA and EDT treatments were performed at the interface of TiO₂ and CZTSe layers in order to increase the adhesion of synthesized CZTSSe QDs onto TiO₂ surface. Fig. 6.7 shows the J-V curves of devices treated with MPA and EDT versus the untreated one. The J-V curves from the dark current allowed confirming the photovoltaic activities of the QDSSC devices as per photogenerated current upon illumination. Table 6.3 shows the electrical properties extracted from the J-V curves. The short circuit current density improved from 85 to 258 $\mu\text{A cm}^{-2}$, respectively from untreated to treated devices demonstrating that devices assembled via treatment of TiO₂ and active layers with EDT and MPA affected the optical and electrical properties. However the higher short circuit voltage of 395 mV was only found in the untreated device. Although the overall efficiency of the device could slightly increase from 0.013 to 0.021%, the fill factor was not affected considerably by MPA or EDT treatment on the device. This can either be related to the differences in the QDs surface such as traps and defects or to the interaction of CZTSSe with the TiO₂ particles. The high absorption observed from UV-Vis spectra together with the size of CZTSSe QDs as measured from TEM images, the quality of the film and the interface CZTSSe QDs-TiO₂ layers could also be the main factors related to the electrical properties of devices. However, the low current densities were indicative of a poor interaction of MPA or EDT with the CZTSSe QDs. On one hand MPA molecules attached to TiO₂ may not be properly linked to QDs due to un eased interaction of QDs. Furthermore, the exchange of the adsorbed ligands can mainly be attributed to the minimum effect of carboxylic group strongly adsorbed onto CZTSSe surface after synthesis rather than that of thiol group found in MPA structure. On the other hand, the double thiol functional groups in EDT or structure may not effectively allow the attachment of EDT from TiO₂ surface to the QD. Steinhagen *et al.* [1] prepared CZTS sizing 7.7-13.5 nm and used ZnO instead of TiO₂ in the device without any linker treatment. A CdS layer was established between CZTS and ITO and the assembled device had the J_{sc},

Voc, FF, and PCE of 1.92 mA cm^{-2} , 321 mV, 37% and 0.23% respectively under AM 1.5 conditions. TiO_2 used in our work may possess good mechanical properties and good crystalline phase that can be compatible with the deposition of QDs due to structure orientation acting as template to accommodate the attachment of QDs. The small currents measured here were attributed to the structure of the QDs, the contact at the interface QD- TiO_2 , the energy generated in the QDs as absorbing layer, the impact of trapped electron in the absorbing layer. Similar findings have been discussed in Chapter 4 and 5. While pyridine seemed to affect the action of EDT as ligands on the surface of CZTSSe the electron could not be easily transferred from the photon absorbing layer to the wide band gap electron accepting material. Thus, the electron transport to FTO electrode was compromised. The concentration of MPA, time for MPA treatment and that of dip-coating in quantum dot solution in order to surpass the FF currently found in this work are parameters to further investigate. The electrolyte can also play a role in electrical properties of the assembled devices. Thus the investigation of other electrolytes beside I^-/I_3^- may be another alternative in improving the performances of the device. The composition of the synthesized materials would be of great role in the device assembly and our materials seemed to be copper rich as per ratio $\text{Cu}/(\text{Zn}+\text{Sn})$ since our initial target was to synthesize $\text{Cu}_2\text{ZnSn}(\text{SSe})_4$. This was investigated by several authors who even buffered the QDs to decrease copper content. Carter *et al.* [26] prepared CZTSSe by selenisation of synthesized CZTS nanoparticles with hexanethiol and Se pellets. The $\text{Cu}/(\text{Zn}+\text{Sn})$ ratio was investigated and CZTSSe was buffered with a CdS layer. About 8% PCE was achieved from the assembled device. Guo *et al.* [27] synthesized CZTS which was alloyed with Ge and $\text{Cu}_{1.64}\text{Zn}_{1.25}\text{Sn}_{0.75}\text{Ge}_{0.25}\text{S}_4$ film in which $\text{Cu}/(\text{Zn}+\text{Sn})$ ratio was 0.82 was then selenized under Se vapour. The CZTGSSe film obtained was buffered with CdS in the device assembly. The device was without any anti-reflection coating and gave a PCE of 8.5%.

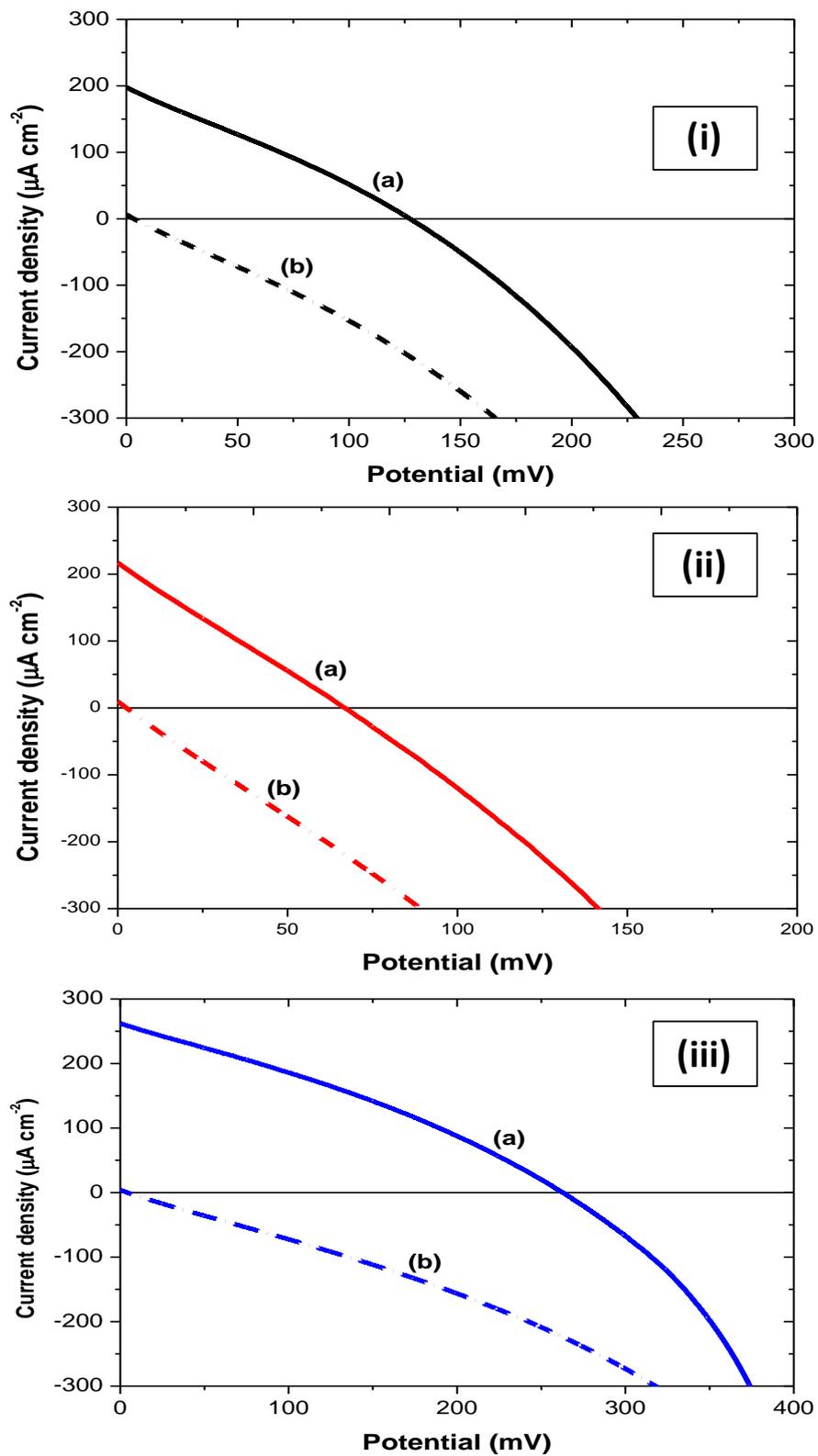


Fig. 6.7 J-V curves obtained from (i) untreated, (ii) MPA and (iii) EDT treated CZTSSe films for QDSSC devices under (a) illumination with white light and (b) dark current

Table 6.3 Electrical properties of CZTSSe devices

CZTSSe film	Jsc (μAcm^{-2})	Voc (mV)	FF (%)	PCE (%)
Untreated	85	395	36	0.013
MPA-treated	195	211	38	0.016
EDT-treated	258	262	31	0.021

6.4 Conclusions

The CCM and MAM were successfully employed in the synthesis of copper zinc tin selenide nanoparticles. Similar properties were observed in both CCM and MAM. Highly monodispersed 9-10 nm sized of nearly hexagonal CZTSSe possessing the blue-shifted absorption band edges of 450-460 nm were obtained from CCM and MAM. The particles had a tetragonal crystalline phase but the MAM synthesized CZTSSe QDs possessed a higher degree of crystallinity. A thin film was therefore made from the MAM synthesized nanoparticles and was later used in QDSSC devices. The energy levels revealed that the QDs had a quantum confinement effect with a large blue-shifted energy of about 0.21 eV from their bulk materials. The application of QDs in the devices as QDSSCs successfully confirmed that QDs can absorb photons and the assembled device had photovoltaic performances. However, relatively low Jsc (up to $258 \mu\text{A cm}^{-2}$) and Voc (up to 395 mV) were obtained here. While the type of QDs affected the device setup as shown from the synthesized CZTSSe QDs, their thin film treatment with EDT and MPA together with the TiO_2 film may lead to a better device assembly for more efficient solar cells.

6.5 References

- [1] Steinhagen, C., Panthani, M.G., Akhavan, V., Goodfellow, B., Koo, B. and Korgel, B.A. (2009). *J. Am. Chem. Soc.* 131, 12554-12555.
- [2] Dai, P.C., Zhang, G., Chen, Y.C., Jiang, H., Feng, Z.Y., Lin, Z.J. and Zhan, J.H. (2012). *Chem. Commun.* 48, 3006.

- [3] Wang, K., Gunawan, O., Todorov, T., Shin, B., Chey, S., Bojarczuk, N., Mitzi, D. and Guha, S. (2010). *Appl. Phys. Lett.* 97,143508.
- [4] Wadia, C., Alivisatos, A.P. and Kammen, D. M. (2009). *Environ. Sci. Technol.* 43, CG2072.
- [5] Katagiri, H., Jimbo, K., Maw, W. S., Oishi, K., Yamazaki, M. H., Araki, H. and Takeuchi, A. (2009). *Thin Solid Films* 517, 2455.
- [6] Lechner, R., Jost, S., Palm, J., Gowtham, M., Sorin, F., Louis, B., Yoo, H., Wibowo, R.A. and Hock, R. (2013). *Thin Solid Films* 535, 5-9.
- [7] Torodov, T.K., Reuter, K.B., Mitzi, D.B. (2010). *Adv. Mater.* 22, E156-E159.
- [8] Blackburn, J.L., Selmarten, D.C. and Nozi, A.J. (2003). *J. Phys. Chem. B* 107, 14154.
- [9] Boix, P.P., Larramona, G., Jacob, A., Delatouche, B., Mora-Seró, I. and Bisquert, J. (2012). *J. Phys. Chem. C* 116, 1579.
- [10] Shen, Q., Kobayashi, J., Diguna, L.J. and Toyoda, T. (2008). *J. Appl. Phys.* 103, 084304.
- [11] Pernik, D.R., Tvrđy, K., Radich, J.G. and Kamat, P.V. (2011). *J. Phys. Chem. C* 115, 13511.
- [12] Gorer, S. and Hodes, G. (1994). *J. Phys. Chem.* 98, 5338.
- [13] Santra, P.K. and Kamat, P.V. (2012). *J. Am. Chem. Soc.* 134, 2508.
- [14] Gratzel, M. (2003). *J. Photochem. Photobiol. C* 4, 145-153.
- [15] Hagfeldt, A., Boschloo, G.B., Sun, L.C, Kloo, L. and Pettersson, H. (2010). *Chem. Rev.* 110, 6595-6663.

- [16] Lee, Y. L. and Lo, Y. S. (2009). *Adv. Funct. Mater.* 19, 604.
- [17] Rühle, S., Shalom, M. and Zaban, A. (2010). *Chem. Phys.Chem.* 11, 2290.
- [18] Mora-Seró, I. and Bisquert, J. (2010). *J. Phys. Chem. Lett.*1, 3046.
- [19] Genovese, M.P., Lightcap, I.V. and Kamat, P.V. (2012). *ACS Nano* 6, 865.
- [20] Zhua, L., Qianga, Y.H., Zhaoa, Y.L. and Guaa, X.Q. (2014). *Applied Surface Science* 292, 55-62.
- [21] Cao, M., Li, L., Zhang, B.L., Huang, J., Wang, L.J., Shen, Y., Sunb, Y., Jiang, J.C., Hub, G.J. (2013). *Solar Energy Materials & Solar Cells*117, 81-86.
- [22] Ulbricht, R., Pijpers, J.H., Groeneveld, E., Koole, R., Donega, C.M., Vanmaekelbergh, D., Delerue, C., Allan, G. and Bonn, M. (2012). *Nano Lett.*12, 4937-4942.
- [23] Pernik, D.R., Tvrdy, K., Radich J.G. and Kamat, P.V.(2011). *J. Phys. Chem. C* 115, 13511.
- [24] Radychev, N., Scheunemann, D., Kruszynska, M., Frevert, K., Miranti, R., Kolny-Olesiak, J., Borchert, H. and Parisi.J. (2012). *Org. Electron.*13, 3154-3164.
- [25] Aldakov, D., Lefrançois, A., and Reiss, P. (2013). *J. Mater. Chem. C* 1, 3756-3776.
- [26] Carter, N.J. Yang, W.C., Miskin, C.K., Hages, C.J., Stach, E.A. and Agrawal, R. (2014). *Solar Energy Materials & Solar Cells* 123 189-196.
- [27] Guo, Q., Ford, G.M., Yang, W.C., Hages, C.J., Hillhouse, H.W. and Agrawal, R. (2012). *Solar Energy Materials & Solar Cells* 105 132-136.

CHAPTER 7:

GENERAL CONCLUSIONS AND RECOMMENDATIONS

7.1 Conclusions

7.1.1 Synthesis and characterization of Cu_xSe , CISE, CIGSe and CZTSSe NPs

Copper chalcogenide quantum dots were successfully synthesized via CCM and MAM. Several parameters affecting the synthesis of the quantum dots were investigated. This includes the kinetics (reaction times), temperature, solvent and precursors. The methods were optimized to obtain particles with desired properties for their applications in various devices. The synthesis of copper selenide (Cu_xSe) nanocrystals was used as a template from which other multinary quantum dots were prepared. The nanocrystals with dominant defined crystalline phases were obtained from the syntheses of copper chalcogenide nanocrystals. Nearly hexagonal shaped copper selenide nanocrystals with less than 9 nm diameter were found in cubic and hexagonal crystalline phases. The particles had a large blue-shifted absorption band edge. The MAM particles were less polydispersed and distinctively crystallized in single cubic Cu_2Se phase. However, the CCM synthesized copper selenide nanoparticles were smaller than those from the MAM sample. The CCM synthesis was optimized at 220 °C for 30 min with Cu/Se ratio of 1:1 using OLA.

The copper indium selenide (CISE) nanoparticles synthesized via MAM and CCM had blue-shifted absorption band edges and possessed nearly hexagonal and spherical facets of less than 9 nm in diameter. The synthesized ternary chalcogenides crystallized in tetragonal orientation. The MAM showed defined crystals with lattices of copper-rich material slightly deviating from those of CuInSe_2 tetragonal phase. The CCM synthesized CISE in OLA using uncapped precursors at 220 °C for 30 min showed better properties and were thus employed as active layer in devices.

The copper indium gallium selenide (CIGSe) nanoparticles synthesized via MAM and CCM had an average diameter of less than 20 nm and possessed blue-shifted absorption band edges. The particles with hexagonal-like facets were observed and crystallized in tetragonal phase. The addition of indium to copper selenide synthesis allowed the change in morphology and crystalline orientation. Nevertheless, the nanocrystals still had better optical properties than their bulk materials. A further addition of gallium for synthesis of the quaternary copper

indium gallium selenide brought more complexity in stoichiometry modulation. The stoichiometric $\text{CuIn}_{0.75}\text{Ga}_{0.25}\text{Se}_2$ synthesized via CCM using OLA showed less polydispersivity and possessed a blue-shift in absorption band edge than the stoichiometric $\text{CuIn}_{0.5}\text{Ga}_{0.5}\text{Se}_2$ and $\text{CuIn}_{0.25}\text{Ga}_{0.75}\text{Se}_2$ NPs. The synthesized $\text{CuIn}_{0.75}\text{Ga}_{0.25}\text{Se}_2$ NPs had an average diameter of 6.5 nm and were highly crystalline.

Copper zinc tin sulphide selenide (CZTSSe) NPs were also successfully prepared via MAM and CCM. Both MAM and CCM synthesized CZTSSe NPs gave similar properties. The NPs with blue-shifted absorption band edges and hexagonal-like shapes were oriented in tetragonal crystalline phase. However, the quinary chalcogenide NPs prepared from MAM were more crystalline than those from CCM.

7.1.2 Devices fabricated from Cu_xSe , CISE, CIGSe and CZTSSe NPs

The evidence of photovoltaic effect was demonstrated in the Schottky device and quantum dot sensitized solar cells fabricated with the synthesized nanocrystals from which higher band gap energies were approximated in their solutions or in thin films. The Schottky device was made of MAM synthesized copper selenide NPs. The electrical parameters extracted from the J-V curve were used to determine the diode parameters following the Cheung's modification theory. The ideality factor, barrier height and series resistance of 1.04, 2.59×10^{-3} eV and 0.870 respectively were found. The device characteristics indicated that the synthesized copper selenide can be used in heterojunction cells. Quantum dot sensitized solar cells were successfully fabricated using copper indium selenide, copper indium gallium selenide and copper zinc tin sulphur selenide nanocrystals. In CISE QDSSC devices, EDT treatment of the thin film improved the device performance. The maxima of J_{sc} , V_{oc} and FF of $324 \mu\text{A cm}^{-2}$, 487 mV and 43% were determined. The untreated CIGSe QDSSC device had the J_{sc} , V_{oc} and FF of $168 \mu\text{A cm}^{-2}$, 162 mV and 33% respectively. The MPA and EDT treatments did not improve the performance of the CZTSSe device under our working conditions. The J_{sc} , V_{oc} and FF had their maxima at $258 \mu\text{A cm}^{-2}$, 395 mV and 38% respectively. Several parameters including the nanocrystals film formation, capping ligand, interaction between the nanocrystals and the wide band gap electron accepting material can affect the performance of the device. Relatively low current densities were obtained from the devices leading to low power conversion efficiencies. The ligand exchange using shorter chain ligands showed improvement of the device performance although further optimizations still need to be done.

7.2 Recommendations

The suggestions for future work can include several topics as from preparation of the metal chalcogenide nanocrystals to various applications. A further optimization to prepare the semiconducting nanocrystals with other shapes and in narrower size distribution can allow a facile modulation in assembling the devices. More study of dark current on assembled devices should be done for further explanation of nanocrystal properties and the electrical behaviour of the cells. The choice of the electron accepting layer in relation to the determined energy gap of the QDs can play a vital role in improving the electrical properties of the QDSSC devices. The modulation of charge generation, the other film deposition methods and the treatment of nanocrystal film such as annealing should be explored for enhancement of any device performance. The possibilities of using the copper chalcogenide QDs in other types of solar cells can then be explored.

APPENDIX

Band gap approximation from the energy curves

The band gap energy is proportional to the absorption of the material as per equation (A.1) below in which α is the absorbance, h is the Planck's constant, ν is the incident light frequency, A is a constant, E_g is the energy gap of the material and m is a index relating to the electronic transition involved in the absorption. For direct transition of materials as the case of the synthesized QDs, m is equal to $\frac{1}{2}$, leading to equation (A.2) then (A.3). A Plot of $(\alpha h\nu)^2$ versus $h\nu$ gives the energy curve from which a straight line is extrapolated to $h\nu$ axis to read E_g .

$$\alpha h\nu = A (h\nu - E_g)^m \quad (\text{A.1})$$

$$\alpha h\nu = A (h\nu - E_g)^{1/2} \quad (\text{A.2})$$

$$(\alpha h\nu)^2 = A (h\nu - E_g) \quad (\text{A.3})$$

Chapter 3

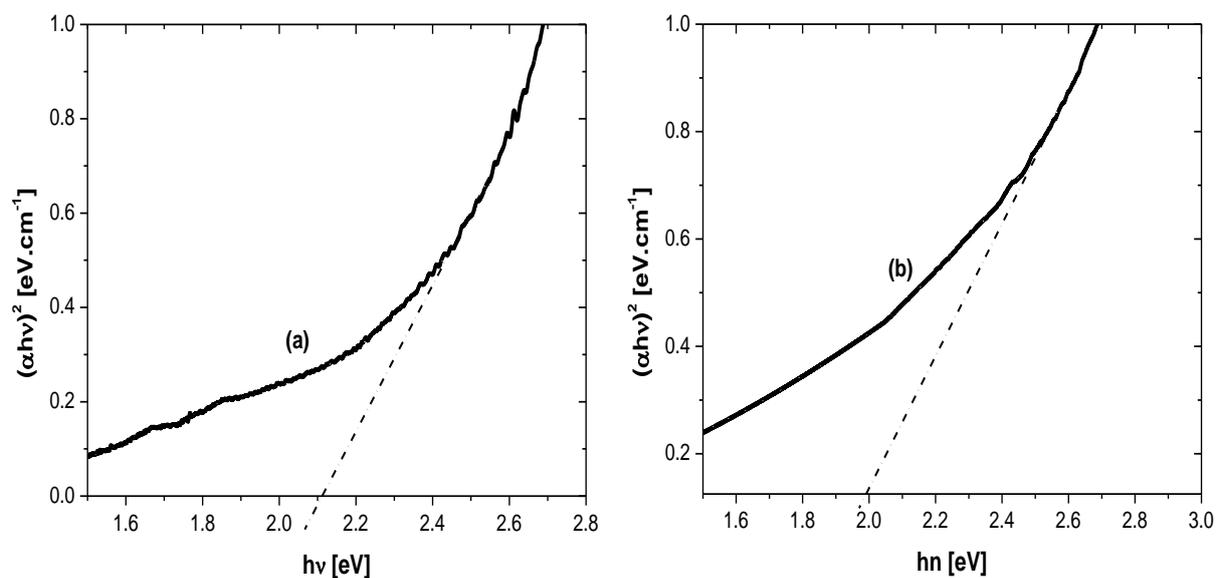


Fig. A3.1 Energy curves of Cu_xSe NPs synthesized via (a) CCM and (b) MAM. The approximated energy gaps of CCM and MAM samples were 2.1 and 2.0 eV respectively.

Chapter 4

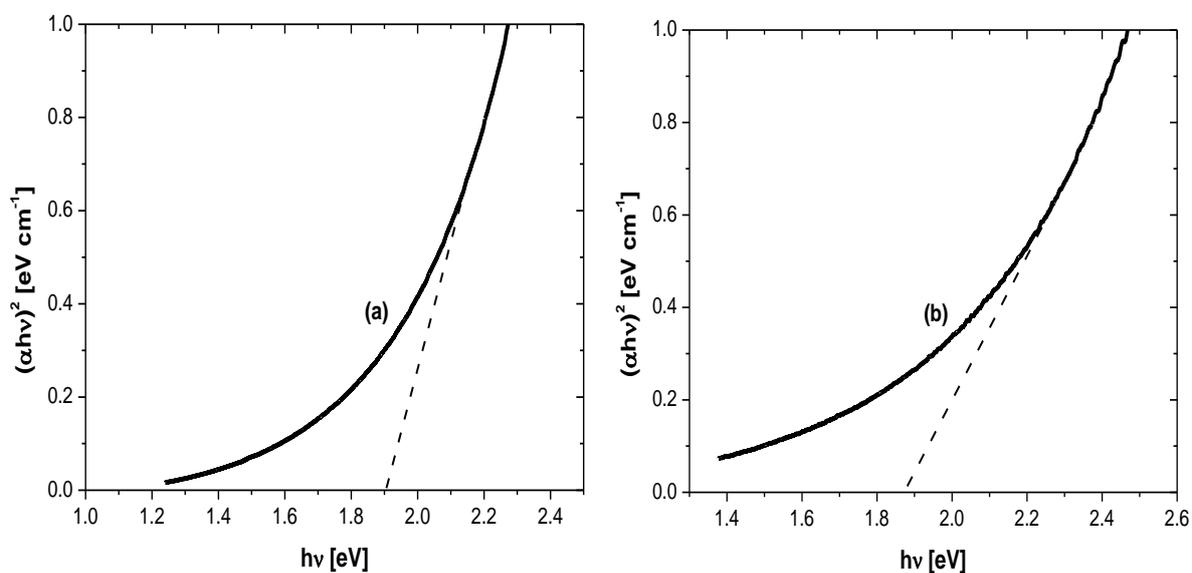


Fig. A4.1 Energy curves of CISE NPs synthesized via (a) CCM and (b) MAM. The band gap energy was estimated at 1.9 eV for both samples.

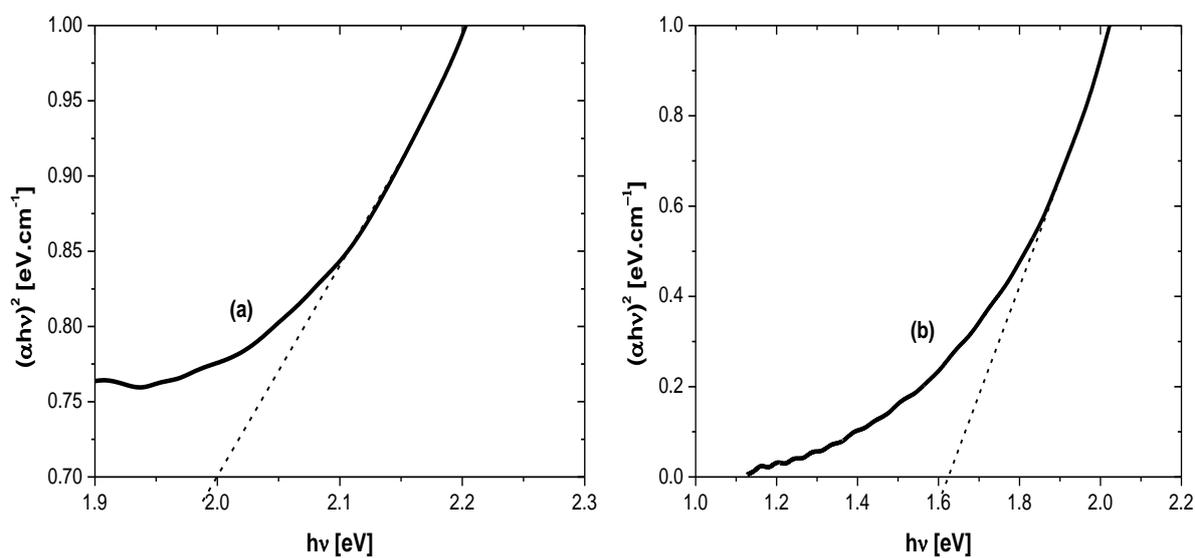


Fig. A4.2 Energy curves of CCM synthesized CISE NPs using (a) uncapped and (b) TOP-capped precursors. The band gap energies were approximated at (a) 2.0 eV and (b) 1.9 eV which were higher than that of the bulk CISE located at 1.05 eV

A.4.1 Structural properties of CISE NPs synthesized at 180 °C, 220 °C and 320 °C

The powder X-ray diffraction patterns (Fig. A4.3) matched well with the tetragonal unit cell of CuInSe_2 (PDF number 01-079-2208) and. The Miller indices of the particles are shown next to the major peaks. It can be noticed that the 220 and 122 peak frequencies were related to the synthesis temperature. The intensity of the peak assigned 220 Miller index decreased from increase in temperature of 180 to 220 °C while the 122 peak follow the opposite trend. This confirmed that copper rich material was obtained with synthesis of CISE at 180 °C from uncapped metal precursors. Increasing the temperature to 220 °C favours the yield of copper poor (indium rich) nanoparticles. However a further temperature increase (to 320 °C) tends to stabilize the ratio of Cu and In. However, Se seemed to provoke the formation of secondary products such as copper selenium and indium selenium as seen from the diffraction patterns. The increase of 422 peak intensity in CISE synthesized at 320 °C was just linked to the all pattern change in frequency. The broadness of the 320 °C synthesized CISE crystals showed that the particle size was larger than those from synthesis at 180 or 220 °C. Furthermore, the diffraction peaks of the 320 °C sample showed some shoulders suggesting that the particles lost their shapes.

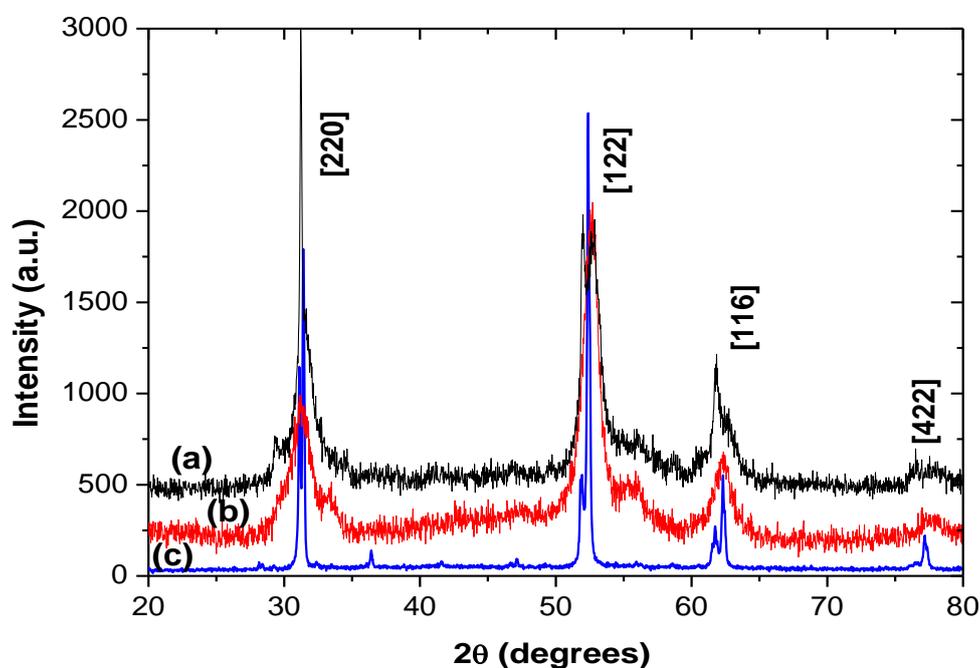


Fig. A4.3 The XRD patterns of CuInSe_2 NPs synthesized at (a) 180, (b) 220, and (c) 320 °C

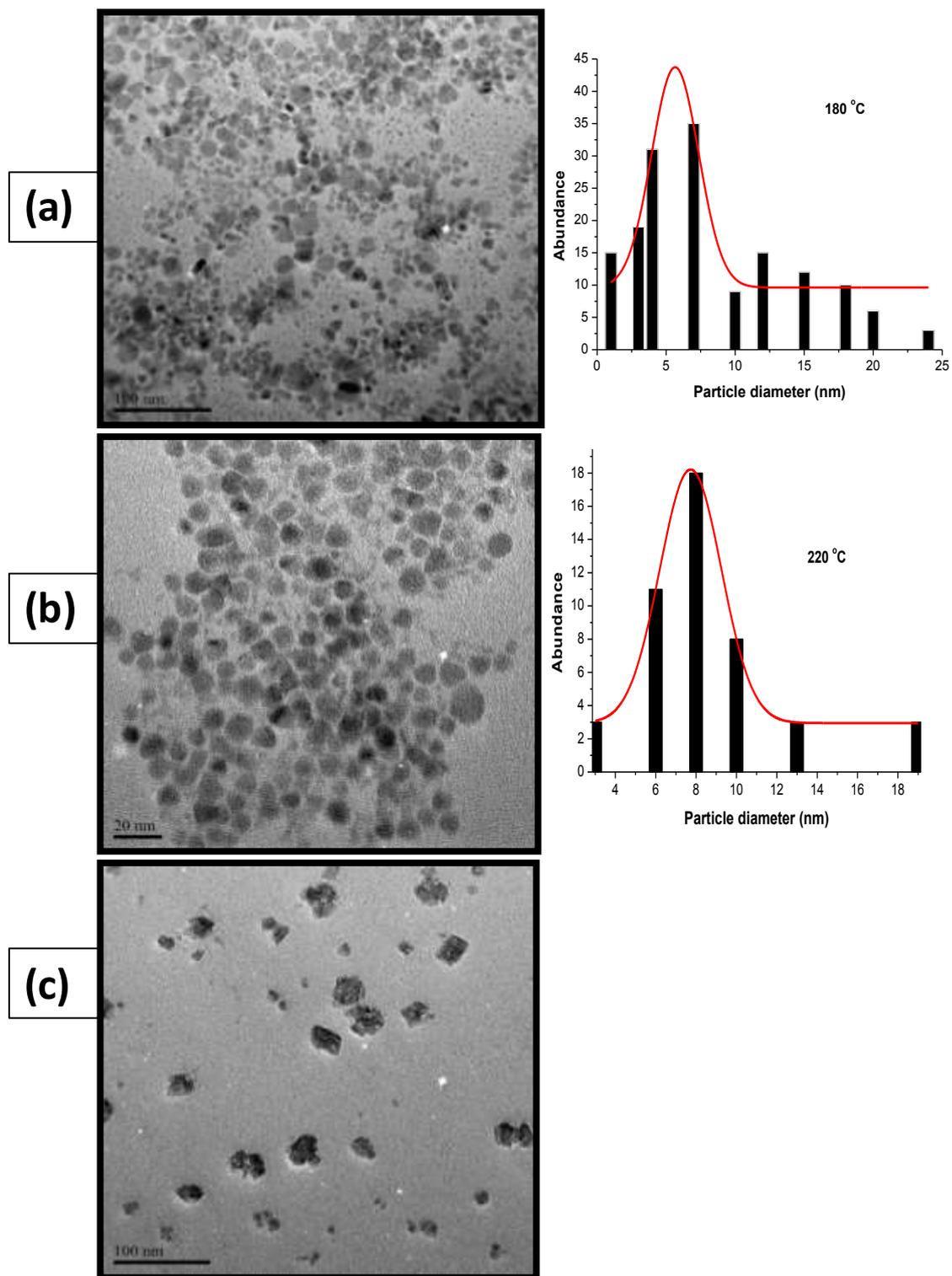


Fig. A4.4 TEM images of CISE nanoparticles synthesized at (a) 180, (b) 220 and (c) 320 °C and their corresponding size distributions. The size distribution of nanoparticles at 320 °C was not determined due to aggregation.

The TEM images showed the size and shape of the synthesized particles at 180, 220 and 320 °C. Fig. A4.4(a) and (b) showed the size distribution of the particles quoted above except from those of 320 °C since it was difficult to measure their individual length. The calculated average particle sizes are shown in Table A4.1. The distribution showed that similar shapes and sizes of particles with 220 °C synthesis. The image of the particles synthesized at 180 °C showed a higher polydispersivity and a wide size distribution was observed although the average size was about 5.7 nm, smaller than the average size of nanoparticles from other temperatures of synthesis. This was in agreement with the more blue-shifted absorption band-edge. The particles synthesized at 220 °C showed a rather well dispersed sample with a narrower distribution leading to the average particle size of 7.7 nm. The bigger size of 220 °C synthesized particles compared to those at 180 °C was consistent with findings from our investigations for the optical properties. The synthesized particles at 320 °C seemed to be attaching to each other forming larger particles as agglomerations which contributed to disguised behaviours encountered in their absorption and emission spectra.

Table A4.1 Temperature effect on the size of synthesized CISE nanoparticle

Temperature (°C)	Average particle size (nm)
180	5.71
220	7.73
320	-

Chapter 5

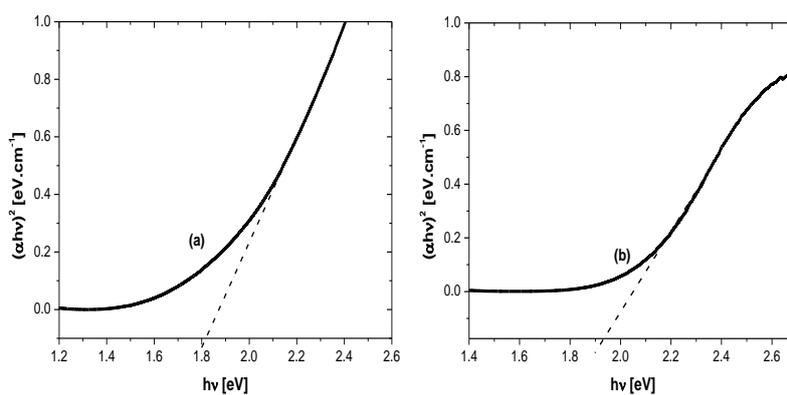


Fig. A5.1 Energy curves of CIGSe NPs synthesized via (a) MAM and (b) CCM. Higher band gap energies were estimated in both samples via their energy curves. The band gap energies of MAM and CCM samples were 1.82 and 1.93 eV respectively. They are higher than the bulk CIGSe (1.04-1.70 eV).

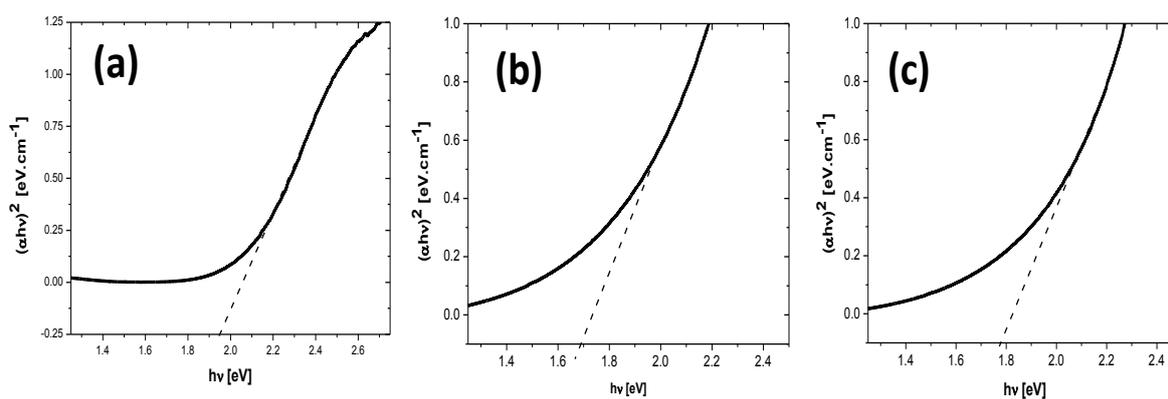


Fig. A5.2 Energy curves of CIGSe synthesized in HDA with In/Ga ratios of (a) 1:1, (b) 1:3 and (c) 3:1. Their corresponding band gaps were 1.93, 1.70 and 1.78 eV respectively.

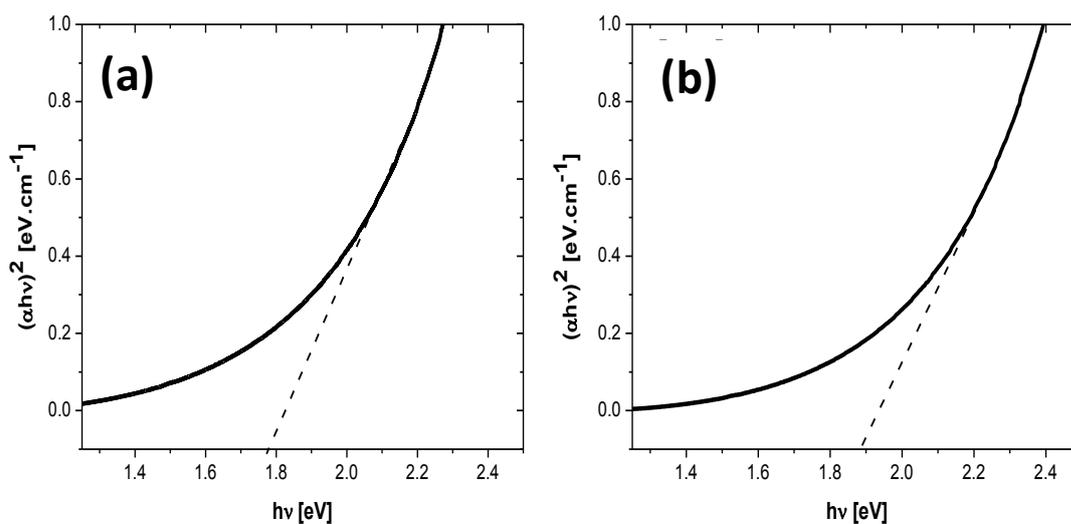


Fig. A5.3 Energy curves of CCM CIGSe synthesized CIGSe using (a) HDA and (b) OLA. Their energies were 1.78 and 1.88 eV respectively.

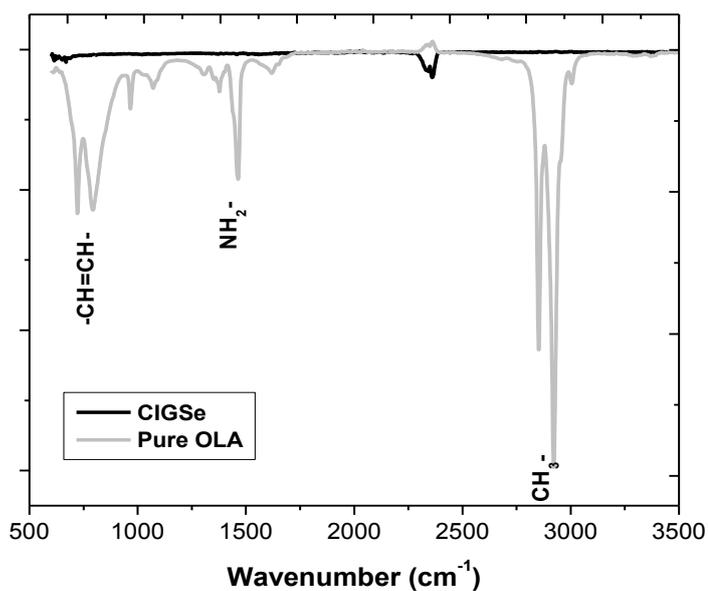


Fig. A5.4 FT-IR spectra of pure OLA and $\text{CuIn}_{0.75}\text{Ga}_{0.25}\text{Se}_2$ NPs synthesized with OLA. No major peaks corresponding to functional groups or carbon-carbon bond from OLA were found in the synthesized CIGSe material.

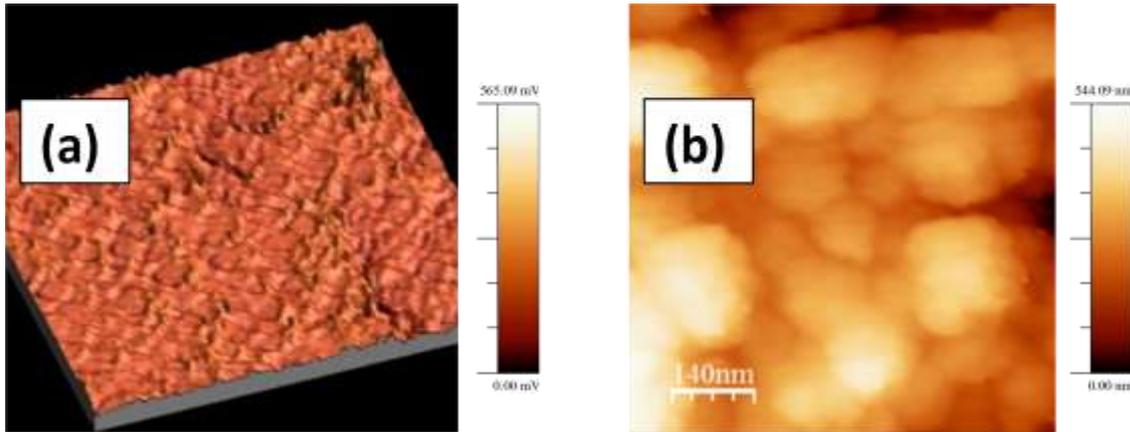


Fig. A5.5 AFM images of CIGSe thin film spin-coated onto substrate. The CIGSe film had a roughness not consistent throughout the entire surface and the CIGSe particles could be found agglomerated. The film was formed by larger building blocks of CIGSe particles deposited on top of one another as shown in (b) and thus creating more grain boundaries that influenced the charge recombination within the device.

Chapter 6

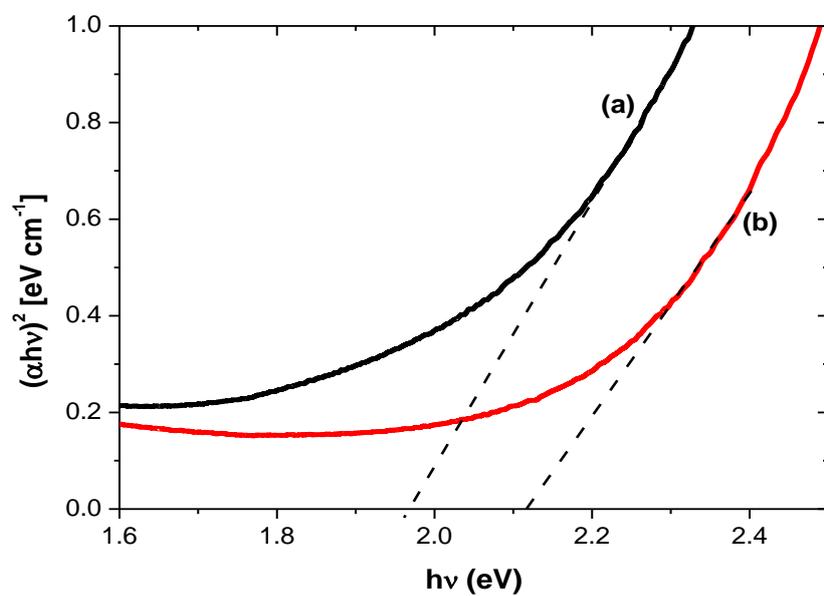
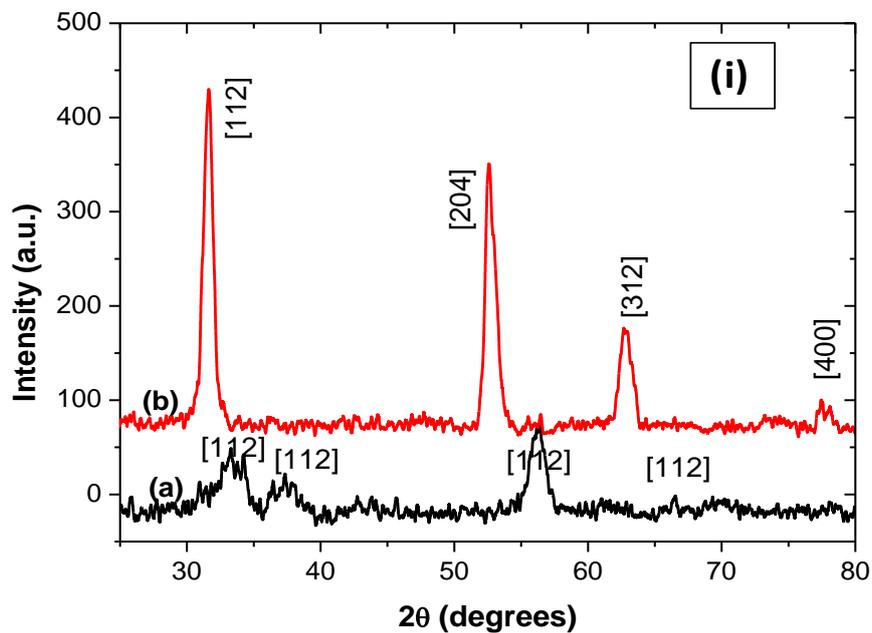


Fig. A6.1 Energy curves of (a) MAM and (b) CCM synthesized CZTSSe NPs



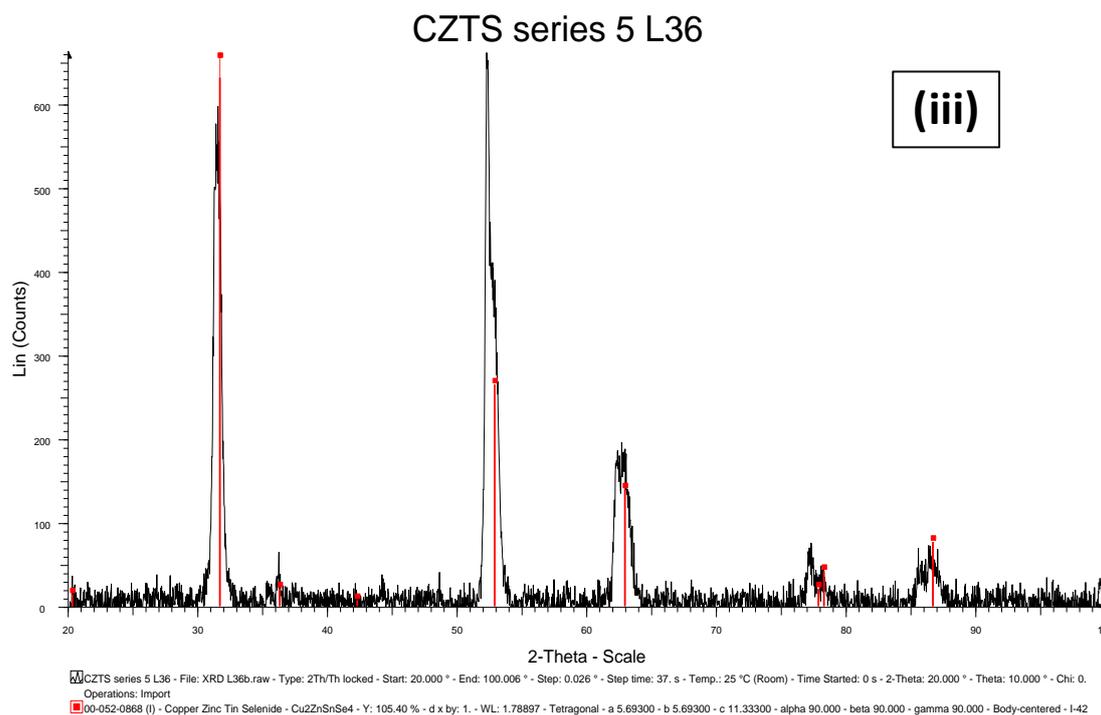
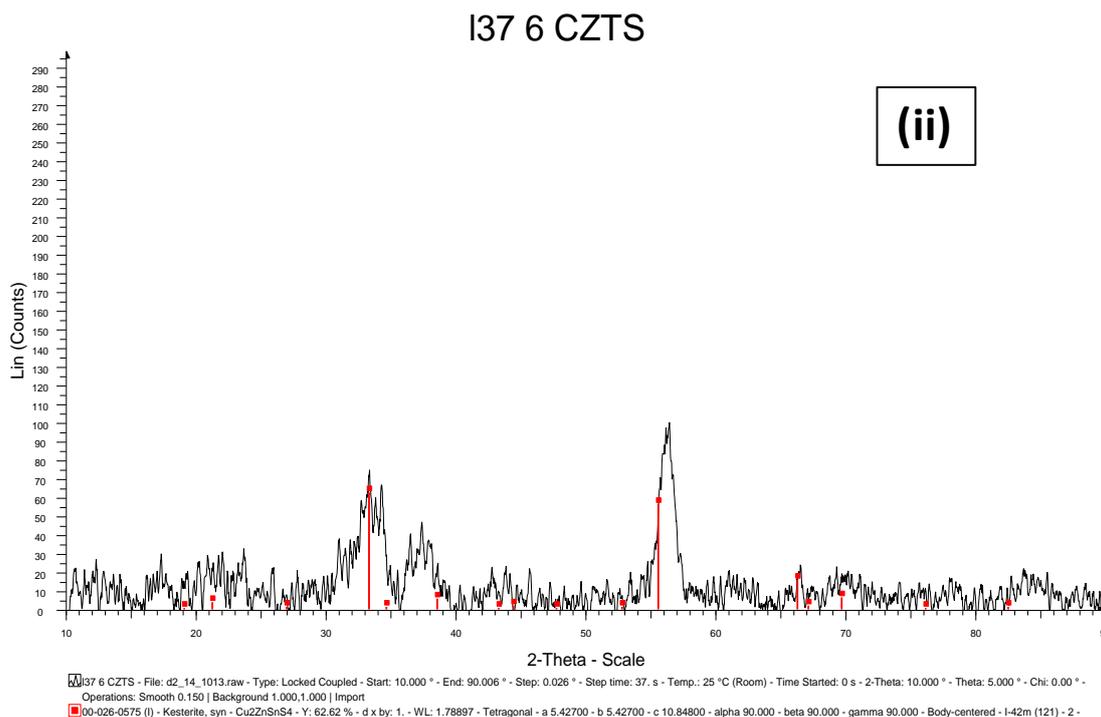


Fig. A6.2 XRD patterns of (a) CZTS and (b) CZTSe synthesized nanoparticles via MAM. The peaks are indexed to tetragonal phases of (a) $\text{Cu}_2\text{ZnSnS}_4$ and (b) $\text{Cu}_2\text{ZnSnSe}_4$ from PDF numbers 000260575 and 000520868 respectively. The peaks of synthesized CZTS and CZTSe matched well with the standards as shown

separately in (ii) and (iii). The CZTSe sample seems to be highly crystalline than CZTS, indicating the change in properties when the crystal lattice is made of S instead of Se atoms.

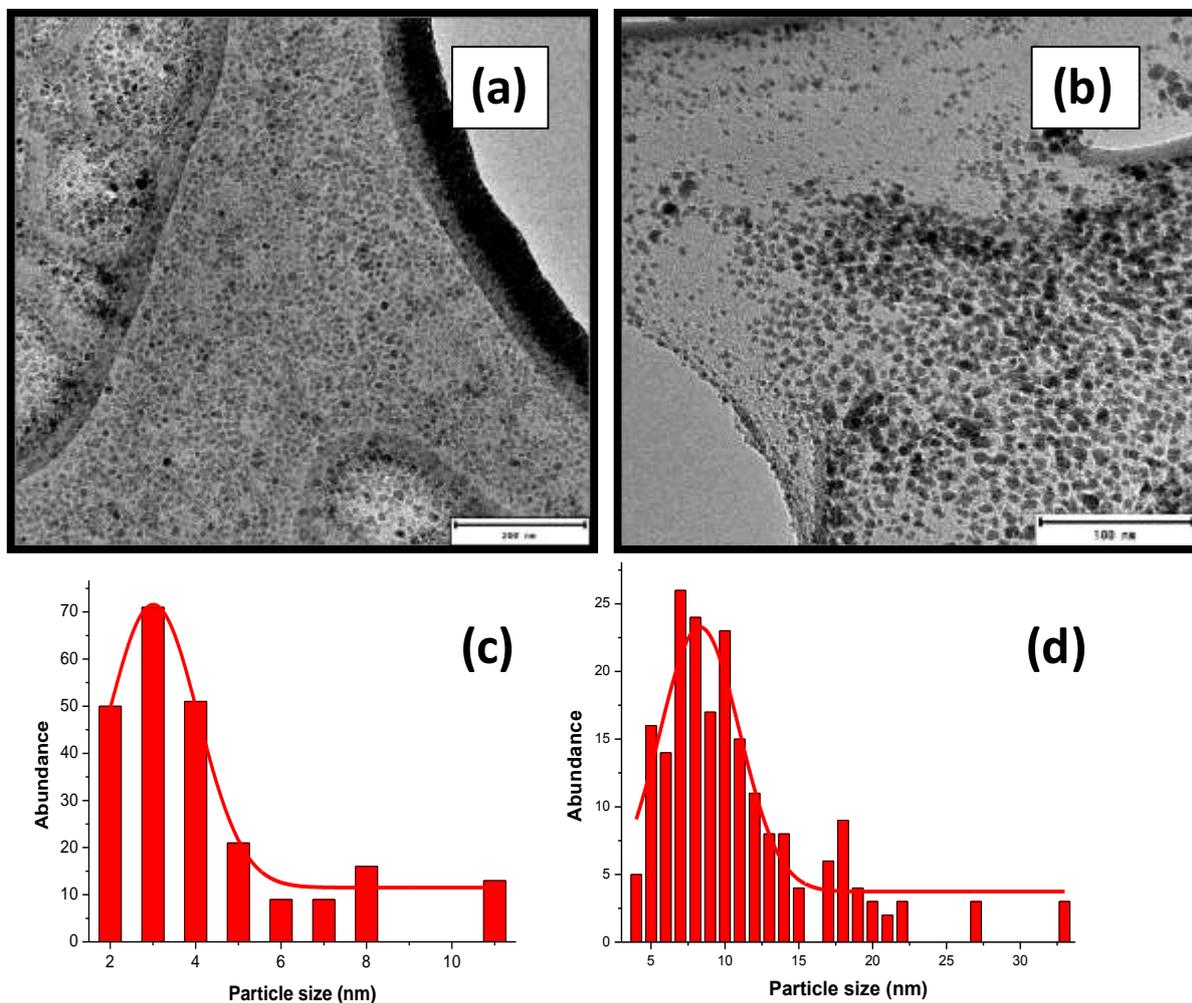


Fig. A.6.3 TEM images and size distribution of MAM synthesized (a,c) CZTS and (b,d) CZTSe. The CZTS particles are more monodispersed and within a narrower size distribution than CZTSe particles.